Transport and energization of planetary ions in the magnetospheric flanks of Mercury

Sae Aizawa

SORBONNE UNIVERSITÉ
CRÉATEURS DE FUTURS DEPUIS 1257

TOHOKU UNIVERSITY

Sorbonne Université

Ecole Doctorale Physique en Île-de-France

Laboratoire de Physique des Plasmas / Equipe des Plasmas Spatiaux

Transport and energization of planetary ions in the magnetospheric flanks of Mercury

Par Sae AIZAWA

Thèse de doctorat de Physique

Dirigée par Dominique DELCOURT et Naoki TERADA

Présentée et soutenue publiquement le 15 Février 2019

Devant un jury composé de :

1. DELCOURT, Dominique, Directeur de Recherches CNRS, Co-directeur de thèse
2. KASABA, Yasumasa, Professeur de Tohoku University, Président du jury
3. KATOH, Yuto, Professeur de Tohoku Univeristy, Examinateur
4. LEBLANC, François, Directeur de Recherches CNRS, Examinateur
5. OBARA, Takahiro, Professeur de Tohoku University, Examinateur
6. RAINES, M. Jim, Chercheur scientifique de University of Michigan, Rapporteur
7. TERADA, Naoki, Professeur de Tohoku University, Co-directeur de thèse
8. USUI, Hideyuki, Professeur de Kobe University, Rapporteur

Doctoral Thesis

Transport and energization of planetary ions in the magnetospheric flanks of Mercury

水星磁気圏側面における惑星起源イオンの輸送および加速の研究

Sae AIZAWA
(相澤　紗絵)

Department of Geophysics
Graduate School of Science
Tohoku University

Thesis Committee Members

Dr. Dominique Delcourt (Co-supervisor, LPP-LPC2E, CNRS)
Professor Yasumasa Kasaba (Chair)
Professor Yuto Katoh
Dr. François Leblanc (LATMOS, CNRS)
Professor Takahiro Obara
Dr. Jim M. Raines (University of Michigan)
Professor Naoki Terada (Co-supervisor)
Professor Hideyuki Usui (Kobe University)

2018

Abstract

Since Mercury is the closest planet to the Sun, historically there have been fewer opportunities to make spacecraft observations of this remarkable planet. Observations from Mariner-10 and MESSENGER spacecraft have brought a wealth of new information on Mercury's environment, i.e., small-scale magnetosphere, a lack of a thick ionosphere, exosphere with heavy compositions (e.g., O^+, Na^+, and K^+). In particular, the major differences between the magnetospheres of Mercury and Earth are their strength and size. Those of Mercury's magnetosphere are about 1.1% and 5% of those of Earth, respectively [e.g., *Ness et al.,* 1974, 1979]. Such smaller values lead to smaller temporal and spatial scales of the physical phenomena than those at Earth [*Ness et al.,* 1974, 1979; *Siscoe et al.,* 1975]. Under these circumstances, many interesting phenomena have been reported. For example, the magnetopause magnetic reconnection that is independent of the magnetic shear angle, short-lived dipolarization events, and modified Kelvin-Helmholtz (KH) waves depending on the gyrofrequency of heavy ions of planetary origin. However, a lot of open issues remain. Especially, one of the major differences between plasma physics of Mercury and Earth is the non-adiabatic motion of charged particles. Since Mercury's exosphere consists of heavy neutral species from the planetary surface, large gyration motion of heavy ions can be expected with a spatial/temporal scale comparable to that of the field variations. In fact, many researchers have investigated the non-adiabatic behavior of ions due to the spatial/temporal variation of the magnetic field. For instance, when the minimum curvature radius of the magnetic field is smaller than the maximum Larmor radii of considered ions, the motion of ions can be non-adiabatic. Such ions can sputter on the planetary surface. They produce secondary ions that circulate around the planet, leading to escape of heavy ions from the planetary surface. On the other hand, there is only one study of non-adiabatic acceleration of ions caused by the electric field variation suggesting that further researches on this particular aspect are required.

In this thesis, the non-adiabatic motion of charged particles due to the electric field variations is investigated using both a numerical approach and data analysis. The KH instability is considered as a key phenomenon because electric field variations are generated during its development. The properties of KH vortices around Mercury have been investigated by several papers. As *Gershman et al.* [2015] suggested, the scale of particle (Na^+) gyration motion along the duskside

magnetopause is of the same order of the thickness of the magnetopause. Here the non-adiabatic charged particle motion, depending on its mass-to-charge ratio, due to the electric field variations by the development of the KH instability can be expected. The non-adiabatic energization may lead to the unusual behavior of ions, which may affect the ion transport. The purpose of this study is to address questions, such as: How heavy ions behave within KH vortices? How are they transported or mixed? Can motion of ions be affected by the electric field variations? Investigation of charged particle motion in the vicinity of the development of KH vortices may lead to new insights into fundamental plasma physics concerning the effect of electric field variations on the gyration motion. In this study, the role of the KH instability on the transport and energization of planetary ions in the magnetospheric flanks of Mercury is revealed.

The general characteristics of the motion of planetary ions within the KH vortex are investigated firstly using a combined numerical code of the MHD simulation and the test particle tracing calculation. It is shown that the electric field variations during the development of the KH instability affect the ion gyration motions, leading to the non-adiabatic energization of ions. Especially, the intensification, rather than the change in orientation of the electric field, is responsible for large non-adiabatic energization (called $\boldsymbol{E}$ burst). Also, it is found that the occurrence of non-adiabatic energization depends on the initial perpendicular energy of ions to the magnetic field line but not on the total ion energy. The energization systematically occurs, resulting in the three-branch pattern on the energization map. If the energy of ions before experiencing the $\boldsymbol{E}$ bursts is smaller than the energy calculated with the maximum $\boldsymbol{E}$x$\boldsymbol{B}$ drift speed when they encounter the $\boldsymbol{E}$ burst along the particle path, $\varepsilon_{ExB} = \frac{1}{2} m v_{ExB,max}^2$, ions may be accelerated up to ε_{ExB}, as shown by the 1st branch on the map. The 2nd branch can be observed where the initial perpendicular energy of ions is approximately ε_{ExB}. Ions can be decelerated depending on the relationship between the particle motion and the orientation of the electric field. When ions initially have a larger energy than the ε_{ExB}, no acceleration occurs. Characterization study of the non-adiabatic energization due to both spatial and temporal electric field variations is done for the first time.

After the investigation of the general characteristics of the acceleration mechanism due to the electric field variations, Mercury's realistic field configurations and parameters are considered. We focus on the effects of the orientation of the convection electric field on the ion energization and transport throughout KH vortices in the magnetospheric flanks of Mercury. For example, the electric field pointing away from the magnetopause can be observed on the dawnside, and toward the magnetopause on the duskside under northward IMF. How the orientation of the convection electric field controls the ion dynamics is investigated. Here, several species of ions are considered and all particles are injected as picked up ions. Common features in both dawn, dusk,

northward, and southward IMF cases are observed on the energization of picked up ions in the magnetosphere. Because the magnetosphere region has a smaller convection electric field, picked up ions can experience a larger intensification of the electric field (***E*** burst) in KH vortices. If there is no development of the KH instability, no energization occurs. In contrast to ion energization, which commonly occurs in all the cases, ion transport depends on the orientation of the magnetosheath electric field. The ions picked up in the magnetosphere are transported across the magnetopause on the dawnside under the northward IMF but no transport occur on the duskside. On the other hand, the ion transport is observed on both the dawn and dusk sides under the southward IMF. On the contrary, ions picked up in the magnetosheath are generally not accelerated because they do not experience a large intensification of the electric field. Lighter ions moving with background protons can be accelerated and transported as exceptional cases.

Lastly, the numerical results discussed above are compared to in-situ measurements from MESSENGER. The data collected by FIPS aboard MESSENGER in the entire orbital phase are analyzed and specifically focused on the duskside magnetopause crossing event under northward IMF by referring to previous KH studies. FIPS is a time-of-flight type particle analyzer with an energy range from 100 eV/e up to 13 keV/e for data analysis. The spacecraft was designed and protected against strong solar heating, which caused FIPS to have a limited field of view (FOV). Limited energy range and FOV made it difficult to investigate particle acceleration. The phase space densities (PSDs) distribution of Na^+-group ions are first analyzed. Because obtained numerical results indicate no energization without the development of the KH instability, and also that the ion energization occurs with KH vortices under northward IMF, some differences on the Na^+ PSDs between the KH and non-KH events can be expected. In order to compare the KH events and non-KH events, first, all KH signatures including events reported in previous researches are collected. Because the Na^+ PSDs should be compared in a similar region of Mercury's magnetosphere, adjacent orbits before and after the orbit of the KH events are taken. We compare the normalized Na^+ PSD behavior of all orbits that fulfilled our criteria for the comparison. As a result, there is no significant difference in the Na^+ PSD behavior between KH and non-KH events. This could be because of the limited FOV and energy range.

The other possible observation fact for the energization and transport within the KH vortices is the density (or counts) of the Na^+-group. Our numerical results indicate that highly energized ions can stagnate in the duskside magnetosphere. Because picked up ions have an initial energy of a few eV, they could not be detected by FIPS immediately after their ionization. Acceleration due to the KH field results in higher energy ions, which can be detected by FIPS and are stagnated inside the magnetopause. This results in FIPS observing a high Na^+ population with the KH events. Our analysis shows that Na^+ counts by FIPS increases with the existence of KH waves.

This can be explained by the ion energization and transport via KH vortices. Meanwhile, such a large population of sodium ions can be explained differently. Previous research pointed out that the dense Na^+ population leads to the development of the KH instability. Our observations show that Na^+ occurrence increased in KH vortices. It remains to be determined whether or not those ions play a role in triggering the development of the KH instability.

The present study indicates that ions would be accelerated significantly inside the magnetosphere with KH vortices. The energized ions predicted by our study could also sputter the planetary surface and they lead to the space weathering and play an important role in supplying ions of planetary origin in Mercury's environment. Since the simple KH models and limited input parameters are used in this study, such as an absence of in-plane components of the magnetic field, and of ions already accelerated, the further investigation by global simulations is required. However, general characteristics of ion transport and energization should be the same.

In addition, further investigation with FIPS data will be done in the future, such as analysis of southward IMF KH case. Also, MIO/BepiColombo has an exhaustive plasma particle analyzer payload (MPPE consortium), having a wider energy range and FOV than FIPS. Low energy ions will be measured by MSA and MIA, which will provide the information on ions of planetary origin with wider energies in the three-dimensional field. Our simulation results will be proven by future MIO observations of direct measurement of picked-up ion acceleration/deceleration.

Abstract

The transport and energization of planetary ions within Kelvin-Helmholtz (KH) vortices developing in the magnetospheric flanks of Mercury are investigated using both numerical methods and data analysis. Due to the presence of heavy ions of planetary origin (e.g., O^+, Na^+, and K^+) and the complicated field structure present during the KH vortex development, the scale of electric field variations can be comparable to that of the ion gyromotion. Therefore, ions may experience non-adiabatic energization as they drift across the magnetopause. In this study, we focus on the effects of the spatial/temporal variations of the electric field along the ion path. We show that the intensification, rather than the change in orientation, is responsible for large non-adiabatic energization of heavy ions of planetary origin. This energization systematically occurs for ions with low initial energies in the direction perpendicular to the magnetic field. The energy gain is of the order of the energy corresponding to the maximum $\boldsymbol{E}$x$\boldsymbol{B}$ drift speed. It is also found that the ion transport across the magnetopause is controlled by the orientation of the magnetosheath electric field. Analyzing data from MESSENGER allow us to compare the observational facts with our numerical results. We find that the counts of Na^+-group detected by FIPS increase with the existence of KH waves, which is consistent with our numerical results. Although some differences in the energy distribution are expected in our numerical results, the data show no significant differences. This will be the subject of further studies using the newly developed BepiColombo instruments.

Keywords : Non-adiabatic energization, Kelvin-Helmholtz instability, MESSENGER

Résumé

Dans cette thèse, par des méthodes numériques et l'analyse de données, le transport et l'accélération d'ions suite aux tourbillons KH qui peuvent se développer dans les flancs de la magnétosphère de Mercure sont examinés. Ici, l'échelle des variations du champ électrique peut être comparable à celle du mouvement de giration des ions lorsque les ions lourds d'origine planétaire (e.g., O^+, Na^+, ou K^+) se combinent à la complexité des champs électromagnétiques issus du développement des tourbillon KH. Les ions peuvent donc être accélérés de façon non-adiabatique lors de leur passage à travers la magnétopause de Mercure. Nous nous concentrons sur les effets des variations spatiale/temporelle du champ électrique le long du trajet ionique. Nos résultats montrent que l'intensification du champ, plutôt que le changement de son orientation, est responsable de l'accélération non-adiabatique à grande échelle des ions. Cette accélération se produit systématiquement pour les ions ayant des faibles énergies initiales dans la direction perpendiculaire au champ magnétique. Le gain énergétique étant du même ordre que l'énergie correspondant à la vitesse maximale de dérive $\boldsymbol{E}x\boldsymbol{B}$. Le transport des ions est aussi contrôlé par l'orientation du champ électrique de la magnetogaine. Comparant les données de MESSENGER, nous pouvons conclure que le nombre d'ion du groupe Na^+ détectés par FIPS augmente avec la présence d'ondes KH. Bien que nos résultats numériques supposent certaines différences dans la distribution énergétique des ions, nous n'avons pas trouvé de telles disparités. Pour mieux étudier ces conclusions, des études plus approfondies basées sur BepiColombo s'avèrent nécessaires.

Mots clés : Processus non-adiabatique, Instabilité Kelvin-Helmholtz, Influence du champ électrique, MESSENGER, Transport de particules, Magnétosphère de Mercure, Simulation de particules, BepiColombo

Sommaire

Puisque Mercure est la planète la plus proche du Soleil, il y a eu historiquement moins d'occasions d'observer cette planète remarquable à l'aide de sondes spatiales. Les observations des deux seules sondes Mariner-10 et MESSENGER ont apporté une mine de nouvelles informations sur l'environnement du Mercure. Mariner-10 a montré que la Mercure a un faible champ magnétique intrinsèque et est exposé à une forte pression du vent solaire. Bien qu'il y ait des moments quadripolaires et octopolaires, nous estimons que le champ magnétique intrinsèque de Mercure est presque dipolaire avec une intensité d'environ 350 nT à l'équateur [*Ness et al.,* 1975; *Whang,* 1977]. Il s'agissait d'une découverte scientifique majeure dans le domaine des sciences planétaires qui contribuerait à améliorer notre compréhension de l'origine du système solaire. Grâce à cette découverte, nous savons maintenant que la Terre n'est pas la seule planète de notre système solaire à être magnétisée comme une planète terrestre. Les principales différences entre les magnétosphères de Mercure et de la Terre sont leur force et leur taille. Celles de la magnétosphère de Mercure représentent le entent environ 1.1 % et 5 % de celles de la Terre, respectivement [e.g., *Ness et al.,* 1974, 1979]. De telles valeurs plus faibles nous amènent à ce que les échelles temporelles et spatiales des phénomènes physiques beaucoup plus petites que celles de la Terre [*Ness et al.,* 1974, 1979; *Siscoe et al.,* 1975].

D'autre part, en plus des observations in-situ effectuées par Mariner-10, d'autres études au sol ont révélé l'environnement neutre de Mercure. La Mercure a une atmosphère non-collisionnelle ($< 10^7$ cm^{-3} au point subsolaire) ou exosphère constituée de particules neutres, notamment O, Na, He, K, H et Ca [*Broadfoot et al.,* 1976; *Potter and Morgan,* 1985, 1997]. Les espèces les plus lourdes (Na, K, O, et Ca) sont originaires de la surface planétaire. Après être libérés par divers processus (e.g., désorption stimulée par photons, désorption thermique, impacts de micrométéoroïdes, pulvérisation ionique et pulvérisation chimique), ces éléments sont ionisés par les UV solaires et immédiatement piégés par les lignes du champ magnétique. Ces particules circulent autour de la planète, guidée par les lignes du champ magnétique et peuvent ensuite être perdues dans le vent solaire ou précipiter à la surface de la planète (recyclage).

L'absence d'une ionosphère épaisse entraîne des interactions spécifiques entre la surface planétaire, l'atmosphère neutre (exosphère) et l'atmosphère ionisée (magnétosphère). Comme

nous l'avons vu plus haut, ces interactions ne sont pas visibles sur Terre et sont spécifiques à l'environnement de Mercure (nous nous référons à l'environnement herméen ci-après). Par conséquent, plusieurs questions intéressantes sur ces processus physiques devraient être abordées. Par exemple : est-il possible que Mercure ait des phénomènes physiques similaires à ceux que nous observons sur Terre ? Comment les particules sont-elles libérées et délivrées de la surface planétaire et où se déplacent-elles ? Quels sont les effets des ions lourds sur l'environnement herméen ?

La première sonde spatiale mise en orbite autour de Mercure, le MEercury Surface, Space ENvironment, GEochemistry, and Ranging (MESSENGER), lancé en 2004, a conduit à des recherches plus poussées. MESSENGER a effectué 3 survols (14 janvier 2008, 6 octobre 2008 et 29 septembre 2009) de Mercure et a été placé en orbite du 11 mars 2011 au 30 avril 2015. Cette sonde a fourni des informations beaucoup plus détaillées sur l'environnement herméen. Le magnétomètre (MAG) a mesuré le champ magnétique ambiant avec un échantillonnage de 20 mesures par seconde, et a confirmé que la magnétosphère de Mercure est largement dipolaire avec un moment magnétique de $195 \pm 10\ \mathrm{nT} - \mathrm{R_M^3}$, où $\mathrm{R_M}$ ($\mathrm{R_M} = 2440\ \mathrm{km}$) est le rayon de Mercure, et un décalage vers le nord d'environ $0.2\mathrm{R_M}$ [*Alexeev et al.,* 2008, 2010; *Anderson et al.,* 2011, 2012; *Johnson et al.,* 2012]. MESSENGER a également fourni des informations sur la composition ionique de la magnétosphère herméen. L'instrument FIPS (FIPS : Fast Imaging Plasma Spectrometer) à bord de MESSENGER a mesuré l'énergie par charge et la composition des ions. Les résultats de FIPS sont cohérents avec les observations précédentes effectuées depuis le sol, qui donnent les abondances de Na, K et Ca, et ont suggéré que la magnétosphère herméen est remplie d'ions d'origine planétaire [*Zurbuchen et al.,* 2008]. De plus, comme les espèces doublement ionisées telles que le $\mathrm{Na^{++}}$, $\mathrm{Mg^{++}}$ ont été détectées, cela indique que les électrons d'énergie inférieure à 1 keV sont accélérés à l'intérieur de la magnétosphère herméen. Ces espèces qui proviennent de l'exosphère de Mercure après ionisation photonique, ont été observées dans la magnétogaine et dans la magnétosphère [*Zurbuchen et al.,* 2011; *Schriver et al.,* 2011a, b; *Raines et al.,* 2011, 2013; *DiBraccio et al.,* 2013; *Gershman et al.,* 2015]. Dans ces circonstances, de nombreux phénomènes intéressants ont été identifiés. Par exemple, la reconnexion magnétique à la magnétogaine qui dépend faiblement de l'angle de cisaillement magnétique, des événements de dipolarisation de courte durée (quelques secondes) et des ondes Kelvin-Helmholtz (KH) modifiées en fonction de la gyrofréquence des ions lourds d'origine planétaire. De plus, des électrons énergétiques ont été détectés par différents instruments à bord de MESSENGER. L'instrument FIPS a également mesuré indirectement des électrons dans la gamme MeV tandis que le spectromètre de particules énergétiques EPS les a mesurés entre 35 keV et 1 MeV. De plus, les spectromètres à rayons X, gamma et neutres ont mesuré des électrons énergétiques de plusieurs

keV à quelques centaines de keV [*Andrews et al.,* 2007; *Goldsten et al.,* 2007; *Lawrence et al.,* 2015; *Ho et al.,* 2016; *Baker et al.,* 2016]. Autour de Mercure, l'accélération a lieu non seulement pour les ions lourds d'origine planétaire mais aussi pour les électrons. Toutes ces recherches antérieures ont révélé que Mercure est un environnement beaucoup plus dynamique que notre planète Terre en raison des petites échelles de la magnétosphère et des effets cinétiques connexes des particules chargées.

Dans cette thèse, nous nous intéressons à l'instabilité Kelvin-Helmholtz (KH) qui est un phénomène-clé autour de Mercure [*Boardsen et al.,* 2010; *Sundberg et al.,* 2011, 2012a; *Liljeblad et al., 2014, 2016*; *Gershman et al.,* 2015]. Généralement, il se produit lorsqu'il y a un cisaillement de vitesse entre deux fluides adjacents [*Helmholtz,* 1986; *Kelvin,* 1871]. Cette instabilité est bien connue en hydrodynamique. Lorsque l'instabilité KH est complètement développée, elle crée des tourbillons qui jouent un rôle dans le transport d'impulsion et dans le mélange de deux fluides différents [*Fritts et al.,* 1996]. Dans le domaine de l'hydrodynamique, cette instabilité est généralement observée dans une couche nuageuse et/ou à la surface de la mer [*Kelvin,* 1871]. Nous pouvons aussi la voir à la magnétogaine et/ou l'ionogaine des planètes dans le domaine de la physique des plasmas spatiaux. Pour les planètes magnétisées, la magnétogaine apparaît comme une couche limite entre le vent solaire et les plasmas planétaires avec un fort cisaillement de vitesse. Dans ces circonstances, nous pouvons s'attendre au développement de l'instabilité KH dans les flancs magnétosphériques. À la magnétogaine terrestre, même en présence de plasmas sans collision, les tourbillons KH jouent un rôle important dans le transport de la masse et d'impulsion ainsi que dans le mélange des plasmas [*Miura et al.,* 1984; *Fujimoto and Terasawa,* 1994]. Le vortex KH peut aussi être un déclencheur de reconnexion magnétique à l'intérieur du vortex [*Nykyri and Otto,* 2001]. Dans les flancs magnétosphériques de la Terre, il existe de nombreux études sur l'instabilité KH à partir des mesure de différentes sondes [e.g., *Chen and Kivelson,* 1993; *Mozer et al.,* 1994; *Fujimoto et al.,* 2003; *Hasegawa et al.,* 2004; *Hwang et al.,* 2011; *Yan et al.,* 2014]. En ce qui concerne les flancs magnétosphériques de Mercure, certains études ont rapporté des observations de tourbillons KH en utilisant les données de MESSENGER [*Slavin et al.,* 2008; *Sundberg et al.,* 2011, 2012a; *Gershman et al.,* 2015; *Lijeblad et al.,* 2014, 2016]. En raison de la conception de MESSENGER et l'instrument, les instabilités de KH ont été principalement observées à la magnétogaine du côté crépuscule. Les auteurs ont conclu que l'apparition de l'instabilité du KH autour de Mercure est caractérisée par une forte asymétrie entre aube et crépuscule (les observations au crépuscule représentent 95 % des cas mesurés). Cette asymétrie peut être causée par l'effet cinétique des particules chargées, ou « effet de rayon Larmor fini », ou par l'absence d'écoulement laminaire à grande échelle du côté aube [*Liljeblad et al.,*

2014; *Paral and Rankin,* 2013]. Dans les flancs magnétosphériques, où les lignes de champ magnétique sont presque perpendiculaires au plan équatorial, on s'attend à une variation rapide du champ électrique en raison du développement de l'instabilité du KH. Comme on l'a vu plus haut, si les champs varient rapidement pendant le mouvement de giration de la particule ($t < \tau$, ou τ est la période de giration), le mouvement des particules peut être affecté par les variations de champ, conduisant à ce que le 1er invariant adiabatique ne soit plus conservé. Dans ce cas, nous ne pouvons plus utiliser l'équation du centre de guidage du mouvement pour tracer le mouvement exact des particules. Le mouvement de giration doit être suivi par une seule équation de mouvement des particules. Ceci est notamment le cas lors de variations rapides du événement de dipolarisation soudaine.

Le mouvement des particules non-adiabatique a été étudié par plusieurs auteurs, en particulier dans la queue de la magnétosphère de la Terre pour étudier la variation spatiale du champ magnétique. Les conditions dans lesquelles se produit le comportement des particules non-adiabatiques ont été discutées dans plusieurs articles utilisant ce κ paramètre. Ce paramètre est défini en prenant la racine carrée du rapport du rayon de courbure minimal du champ magnétique et du rayon de gyration maximum pendant tout le mouvement des particules. Lorsque $\kappa > 3$ que l'on peut voir par exemple à la limite de l'isotropie dans la magnétosphère de la Terre, on peut utiliser l'équation du centre de guidage du mouvement [e.g., *Sergeev et al.,* 1983, 1994]. Dans le régime $1 \leq \kappa \leq 3$, appelé régime "chaotique", le mouvement des particules peut être hélicoïdal et n'avoir aucun mouvement en méandres. L'inversion du champ magnétique dans la région équatoriale n'est pas assez nette pour permettre une orbite de Speiser, mais elle est suffisante pour casser l'approximation du centre de guidage. En d'autres termes, le moment magnétique μ n'est pas conservé [e.g., *Büchner and Zelenyi,* 1989; *Delcourt and Martin,* 1994]. Particulièrement, $\kappa \approx 1$ est la limite à laquelle le mouvement sinueux devient possible. Le mouvement non-adiabatique peut se produire en raison de la force centrifuge impulsive, et sa variation du moment magnétique est organisée selon un modèle à trois branches. L'amélioration systématique μ est observée pour les petits angles de tangage, tandis que des changements négligeables μ sont observés pour les grands angles de tangage. Dans le régime actuel, le mouvement ou l'accélération non-adiabatique cause plusieurs caractéristiques intéressantes liées à la dynamique ionique et à l'environnement plasma autour de la planète [e.g., *Ashour-Abdalla et al.,* 1993a, b]. *Ashour-Abdalla et al*. [1993b] a signalé que l'amélioration du piégeage avec un gain d'énergie important pendant le grand mouvement de dérive vers le côté du crépuscule. De plus, le groupement de phases peut être causé par le mouvement non-adiabatique. Ceci conduit au développement d'une mince feuille de courant, comme c'est le cas pour les ions se déplaçant dans la feuille de plasma

proche de la Terre [*e.g., Delcourt et al,* 1995, 1996a, b]. De plus, nous avons également signalé les conséquences de la précipitation des ions sur les aurores, les structures ioniques dispersées en énergie et les activités ionosphérique et plasmatique [*e.g., West et al.,* 1978a, b; *Wagner et al.,* 1979; *Lyons and Speiser,* 1982; *Ashour-Abdalla et al.,* 1991, 1992; *Keiling et al.,* 2004]. Pour le régime $\kappa < 1$ (ce qui signifie que le rayon de Larmor de la particule est plus grand que le rayon de courbure de la ligne de champ) est discuté. En d'autres termes, les particules subissent toujours le champ magnétique dirigé en sens inverse lorsqu'elles traversent l'équateur magnétique et le moment magnétique peut donc ne pas être conservé. *Delcourt et al.* [1996] a examiné la diffusion de l'angle de tangage affectant la précipitation ionique, révélant qu'un modèle à trois branches a émergé près de l'énergie de résonance (précédemment rapporté par *Burkhart and Chen* [1991]). La variation du motif à trois branches dépend du paramètre κ, et les branches disparaissent lorsqu'elles se trouvent dans le régime de l'off-résonance. Toutes les recherches mentionnées ci-dessus ont été faites en considérant seulement les variations spatiales du champ magnétique, paramétrées par κ. Ci-dessous, nous discuterons de quelques études sur les variations temporelles du champ magnétique, par exemple, le cas de l'événement de dipolarisation [e.g., *Aggson et al.,* 1983; *Delcourt et al.,* 1990, 2002, 2010; *Nosé et al.,* 2000a, b; *Daglis,* 2001]. En considérant une variation graduelle des niveaux de Kp, on a modélisé la reconfiguration de courte durée de la magnétosphère, équivalente aux sous orages auroraux. Comme pour le mouvement non-adiabatique dû à la variation spatiale du champ magnétique, les variations temporelles du champ peuvent causer un mouvement non-adiabatique, y même lorsque les $\kappa > 3$. Ils ont observé le même schéma à trois branches et un gain d'énergie important pendant les événements de dipolarisation par rapport aux temps non dépolarisants. En particulier, *Delcourt et al.* [2010] ont étudié l'excitation non-adiabatique pendant la compression du champ magnétique à Mercury. Ils montrent que nous nous' attend à ce qu'un changement important soit efficace lorsque l'échelle des variations de champ et la période cyclotronique sont comparables. Il s'agit d'un type de gain d'énergie "en résonance".

Si nous considérons le mouvement non-adiabatique dû aux variations du champ électrique, il n'y a qu'une seule étude étudiée par *Rothwell et al.* [1994]. Ils ont injecté des ions dans le domaine du gradient de champ électrique (la discontinuité de Harang dans la magnétosphère proche de la Terre) et étudié le comportement des particules. L'existence de la discontinuité de Harang provoque le groupement gyro-phasique des ions oxygène, qui est équivalent aux changements de distribution de vitesse, ce qui entraîne des striations de densité. Actuellement, il s'agit de la seule étude du mouvement non-adiabatique causé par la variation du champ électrique, ce qui suggère que des recherches supplémentaires sur cet aspect particulier sont nécessaires.

Étant donné que le mouvement non-adiabatique est causé en fonction de la relation entre l'échelle du mouvement de giration des particules et celle des variations de champ, seules certaines espèces d'ions peuvent être affectées par celui-ci.

Puisque nous nous concentrons sur le mouvement des particules dans le champ KH en adoptant une revue dans une configuration de champ obtenue par de simulations MHD. Pour simplifier, nous avons adopté ici une approche en deux étapes, c'est-à-dire que nous avons d'abord analysé la dynamique ionique dans une configuration de tourbillons statique, puis dans une configuration d'éliminer les effets de phasage entre les trajectoires des particules et les tourbillons KH rapidement obtenu en premier lieu.

Dans nos calculs, la position des particules, l'énergie totale, l'angle de tangage et l'angle d'attaque et la phase de gyration sont entrés comme paramètres initiaux. De plus, le moment magnétique instantané est calculé à chaque pas de temps. Afin de combiner le tracé des particules d'épreuve et la simulation MHD, nous calculons d'abord les informations sur les champs par la simulation MHD. Plus, toutes les grandeurs physiques normalisées sont transformées en valeurs physiques et utilisées pour le suivi des particules. Dans la simulation MHD, les valeurs physiques sont reliées au centre de chaque grille et calculées par des lois de conservation. Afin d'obtenir les valeurs du champ électrique/magnétique à une position de particules arbitraire, nous utilisons la méthode de pondération de surface comme méthode d'interpolation.

Ce faisant, nous avons pu montrer que les variations du champ électrique pendant le développement de l'instabilité du KH affectent le mouvement de gyration des ions, ce qui conduit au déclenchement de comportements non-adiabatique. Des études antérieures sur ce transport ont porté sue les effets des variations spatiales et temporelles des variations du champ magnétique. Nous avons introduit ici un nouveau type d'excitation non-adiabatique causée à la fois par les variations temporelles et spatiales du champ électrique, que nous dénommons « $\boldsymbol{E}$ burst ». *Rothwell et al*. [1994] ont déjà montré qu'un regroupement en phase de gyration peut se produire en raison de gradients du champ électrique, d'où la formation de distributions non-gyrotropiques. Ici, nous avons caractérisé le gain d'énergie systématique du aux « $\boldsymbol{E}$ bursts ». Nous avons montré que le comportement non-adiabatique dépend de l'énergie perpendiculaire initiale des ions et non pas de l'énergie totale. Deuxièmement, nous avons également obtenu trouve un modelé a trois branches pour le processus d'accélération, à savoir : si la particule a une énergie perpendiculaire inférieure à celle de la vitesse de dérive $\boldsymbol{E}\times\boldsymbol{B}$ maximale le long de la trajectoire des particules. Alors la particule peut gagner de l'énergie jusqu'à ~ $\varepsilon_{ExB} = \frac{1}{2} m v_{ExB,max}^2$, contribuant ainsi à une première branche du schéma. La deuxième branche est produite par les particules dont l'énergie perpendiculaire initiale est de l'ordre de ε_{ExB}. Les ions peuvent perdre de l'énergie en fonction de

l'angle entre direction de déplacement et direction du champ électrique. Enfin, si la particule a une énergie initiale supérieure à $\varepsilon_{E\times B}$, elle ne gagne pas d'énergie de façon significative. De plus, nous avons constaté que l'augmentation de l'amplitude des « $\boldsymbol{E}$ bursts » peut entrainer des changements d'énergie nette plus marques. L'effet de l'échelle de temps et de l'amplitude des « $\boldsymbol{E}$ bursts » a été examiné en détails. Nous avons constaté que, comme attendu, le gain en énergie varie en proportion de l'amplitude du « $\boldsymbol{E}$ bursts ». Toutefois, il est apparu que si l'échelle de temps de ce burst est comparable à la période de gyration, plus précisément lorsque $\tau/\tau_C \sim 0.5$, la variation de champ peut modifier considérablement le mouvement des particules même si l'amplitude est faible. Dans cette étude, nous avons pour la première fois caractérisé l'activation non-adiabatique due aux variations spatiales et temporelles du champ électrique. Cette étude a été réalisée en utilisant des champs KH fixes (champ non-variable dans le temps) par souci de simplicité. Les mêmes caractéristiques ont été obtenues dans le champ KH variable dans le temps et nous voyons surtout que l'excitation des particules se produit lorsque le vortex KH se forme.

Après l'étude des caractéristiques générales du mécanisme d'accélération due aux variations du champ électrique présentée dans le Chapitre 4, des configurations de champ représentatives de l'environnement herméen et des paramètres ioniques ont été examinées au Chapitre 5. Dans ce chapitre, nous nous sommes concentrés sur les effets de l'orientation du champ électrique de convection sur l'accélération des ions à travers les tourbillons KH dans les flancs magnétosphériques. Lorsque le champ magnétique interplanétaire (IMF) pointe vers le nord, un champ électrique s'éloignant de la magnétogaine peut être observe a l'aube, et vers la magnétogaine au crépuscule. Nous avons étudié comment cette orientation du champ électrique de convection contrôle la dynamique ionique.

En injectant 10 000 ions test avec une certaine énergie cinétique initiale totale des particules et un angle de phase aléatoire, une analyse quantitative de l'activation et du transport des ions a été réalisée. Nous avons examiné la dynamique des ions dans un champ KH variant dans le temps du côté de l'aube et du côté du crépuscule afin d'explorer l'effet de l'orientation du champ électrique à grande convection. Une variété d'ions d'origine planétaire (H^+, H_2^+, O^+, Na^+, ou K^+) a été injectés sous forme d'ions captés à trois temps d'injection différents correspondant à différents stades du développement de l'instabilité du KH (au début, dans la phase de croissance linéaire et dans la phase de croissance non linéaire de l'instabilité du KH). Quant aux plasmas du vent solaire, deux espèces (H^+, He^{++}) sont prises en compte. Ils ont été injectés sur la trame $\boldsymbol{E}\times\boldsymbol{B}$ au début du calcul MHD. Les conditions du IMF vers le nord et vers le sud ont été prises en compte.

Des caractéristiques communes à l'aube et au crépuscule, ainsi qu'au nord et au sud, ont été observées sur l'excitation des ions captés dans la magnétosphère. Dans les régions de la magnétosphère ou le champ électrique de convection est plus faible, les ions piégés peuvent subir

une plus grande intensification du champ électrique (***E*** burst) dans les tourbillons KH, et l'accélération des ions dépend donc de l'orientation du champ électrique dans la magnétogaine. Dans le secteur du matin, les ions de la magnétosphère peuvent être transportes à travers la magnétogaine dans le cas d'un IMF nord, mais aucun transport de ce type n'est pas obtenu du côté soir. Un tel transport se produit par contre dans les deux secteurs dans le cas d'un IMF pointant vers le sud. A l'inverse, les ions captés vers la magnétosphère depuis la magnétogaine ne sont généralement pas accélérés car ils ne subissent pas de forte intensification du champ électrique. La comparaison des résultats obtenus dans les cas IMF nord et IMF sud nous a amené à examiner l'importance de l'orientation du champ électrique de convection. Le premier cas montre un plus grand nombre d'ions accélérés et transportés que dans le deuxième cas. Dans le premier cas, les champs électriques de la magnétogaine et de la magnétosphère sont opposés. A l'inverse, les champs électriques pointent dans la même direction dans le deuxième cas. Lorsque le vortex KH évolue dans le temps, le champ électrique change également de configuration, c'est-à-dire qu'une composant de rotation apparait dans le vortex. Les champs électriques opposés (Cas 1) peuvent développer un champ électrique uni-directionnel depuis le centre du vortex vers l'extérieur ou vice-versa, qui est la même direction que celle initiale. Les champs électriques de même direction (Cas 2) font également une configuration similaire dans le tourbillon, mais ils peuvent contenir un champ électrique dirigé à l'opposé de la configuration initiale du champ électrique. Dans ce cas, les ions peuvent subir un champ électrique à orientation variable pendant leur mouvement de gyration, ceci, conduisant à une accélération ou une décélération nette.

Les résultats que nous avons obtenus ont des conséquences pour les mesures in-situ. En effet, les ions énergétiques peuvent stagner a la magnétosphère du cote du crépuscule, tandis que des populations moins denses existent a la magnétosphère du cote aube dans le cas IMF vers le nord. Pour les ions de la magnétogaine, même s'ils sont captes loin de la magnétogaine, nous montrons qu'ils peuvent pénétrer dans la magnétosphère en raison de leur grand rayon de Larmor. Nos résultats suggèrent que ce transport se produit au crépuscule dans le cas IMF nord et que pour un tel IMF, il n'y a pas de pénétration de la magnétogaine du côté aube. En revanche, un transport ionique est observable à l'aube et au crépuscule dans le cas IMF sud.

Nous avons examiné ensuite le gain en énergie et le transport des ions pour des IMF nord ou sud sans aucune autre composante. D'autres composants du champ magnétique peuvent modifier le transport et/ou l'énergie des ions, mais nous sommes concentrés sur les flancs magnétosphériques où la composante z du champ magnétique est dominée. Il est vraisemblable que les caractéristique générales de la dynamique ionique des ions sont similaires avec d'autre composantes.

Nous avons aussi étudié l'entrée du plasma dans le vent solaire (H^+ et He^{++}). Nous avons constaté que le comportement des plasmas du vent solaire est semblable à celui de la MHD et que

l'entrée du vent solaire ne se produit que près de la magnétopause, déterminée par la taille du vortex KH. Les mécanismes d'accélération sont les mêmes que ceux des ions d'origine planétaire, les structures fines dues à la rupture des tourbillons KH à un stade ultérieur du développement de l'instabilité KH, correspondant à la petite échelle du mouvement des ions légers, accélèrent les plasmas du vent solaire. Cette accélération non-adiabatique des protons du vent solaire conduirait à la violation de l'approximation MHD. Puisque les paramètres initiaux des protons injectés et des protons MHD de fond ne sont pas les mêmes, nous ne pouvons pas montrer un certain temps de la violation de l'approximation MHD. L'effet de la cinétique ionique doit être pris en compte dans le stade ultérieur de l'instabilité de la KH.

Les résultats numériques des Chapitres 4 et 5 ont été comparés aux mesures in situ de MESSENGER au Chapitre 6. Nous avons analysé les données recueillies par la FIPS à bord du MESSENGER en phase orbitale complète du 11 mars 2011 au 30 avril 2015. En particulier, nous avons analysé l'événement de traversée de la magnétopause à la tombée de la nuit dans le cadre de l'étude du IMF vers le nord en nous référant à des études KH antérieures. FIPS est un analyseur de particules de type temps de vol avec une gamme d'énergie de 100 eV/e à 13 keV/e pour l'analyse de données. La conception du vaisseau spatial et la protection contre le fort ensoleillement, FIPS a un champ de vision limité (FOV).

La gamme d'énergie limitée et la FOV nous rendent difficile d'étudier l'accélération des particules. Nous avons commencé avec la distribution de la densité de l'espace de phase (PSD) des ions du groupe Na^+ . Puisque nos résultats numériques n'indiquaient aucune excitation sans le développement de l'instabilité du KH et qu'il y a excitation ionique avec les tourbillons KH dans le cas d'IMF vers le nord, nous nous attendions à certaines différences sur les Na^+ PSD entre les événements du KH et les autres. Afin de comparer l'événement KH et l'événement non-KH, nous avons d'abord recueilli toutes les signatures KH, y compris les événements rapportés dans les articles précédents. Comme les Na^+ PSD doivent être comparées dans une région similaire de la magnétosphère herméen, nous avons pris une orbite adjacente avant et après l'orbite des événements KH. Nous avons comparé le comportement Na^+ PSD normalisé de toutes les orbites remplissant nos critères pour la comparaison. Par conséquent, nous n'avons malheureusement pas pu trouver de différence significative sur le comportement Na^+ PSD entre les événements KH et non-KH. Il y a une petite différence dans le comportement normalisé du PSD dans la magnétosphère, mais il s'agit d'une signature de décélération. Aucune différence significative n'a pu être constatée en raison de la portée FOV et de la gamme d'énergie limitées. Cependant, la proximité de la magnétopause nocturne (19LT - 21LT) peut être peuplée d'ions à haute énergie provenant de la région de la queue de magnétosphère. Ils ont été facilement détectés par la FIPS. Bien que les ions captés devraient être présents, si une telle population d'ions lourds accélérés

d'origine planétaire est dominée dans cette région, le comportement du PSD ne peut pas être beaucoup changé. L'accélération n'a pas pu être vue mais la décélération de tels ions déjà accélérés peut-être ralentie si l'énergie des ions est comparable à l'énergie correspondant à la vitesse de dérive $\boldsymbol{E}x\boldsymbol{B}$. En estimant la vitesse du vent solaire des événements KH, nous avons constaté que cette explication peut être raisonnable.

Les autres faits d'observation possibles pour l'excitation et le transport dans les tourbillons KH sont la densité (ou le nombre) du groupe Na^+. Les ions à haute énergie peuvent stagner dans la magnétosphère au crépuscule. Comme les ions captés ont une énergie initiale de peu d'eV, ils ne peuvent pas être détectés par la FIPS juste après leur ionisation. L'accélération due au champ KH produit des ions d'énergie plus élevée qui peuvent être détectés par FIPS, et ils stagnent à l'intérieur de la magnétopause. Il en résulte que la FIPS peut observer une forte population de Na^+ avec les événements KH. Notre analyse a montré que les comptes par FIPS augmentent avec l'existence d'ondes KH. Ceci peut s'expliquer par l'excitation ionique et le transport via les tourbillons KH. Entre-temps, une population aussi importante d'ions sodium peut s'expliquer différemment. Des recherches antérieures ont montré que la densité de la population de Na^+ conduit au développement de l'instabilité des KH. Nos observations montrent que la présence de Na^+ augmente dans les tourbillons KH augmente. Il permet de voir si ces ions jouent un rôle dans le déclenchement du développement de l'instabilité du KH.

En plus des grands comptes de Na^+ dans les FIPS avec l'existence d'ondes KH, nous avons constaté que l'instabilité de KH se produit probablement lorsque la composante Z du champ magnétique est plus forte. En obtenant la distribution du nombre d'ions de groupe dans la magnétogaine et dans la magnétosphère en fonction de la composante Z moyenne du champ magnétique de la magnétogaine, on constate que les événements KH ont une amplitude de champ magnétique supérieure à 15 nT, et que le nombre d'événements KH augmente avec la composante Bz croissante. D'autre part, le nombre de groupes dans les événements non KH a également de grands nombres dans la magnétogaine-magnétique, même si la magnitude correspondante de Bz est petite. Cela peut s'expliquer par la théorie linéaire de la croissance du KH. La composante parallèle du champ magnétique au nombre d'ondes de l'onde KH (ici Bx et By) stabilise le développement de l'instabilité comme tension magnétique. Cette caractéristique est cohérente avec la prédiction de la théorie linéaire.

Notre étude numérique a indiqué que les ions seront accélérés de manière significative à l'intérieur de la magnétosphère avec des tourbillons KH et que le transport est contrôlé par l'orientation du champ électrique dans la région de la magnétogaine, et nos résultats d'analyse des données les soutiennent. Des études antérieures sur l'énergie non-adiabatique ont montré que de

tels ions non-adiabatiques peuvent pulvériser la surface planétaire. Une telle pulvérisation superficielle produit une atmosphère neutre secondaire qui constitue l'exosphère. Les ions énergisés prévus par notre étude peuvent également pulvériser la surface planétaire et ils conduisent à l'altération de l'espace et à un rôle important des ions d'origine planétaire dans l'environnement herméen. De nombreuses études sur l'excitation non-adiabatique à Mercure ont pris en compte les phénomènes physiques près de la queue de magnétosphère, et donc, un tel processus de pulvérisation cathodique a été considéré comme un important processus de fabrication de l'exosphère dans la région du côté nocturne. En ce qui concerne l'apparition de l'instabilité KH, elle se développe également dans la région diurne, ce qui signifie que le processus de pulvérisation peut également être considéré dans la surface diurne. Afin d'étudier cette interaction, une analyse plus poussée des données est nécessaire. Et aussi, le transport global devrait se faire par l'approche numérique.

D'autres recherches avec des données FIPS seront effectuées à l'avenir, comme l'analyse du cas KH avec IMF vers le sud. Par ailleurs, le satellite MIO/BepiColombo possède une charge utile d'analyseur de particules plasmatiques exhaustive (consortium MPPE), ayant une gamme d'énergie et des FOV plus larges que ceux de FIPS. Les mesures de instruments MSA et MIA nous fourniront l'information des ions d'origine planétaire avec des énergies plus larges dans le champ tridimensionnel. Nos résultats de simulation seront ainsi mis en perspective par les gutures observations de MIO.

BepiColombo a été lancé avec succès le 19 octobre 2018 et 7 ans de voyage vers Mercure viennent de commencer. La découverte majeure de Mariner-10 a été l'existence du champ magnétique intrinsèque de Mercure. Après le Mariner-10, le vaisseau spatial MESSENGER a apporté quelques informations détaillées sur l'environnement et la surface de Mercure. Toutefois, de nombreuses questions restent en suspens. BepiColombo qui est une mission conjointe de l'ESA et de la JAXA, dispose de deux séries de vaisseau spatiaux pour étudier les mystères de cette planète-là plus profonde de notre système solaire. La révélation de l'environnement de Mercure est une partie importante de l'approche de l'histoire de notre système solaire.

MIO, principalement développé par la JAXA, est l'un des deux satellites de cette mission. Les objectifs de MIO sont d'observer le champ magnétique planétaire, l'exosphère libérée de la surface, l'espace interplanétaire, ses variations et sa physique. Un grand sujet lié à notre étude est : Comment le champ magnétique, la magnétosphère et l'exosphère de Mercure interagissent-ils avec le vent solaire ? Quelle est l'importance des ions lourds dans l'environnement herméen ?

Puisque Mercure est la planète terrestre aimantée, des phénomènes similaires à ceux que nous avons sur Terre devraient se produire sur la Mercure. Différents instruments à bord du MIO

aborderont ces phénomènes et questions ouvertes. En particulier, les analyseurs de particules plasmatiques font partie du consortium MPPE. Pour les analyseurs d'énergie inférieure pour les ions lourds d'origine planétaire et les plasmas de vent solaire, nous avons MSA et MIA. Le MSA est un spectromètre temps de vol MSA (Mass Spectrum Analyzer) fournira des informations sur la composition du plasma et les fonctions de distribution des ions [*Delcourt et al*., 2009b] parmi les capteurs MPPE. Le MSA a amélioré la capacité de résolution de masse grâce au champ de vision tridimensionnel, ce qui nous permet d'avoir une identification détaillée de divers matériaux et espèces d'origine planétaire et de leur propagation, et fournit des informations sans précédent sur l'environnement herméen. Le MSA dispose de deux détecteurs pour obtenir la distribution et la composition du plasma : LEF (LEF : linear electric field) qui fournira des données à haute résolution de masse en utilisant une technique exercée, et l'autre est ST (ST : straight-through) qui fournira des distributions de comptage élevées. La figure 7.1 présente une illustration schématique de l'algorithme MSA, et des informations détaillées sont disponibles dans *Delcourt et al*. [2009b]. Ces deux types différents de modes d'observation sont utilisés en réponse aux objectifs.

Les grandes différences entre la magnétosphère terrestre et la magnétosphère de Mercure sont leur taille et leur composante plasma. Nous pensons que les ions lourds d'origine planétaire jouent un rôle important dans la dynamique magnétosphérique à Mercure, et donc que les phénomènes physiques seraient attendus différemment comme nous les voyons sur Terre. Cependant, sa densité de la population d'ions lourds et sa distribution tridimensionnelle n'ont pas encore été révélées. MSA à bord de MIO collectera divers composants ioniques à haute résolution de masse et à plus grande portée énergétique dans le champ de vision tridimensionnel. Cela nous aidera à comprendre la physique générale des plasmas spatiaux à Mercure. En plus de l'observation par le seul MIO, des mesures simultanées par les deux séries de vaisseau spatiaux de BepiColombo sont prévues pendant sa phase orbitale.

Dans notre étude, bien que l'accélération et le transport des ions aient été démontrés numériquement, nous n'avons pas pu obtenir de différence significative dans la PSD entre les événements KH et non-KH en raison des conditions FIPS limitées. La détection d'ions avec une énergie inférieure, environ quelques eV est permise par MSA et ainsi, l'accélération ionique devrait être mesurée directement. La propagation des ondes le long de la magnétopause est également un intérêt clé pour le développement de l'instabilité du KH. Il serait fourni par l'observation de conjonction.

Les découvertes de Mariner-10 au cours des trois survols de Mercure ont eu un impact sur tous les chercheurs et ont dépassé toutes les attentes pour l'environnement herméen. L'exploration de Mercure par MESSENGER a donné lieu à de nombreuses nouvelles connaissances et perspectives

mondiales sur la Mercure, telles que sa surface, l'exosphère et la magnétosphère en tant que système couplé autour de la planète. Bien que deux vaisseaux spatiaux antérieurs aient apporté autant d'information que possible, les limites de nos connaissances et de notre compréhension en raison des capacités de ces vaisseaux spatiaux se sont révélées en même temps. La mission BepiColombo devrait mener d'autres enquêtes. BepiColombo lancera la nouvelle ère de l'étude intensive de Mercure, incluant la surface, l'exosphère et la magnétosphère et leurs interactions mutuelles. Du point de vue de la physique magnétosphérique, plusieurs nouveaux types d'instruments ont été sélectionnés en plus des types similaires avec une résolution plus élevée et une gamme plus large de FOV et d'énergie. BepiColombo devrait apporter de nouvelles découvertes majeures, et la compréhension de la dynamique ionique de Mercure permettra également de mieux comprendre la dynamique des ions terrestre.

Acknowledgement

I deeply appreciate to my two supervisors, Prof. Naoki Terada at Tohoku University and Dr. Dominique Delcourt at Laboratoire de Physique des Plasmas (LPP) for providing this precious opportunity to engage this work with continuous stimulating guidance and encouragement. I have learned many things from them, the space plasma physics, numerical techniques, thinking and explaining the problems in a logical way, what is the good figures and presentations. I would not be able to accomplish the thesis without their support. They gave me many opportunities to study abroad and to challenge new things.

I would also like thank to Dr. Jim M. Raines from the University of Michigan. He welcomed me to his laboratory twice and taught me how to start analyzing MESSENGER FIPS data. He kindly gave me an introduction of data analysis, engaging discussions, and also contributed to this thesis. I'm also thankful to Dr. James A. Slavin for his useful comments, and the entire group in University of Michigan welcomed me with warm and friendly atmosphere, and their support during my stay at the University of Michigan was helpful for me.

My heartful thanks go to Prof. Hideyuki Usui from Kobe University for his meaningful comments and discussions and it contributes to this thesis. Dr. Manabu Yagi from RIKEN is also acknowledged here. In particular, as one of the few researchers working with magnetospheric physics of Mercury in Japan, discussions with him were always fruitful.

I also would like to express my deep thanks to the rest of the members of my jury: Prof. Takahiro Obara, Prof. Yasumasa Kasaba, Prof. Yuto Katoh from Tohoku University, and Dr. François Leblanc from LATMOS.

I'm grateful to all members in C-group of Tohoku University for always giving me helpful advices: Associate Prof. Isao Murata, Associate Prof. Atsushi Kumamoto, Associate Prof. Takeshi Sakanoi, Associate Prof. Hiroaki Misawa, Dr. Hiromu Nakagawa, Dr. Fuminori Tsuchiya, Dr. Masato Kagitani, Dr. Takeshi Kuroda, and Dr. Tomoki Kimura. In addition, Dr. Masahiro

Kitahara and Dr. Claudia Martinez are also acknowledged here. Their comments and advices helped me improve my work and this thesis for the best.

On October 19, 2018, the Japan Aerospace Exploration Agency (JAXA) and the European Space Agency (ESA) successfully launched BepiColombo spacecraft by Ariane-5. We are now on the start of seven year journey to Mercury. I am thankful to Dr. Dominique Delcourt, Dr. Go Murakami, and the Young Scientist Working Group (YSWG) for providing me the opportunity to join the BepiColombo mission.

My thanks also go to Dr. Anne Bordon and Dr. Dominique Fontaine at LPP for their mentoring. When I was facing problems, they would always support and encourage me. In addition, I thank Ms. Filomena Catapano, Ms. Giulia Cozzani, Dr. Alexandra Alexandrova, and Dr. Nahuel Andrés at LPP for spending a lot of time with me, and all people I met in Paris, especially at La Maison du Japon.

I specially thank all members of the Planetary Atmosphere laboratory and all colleagues in the C-group for giving me useful comments, discussions, and encouragements. I have enjoyed my daily life within them and it has been one of the most cherished precious memories in my life.

Lastly, I would like to express gratitude to all my precious people close to me for their affection, understanding and support to finish the present work.

This work is supported by the International Joint Graduate Program in Earth and Environmental Sciences (GP-EES). I give a deep thank you to the GP-EES and its secretary, Ms. Shinobu Okuyama for her administrative support. The present work would not have been possible without their support. And also, deepest my thanks to the Morinokuni scholarship foundation for their financial supports. It enables me to continue my work during my graduate studies.

Contents

List of Tables

List of Figures

Chapter 1

Introduction

1.1 Mercury's magnetosphere and its environment

Since Mercury is the closest planet to the Sun, historically there have been fewer opportunities to make spacecraft observations of this remarkable planet. Mariner-10, launched on November 3, 1973, did some flybys of Mercury. It surprisingly showed that Mercury has a weak intrinsic magnetic field and is exposed to strong solar wind. Though there are quadrupole and octupole moments, Mercury's intrinsic magnetic field was estimated to be nearly dipolar with an intensity of approximately 350 nT at the equator [*Ness et al.,* 1975; *Whang,* 1977]. This was a major scientific discovery in the field of planetary sciences and would help to improve our understanding of the origin of the solar system. Because of this discovery, now we know that the Earth is not the only planet in our solar system to be magnetized Earth-like, terrestrial planet. The major differences between the magnetospheres of Mercury and Earth are their strength and size. Those of Mercury's magnetosphere are about 1.1% and 5% of those of Earth, respectively [e.g., *Ness et al.,* 1974, 1979]. Such smaller values lead to the smaller temporal and spatial scales of the physical phenomena than those at Earth [*Ness et al.,* 1974, 1979; *Siscoe et al.,* 1975]. In addition, energetic particles bursts detected by Mariner-10 [*Simpson et al.,* 1974; *Christon et al.,* 1979] make us wonder whether high energy charged particles can exist inside Mercury's magnetosphere. We can also discuss what type of mechanisms regulate this particular environment of Mercury.

On the other hand, in addition to in-situ observations by Mariner-10, further ground-based investigations have revealed Mercury's neutral environment. Mercury has a collisionless atmosphere ($< 10^7$ cm^{-3} at the subsolar point) known as the exosphere, is filled with neutral particles including O, Na, He, K, H and Ca [*Broadfoot et al.,* 1976; *Potter and Morgan,* 1985, 1997]. It is believed that heavier species (Na, K, O, and Ca) are originally from the planetary surface. As they are released by various processes (e.g., photon-stimulated desorption, thermal desorption, micro-meteoroid impacts, ion sputtering, and chemical sputtering), ionized by solar UVs and they are immediately trapped by the magnetic field lines. These particles circulate

around the planet guided by the magnetic field line and could be lost in the solar wind or returned to the planetary surface (ion recycling).

A lack of a thick ionosphere leads to specific interactions between the planetary surface, the neutral atmosphere (exosphere), and the planetary ions in the magnetosphere. As introduced above, these interactions cannot be seen on Earth and are specific to Mercury's environment (we refer to as Hermean environment hereafter). Therefore, several interesting questions on these physical processes should be addressed. For instance: is it possible for Mercury to have similar physical phenomena as we observe on Earth? How are particles freed and delivered from the planetary surface and where are they moving to? What are the effects of heavy ions on the Hermean environment?

Further investigations have been done by the first orbital spacecraft sent to Mercury, the MEercury Surface, Space ENvironment, GEochemistry, and Ranging (MESSENGER) spacecraft, which was launched in 2004. MESSENGER had 3 flybys (January 14, 2008, October 6, 2008, and September 29, 2009) of Mercury and was in orbit from March 11, 2011 until April 30, 2015. This spacecraft has provided much more detailed information about the Hermean environment. The magnetometer (MAG) measured the ambient magnetic field with a sampling of 20 steps per 1 sec, and confirmed that Mercury's magnetosphere is largely dipolar with a magnetic moment of $195 \pm 10\ \mathrm{nT} - \mathrm{R_M^3}$, where $\mathrm{R_M}$ ($\mathrm{R_M} = 2440$ km) is Mercury's radius, and a northward offset of about $0.2\mathrm{R_M}$ [*Alexeev et al.,* 2008, 2010; *Anderson et al.,* 2011, 2012; *Johnson et al.,* 2012]. MESSENGER also provided the information of the ion composition of the Hermean magnetosphere. The Fast Imaging Plasma Spectrometer (FIPS) aboard MESSENGER measured the energy per charge and composition of ions. The results from FIPS are clearly consistent to results from previous ground-based observations, which yields Na, K, and Ca abundances, and proved that the Hermean magnetosphere is filled with ions of planetary origin [*Zurbuchen et al.,* 2008]. Moreover, since doubly ionized species such as $\mathrm{Na^{++}}$, $\mathrm{Mg^{++}}$ were detected, this indicates that electrons with energies below 1 keV are energized inside the Hermean magnetosphere. Such heavy species are coming from Mercury's exosphere by the photon-ionization, were observed in the magnetosheath and throughout the magnetosphere [*Zurbuchen et al.,* 2011; *Schriver et al.,* 2011a, b; *Raines et al.,* 2011, 2013; *DiBraccio et al.,* 2013; *Gershman et al.,* 2015]. In addition, energetic electrons were detected by different instruments aboard MESSENGER. FIPS detected electrons in the MeV range while the Energetic Particle Spectrometer (EPS) measured them from 35 keV up to 1 MeV. Additionally, both the X-Ray Spectrometer (XRS) and the Gamma-Ray and Neutron Spectrometer (GRNS) measured energetic electrons from several keV up to a few hundred keV [*Andrews et al.,* 2007; *Goldsten et al.,* 2007; *Lawrence et al.,* 2015; *Ho et al.,* 2016;

Baker et al., 2016]. Around Mercury, ion acceleration occurs not only on heavy ions of planetary origin but also on electrons. All these previous researches have revealed that Mercury is a much more highly dynamic world than our planet Earth due to the small scales of the Hermean magnetosphere and related kinetic effects of charged particles.

1.2 Key dynamical processes and its questions

As mentioned above, due to its weak intrinsic magnetic field, Mercury has a more dynamical environment for charged particles than that on Earth. Charged particle motion in Mercury is significantly different from that of Earth and this means that the kinetic effects of the charged particle become more efficient on the physical phenomena. Figure 1.1 shows a schematic view of Mercury's magnetosphere based upon the MESSENGER's three flybys' measurements [*Zurbuchen et al.,* 2011]. On the dayside, Mercury's intrinsic magnetic field is compressed by the solar wind while on the nightside the magnetic field forms a long magnetic tail. The mean distance from the center of the planet to the bow shock is ~ $1.96R_M$, and to the nose of the magnetopause is ~ 1.4 to $1.5R_M$ [*Slavin et al.,* 2009b; *Winslow et al.,* 2013]. The tail diameter is ~ $5.0R_M$ under the average solar wind conditions [*Slavin et al.,* 2012; *Winslow et al.,* 2013]. The structure of the Hermean magnetosphere is quite similar to Earth's, although its size is 5% of that of Earth. The internal convection speed in the Mercury's magnetosphere is expected to be high because of a lack of a thick ionosphere. Though a Dungy cycle time of several hours has been observed on Earth, it would be of a few minutes for Mercury [*Siscoe et al.,* 1975; *Slavin et al.,* 2010a]. Thus, Mercury's magnetosphere would respond to varying solar wind conditions within a few minutes, and such a quick variation will affect the ion dynamics in Mercury's magnetosphere. Considering the abundant population of heavy ions in the magnetosphere, as well as the small scales of Mercury's magnetosphere, dynamical processes peculiar to Mercury are expected to exist. Some of which have been already reported by MESSENGER observations, in the following paragraphs we will introduce some key dynamical processes.

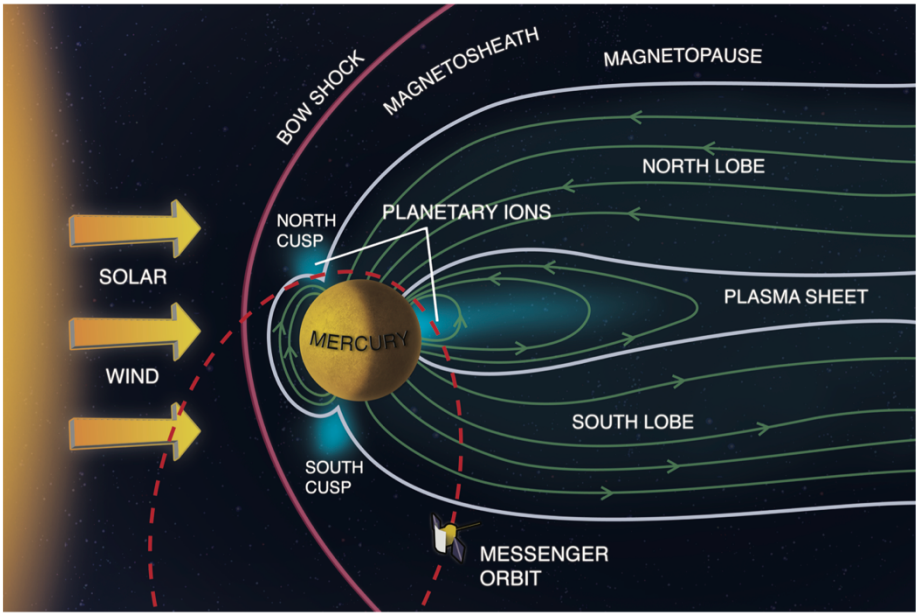

Figure 1.1 Schematic view of Mercury's magnetosphere derived from MESSENGER measurements. Figure is adapted from *Zurbuchen et al*. [2011].

The first key dynamical process is the magnetopause magnetic reconnection. This is a common phenomenon around magnetized planets. The magnetic reconnection, the major driver of magnetospheric convection, occurs as a consequence of the interaction between the solar wind and the planetary magnetosphere [e.g., *Slavin et al*., 2009a, 2014; *DiBraccio et al*., 2013]. The first analysis of the magnetic reconnection on Mercury was done by *Slavin et al*. [2009a], and reported a reconnection rate of ~ 0.13 under the strong steady southward interplanetary magnetic field (IMF) conditions. Generally, the reconnection rate is obtained by either, the ratio of flow and outflow speed (Alfvén speed) into the diffusion region, or the ratio of the normal component of the magnetic field to the magnetopause to the magnetic field intensity inside the magnetosphere. Since no instruments aboard MESSENGER could provide three-dimensional plasma velocities, the latter method was applied to obtain the rate of the magnetic reconnection. With an estimated uncertainty of 10 - 30 %, they statistically evaluated the dimensionless magnetic reconnection rates to be 0.02 to 0.8. This rate is a factor of ~ 3 times larger than the values estimated around the Earth (typically 0.01 – 0.05), as predicted by *Slavin and Holzer* [1979]. *Slavin and Holzer* [1979] argued that higher reconnection rates at Mercury are expected by the estimation of lower Alfvén Mach number and decreasing plasma β going into the inner solar system. Moreover,

previous studies have shown interesting features on the magnetopause magnetic reconnection. *Fuselier and Lewis* [2011] reported that the magnetopause reconnection for Earth highly depends upon the magnetic shear angle (see Figure 1.2(b)). Here the magnetic shear angle is defined as the rotation of the magnetic field from the magnetosheath to the magnetosphere. In contrast, Mercury shows small dependence on the shear angle, as shown in Figure 1.2(a) [*DiBraccio et al.*, 2013]. The magnetopause reconnection is one of the most important processes in the magnetospheric dynamics, in order to understand the large-scale circulation of plasmas as we understand in terms of the Dungy cycle [*Dungy*, 1961]. In addition, some of the magnetic flux will be connected to the IMF during the reconnection. When the frontside magnetic reconnection occurs multiply, they are combined into flux ropes and called flux transfer events (FTEs) [e.g., *Russell and Elphic*, 1978; *Slavin et al.*, 2010b].

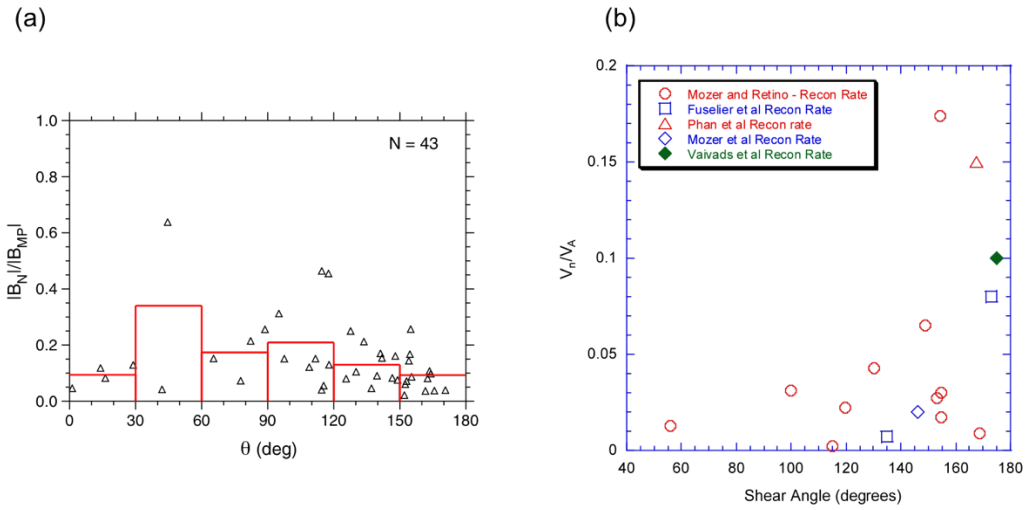

Figure 1.2 Comparison of reconnection rates at (a) Mercury and (b) Earth as a function of magnetic shear angle. Each figure has been adapted from (a) *DiBraccio et al.* [2013] and (b) *Fuselier and Lewis* [2011], respectively.

Another key magnetospheric dynamical process of Mercury is the dipolarization event in the magnetotail [e.g., *Sundberg et al.,* 2012b]. In this event, flux tubes are transported sunward by a fast flow due to the magnetic reconnection in the tail. This can be identified by a sudden increase in the normal component of the magnetic field, or low density plasma streams traveling with high speeds in the central plasma sheet. It corresponds to the rapid reconfiguration from a tail-like to a dipolar-like structure. Such signatures can also be seen on Earth, where the dipolarization is associated with substorms [e.g., *Baumjohann et al.,* 1999] or with the development of a field-aligned current (FACs) system. At Mercury, Dipolarization signatures were observed by Mariner-10, reporting the existence of substorm-like events, and observations of large fluxes of energetic electrons (> 0.3 MeV) and protons (energies between 0.53 and 1.9 MeV) [*Eraker and Simpson,* 1986; *Christon et al.,* 1987; *Baker et al.,* 1986, 1996]. On Earth, the entire interval of dipolarization is about several tens of minutes [*Lee et al.,* 2012; *Russell and Walker,* 1985], whereas on Mercury it is shorter, on the order of 10 s (see Figure 1.3). Such a rapid dipolarization event in Mercury's magnetotail may lead to non-adiabatic acceleration and subsequent injection of heavy ions of planetary origin towards the planetary surface. By estimating typical gyroperiods of electrons ($\sim 10^{-3}$ s), protons (~ 1 s), and other heavy ion species (a few 10 s), the ion species will experience non-adiabatic acceleration as they drift, while electrons experience adiabatic acceleration, also known as betatron acceleration [e.g., *Delcourt et al.,* 1990, 2005]. Using the particle tracing technique, *Delcourt et al.* [2007] have also investigated behavios of various ions during a dipolarization event on Mercury. Because of the quick reconfiguration of the magnetic field to a dipolar-structure, the field accelerates non-adiabatically ion species of a small mass-to-charge ratio such as H^+ and He^+, relating to the quickness of reconfigurations. On the other hand, *Delcourt et al.* [2003] have reported significant acceleration of heavy ions such as Na^+, K^+, and Ca^+ during magnetosphere compression events. In both of these cases, the key parameters are the time scale of the phenomena and the gyroperiod of particles. When the phenomenon has a similar time scale to the gyroperiod, only selected ion species are affected and energized effectively. Considering the heavy ions around the planet, like Na^+, Mg^+, Ca^+, K^+ and O^+, and small scale variations of the magnetic and/or electric field, the kinetic effect of the charged particles becomes more efficient. This leads to different dynamics of the planet's magnetosphere and its surrounding environment.

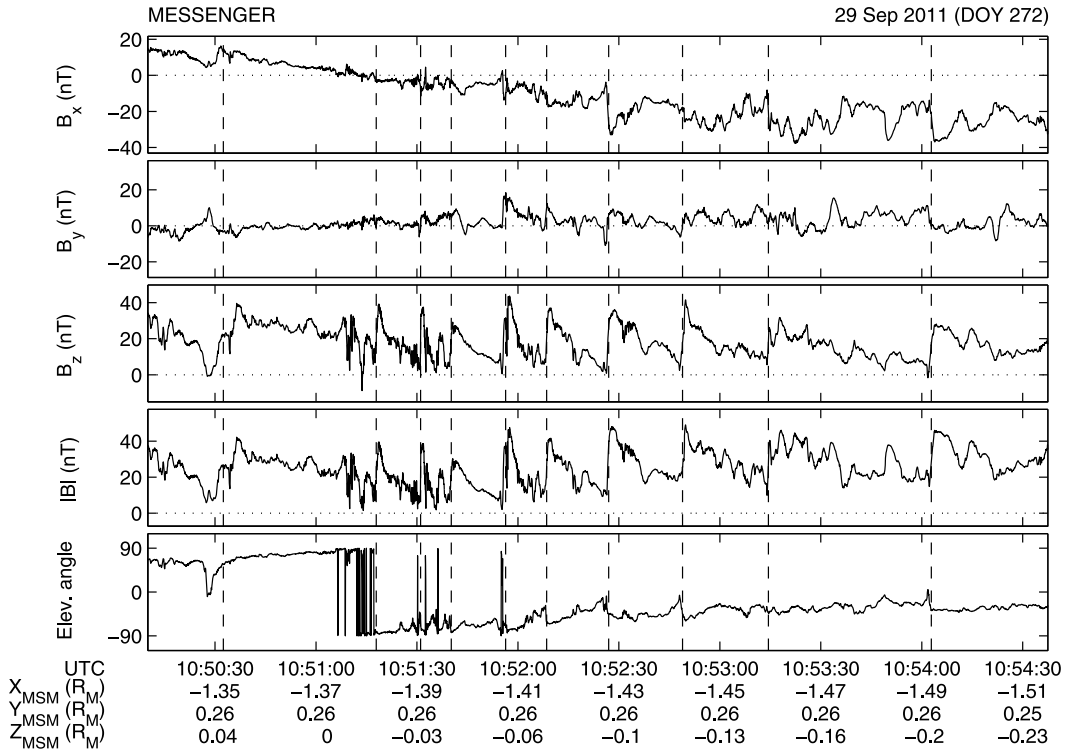

Figure 1.3 Example of MAG measurements during a plasma sheet crossing on September 29, 2011. From top to bottom, panels show the x, y, and z components of the magnetic field, and its intensity. Bottommost panel shows the elevation angle, defined as $\tan^{-1}(\frac{B_z}{B_x})$. Vertical dashed lines a series of 10 dipolarization events. Figure is adapted from *Sundberg et al*. [2012b].

1.3 Kelvin-Helmholtz instability in the magnetospheric flanks

Considered as a key phenomenon around Mercury in this thesis is the Kelvin-Helmholtz (KH) instability [*Boardsen et al.,* 2010; *Sundberg et al.,* 2011, 2012a; *Liljeblad et al., 2014, 2016*; *Gershman et al.,* 2015] (see Figures 1.4 and 1.5). Generally, it occurs when there is a velocity shear between two adjacent fluids [*Helmholtz,* 1868; *Kelvin,* 1871]. This instability is well known as a hydrodynamic instability. When the KH instability is fully developed, it creates KH vortices, which plays roles in the transport of mass and momentum, resulting in mixing two different fluids [*Fritts et al.,* 1996]. In the field of hydrodynamics, this instability is usually seen in a cloud layer and/or sea surface [*Kelvin,* 1871]. It can also be seen in the planets' magnetopause and/or ionopause in the field of space plasma physics. For magnetized planets, their magnetopause can be a boundary layer between solar wind and planetary plasmas with a strong velocity shear. Under these circumstances, we can expect the development of the KH instability in the magnetospheric flanks. In the Earth's magnetopause, even where there are collisionless plasmas, KH vortices play similar roles in the transport of momentum as well as mixing plasmas [*Miura et al.,* 1984; *Fujimoto and Terasawa,* 1994]. The KH vortex can also be a trigger of the magnetic reconnection inside the vortex [*Nykyri and Otto,* 2001].

In the Earth's magnetospheric flanks, there are many observational reports on the KH instability provided by various spacecraft [e.g., *Chen and Kivelson,* 1993; *Mozer et al.,* 1994; *Fujimoto et al.,* 2003; *Hasegawa et al.,* 2004; *Hwang et al.,* 2011; *Yan et al.,* 2014]. Regarding the Mercury's magnetospheric flanks, some authors reported observations of KH vortices using MESSENGER data [*Slavin et al.,* 2008; *Sundberg et al.,* 2011, 2012a; *Gershman et al.,* 2015; *Liljeblad et al.,* 2014, 2016]. Because of the orientation of FIPS, KH instabilities were mostly observed on the duskside magnetopause. The authors concluded that the occurrence of the KH instability around the Mercury indicates a strong dawn-dusk asymmetry (duskside observation accounts for 95% of the observations) in the Hermean environment. The asymmetry may be caused by the kinetic effect of charged particles, called the finite Larmor radius effect, or by the lack of large-scale laminar flow in the dawnside [*Liljeblad et al.,* 2014; *Paral and Rankin,* 2013].

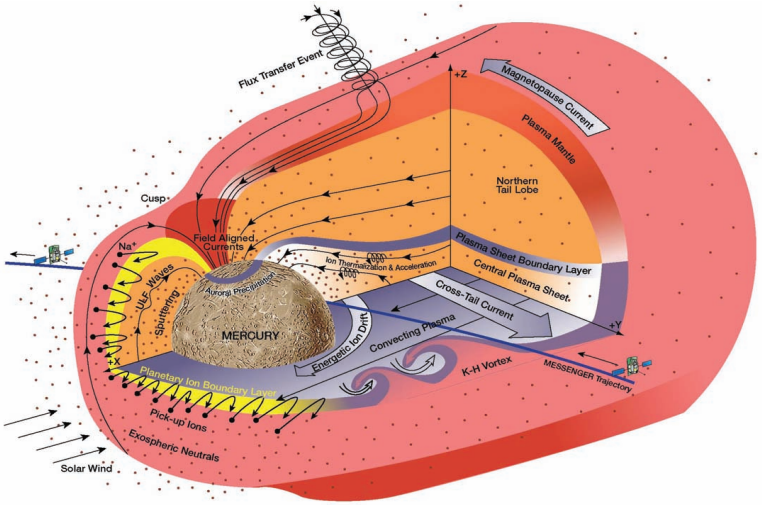

Figure 1.4 Overview of various physical phenomena around Mercury. Adapted from *Slavin et al*. [2008]. KH vortices are observed in the duskside magnetospheric flanks.

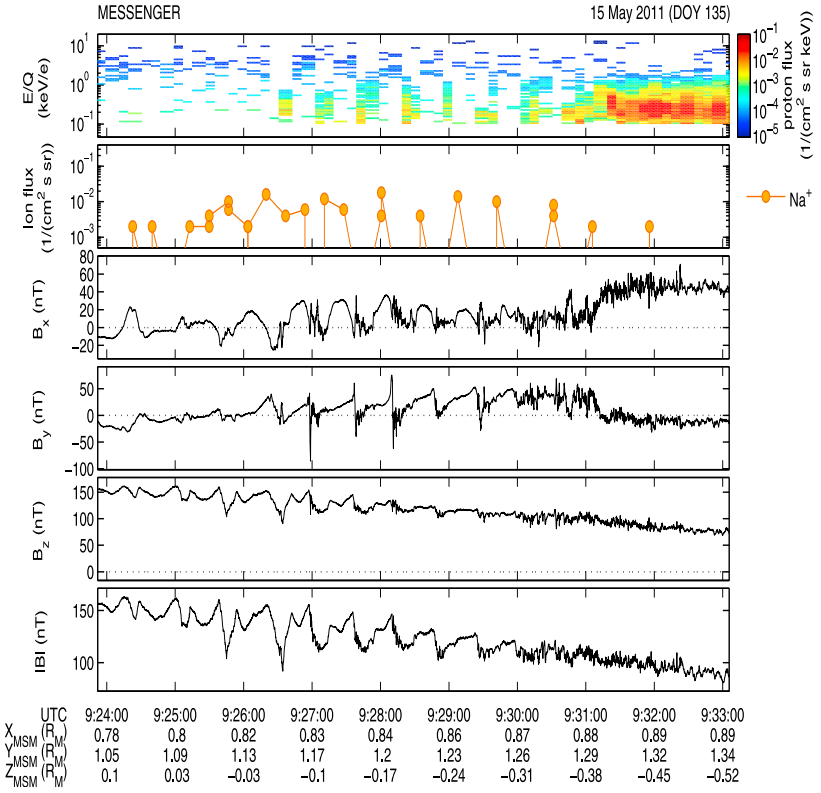

Figure 1.5 Typical signature of KH waves observed by MESSENGER. This figure is adapted from *Sundberg et al.* [2012a]. From top to bottom, proton energy spectrogram, Na^+ total ion flux, the three magnetic field components and magnetic field intensity as a function of time. Successive rotations of x-component in the magnetic field (3rd panel) and successive irruptions of proton (top panel) are typical KH signatures.

The properties of KH vortices in the duskside magnetospheric flanks of Mercury have been reported by several authors [*Slavin et al.*, 2008; *Sundberg et al.*, 2010, 2011, 2012a; *Gershman et al.*, 2015; *Liljeblad et al.*, 2014]. The typical wavelength of the KH is ~1.5 R_M, with a frequency of 0.01 ~ 0.05 Hz. Although these values do not exactly correspond to the fast-growing mode of the KH instability from theoretical predictions, they remain reasonable values.

Although the KH instability commonly occurs at the magnetopause of magnetized planets, KH vortices on Mercury are likely affected by the kinetic effect in the Hermean environment. *Gershman et al.* [2015] reported that KH signatures vary depending on the Na^+ gyrofrequency when they develop in a Na^+ dominant region (see Figure 1.6) because of the similar time scale

between them. The dayside KH events maintain a constant magnetic fluctuation frequency (KH frequency) of ~ 0.025 Hz while for the nighside events it varies from 0.01 to 0.05Hz, correlating with the estimated Na^+ gyrofrequency (~ 0.01 to ~ 0.05 Hz for the magnetic field of 30 ~ 80 nT). The presence of heavy ions is one of Mercury's specific features and their influence on the physical phenomena (and its vice-versa) are particular interesting questions.

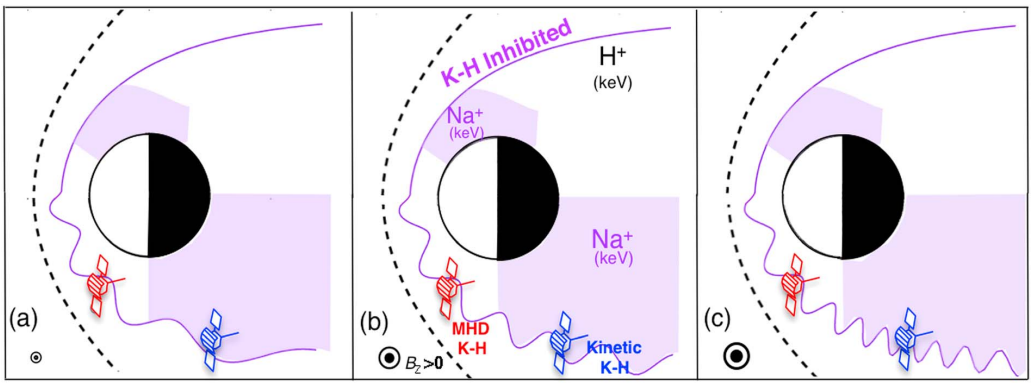

Figure 1.6 Schematic illustration of the KH wave growth along duskside magnetopause. Since MESSENGER is a single spacecraft, statistical survey compared between dayside KH waves and nightside KH waves has been done. Each panel shows that observed Na^+ gyrofrequency on the nightside is (a) less than (b) equal to, and (c) greater than that observed on the dayside. This figure is adapted from *Gershman et al*. [2015]

Another interesting numerical study related to the KH growth around Mercury has been done by *Gingell et al*. [2015]. They investigated the KH growth in the dawn and dusk side in the sodium ion rich field using hybrid simulation. In this calculation, because of the effect of the gyroresonance, the KH growth in the dawnside is inferior to that in the duskside. On the other hand, *Liljeblad et al*. [2016] investigated the occurrence of Ultra Low Frequency (ULF) waves associated with the KH instability (frequency of 0.02 – 0.04 Hz, which is well below the estimated local Na^+ gyrofrequency of 0.08 – 0.015 Hz for the magnetic field of ~ 24 nT). They found that ULF waves in the dayside are driven by KH waves at the magnetopause. It is known that KH waves can cause other physical phenomena and/or secondary instabilities around planets, but some questions remain open: what is the mechanism behind the clear dawn-dusk asymmetry of the KH growth, how important is the KH growth to the Hermean environment, or further specific unrevealed effects of the KH growth on the Hermean environment.

As *Gershman et al*. [2015] suggested, the scale of particle (Na^+) gyration motion along the duskside magnetopause is of the same order of the thickness of the magnetopause. We could expect here one of the unrevealed effects of the KH instability: the non-adiabatic charged particle motion due to the electric field variation by the development of the KH instability. According to the previous theoretical and numerical studies of non-adiabatic charged particle motion in the domain of space plasma physics, many authors have discussed that non-adiabatic motion of charged particles is caused by the spatial and temporal variations of the magnetic field [*Speiser,* 1965; *Büchner and Zelenyi,* 1989, 1990; *Chen et al.,* 1990; *Chen and Palmadesso,* 1986; *Chen,* 1992; *Delcourt and Sauvaud,* 1994; *Delcourt and Martin,* 1994]. Few people have studied the effect of electric field variations on the charged particle motion [*Rothwell et al.,* 1994] and no systematic analysis on this has been done. In particular, electric field variations are generated during the development of the KH instability, and their variations in space and/or time may lead to non-adiabatic ion acceleration inside KH vortices, depending on its mass-to-charge. When particles are non-adiabatically accelerated, they may also sputter on the planetary surface. They produce secondary ions that circulate around the planet, leading to escape of heavy ions from the planetary surface.

In order to discuss the ion acceleration and transport due to the development of the KH instability, we need to know how the particles are transported to the region where the instability likely occurs. A possible path of the ion transport on the Mercury starts from the cusp region [*Delcourt et al.,* 2003, 2012]. One of the possible sources of heavy ions around the cusp is the ions locally produced by photo-ionization of exospheric neutrals and accelerated upward. They move toward to the magnetotail region. Due to the large convection in the dawn-to-dusk electric field makes the ions move to the duskside magnetopause region [*Potter and Killen*, 2008; *Raines et al.,* 2014;

Delcourt et al., 2003; *Zurbuchen et al.,* 2011]. In fact, high Na^+ population in the cusp region and at the duskside magnetopause has been reported by MESSENGER [*Zurbuchen et al.,* 2011; *Raines et al.,* 2014].

1.4 Purpose of this study in the context of MESSENGER and BepiColombo

The purpose of this study is to address questions, such as: How heavy ions behave within KH vortices? How are they transported or mixed? Can ions be affected by the electric field variations? Observations from Mariner-10 and MESSENGER spacecraft have brought a wealth of new information on the Hermean environment, i.e., small-scale magnetosphere, a lack of a thick ionosphere, exosphere with heavy compositions. Under these circumstances, many interesting phenomena have been reported. For example, the magnetopause magnetic reconnection which is independent of the magnetic shear angle, short-lived dipolarization events, and modified KH waves depending on the gyrofrequency of heavy ions of planetary origin. However, a lot of open issues remain. Especially, one of the major differences between plasma physics of Mercury and Earth is the non-adiabatic motion of charged particles. Since Mercury's exosphere consists of heavy neutral species from the planetary surface, large gyration motion of heavy ions can be expected with a spatial/temporal scale comparable to that of the field variations. In addition, investigation of charged particle motion in the vicinity of the development of KH vortices may lead to new insights into fundamental plasma physics concerning the effect of electric field variations on the gyration motion. In this study, we would like to reveal the role of the KH instability on the transport and energization of planetary ions in the magnetospheric flanks of Mercury by both a numerical approach and observational data analysis. We demonstrate how particle behaves with the spatial and temporal variations of the electric field.

Since MESSENGER mission focused on the planetary surface composition, geologic history, and nature of the exosphere, the ion detection capability was limited. Thus, FIPS was not enough to reveal the details of charged particle motions and accelerations. After the MESSENGER era, the next journey to Mercury is the BepiColombo mission by the Japan Aerospace Exploration Agency (JAXA) and the European Space Agency (ESA). BepiColombo has been prepared to investigate the Hermean environment with two spacecraft, named MPO and MIO. The science objectives of this new mission, especially of MIO, are to investigate the plasma/wave environment around Mercury. From the point of view of detecting plasma, MIO has the Mercury Plasma Particle Experiment (MPPE) consortium. For ions, we have the Mercury Ion Analyzer (MIA), Mercury mass Spectrum Analyzer (MSA), and High Energy Particle instrument for ions (HEP-

ion). They will be used depending on a wide range of science topics. For lower energy plasma detection, FIPS aboard MESSENGER had the energy range from 50 eV/e to 13 keV/e, while MIA and MSA will cover from 5 eV/e to 40 keV/e (see Figure 1.7) [*Saito et al.,* 2010; *Delcourt et al.,* 2016]. In addition to this wider energy range, MSA has a three-dimensional field of view due to the three-axes spinning spacecraft. These improvements will allow us to investigate the ion dynamics in detail. We will investigate the Hermean plasma environment, using combined spacecraft to understand how plasma affects the planetary surface and exosphere. Mercury is now treated as a natural laboratory in space to examine fundamental plasma processes. BepiColombo is planned to arrive at Mercury in December, 2025, and observe the Hermean environment for 1 year (nominal operation). Several studies will be done by then, and new insights should be brought to light. This study will be one of them, and will contribute to the forthcoming study of the BepiColombo mission by ESA/JAXA, especially in the ion acceleration, trapping, transport, and/or loss.

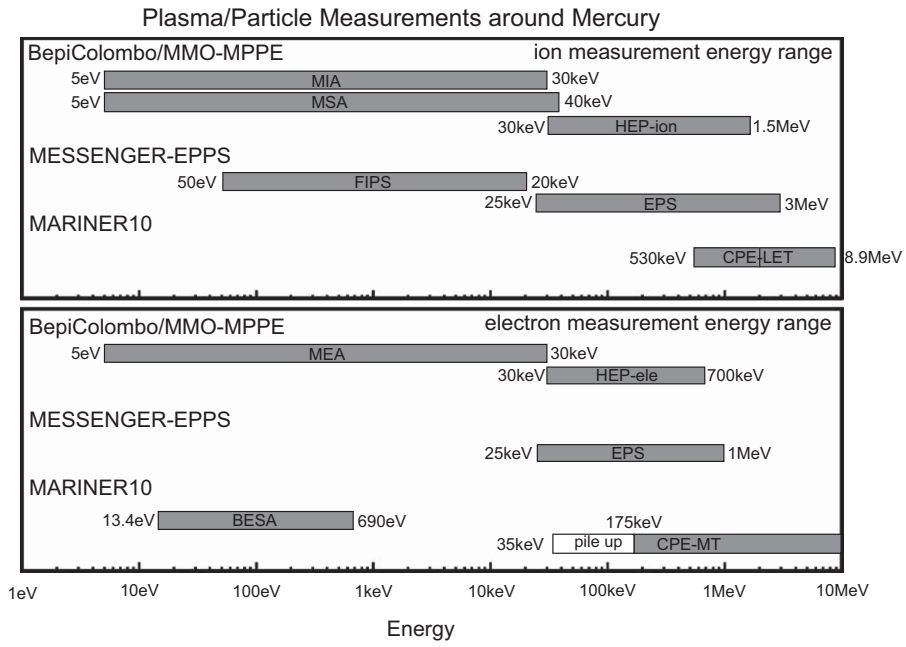

Figure 1.7 Energy coverage of plasma/particle sensors onboard Mariner-10, MESSNEGER, and BepiColombo/MIO. The figure is adapted from *Saito et al*. [2010].

Chapter 2

Charged particle dynamics

Charged particles are coupled to an electromagnetic field by their charge. The electromagnetic field affects their motions and vice-versa. In a situation where the charged particles do not directly interact with each other and do not affect the ambient electromagnetic field significantly, the motion of each particle can be treated independently. This is the simplest situation to consider the charged particle dynamics in an electromagnetic field.

In order to start our investigation on the non-adiabatic behavior of charged particles in Mercury's magnetosphere, we introduce the basic theory for the motion of charged particles and related previous studies.

2.1 Basic theory of charged particle motion

Charged particles and their motions are affected by electromagnetic forces. On the other hand, charged particles are also sources of electromagnetic fields ($\boldsymbol{E}$, $\boldsymbol{B}$), which are described by the Maxwell's equations. In consequence, the motion of such a particle is expressed by the Newton-Lorentz equation:

$$m\frac{d\boldsymbol{v}}{dt} = q(\boldsymbol{E} + \boldsymbol{v}\times\boldsymbol{B}), \tag{2.1}$$

where m, q and $\boldsymbol{v}$ are the mass, charge, and the velocity of the charged particle, respectively. $\boldsymbol{E}$ and $\boldsymbol{B}$ represent the electric and magnetic fields, respectively.

The Lorentz force accelerates charged particles in the perpendicular direction to the particle velocity and the ambient magnetic field. If we consider a uniform magnetic field in the absence of an electric field, the particle motion is expressed as the circular motion around the magnetic field line. This is called a gyration motion (gyromotion) or cyclotron motion. By reducing the Coulomb force term, the Newton-Lorentz equation then becomes:

$$m\frac{d\boldsymbol{v}}{dt} = q(\boldsymbol{v}\times\boldsymbol{B}). \tag{2.2}$$

The direction of the circular motion depends on the sign of the charge.

Taking the dot product of Equation (2.2) with a velocity $\boldsymbol{v}$, and using vector relations, we obtain

$$m\frac{d\boldsymbol{v}}{dt}\cdot\boldsymbol{v} = \frac{d}{dt}\left(\frac{mv^2}{2}\right) = 0. \tag{2.3}$$

This equation shows that the kinetic energy of the particle is conserved under a uniform magnetic field in the absence of an electric field. If we separate the total velocity $\boldsymbol{v}$ into two directions, parallel and perpendicular to $\boldsymbol{B}$, the equation becomes

$$\frac{dv_{\parallel}}{dt} + \frac{dv_{\perp}}{dt} = \frac{q}{m}(v_{\perp}\times\boldsymbol{B}), \tag{2.4}$$

since $v_{\parallel}\times\boldsymbol{B} = \left|v_{\parallel}\right|\left|\boldsymbol{B}\right|sin\theta = 0$. Finally, we obtain the following two equations describing each component of the particle motion as:

$$\frac{dv_{\perp}}{dt} = \frac{q}{m}(v_{\perp}\times\boldsymbol{B}), \tag{2.5}$$

$$\frac{dv_{\parallel}}{dt} = 0. \tag{2.6}$$

Assuming a uniform magnetic field $\boldsymbol{B} = (0, 0, B)$, the components of Equation (2.1) are:

$$m\frac{dv_x}{dt} = qBv_y, \tag{2.7}$$

$$m\frac{dv_y}{dt} = -qBv_x. \tag{2.8}$$

By taking the second derivative and substituting into the corresponding equations, then we get

$$\ddot{v_x} = -\left(\frac{qB}{m}\right)^2 v_x, \tag{2.9}$$

$$\ddot{v_y} = -\left(\frac{qB}{m}\right)^2 v_y. \tag{2.10}$$

with $\omega_g = qB/m$, known as the gyro-frequency or cyclotron frequency. ω_g has opposite signs for positive and negative charges. This equation describes a simple harmonic oscillations, thus we can introduce the complex value, $u = v_x + iv_y$, which help us to rewrite as:

$$\frac{du}{dt} + i\omega_g u = 0. \tag{2.11}$$

The solution of this equation is:

$$u = v_{\perp}e^{-i\omega_g t}, \tag{2.12}$$

where $v_\perp$ is the magnitude of the perpendicular velocity to $\boldsymbol{B}$. Note that $v^2 = v_\parallel^2 + v_\perp^2$. The circulation orbit of a charged particle is expressed by:

$$x - x_0 = \rho_L sin\omega_g t, \tag{2.13}$$

$$y - y_0 = \rho_L cos\omega_g t. \tag{2.14}$$

The Larmor radius (gyroradius or cyclotron radius) of the particle is defined by:

$$\rho_L = \frac{v_\perp}{|\omega_g|} = \frac{mv_\perp}{|q|B}, \tag{2.15}$$

where $v_\perp = (v_x^2 + v_y^2)^{\frac{1}{2}}$ is a constant speed which is perpendicular to $\boldsymbol{B}$.

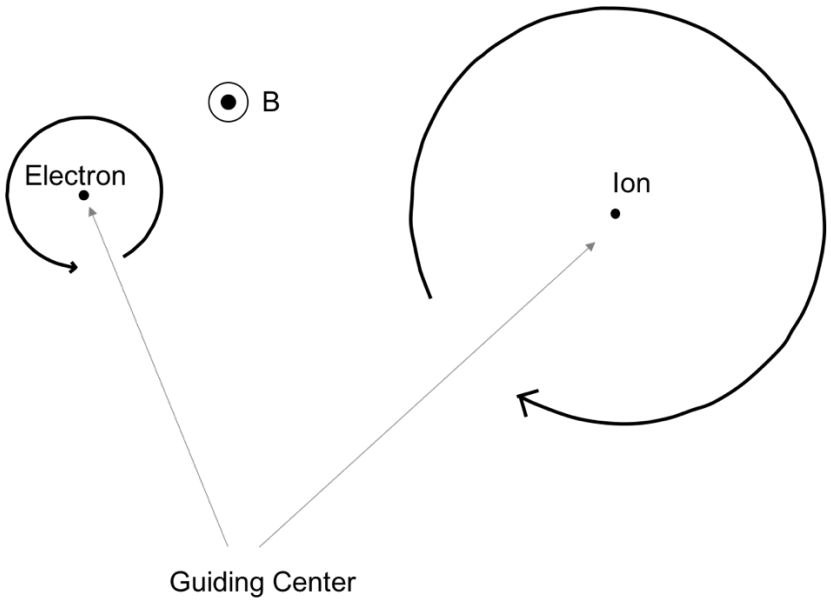

Figure 2.1 Gyration motion of a charged particle around the guiding center. Modified figure from *Baumjohann and Treumann* [1996].

Equations (2.13) and (2.14) describe a circular motion of the particle around the magnetic field line with a clockwise rotation in case of a positive charge, or anti-clockwise rotation for a negative charge of a particle. The center of the orbit (x_0, y_0) is called 'Guiding Center'. In addition, if the particle has a velocity component parallel to the magnetic field, $v_{\parallel}$, the trajectory of the particle is three dimensional and helical. In this case, the angle between the magnetic field line and the particle velocity is known as the pitch angle, α (see Figure 2.2). The pitch angle is defined as:

$$\alpha = \tan^{-1}\left(\frac{v_{\perp}}{v_{\parallel}}\right). \tag{2.16}$$

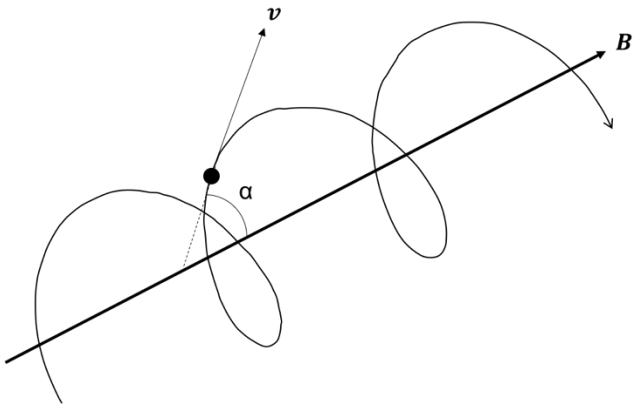

Figure 2.2 Illustration of the definition of the pitch angle α.

When a spacecraft observes plasmas around a planet, charged particles are detected by energy selection and their properties are discussed depending on their kinetic energy. If we introduce this notion as total (ε), perpendicular ($\varepsilon_\perp$), and parallel ($\varepsilon_\parallel$) kinetic energy, we can write:

$$\varepsilon_\perp = \frac{mv_\perp^2}{2}, \tag{2.17}$$

$$\varepsilon_\parallel = \frac{mv_\parallel^2}{2}, \tag{2.18}$$

$$\varepsilon = \varepsilon_\perp + \varepsilon_\parallel. \tag{2.19}$$

Since we have discussed about the gyration motion of a charged particle in a uniform magnetic field, now we describe a particle motion in the presence of an external force. If we consider an external force $\boldsymbol{F}$ in addition to the Lorentz force, the equation of motion becomes:

$$m\frac{d\boldsymbol{v}}{dt} = q(\boldsymbol{v}\times\boldsymbol{B}) + \boldsymbol{F}. \tag{2.20}$$

Consideration of an external force $\boldsymbol{F}$ results in a drift motion of a charged particle in addition to its gyration motion. By using the guiding center as a reference frame, the particle motion due to a force $\boldsymbol{F}$ can be separated from the gyration motion due to $\boldsymbol{B}$. Thus, we can set various types of forces and obtain the particle motion in the reference frame, allowing us to express various drift motions. For example, if we assume that the constant force $\boldsymbol{F}$ is the Coulomb force, $\boldsymbol{F_c} = q\boldsymbol{E}$, then we describe a **E**x**B** drift motion. If the electric field varies slowly compared to the particle gyration motion, then polarization drift occurs. This means that there is a shift in the guiding center of the particle following the electric field vector which polarizes plasmas. Moreover, if we assume a weak non-uniformed magnetic field, we obtain a **grad** $\boldsymbol{B}$ drift motion. Further details on the derivation and explanation of various kinds of drift motions can be found in plasma physics textbooks, for instance *Baumjohann and Treumann* [1996]. If we take the average of a particle's gyration motion over the gyration period, we obtain the trajectory of its guiding center. The particle trajectory can then be described by a combination of the trajectory of the guiding center and its gyration motion.

Since the electric field does not affect to the circulation motion itself but affects to the trajectory of the guiding center, when we consider the Coulomb force in the equation of motion, the trajectory of the particle can be expressed by the trajectory of the guiding center only. It is important to keep in mind that the gyration motion is conserved when we consider the trajectory of the guiding center only. The conservation of the circular motion of a particle is described using the magnetic moment, μ. The circular orbit of the charged particle represents the circular current which produces the magnetic moment. The magnetic moment is described by the ratio of the

perpendicular kinetic energy (to the magnetic field) to the magnetic field intensity: $\mu = \frac{\varepsilon_\perp}{B} = \frac{\frac{1}{2}mv_\perp^2}{B}$.

This quantity is also known as the 1st adiabatic invariant, which is an important parameter for the ion dynamics. When it is conserved over one gyration, the motion of the particle is adiabatic. In this case, the equation of motion of the guiding center works well to describe the particle trajectory. The equation of motion of the guiding center for a particle with a charge q and a mass m is described as:

$$\ddot{\boldsymbol{R}} = \frac{q}{m}\left\{\boldsymbol{E}(\boldsymbol{R}) + \dot{\boldsymbol{R}}\times\boldsymbol{B}(\boldsymbol{R}) - \left[\frac{\mu}{m}\nabla\boldsymbol{B}(\boldsymbol{R})\right]\right\} + \mathcal{O}(\epsilon), \tag{2.21}$$

where $\boldsymbol{R}$ is the guiding center position, $\boldsymbol{E}$ and $\boldsymbol{B}$ are the electric field and magnetic field which are evaluated at the guiding center, respectively. μ represents the magnetic moment of the particle. As shown in Equation (2.21), an additional term to Equation (2.17) appears because of some assumptions in the derivation. For details on these assumption and derivation, we refer to *Northrop* [1963]. The guiding center approximation and its equation of motion works well in most of Earth's magnetosphere.

In the case where either the magnetic or the electric field changes rapidly in time and/or space, these field variations may affect the particle gyration motion meaning that the 1st adiabatic invariant may not be conserved. In this case, we talk about non-adiabatic motion. The 2nd and 3rd adiabatic invariants also exist and are parameters showing the conservation of the bounce motion between two mirror points and of the drift motion around a planet. Although they also may not be conserved by field variations, here we use the word 'non-adiabatic' only in the context of the violation of the 1st adiabatic invariant.

2.2 Adiabatic invariant violation

As described above, if the fields vary rapidly during the particle's gyration motion ($t < \tau$, where τ is the gyration period), the particle motion may be affected by the field variations, leading to the 1st adiabatic invariant no longer being conserved. In that case, we cannot use the guiding center equation of motion to trace the exact particle motion anymore. The gyration motion should be tracked by a single particle equation of motion. These types of rapid varying fields, for instance a sudden dipolarization event, can be expected to be observed for Mercury.

Non-adiabatic particle motion has been investigated by several authors, in particular in the Earth's magnetotail to study the spatial variation of the magnetic field. *Speiser* [1965] first reported using a simple model, that particles experience a meandering motion (so called Speiser orbit) near the field's minimum. They examined the particle motion under a simple field configuration consisting of a neutral sheet with an additional small perpendicular magnetic field (see Figure 2.3 for details). The particle motion is expressed here by a combination of the slow gyration motion and fast oscillations. If there is no perpendicular component of the magnetic field, then the particle can be transported in the $-z$ direction as shown in Figure 2.3, never exit of the neutral sheet. In the presence of a perpendicular magnetic field as magnetized planets have, particles are accelerated in the $-y$ and $-z$ directions with a circular drift in the current sheet, and particles may be ejected out of the current sheet. After the work done by *Speiser* [1965], *Sergeev et al*. [1983] investigated the non-adiabatic pitch angle scattering in the magnetotail current sheet by implementing the Tsyganenko model [*Tsyganenko,* 1982]. They introduced the K_{CR} parameter, which depends only on the particle mass, energy and the charge of the particle, and on the magnetic field distribution at the magnetospheric equator. They discussed the conditions in which we have the non-adiabatic motion. For example, they found that as long as $K_{CR} > 8$, the guiding center approximation is valid. *Chen and Palmadesso* [1986] investigated the chaotic motion of charged particles in Hamiltonian dynamics using the Harris-type magnetic field model, showing in a Poincaré map. In this case, the examined parameter of the dimensionless Hamiltonian was in the regime of $1 < K_{CR} < 8$, if we translate it to the K_{CR} values. They found that the particle motion can be classified into three types of orbits: transient (Speriser), stochastic (quasi-adiabatic, introducing a new constant parameter J), and trapped orbit. During the Speiser type non-adiabatic interaction in the current sheet, the particles may turn back and subsequently escape while executing an integer number of oscillations. This is known as the "resonance" between the fast oscillations and the slow gyration motion. Each orbit is characterized by a different time scale. Quasi-adiabatic particle motion can be classified by the specific value of the dimensionless Hamiltonian.

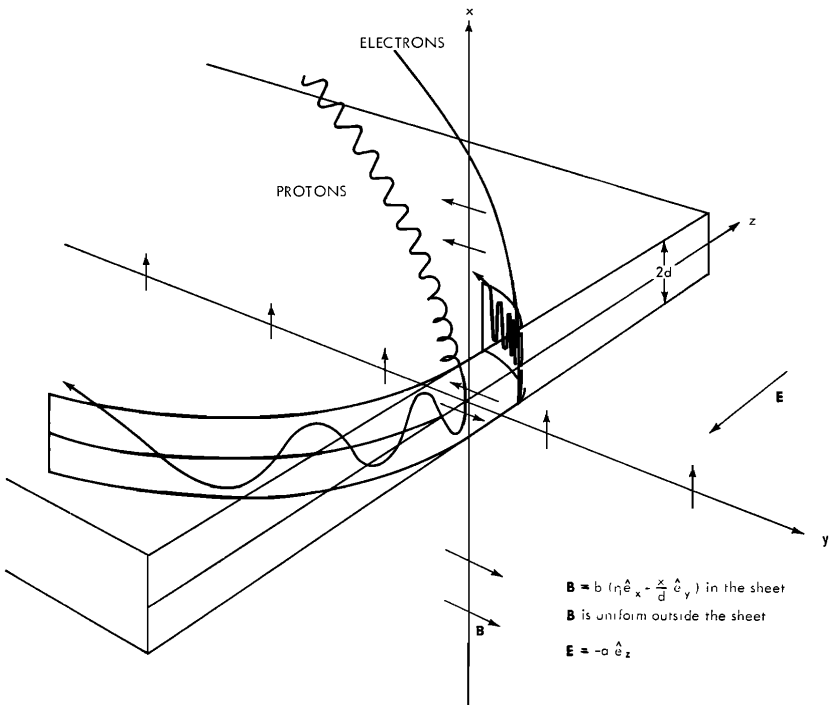

Figure 2.3 Meandering motion adopted from *Speiser* [1965]. Model description is at the bottom right. Protons and electrons have opposite directions because of the sign of their respective charges. Ejection from the current sheet (thickness is 2d) depends on the resonance between gyration motion and fast oscillations.

Burkhart and Chen [1991] investigated the resonance effect between the fast oscillations and the slow gyration motion. They found the following relationship to characterize the i th resonance:

$$\kappa_i \sim \frac{0.8}{i + 0.6}, \tag{2.22}$$

where the first resonance is about $\kappa_i \sim 0.5$ for instance, also known as beamlets.

Moreover, *Büchner and Zelenyi* [1989] have investigated in detail the condition of non-adiabatic motion in the Harris-type magnetic field model. They use the κ parameter instead of K_{CR}, which is nowadays much more common to describe the non-adiabatic condition. The relation between κ and K_{CR} is:

$$\kappa = [K_{CP}]^{\frac{1}{2}} = \left[\frac{R_{c,min}}{\rho_{L,max}}\right]^{\frac{1}{2}}, \tag{2.23}$$

where $R_{c,min}$ shows the minimum curvature radius of the magnetic field (generally at the equatorial plane), and $\rho_{L,max}$ shows the maximum gyro radii during the entire particle motion. If κ is large enough, meaning the curvature radius of the magnetic field is large compared to the particle gyration radius, the particle motion is adiabatic. But if κ is small, non-adiabatic motion may occur. In Figure 2.4, the meaning of the κ parameter is illustrated.

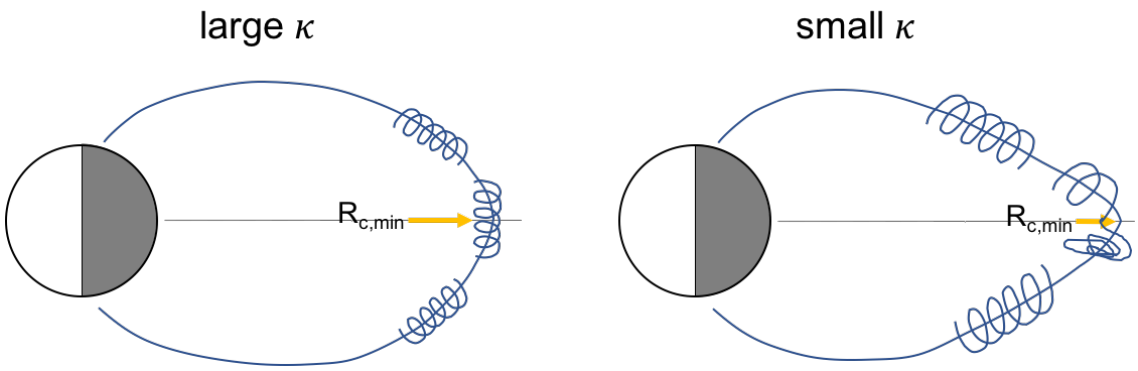

Figure 2.4 Illustration of the meaning of κ parameter. If κ is large enough, particle keeps its gyration motion without any disruption from field variations (see left). If κ is small, particle may experience a reversal magnetic field component across the equatorial plane.

The conditions in which non-adiabatic particle behavior occurs have been discussed in several papers. Some of which have been mentioned above, further detailed conditions will be presented hereafter using the κ parameter.

When $\kappa > 3$ ($K_{CR} > 8$) which can be seen for example at the isotropy boundary in Earth's magnetosphere, we can use the guiding center equation of motion [e.g., *Sergeev et al.,* 1983, 1994]. In the $1 \leq \kappa \leq 3$ regime, so called 'chaotic' regime, the particle motion can be helical and have no meandering motion. The magnetic field reversal at the equatorial region is not sharp enough to allow Speiser orbit but it is enough to break the guiding center approximation. In other words, the magnetic moment μ is not conserved [e.g., *Büchner and Zelenyi,* 1989; *Delcourt and Martin,* 1994]. Especially, $\kappa \approx 1$ is the limit at which meandering motion becomes possible. The non-adiabatic motion can occur as a result of the impulsive centrifugal force, and its magnetic moment variation is organized according to a three-branch pattern (Figure 2.5). Systematic μ enhancement at small pitch angles is observed, while negligible μ changes are seen at large pitch angles. In the present regime, non-adiabatic motion or acceleration causes several interesting features related to the ion dynamics and plasma environment around the planet [e.g., *Ashour-Abdalla et al.,* 1993a, b]. *Ashour-Abdalla et al*. [1993b] reported that enhanced trapping with large energy gain during the large drift motion toward the duskside (Figure 2.6). Also, the phase bunching can be caused as a result of the non-adiabatic motion. This leads to the development of a thin current sheet, as is the case of ions traveling in the near-Earth plasma sheet [*e.g., Delcourt et al,* 1995, 1996a, b]. In addition, the aurora consequence of ion precipitating, energy-dispersed ion structures, and ionospheric and plasma sheet activities have been also reported [*e.g., West et al.,* 1978a, b; *Wagner et al.,* 1979; *Lyons and Speiser,* 1982; *Ashour-Abdalla et al.,* 1991, 1992; *Keiling et al.,* 2004].

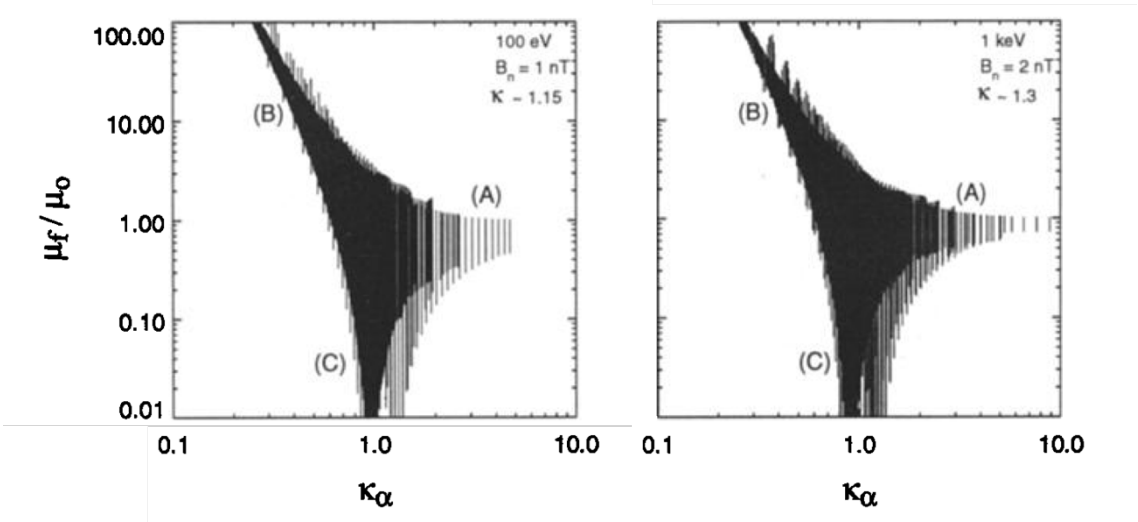

Figure 2.5 Three-branch pattern in the regime of $1 \leq \kappa \leq 3$. Here κ_α is a function of the initial pitch angle and distance to the equator, defined by $\kappa_\alpha = \kappa \frac{(sin\alpha_m)^{1/2}}{cos\alpha_m}$, where α_m is initial particle pitch angle (at the field minimum). $\kappa_\alpha \gg 1$ corresponds to negligible μ change (branch (A)), regions with $\kappa_\alpha \sim 1$ corresponds to possible large damping (branch (C)), and with $\kappa_\alpha \ll 1$ corresponds to large μ changes shown in branch (B). Figure is reorganized from *Delcourt and Martin* [1994].

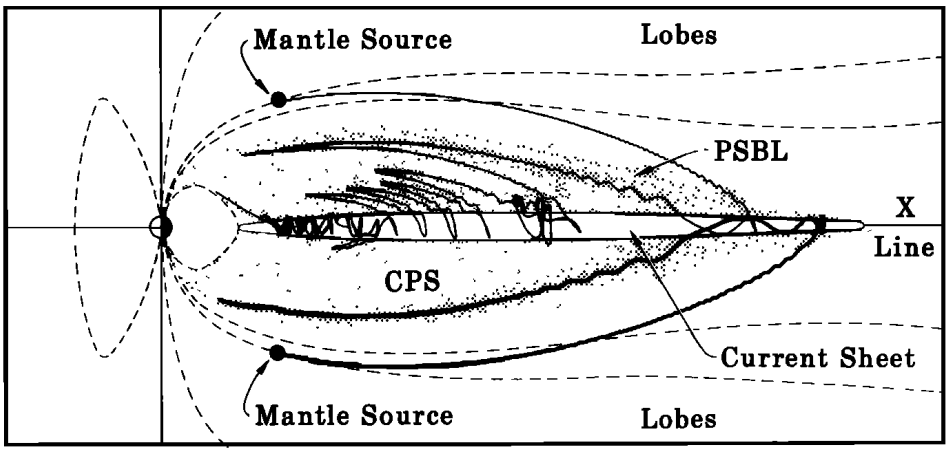

Figure 2.6 Illustration of the model for populating the plasma sheet from the mantle. Some trajectories are in quasi-adiabatic while others follow Speiser orbit. Adapted from *Ashour-Abdalla et al*. [1993b].

The $\kappa < 1$ regime, meaning the particle's Larmor radius is larger than the field line curvature radius, is discussed. In other words, particles always experience the opposite-directed magnetic field when they go through the magnetic equator and thus the magnetic moment may not be conserved (see Figure 2.7). *Delcourt et al*., [1996b] examines the pitch angle scattering affecting the ion precipitation, revealing that a three-branch pattern emerged near the resonance energy (previously reported by *Burkhart and Chen* [1991]). The three-branch pattern variation depends on the κ parameter (see Figure 2.8), and branches disappear when κ is in the regime of off-resonant. According to this figure, the fit relationship for i-th resonant is given by:

$$\kappa_i \sim \frac{0.775}{i + 0.456}. \tag{2.24}$$

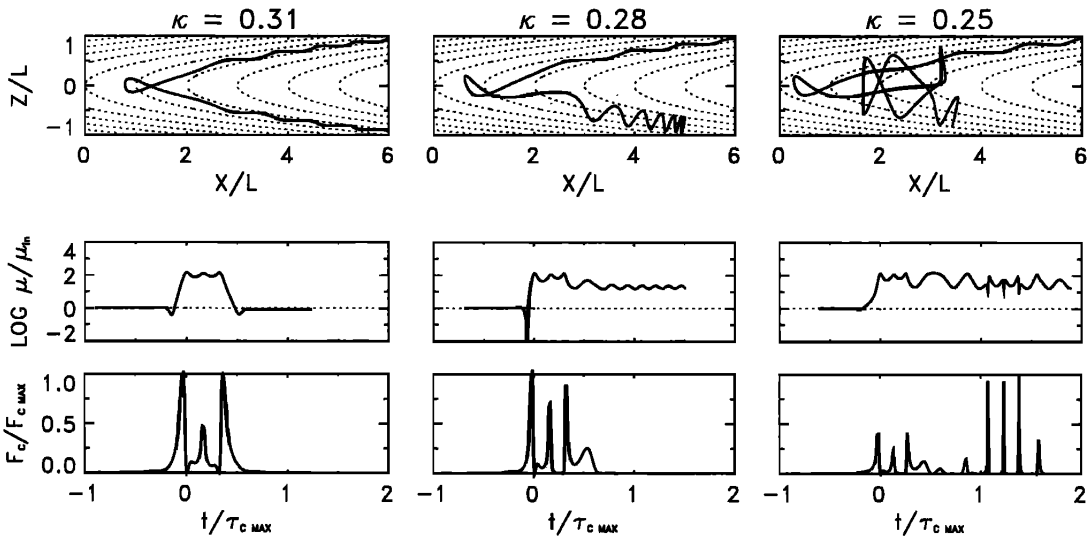

Figure 2.7 Some model examples of ion behavior for $\kappa < 1$. Top panels show the trajectory projected in $x - z$ plane, where z is northwards and X is sunwards. Middle and bottom panels are the magnetic moment (normalized to the initial value) and centrifugal force (normalized to the maximum value) as a function of time. Time is normalized by the cyclotron period at the field minimum. Three different κ are examined here, $\kappa = 0.31, 0.28, 0.25$ (left to right). Figure is adapted from *Delcourt and Martin* [1999].

Large magnetic moment changes may be equivalent to the mirror point changes, suggesting that this type of non-adiabatic motion causes the ion precipitation. For example, ion precipitating from the plasma sheet to planet's ionosphere enhancing auroral activity [e.g., *Delcourt et al,* 1996a]. *Keiling et al*. [2004] reported that energy-dispersed ion structures (EDIS) in the plasma sheet boundary layer which is substructured into several beamlets. According to the numerical model in *Ashour-Abdalla et al*. [1992], plasma mantle ions are convecting into the magnetotail current sheet and are trapped and then ejected following the Speiser orbit. They give the EDIS its particular beamlet structure.

All researches mentioned above were done considering only spatial variations of the magnetic field, parameterized by κ. Below we will discuss some studies on temporal variations of the magnetic field, for instance, the case of the dipolarization event [e.g., *Aggson et al.,* 1983; *Delcourt et al.,* 1990, 2002, 2010; *Nosé et al.,* 2000a, b; *Daglis et al.,* 1998; *Daglis,* 2001]. By considering a gradual variation of Kp levels, the short-lived reconfiguration of the magnetosphere, equivalent to auroral substorms, was modelled. Similar to the non-adiabatic motion due to the spatial variation of the magnetic field, temporal variations can also cause non-adiabatic motion even when $\kappa > 3$. They observed the same three-branch pattern and large energy gain during dipolarization events compared to non-dipolarization timings. Particularly, *Delcourt et al*. [2010] investigated the non-adiabatic energization during the magnetic field compression at Mercury. They show that large μ change is expected to be effective when the scale of the field variations and the cyclotron period are comparable. This is a type of "resonance like" energy gain (Figure 2.9).

Since non-adiabatic motion is caused depending on the relationship between the scale of particle gyration motion and that of the field variations, only selected ion species can be affected by it. Quasi-adiabaticity evolution depending upon the time scale of the magnetic field reconfiguration is summarized in Figure 2.10.

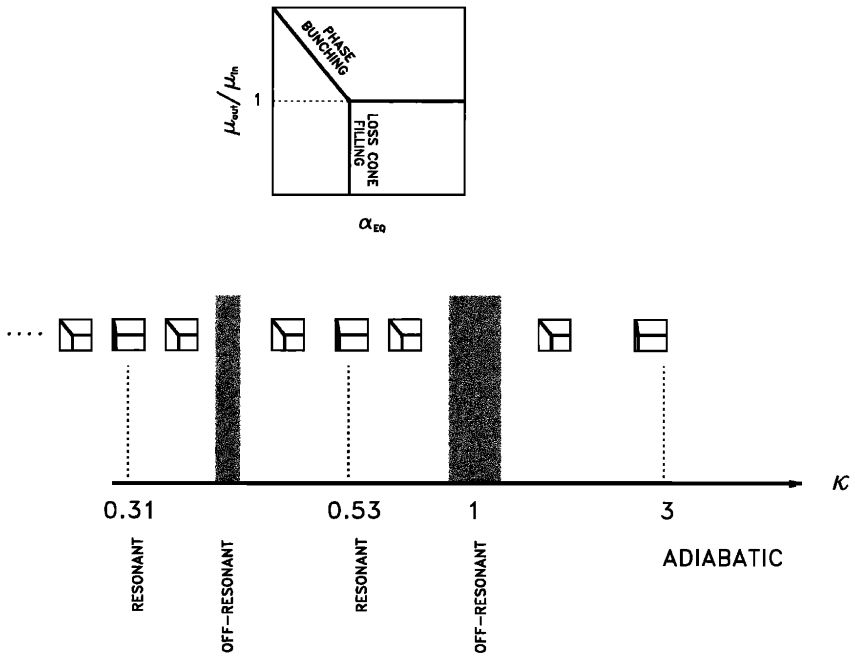

Figure 2.8 Three-branch pattern dependence on κ. Resonance region is obtained from Equation (2.22). The three-branch disappears when the region is off-resonant. Adapted from *Delcourt and Martin* [1999].

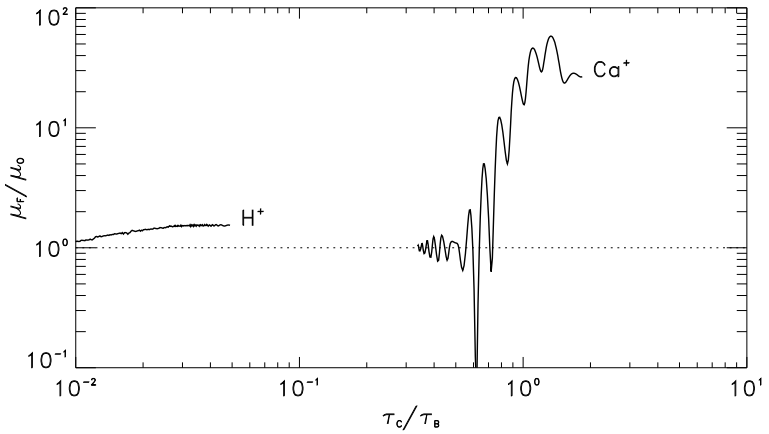

Figure 2.9 The magnetic moment variation as a function of the ratio of cyclotron period (τ_c) to the temporal magnetic field variation (τ_B). Two ion species are examined here, proton and Calcium ion. Large μ changes can be expected where $\tau_c \sim \tau_B$. Adapted from *Delcourt et al.* [2010].

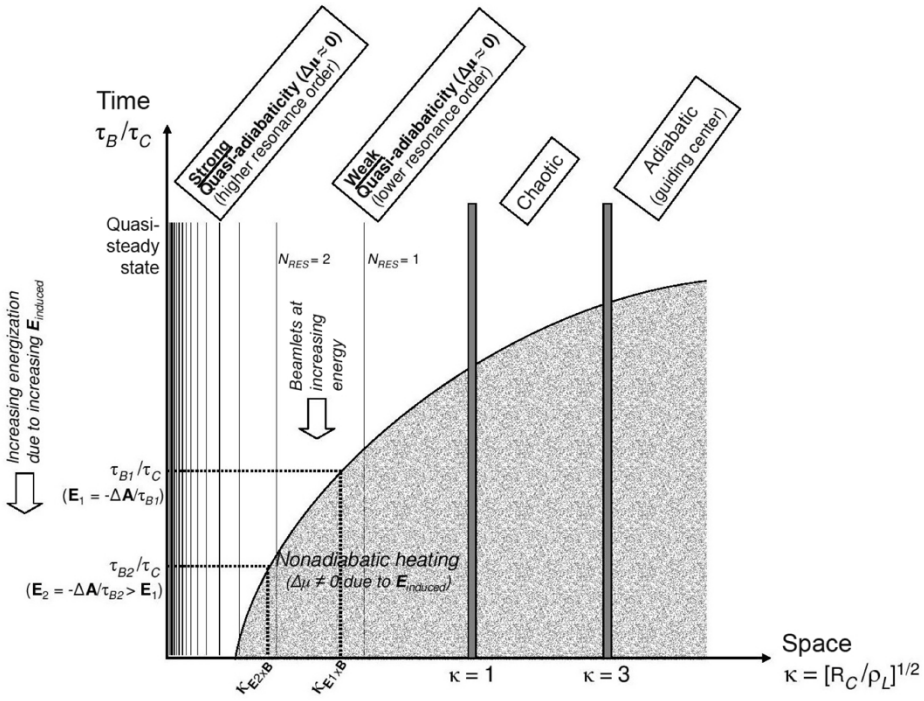

Figure 2.10 Schematic representation of quasi-adiabaticity evolution depending on the time scale of the magnetic field line reconfiguration. Figure is adapted from *Delcourt et al*. [2017].

Since different authors named particle orbits differently for $\kappa < 1$, we divide the nomenclature below. We have three classes at $\kappa < 1$, class 1: Speiser [*Speiser,* 1965], transient [*Chen and Palmadesso,* 1986], quasi-adiabatic [*Büchner and Zelenyi,* 1989] orbit, and resonant particles. Class 2: quasi-trapped [*Chen and Palmadesso,* 1986], cucumber [*Büchner and Zelenyi,* 1989], and stochastic orbit which means non-resonant. Finally, class 3: trapped orbit.

If we look at the non-adiabatic motion due to the electric field variations, there is only one study investigated by *Rothwell et al*. [1994]. They injected ions in the domain of the electric field gradient (the Harang discontinuity in the near-Earth magnetosphere, see Figure 2.11), and investigated how particles behave. The existence of the Harang discontinuity causes the gyro-phase bunching of oxygen ions, which is equivalent to the velocity distribution changes, resulting in the density striations. Currently, this is the only one study of non-adiabatic motion caused by the electric field variation suggesting that further researches on this particular aspect are required.

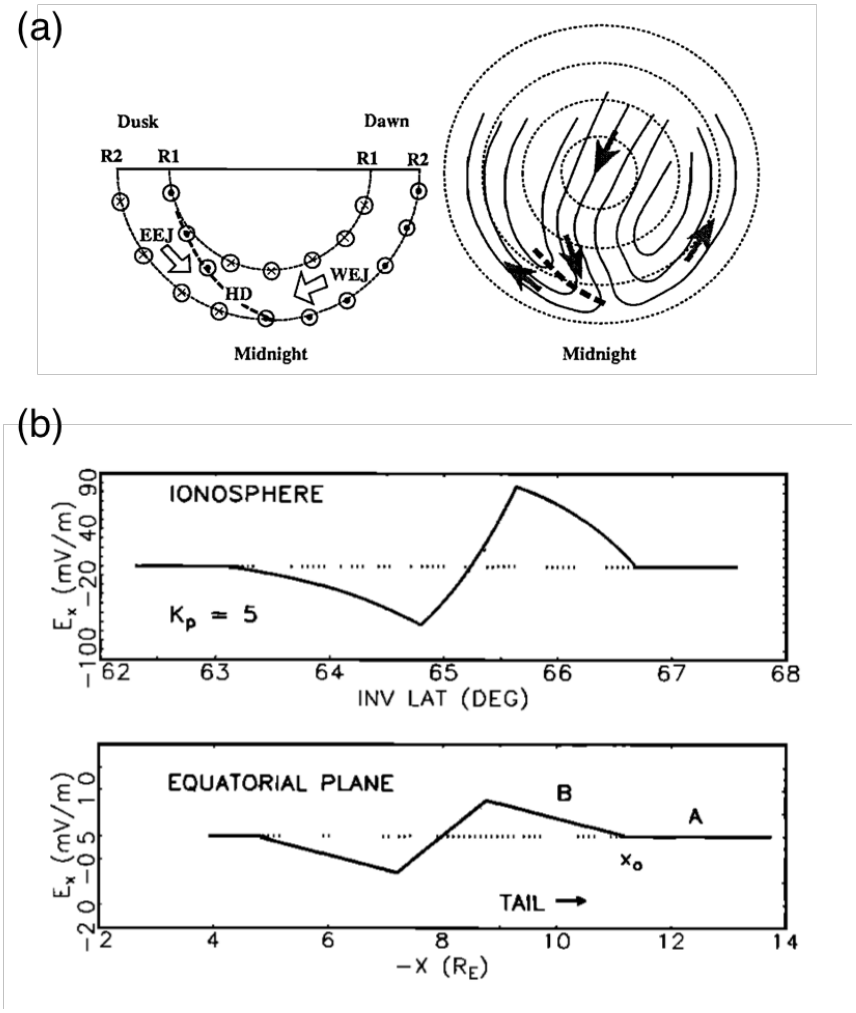

Figure 2.11 (a) Schematic picture of the Harang discontinuity (HD) in the nightside northern hemisphere of Earth. The HD is indicated by the dashed line. In the left panel, the HD is illustrated in the electrojets (EEJ: eastward electrojets, WEJ: westward electrojets) and large-scale FACs (R1: region 1, R2: region 2) and in the right panel the HD is illustrated in the plasma flow in the nightside ionosphere. The figure is adapted from *Koskinen and Pulkkinen* [1995]. (b) A simplified Harang discontinuity model in the ionosphere (upper) and the equatorial plane (bottom). Both panels show the electric field as a function of invariant latitude (upper) and of distance from the center of the planet (bottom). The figure is adapted from *Rothwell et al*. [1994].

Chapter 3

Method

In the field of space plasma physics, many researchers have been working in developing numerical methods for better understanding the physical mechanisms behind plasma dynamics. Each numerical method is selected and applied depending on the nature of the considered problem. In this study, we focus on the non-adiabatic motion of charged particles, especially of heavy ions of planetary origin, within Kelvin-Helmholtz (KH) vortices.

The KH instability, a well-known as magnetohydrodynamic (MHD) instability, has been studied by several papers. Its quantitative characteristics have been investigated using numerical methods. The most widely used numerical approach for the study of the KH instability is the MHD simulation where the plasma is treated as a magnetized fluid. The MHD simulation is able to provide us a macroscopic description of the system, whereas it does not allow us to investigate the motion of individual charged particles. Since we focus on the particle motion in the KH field in this thesis, we adopted an approach similar to that used in Large-Scale Kinetics (LSK) studies at Earth [e.g., *Ashour-Abdalla et al.,* 1994]. That is, we trace test particles within a field configuration derived from the MHD simulation. In this chapter, these two different numerical methods are described.

3.1 KH field from MHD simulation

In the MHD simulation, a set of MHD equations describing the conservation of mass, momentum, total energy, and the induction of the magnetic field are solved. This conservation system of equations can be written as:

$$\frac{\partial}{\partial t}\rho + \nabla \cdot (\rho \boldsymbol{V}) = 0\,, \tag{3.1}$$

$$\frac{\partial}{\partial t}\rho \boldsymbol{V} + \nabla \cdot \left(\rho \boldsymbol{V}\boldsymbol{V} + \Pi \boldsymbol{I} - \frac{\boldsymbol{B}\boldsymbol{B}}{\mu_0}\right) = 0\,, \tag{3.2}$$

$$\frac{\partial}{\partial t}e + \nabla \cdot \left[(e + \Pi)\boldsymbol{V} - \frac{(\boldsymbol{B}\cdot\boldsymbol{V})\boldsymbol{B}}{\mu_0}\right] = 0\,, \tag{3.3}$$

$$\frac{\partial}{\partial t}\boldsymbol{B} + \nabla \cdot (\boldsymbol{V}\boldsymbol{B} - \boldsymbol{B}\boldsymbol{V}) = 0\,, \tag{3.4}$$

where ρ is the mass density, $\boldsymbol{V}$ is the velocity of background protons, $\boldsymbol{B}$ is the magnetic field, Π is the total pressure, μ_0 is the permeability in vacuum, and e is the total energy density. The total energy density e is given by:

$$e = \frac{p}{\gamma - 1} + \frac{\rho V^2}{2} + \frac{B^2}{2\mu_0}\,, \tag{3.5}$$

where p is the plasma thermal pressure and γ is the ratio of specific heats ($\gamma = 5/3$). The total pressure Π is the sum of thermal pressure and magnetic pressure:

$$\Pi = p + \frac{B^2}{2\mu_0}\,. \tag{3.6}$$

The system of MHD equations is rewritten in a general conservative form as:

$$\frac{\partial U}{\partial t} + \nabla \cdot \mathcal{F}(U) = 0. \tag{3.7}$$

We also work with normalized quantities

$$\rho = \rho_n \tilde{\rho}, \qquad \boldsymbol{V} = V_n \tilde{\boldsymbol{V}}, \qquad \Pi = \rho_n V_n^2 \tilde{\Pi}, \qquad \boldsymbol{B} = \sqrt{\mu_0 \rho_n V_n^2}\,\tilde{\boldsymbol{B}}, \tag{3.8}$$

where normalized quantities are denoted with a tilde on top. ρ_n and V_n are the mass density and the plasma velocity for normalization. The temporal scale is normalized using proton mass, charge and the magnetic field, $t_{\mathrm{n}} = \frac{m_{\mathrm{p}}}{eB_{\mathrm{n}}}\tilde{t}$ and the spatial scale is determined by the velocity and time. The typical thickness will be given as a for boundary layer. In this study, a and V_n are given by MESSENGER observational results [*Gershman et al.*, 2015]. ρ_{n} is $m_{\mathrm{p}} \times n_{\mathrm{msh}}$ [ions/cm^3],

where m_p is the mass of a proton and n_{msh} is the number of ions in the magnetosheath region, respectively. Further in this text, for readability, the tilde will be omitted.

To focus on the ion dynamics in the KH field, we perform the local MHD simulation, considering one KH vortex in the simulation domain. The periodical boundary condition is set to the x-axis and the free boundary condition is set to the y-axis (Figure 3.1(a)). Physical quantities are varied across the transition layer, which is now equivalent to the magnetopause. The magnetic field has only the B_z component to consider the most unstable case for the KH instability, i.e., the wave is perpendicular to the magnetic field ($k_x \perp \boldsymbol{B}$) is investigated. The initial profiles of the velocity, magnetic field and mass density across the transition layer are given by 'tanh' following in the usual way of the numerical KH study:

$$\begin{aligned} \rho(y) &= 0.5\rho_0\left[1-\tanh\left(\frac{y}{a}\right)\right] + 0.5\rho_1\left[1+\tanh\left(\frac{y}{a}\right)\right], \\ V_x(y) &= 0.5V_{x0}\left[1-\tanh\left(\frac{y}{a}\right)\right] + 0.5V_{x1}\left[1+\tanh\left(\frac{y}{a}\right)\right], \\ B_z(y) &= 0.5B_{z0}\left[1-\tanh\left(\frac{y}{a}\right)\right] + 0.5B_{z1}\left[1+\tanh\left(\frac{y}{a}\right)\right], \end{aligned} \tag{3.9}$$

where ρ_0, V_{x0} and B_{z0} denote the normalized mass density, velocity, and the magnetic field in the magnetosheath region, and ρ_1, V_{x1} and B_{z1} are the values in the magnetosphere region, respectively. The initial total pressure is:

$$\frac{\partial \Pi}{\partial y} = 0\,. \tag{3.10}$$

To fulfill Equation (3.10), the initial total pressure Π is constant so the initial plasma pressure is calculated from

$$p(y) = \Pi - \frac{B_z^2(y)}{2}\,. \tag{3.11}$$

These initial profiles can be seen in Figure 3.1(b). In addition, for the KH instability to happen, we give an initial perturbation by a white noise, defined as:

$$V_y(x,y) = \delta V_y \exp\left(-\left(\frac{y}{2a}\right)^2\right)\cdot random(x)\,, \tag{3.12}$$

where δV_y is the amplitude of the initial perturbation. The size of simulation box in x-axis is set to a typical KH wavelength that was observed in the magnetospheric flanks of Mercury by MESSENGER as $\sim 1.5 R_M$ [*Sundberg et al.,* 2011; *Gershman et al.,* 2015].

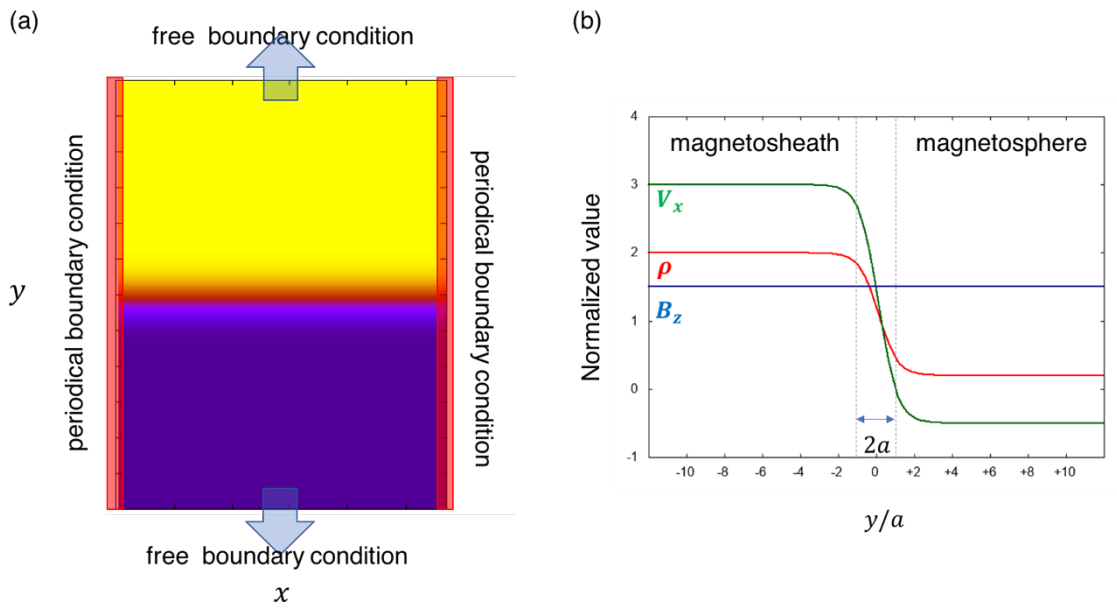

Figure 3.1 (a) Sketch of boundary conditions and (b) initial profiles of input parameters.

In this section, we explain the numerical schemes in the MHD simulations. In our MHD code, the semidiscrete central scheme [*Kurganov and Tadmor,* 2000] is combined with a 4th order uniform non-oscillatory (UNO) limiter [*Peer et al.,* 2008] that is used for space discretization, and the 3rd order total variation diminishing (TVD) Runge-Kutta scheme [*Shu and Osher,* 1989] is used for time discretization.

Generally, central schemes are the finite-difference methods for solving nonlinear convection and diffusion equations. They are not restricted to the specific eigenstructure of the problem and thus general conservation laws and related questions are solved effectively. For instance, Lax-Friedrichs scheme and the central Nessyahu-Tadmor (NT) scheme are typical examples of this type of central schemes with high resolution while retaining the simplicity of the Riemann-solver-free approach. However, this type of central schemes has a large numerical viscosity for a small time-steps. In this study, we implemented the semidiscrete central scheme, which is introduced by *Kurganov and Tadmor* [2000]. This was developed for a much smaller numerical viscosity even though it can provide us with retaining the simplicity of being independent of the eigenstructure of the problem. In this scheme, the hyperbolic conservation law is solved componentwise. The solution of a scalar hyperbolic conservation law is given by:

$$\frac{d\overline{u}_j}{dt} = -\frac{H_{j+\frac{1}{2}}(t) - H_{j-\frac{1}{2}}(t)}{\Delta x}\,, \tag{3.13}$$

with the numerical flux:

$$H_{j+\frac{1}{2}}(t^n) = \frac{f\left(u^+_{j+\frac{1}{2}}(t^n)\right) + f\left(u^-_{j+\frac{1}{2}}(t^n)\right)}{2} + \frac{a_{j+\frac{1}{2}}(t^n)}{2}\left(u^+_{j+\frac{1}{2}}(t^n) - u^-_{j+\frac{1}{2}}(t^n)\right), \tag{3.14}$$

here the intermediate values $u^{\pm}_{j+\frac{1}{2}}$ are given by:

$$u^+_{j+\frac{1}{2}} = u_{j+1}(t^n) - \frac{\Delta x}{2}(u_x)_{j+1}(t^n)\,, \tag{3.15}$$

$$u^-_{j+\frac{1}{2}} = u_j(t^n) + \frac{\Delta x}{2}(u_x)_j(t^n)\,, \tag{3.16}$$

and $a_{j+\frac{1}{2}}$ is the maximum propagation speed of u_j at the cell interface. If a non-oscillatory piecewise polynomial reconstruction of cell averaged data at time $t = t^n$ as $P_j(x)$, then Equations (3.15) and (3.16) are rewritten as:

$$u^+_{j+\frac{1}{2}} = P_{j+1}\left(x_{j+\frac{1}{2}},\, t^n\right), \tag{3.17}$$

$$u^-_{j+\frac{1}{2}} = P_j\left(x_{j+\frac{1}{2}},\, t^n\right). \tag{3.18}$$

Here a 4th order reconstruction which is proposed by *Peer et al*. [2008] is used. Although *Peer et al*. [2008] used a staggered integration, we apply it to the non-staggered scheme proposed by *Kurganov and Tadmor* [2000]. The piecewise cubic polynomial is defined by:

$$P_u(x, t^n) = \sum_j R^n_j(x)\chi_j(x)\,, \tag{3.19}$$

where $\chi_j(x)$ is the characteristic function of the cell $I_j = [x_{j-\frac{1}{2}},\, x_{j+\frac{1}{2}}]$ and $R^n_j(x)$ is a cubic polynomial in I_j reconstructed from cell averages $\{\overline{u}^n_j\}$. The interpolation polynomial $R^n_j(x)$ on I_j has the form:

$$R^n_j(x) = u^n_j + u'_j\left(\frac{x - x_j}{h}\right) + \frac{1}{2!}u''_j\left(\frac{x - x_j}{h}\right)^2 + \frac{1}{3!}u'''_j\left(\frac{x - x_j}{h}\right)^3, x \in I_j, \tag{3.20}$$

In addition, $R^n_j(x)$ follows the conservation property:

$$\overline{u}^n_j = \frac{1}{h}\int_{I_j} R^n_j(x)dx\,, \tag{3.21}$$

and then, u_j^n should satisfy

$$u_j^n = \bar{u}_j^n - \frac{1}{24}u_j'' \,. \tag{3.22}$$

In order to get 4th order accuracy, *Peer et al*. [2008] employed the uniformly modified high order accurate non-oscillatory limiter below:

$$u_j' = MM\begin{pmatrix} \Delta\bar{u}_{j-\frac{1}{2}} + \frac{1}{2}MM\left(\Delta^2\bar{u}_{j-1} + \nu_1 u_j''', \Delta^2\bar{u}_j + \nu_2 u_j'''\right), \\ \Delta\bar{u}_{j+\frac{1}{2}} + \frac{1}{2}MM\left(\Delta^2\bar{u}_j + \nu_3 u_j''', \Delta^2\bar{u}_{j+1} + \nu_4 u_{j+1}'''\right) \end{pmatrix}, \tag{3.23}$$

$$u_j'' = MM\left(\Delta^2\bar{u}_{j-1} + u_{j-1}''',\ \Delta^2\bar{u}_j,\ \Delta^2\bar{u}_{j+1} - u_{j+1}'''\right), \tag{3.24}$$

$$u_j''' = MM\left(\Delta^3\bar{u}_{j-\frac{1}{2}},\quad \Delta^3\bar{u}_{j+\frac{1}{2}}\right), \tag{3.25}$$

where MM denotes the MinMod limiter, which is a typical flux limiter, and here we have $\nu_1 = \frac{7}{12}, \nu_2 = -\frac{5}{12}, \nu_3 = \frac{5}{12}, \nu_4 = -\frac{7}{12}$.

For time discretization, the TVD Runge-Kutta scheme is performed. It is written as:

$$\phi^{(i)} = \sum_{k=0}^{i-1}\left\{\alpha_{ik}\phi^{(k)} + \beta_{ik}f\left(\phi^{(k)}\right)\right\}, \qquad i = 1, 2, \dots, m\,, \tag{3.26}$$

with:

$$\phi^{(0)} = \phi^n,\ \phi^{(m)} = \phi^{n+1}\,, \tag{3.27}$$

$$\alpha_{ik} \geq 0, \qquad \sum_{k=0}^{i-1}\alpha_{ik} = 1\,, \tag{3.29}$$

$$\beta_{ik} = c_{ik} - \sum_{l=k+1}^{i-1} c_{lk}\alpha_{ik}\ , \tag{3.30}$$

where $f\left(\phi^{(k)}\right)$ denotes terms of the advection equation except the term of the time derivative. In detail, the 3rd order scheme is used, therefore m = 3 is set. We can thus write down Equation (3.26) as:

$$\phi^{(1)} = \alpha_{10}\phi^{(0)} + \beta_{10}f\left(\phi^{(0)}\right), \tag{3.31}$$

$$\phi^{(2)} = \alpha_{20}\phi^{(0)} + \beta_{20}\Delta t f\left(\phi^{(0)}\right) + \alpha_{21}\phi^{(1)} + \beta_{21}\Delta t f\left(\phi^{(1)}\right), \tag{3.32}$$

$$\phi^{(3)} = \alpha_{30}\phi^{(0)} + \beta_{30}\Delta t f\left(\phi^{(0)}\right) + \alpha_{31}\phi^{(1)} + \beta_{31}\Delta t f\left(\phi^{(1)}\right) + \alpha_{32}\phi^{(2)} + \beta_{32}\Delta t f\left(\phi^{(2)}\right). \tag{3.33}$$

Using Equation (3.29) and (3.30), the coefficients of the Runge-Kutta method are obtained (see Table 3.1).

Once the MHD simulation is performed, all physical quantities are un-normalized and given to the test particle tracing calculation as a field information.

Confirmation of the accuracy of the MHD simulation for the development of the KH instability was done by reproducing the numerical runs which were performed in *Amerstorfer et al*. [2010].

Table 3.1 Coefficients of the 3rd order Runge-Kutta method

order	α			β			CFL coefficient
3	1			1			1
	3/4	1/4		0	1/4		
	1/3	0	2/3	0	0	2/3	

3.2 Test particle tracing technique

Test particle tracing refers to the numerical method for calculation of the motion of individual charged particles in a particular environment, whereas the MHD simulation does not allow us to trace individual ions. This test particle tracing technique is commonly used for the plasma physics, especially for studies of charged particle motion and its transport in a given region where the guiding center approximation may not be valid (e.g., current sheet). Although there are other numerical methods implementing the kinetic effect of charged particles, for instance, the Particle-in-Cell (PIC) or hybrid methods, they cannot describe the motion of individual charged particles properly when the guiding center theory is not valid. In order to resolve the particle gyration motion, we need a few degrees of ion's gyration as an advanced time step. Generally, PIC or Hybrid methods have relatively large time step such as $0.05\Omega^{-1}$ where Ω is the proton gyrofrequency [e.g., *Lin et al.,* 2010], and it is not enough to describe the full motion of charged particles. Therefore, the test particle tracing calculation is the most reasonable method to understand such a micro scale physics. On the other hand, the test particle tracing calculation is not a self-consistent model. It does not allow us to have feedback from the motion of the test particles to the field, even though charged particle motion can be a source for the electric/magnetic field. In this sense, the species of test particles should not be a dominant component in the considered domain.

Previous MESSENGER observations had not provided information on which ion species can be dominant in the magnetospheric flanks of Mercury, or how high is the flux of our focused species (heavy ions of planetary origin) compared to that of solar wind proton. Therefore, we refer to previous numerical studies to consider whether the test particle technique is appropriate or not [e.g., *Leblanc et al.,* 2003; *Delcourt et al.,* 2009a; *Wang et al.,* 2010]. For example, *Delcourt et al.* [2009a] shows the results of the simulation of both H^+ and Na^+ response to the depolarization model in the Mercury's magnetotail. In this situation, the proton density shows at least ten times larger value than that of sodium ions. Relying on these values, we say that the test particle tracing technique is appropriate and thus, we apply the test particle tracing technique in the MHD field.

Generally, the test particle tracing calculation is equivalent to the calculation of individual particle trajectories which do not interact with each other and do not affect to the field configuration significantly. This method requires to explicitly solve of the single particle equation of motion in a certain environment given by corresponding physical questions. For example, to understand particle behaviors in the magnetotail region, a global magnetospheric configuration for each planet is used [e.g., *Tyganenko* 1989]. In this study, we use the KH field obtained from the MHD simulation and interpolate it to obtain the field values at each particle position during

its gyration motion. First of all, we explain the interpolation method for the field and then we explain detailed numerical approach.

In the MHD simulation, physical values are connected to the center of each grid and calculated by the conservative laws. In order to obtain the values of the electric/magnetic field at an arbitrary particle position, we implement the area-weighting method as an interpolation method.

Let's consider a two-dimensional electric field (Figure 3.2). Now we calculate the field information at each successive point: (x_i, y_j), (x_{i+1}, y_j), (x_i, y_{j+1}), (x_{i+1}, y_{j+1}). Using the field values at each point, the electric field at an arbitrary position in this area, for a particle position at (x_p, y_p), can be described as:

$$\begin{aligned} E_x(x_p, y_p) = & \left(1 - i + \frac{x_p}{\Delta x}\right)\left(1 - j + \frac{y_p}{\Delta y}\right) E_x(x_i, y_j) \\ & + \left(\frac{x_p}{\Delta x} - i\right)\left(1 - j + \frac{y_p}{\Delta y}\right) E_x(x_{i+1}, y_j) \\ & + \left(1 - i + \frac{x_p}{\Delta x}\right)\left(\frac{y_p}{\Delta y} - j\right) E_x(x_i, y_{j+1}) \\ & + \left(\frac{x_p}{\Delta x} - i\right)\left(\frac{y_p}{\Delta y} - j\right) E_x(x_{i+1}, y_{j+1}) \\ & = S_1 E_x(x_i, y_j) + S_2 E_x(x_{i+1}, y_j) \\ & + S_3 E_x(x_i, y_{j+1}) + S_4 E_x(x_{i+1}, y_{j+1}) . \end{aligned} \tag{3.34}$$

You may realize that a shape function can be directly used as an interpolation function. In our calculation, a three-dimensional interpolation method (the volume weighting method) is applied in a similar way.

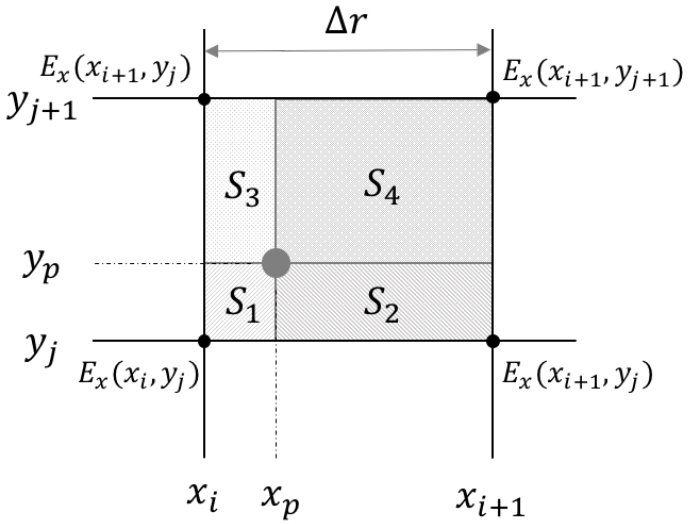

Figure 3.2 Sketch of the area-weighting method.

After obtaining the field information at each particle point, we calculate the equation of motion for a particle from the formula shown in Chapter 2.

$$m\frac{d\boldsymbol{v}(t)}{dt} = q(\boldsymbol{E}(r,t) + \boldsymbol{v}(t)\times\boldsymbol{B}(r,t)), \tag{3.35}$$

Please note that each field quantity shows the value at a particle position r at the given time t. The electric field is not obtained explicitly in the MHD simulation, but it is calculated by Ohm's law ($\boldsymbol{E} = -\boldsymbol{V}\times\boldsymbol{B}$) taking into account that $\boldsymbol{V}$ is the background proton velocity. In the test particle tracing calculation, we use the 4th order Runge-Kutta which is the one of the most widely used numerical method to solve differential equations. This is an explicit calculation and the error term is calculated 4 times per step before moving on to the next particle position. This is done in order to retain the accuracy in the calculation of the entire step. The 4th order Runge-Kutta method can be described as:

$$y_{n+1} = y_n + \frac{1}{6}[k_0 + 2k_1 + 2k_2 + k_3]\,, \tag{3.36}$$

where, error terms are shown with the k with suffix and they are determined as:

$$k_0 = hf(x_n, y_n)\,, \tag{3.37}$$

$$k_1 = hf\left(x_n + \frac{1}{2}h, y_n + \frac{1}{2}k_0\right), \tag{3.38}$$

$$k_2 = hf\left(x_n + \frac{1}{2}h, y_n + \frac{1}{2}k_1\right), \tag{3.39}$$

$$k_0 = hf(x_n + h, y_n + k_2)\,. \tag{3.40}$$

An illustration of the principle of the 4th order Runge-Kutta is shown in Figure 3.3 [*Press et al.*, 1992]. To get high accuracy, the derivative is evaluated at each small step. In addition, the advanced time step Δt is not fixed but corresponding to the angle of 2 degrees of the gyration at each step to make sure that the particle trajectory is traced correctly.

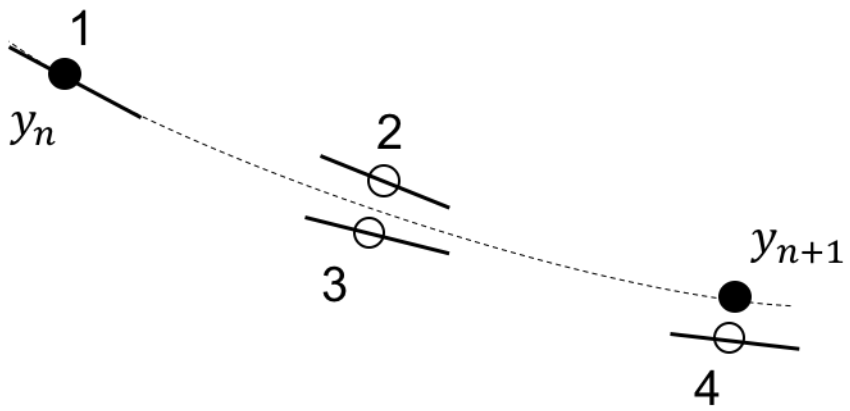

Figure 3.3 Illustration of the 4th order Runge-Kutta method. Derivative is estimated at each small step.

In our calculation, the particle position, total energy, pitch angle, and phase angle are input as initial parameters. In addition, the instantaneous magnetic moment is calculated at each time step. The particle behavior at the boundary is treated depending on the physical parameter to study, meaning that each case will be described in their corresponding chapter. Moreover, in order to trace particles with an arbitrary pitch angle, a three-dimensional field information is required. For simplicity, we perform the two-dimensional MHD simulation, and obtained field configurations are used in the 3rd dimension.

Chapter 4

General features of ion dynamics in KH fields

As introduced in Chapter 2, non-adiabatic behaviors of ions in the magnetotail are generally associated with prominent changes of the magnetic field, be they spatial [e.g., *Büchner and Zelenyi*, 1989; *Ashour-Abdalla et al*., 1993b; *Delcourt et al*., 2003] or temporal [e.g., *Delcourt*, 2007]. In this study, we focus on a specific type of non-adiabaticity, i.e., non-adiabatic behaviors related to the rapid changes of the electric field or of the $\boldsymbol{E}\times\boldsymbol{B}$ flow field associated with the development of the Kelvin-Helmholtz (KH) instability in the magnetospheric flanks of Mercury. In this chapter, general features of ion dynamics in KH fields are investigated by using simple KH configurations. The realistic field configuration in the Hermean environment will be considered in Chapter 5.

Generally speaking, studying particle transport allows us to consider the net change of the population of heavy ions in Mercury's magnetosphere. The typical trajectory of heavy ions of planetary origin is globally considered as incoming from the cusp region [e.g., *Delcourt et al*., 2003]. Exospheric neutrals are ionized in the cusp region by solar UV, and they move to the magnetosphere guided by the magnetic field lines. In the nightside magnetosphere, the curvature drift makes ions move toward the duskside magnetopause, which is the boundary layer between the dominated region of planetary and solar wind plasmas. In the duskside magnetospheric flanks of Mercury, MESSENGER observed KH vortices. In that area, the magnetic and electric fields vary in time and space, and thus particle motion is influenced to a greater or lesser degree by these variations. When the temporal or spatial field variations are larger than the scales of the gyromotion of ions, then the magnetic moment is conserved and the particles can retain its circular orbit. On the contrary, if fields vary rapidly, the magnetic moment may not be conserved, making

the particles gain energy in a non-adiabatic manner, and thus their motion may change chaotically. In the magnetospheric flanks, the main component of the magnetic field is along the z-direction (in the Mercury solar orbital (MSO) coordinates) and does not change drastically when the IMF is northward. This is the case as we observe the most unstable condition for the KH instability. In this situation, the electric field calculated by Ohm's law may vary rapidly associated with the development of the KH instability.

Theoretically, the electric field variation may affect the motion of charged particles meaning the ion dynamics and it may lead to particle energy gain in a non-adiabatic manner. A similar type of a non-adiabatic behavior was reported in the region connected to the Harang discontinuity in the near-Earth magnetosphere by *Rothwell et al*. [1994]. However, currently this is the only one study for non-adiabatic signatures due to the electric field variations. Thus, in our study we will focus especially on heavy ions of planetary origin (Na^+, K^+, and O^+) since those ions have a large-scale gyromotion in our area of interest.

The questions we would like to answer in this chapter are as follows:

1) How are particles transported within KH vortices?

2) Can we expect non-adiabatic acceleration of heavy ions in KH fields?

3) If so, how much energy can the particle gain?

To investigate these questions, we performed test particle tracing calculations in the KH field obtained from the MHD simulation. For simplicity, we adopted here a two-step approach, that is, we first analyzed the ion dynamics in a steady vortex configuration, and second in a time-varying configuration. The first step allowed us to remove phasing effects between the particle trajectories and the rapidly changing KH vortices and to concentrate on the effect of abrupt electric field variations. The second step allowed us to catch the particle response in a realistic time-varying case and to generalize the non-adiabatic behaviors that were first obtained. In Sections 4.1 and 4.2, we show the results of particle behavior in a fixed field configuration, then, as a second step, test particles are traced in a time-varying KH field and it will be detailed in Section 4.3.

4.1 Field configuration and model trajectories

The MHD simulation described in Chapter 3 was used to obtain electromagnetic field associated with the development of the KH instability. In the present MHD simulations, as mentioned above, first we consider the simple KH configuration. The size of simulation box is set with 100×100 grids in x and y dimension with square boxes. The half thickness of the boundary layer is set, ~ 360 km. The x-component of the velocity is set to 50 km/s and -50 km/s in the magnetosphere (i.e., $0 \leq y < 1.5$ in Figure 4.1) and magnetosheath region (i.e., $1.5 < y \leq 3.0$ in Figure 4.1), respectively. The ions number density is set to 10 ions/cc and to 100 ions/cc in the magnetosphere and the magnetosheath, and the homogeneous magnetic field is set to 21.75 nT in the z-direction. The characteristic time scale for growth of the KH instability directly depends on these values. For example, if a twice larger velocity shear across the boundary layer would be considered, the characteristic linear growth time for the KH development would be twice shorted. The propagation speed of the perturbation along the magnetopause, it is controlled not only by the velocity shear but also by the mass density ration across the boundary. In Figure 4.1, we show the electric field configuration of the KH development, which is calculated by Ohm's law, in color-coded map at distinct time. Starting from two well-delineated regions in Figure 4.1(left), it can be seen in the other panels that gradual mixing occurs as time goes on (from left to right), with the development of a large rolled up vortex.

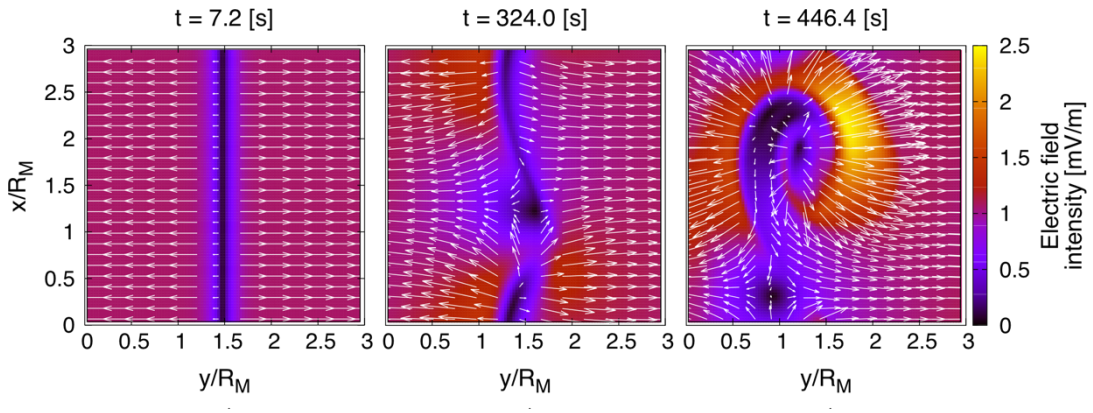

Figure 4.1 Color-coded electric field intensity obtained from MHD modelling in the equatorial (x-y) plane. Panels from left to right are corresponding to distinct times of KH instability development. White arrows show the orientation of the electric field. Spatial scale is normalized by the Mercury radius R_M. Figure is adapted from *Aizawa et al.* [2018].

Then, test Na^+ ions traced in a fixed field configuration were obtained. This test particle tracing was performed using the full equation of motion (introduced in Chapter 3) in order to account for possible variations of the particle magnetic moment. Indeed, for the guiding center approximation to be valid, negligible field variations must occur within a cyclotron turn [see, e.g., *Northrop*, 1963]. It will be shown hereinafter that, although the magnetic field is nearly constant (in the z-direction), the rapid change of the electric field (***E***) within KH vortices can lead to significant change of the particle magnetic moment (denoted μ hereinafter).

In these present computations, the periodical boundary condition in the y-direction that was assumed in our MHD simulation was not used for particle tracing in a fixed simulation frame. This tracing was interrupted when the test particle exits the simulation box. In situ measurements by MESSENGER suggest that the typical wavelength of KH vortices is ~ $1.5R_M$[e.g., *Sundberg et al*., 2011], a typical spatial scale that is well reproduced in our simulation box (see Figure 4.1). As for the velocity shear, it was assumed to spread over $1.0R_M$ which was considered as an upper limit for this characteristic scale. Simulations like the present ones usually contain sets of parameters that can be adjusted in different ways, but these do not affect in essence the main outcomes such as the violation of the 1st adiabatic invariant that we describe hereinafter.

Figure 4.2 shows an example of Na^+ trajectories obtained. The particle was injected with an initial energy of 10 eV in the nearly perpendicular direction (95° pitch angle), this condition is named Case 1. It would be the case for instance for a sodium neutral in the extended exosphere of Mercury that would be located in the vicinity of the magnetopause and that would be suddenly ionized by a solar UV photon. In the right panel of Figure 4.2, this test Na^+ was launched from an arbitrary position inside the KH vortex and traced until it leaved the simulation box. In the left panels of Figure 4.2 it can be seen that after ~150 s time of flight, the Na^+ magnetic moment rapidly increases by about two orders of magnitude. This μ change coincides with an impulsive enhancement of the electric field intensity (top left panel) up to ~2.5 mV/m, while the electric field orientation (second panel from top) does not change appreciably. On the other hand, looking at the bottom left panel of Figure 4.2 it can be seen that the final energy realized by the test Na^+ corresponds approximately to the maximum energy associated with the ***E***×***B*** drift (green profile). Figure 4.2 thus suggests that particle motion inside KH vortices is essentially adiabatic except for short time intervals during which particles are subjected to bursts of the electric field that rapidly raise the ion perpendicular energy up to the peak ***E***×***B*** drift energy (denoted by $\varepsilon_{ExB,max}$ hereinafter).

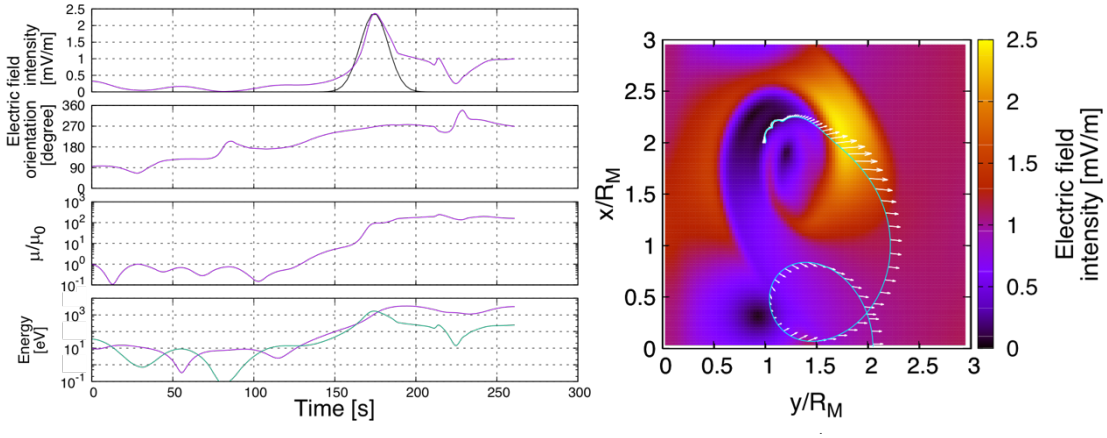

Figure 4.2 (Case 1) Model Na^+ trajectory in the electric field configuration obtained from MHD modelling. The particle trajectory in x-y plane is shown on the electric field intensity color-coded map with a blue line and white arrows for selected electric field orientations. The left panels show (from top to bottom) the electric field intensity, orientation, and Na^+ magnetic moment (normalized to the initial value), and Na^+ energy as a function of time. The test Na^+ is initialized with 10 eV energy and 95° pitch angle, and launched from an arbitrary position. The black profile (top left panel) shows a Gaussian fit to the prominent $\boldsymbol{E}$ burst. The green profile (bottom left panel) shows the corresponding kinetic energy to the $\boldsymbol{E}\times\boldsymbol{B}$ drift speed along the particle path. Figure is adapted from *Aizawa et al.* [2018].

Other cases are shown in Figure 4.3. In Case 2, a particle was injected with a completely large initial energy, i.e., 1000 eV for a 5° pitch angle (Figure 4.3(a)). Case 3 considered the same initial energy but with 90° pitch angle (Figure 4.3(b)). Similar non-adiabatic behavior with large μ increase was obtained for Case 2, nearly field-aligned particles with large initial energies (equivalently, small perpendicular energy). In contrast, no μ change was obtained for Case 3, test ions with initial energies and pitch angles such that their initial perpendicular energy exceeds $\varepsilon_{E\times B}$. The non-adiabatic character of the motion thus appears to depend upon the initial perpendicular energy that particles have with respect to the maximum kinetic energy $\varepsilon_{E\times B}$ (equivalently, maximum $\boldsymbol{E}\times\boldsymbol{B}$ drift speed) encountered along their path.

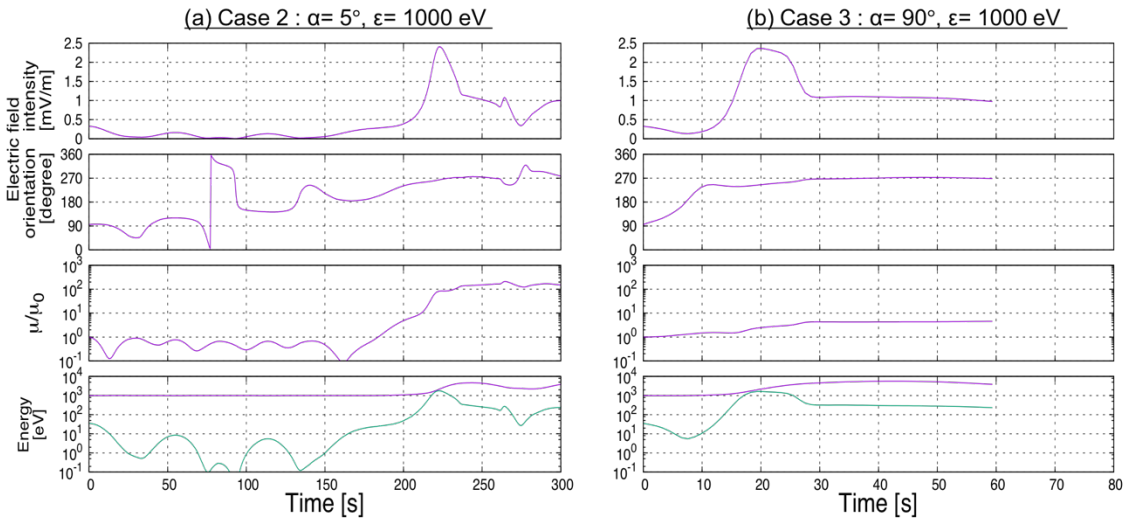

Figure 4.3 Other examples of Na^+ model trajectories in the same field configuration as Case 1, in the same format as left panels in Figure 4.2. (a) Test Na^+ is initialized 1000 eV with 5°, particle motion is mostly parallel to the magnetic field. (b) Test Na^+ is initialized 1000 eV with 90°, particle motion is mostly perpendicular to the magnetic field. Although clear ***E*** burst can be seen in both cases and its time scale is mostly same, (a) has large μ change while (b) does not. Figure is adapted from *Aizawa et al*. [2018].

4.2 Statistical analysis of ion energization

To investigate the transport of heavy ions through KH vortices in a more quantitative manner, we performed systematic Na^+ trajectory computations and compiled a statistics of $\boldsymbol{E}$ bursts and associated μ changes. These statistics were obtained by considering test Na^+ in different simulation frames after the linear growth phase (396 s, 424.8 s, and 446.4 s) with different initial energies (10 eV, 50 eV, 100 eV, 500 eV, 1 keV, 2.5 keV, 5 keV, and 10 keV), pitch angles (from 0° to 180° by steps of 10°), gyration phases (from 0° to 360° by steps of 10°) and launched in the vicinity of KH vortices. In this statistical analysis, $\boldsymbol{E}$ bursts were characterized using a Gaussian fit of the form:

$$E = E_{max} \exp\left\{-\left[\frac{t - t_0}{\tau}\right]^2\right\},$$

here E_{max} is the maximum $\boldsymbol{E}$ intensity, t_0 is the time of the burst center, and τ, the characteristic time scale of the burst. We checked all particle trajectories by eye and selected only those who showed clear $\boldsymbol{E}$ burst and/or multiple $\boldsymbol{E}$ bursts. A dataset of ~ 500 model cases of $\boldsymbol{E}$ bursts and associated μ changes was obtained and is summarized in Figure 4.4. Here, the post-burst perpendicular energy of Na^+ (normalized to $\varepsilon_{E\times B}$) is presented as a function of the pre-burst perpendicular energy (normalized to $\varepsilon_{E\times B}$) together with color-coded time scale of the $\boldsymbol{E}$ bursts encountered along the ion trajectories.

Figure 4.4 displays several features of interest. First, it can be seen that ions that have an initial perpendicular energy $(\mu B)_{\text{ini}}$ smaller than $\varepsilon_{E\times B}$ tend to be systematically energized up to $\varepsilon_{E\times B}$ (horizontal branch encircled in red). This behavior corresponds to that illustrated in Figure 4.2. Figure 4.4 also reveals that ions with initial perpendicular energies comparable to $\varepsilon_{E\times B}$ may actually lose energy during transport (vertical branch encircled in blue). This latter behavior is that of particles traveling against the electric field during the burst. Finally, a third behavior is noticeable in Figure 4.4 for ions with initial energies larger than $\varepsilon_{E\times B}$. Here, no significant energization is obtained and post-burst perpendicular energies spread along the first bisector, which is the case in Figure 4.3 (b) (oblique branch encircled in green).

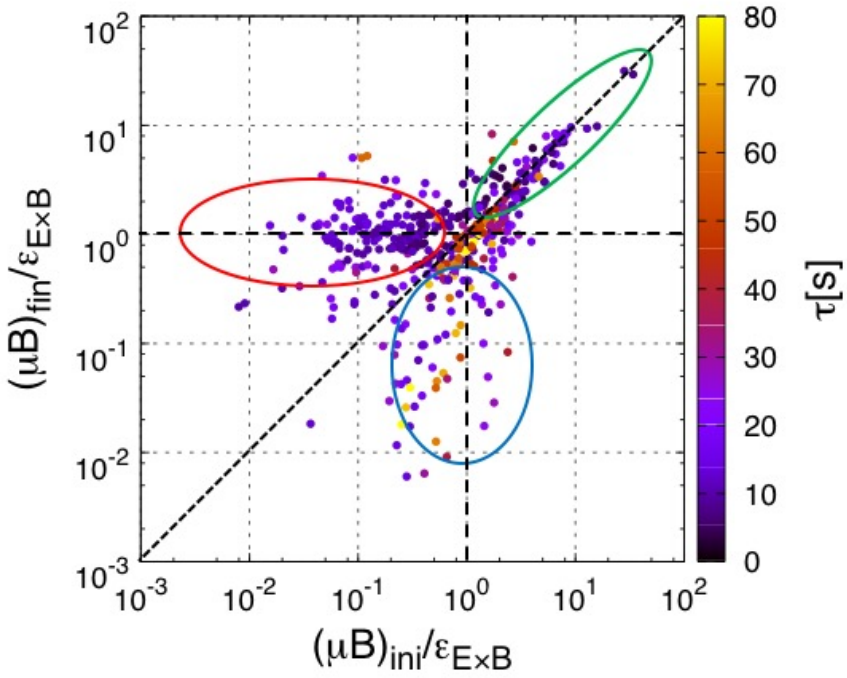

Figure 4.4 Final perpendicular energy of Na^{+} ions as a function of initial perpendicular energy (both normalized to the maximum $\boldsymbol{E}\times\boldsymbol{B}$ drift energy). The time scale of the corresponding $\boldsymbol{E}$ burst is given on the right. Figure is adapted from *Aizawa et al*. [2018].

Another view of the ion behavior during its transport through KH vortices can be obtained from Figure 4.5 that shows the above statistical results using a different format, viz., net energy change versus $\boldsymbol{E}$ burst time scale (normalized to the ion gyroperiod, τ_C) in the left panel and versus $\boldsymbol{E}$ burst amplitude in the right panel. Not surprisingly, the right panel of Figure 4.5 shows that the larger the burst amplitude ΔE, the larger the energy gain. Note here the nearly linear correlation between these two quantities (oblique dashed line). On the other hand, in the left panel of Figure 4.5 shows when the $\boldsymbol{E}$ burst duration nears the gyroperiod (i.e., $2\tau = \tau_C$, or equivalently $\tau/\tau_C = 0.5$ as indicated by the vertical dashed line), ions may be subjected to energy loss. In contrast, when the $\boldsymbol{E}$ burst duration is significantly smaller than the gyroperiod (i.e., $\tau/\tau_C \ll 0.5$), most ions are subjected to energy gain, this gain being more pronounced for larger burst amplitude as evidenced from the color-coded ΔE variations.

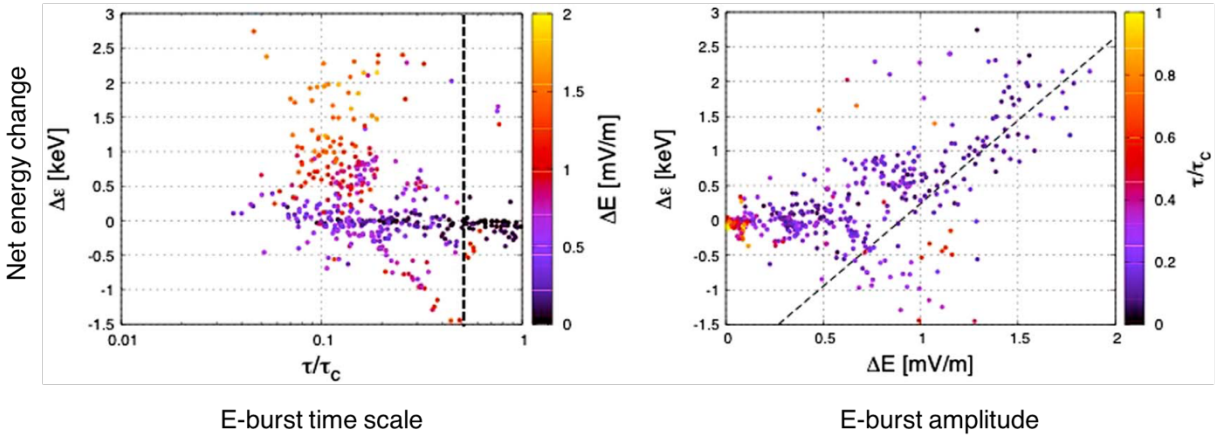

Figure 4.5 Net energy change of Na^+ ions as a function of (left) E-burst time scale (normalized to the ion gyroperiod) and (right) ***E*** burst amplitude. Color codes correspond to (left) ***E*** burst time. The dashed lines in the right and left panels show the linear profile obtained from a least squares fit and the $\tau/\tau_C = 0.5$ ratio, respectively. Figure is adapted from *Aizawa et al*. [2018].

4.3 Non-adiabatic energization in the time-varying KH field

The features of heavy ion's behavior in KH vortices described above correspond to a steady state configuration. Because the KH instability grows in time, ion dynamics in the time-varying field should be explored as well. In contrast with calculations in a fixed KH field configuration, the periodical boundary condition is used for the time-varying field.

Test Na^+ was injected at the beginning of MHD modeling with an energy of 10 eV and 90° of pitch angle in the ***E***×***B*** frame. Using the periodical boundary condition allows us to trace particle in the KH frame. Figure 4.6 shows the model trajectory in the time-varying KH configuration. Red vertical dashed line indicates the linear growth time of the KH instability, and post-linear growth time. The magnetic moment in the third panel from top shows two times larger change with a change in the electric field intensity (second panel), which is the similar feature that obtained in a steady state configuration shown in Figure 4.2.

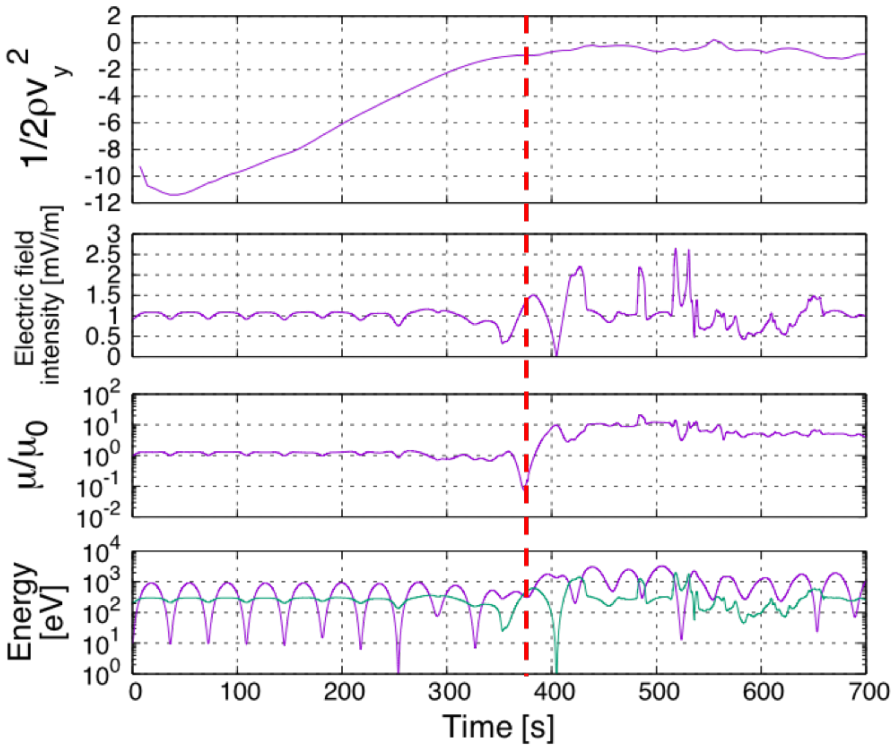

Figure 4.6 (top) Time evolution of the maximum kinetic energy in the direction perpendicular to the shear layer, $0.5\rho V_y^2$. The vertical dotted line near 370 s indicates the duration of KH linear growth. (bottom) Trajectory parameters of a test Na^+ in the time-varying case : ***E*** intensity, Na^+ magnetic moment which is normalized to the initial value, and energy as a function of time. The test Na^+ is initialized with 10 eV energy with 90° pitch angle. The green profile in the bottommost panel shows the kinetic energy corresponding to the ***E***×***B*** drift speed. Figure is adapted from *Aizawa et al*. [2018].

4.4 Chapter summary

In this chapter, we examined the non-adiabatic motion of charged particles throughout the KH development. We showed that non-adiabatic behavior can be caused not by the magnetic field changes but by electric field variations. This study is the one of a few focusing on the effects of electric field variations on the ion dynamics and its quantitative energy gain which had been explored by numerical calculations.

(1) Systematic energy gain

Non-adiabatic motion can be caused by the electric field variation. We found that the energization is controlled by the particle's perpendicular energy and the energy corresponding to the maximum $\boldsymbol{E}\times\boldsymbol{B}$ drift speed along the particle path, $\varepsilon_{E\times B}$. There are three different trend related to the energy gain. If the particle has a smaller perpendicular energy compared to that of the maximum $\boldsymbol{E}\times\boldsymbol{B}$ drift speed along the particle trajectory, then the particle can gain energy up to ~ $\varepsilon_{E\times B}$. If the particle has a comparable energy compared to $\varepsilon_{E\times B}$, it may lose energy depending upon the angle between the direction of particle moving and electric field vector felt by the particle. Lastly, if the particle has a large enough energy compared to $\varepsilon_{E\times B}$, then it does not gain energy anymore.

(2) Characteristics of the electric field variation

We found that increasing the amplitude of $\boldsymbol{E}$ bursts may lead to larger net energy changes. If the ion experiences an $\boldsymbol{E}$ burst with a time scale smaller than particle's gyration motion, then they are energized. Especially, if the $\boldsymbol{E}$ burst time scale is close to the gyration motion, i.e., τ/τ_C~0.5, then the field variation will significantly modify the particle motion even if the amplitude of the burst is small.

Chapter 5

Ion dynamics in Mercury's realistic configuration

General features of the non-adiabatic energization of planetary ions in the vicinity of KH vortices were discussed in the previous chapter. In the present chapter, we consider the ion dynamics in realistic configurations for the Hermean environment. The numerical settings described in this chapter are almost identical to those used in Chapter 4 except for selected parameters. In a Mercury's realistic configuration, a large convection electric field in the magnetosheath should be implemented. In this way, we are able to investigate the acceleration/deceleration and transport of planetary ions across the magnetopause of Mercury. For instance, when ions experience large $\boldsymbol{E}$ bursts, they tend to move towards the direction of the larger electric field. The field described in Chapter 4 was more similar to the dawnside configuration, i.e., orientations of the convection electric fields pointed away from the magnetopause in both sides of the magnetopause. Conversely, this kind of the electric field orientation is opposite on the duskside magnetopause. Moreover, we would expect that the distance from the location of ion generation (e.g., photo-ionization of exospheric atoms) from the magnetopause would be a key factor in determining the intensities of the energization and transport of newly picked up ions.

In this chapter, quantitative and systematic calculations were performed in realistic Mercury's configurations in both dawn and dusk sides. All parameters are carefully set from observational data when available. In addition, a various ion species, not only the Na^+, but also O^+, K^+ (heavy ions of planetary origin), H^+, H_2^+ (lighter ions of planetary origin), and H^+, He^{++} (solar wind plasmas) are considered [*Zurbuchen et al.,* 2008].

We use the same numerical method as in Chapter 4 with the time-varying KH field. Picked up ions are injected at given times. The size of a simulation box in the x-direction, corresponding to the KH wavelength, is set to exactly $1.5R_M$, and the size in the y-direction is taken as $12R_M$ with a spatial resolution of 32.2 km (114 × 909 grids). The thickness of the magnetopause (boundary layer) is ~ 515 km from *Gershman et al*. [2015]. Ions are traced in the frame of the average motion of the KH wave. The periodical boundary condition is set in the x-direction. All parameter settings

are summarized in Table 5.1. Physical quantities vary across the magnetopause as explained in Chapter 3.

Table 5.1 Parameter settings

(a) Fixed parameter

	Magnetosheath region	Magnetosphere region
Background H^+ number density	100 ions/cc	10 ions/cc
Flow velocity (MSO)	variable	$+\,50$ km/s
Injected planetary ion species (m/q)	$H^+(1), H_2^+(2), O^+(16), Na^+(23), K^+(39)$	
Solar wind ions on ***E***x***B*** frame (m/q)	$H^+(1), He^{++}(2)$	
Initial ion energy	$H^+(1), H_2^+(2)$: 0.047 eV(540K) in Mercury frame	
	$O^+(16), Na^+(23), K^+(39)$: 1 eV in Mercury frame	
	$H^+(1), He^{++}(2)$: 10eV in ***E***x***B*** frame	
Injection time	32.2 s, 80.5 s, 128.8 s	
Magnetic field ($B_{z'}$)	$\pm$ 48.7 nT	$+$ 48.7 nT

(b) Variable parameter

	IMF(B_z)	Magnetosheath velocity(MSO)	Magnetopause thickness	KH Wavelength
Case 1	$+$ 48.7 nT	$-$ 300 km/s	515 km	1.5 R_M km
Case 2	$-$ 48.7 nT	$-$ 300 km/s	515 km	1.5 R_M km

MESSENGER had not observed the velocity of the magnetospheric convection, but we set 300 km/s of anti-sunward flow in the magnetosheath and 50 km/s of sunward flow in the magnetosphere by referencing previous numerical studies [e.g., *Seki et al*., 2013; *Fujimoto et al*., 2007; *Jia et al*., 2015; *Wang et al*., 2010]. The magnitude of Bz is identical across the boundary layer and values were set by using MESSENGER data [e.g., *Wang et al*., 2010]. Ions were injected as picked up ions at given times. We set three different injection times so that we could investigate characteristics of the ion dynamics in different stages of the development of the KH instability. Illustrations of the simulation condition are shown in Figure 5.1. Although illustrated figures on the right side in Figure 5.1 have only $\pm$ 1.0R_M in the y-direction, the calculation domain was set so that the outermost ion could close its gyration motion in the simulation box. You may point out that the development of the KH instability seems to be different between the dawn and dusk side configurations. We confirmed that the growth of the KH instability is almost same. This can be explained by an initial perturbation to cause the instability. Even though we add small perturbations as white noise, the unstable wavelength can grow in the simulation domain. However, the timing of starting to grow is not the same. This leads to the different view of the KH growth in Figure 5.1 even at the same given time. According to previous studies [e.g., *Paral and Rankin*, 2013], the MHD approximation may not be valid especially in the dawnside magnetopause of Mercury. However, to understand the effect of a large convection field on the ion dynamics and transport, we considered both sides. In addition, southward IMF was also considered so that we could explore the physical mechanisms of energization and transport of ions more thoroughly.

An overview of ion behavior for Case 1 of Na^+ is shown in Figure 5.2. Here 10,000 ions were injected in three different regions as picked up ions. Blue dots represent each ion in the magnetosheath, while magenta and yellow dots show each ion in the boundary layer (magnetopause) and magnetosphere region, respectively. The spatial scale is normalized to the Mercury radius. Because the boundary layer is the transition layer for the physical quantities, only blue (magnetosheath) and yellow (magnetosphere) dots are analyzed. Initial ion positions were determined by a given function and its distribution is shown in the panel at t = 32.2 [s] in Figure 5.2. Because of the different directions of the large convection electric field between the dawn and dusk sides, the ion distribution is significantly different in the later stage of the development of the KH instability. This means that a large ion gap can be observed near the magnetopause on the dawnside while no such a gap is seen on the duskside. Moreover, ions presented in yellow could enter the magnetosheath region at t = 96.6 [s] due to the development of KH vortices in the dawnside but those in the duskside could not cross the magnetopause. On the dawnside, once ions penetrate to the magnetosheath region, they seem to move freely from the filament structure of

the KH vortex. On the other hand, planetary ions picked up in the magnetosheath (blue) did not penetrate into the magnetosphere. In contrast, the transport of both yellow and blue plasma went in the opposite direction on the duskside. Ions in the magnetosheath (blue) could enter the magnetosphere region. However, ions in the magnetosphere penetrated less into the magnetosheath region compared to those in case of the dawnside configuration.

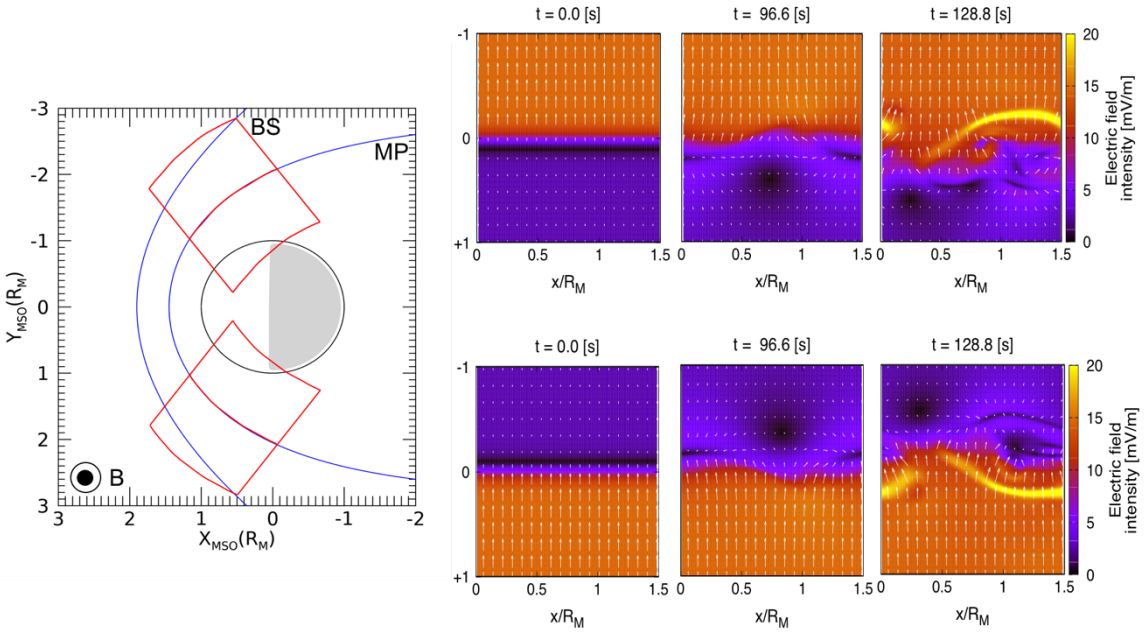

Figure 5.1 Illustration of simulation condition for Case 1.

The left panel shows the sketch of bow shock (BS) and magnetopause (MP) from models by *Slavin et al*. [2009b] for BS and *Shue et al*. [1998] for MP in MSO coordinates, respectively. The two red boxes correspond to the area of the KH occurrence on both sides of Mercury and the simulation domain. Color-coded electric field intensity obtained from MHD modeling are shown on right side. White arrows indicate the electric field orientation. The upper and lower panels are the electric field map in the evolution of the KH instability on dawn and dusk sides, respectively. Here we assumed that the solar wind velocity is 300 km/s of tailward and the velocity of magnetospheric convection is 50 km/s which flows from the nightside to the dayside. Initial profiles of physical quantities (number density of proton, velocity) except the magnetic field vary across the magnetopause using a hyperbolic tangent profile. Thickness of the magnetopause is 515 km and the wavelength of the KH instability is set to 1.5R_M km, which is consistent with MESSENGER observation results.

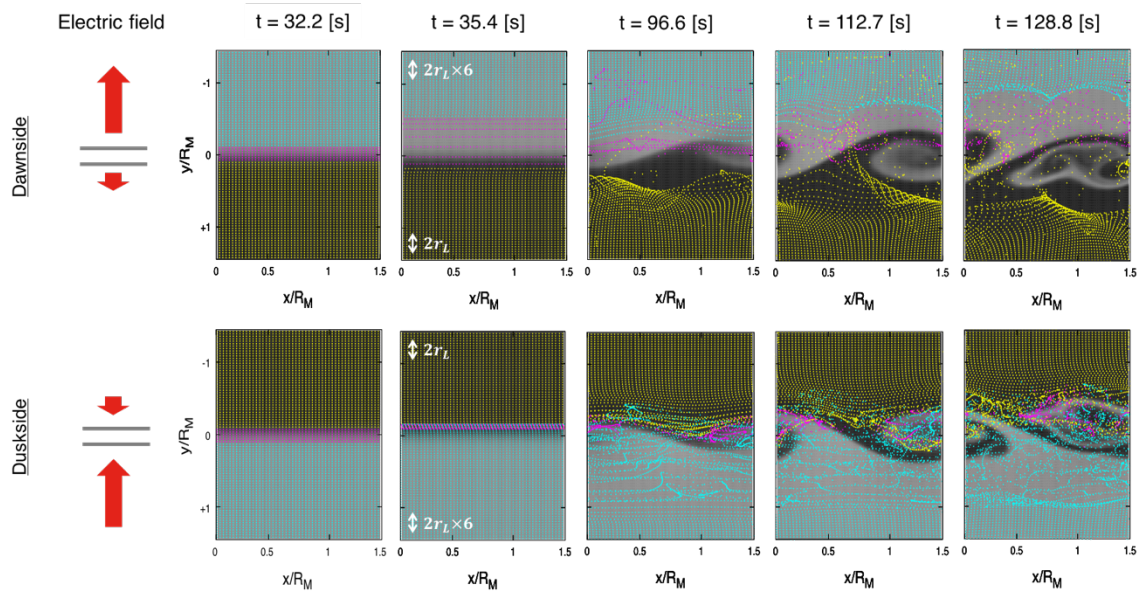

Figure 5.2 Behavior of sodium ions at distinct times of the KH instability development for Case 1. Background grey scale color shows the proton number density (light (dark) colors indicate higher (lower) density). Yellow, magenta and cyan dots represent sodium ions picked up in the magnetosphere, boundary layer, and magnetosheath regions, respectively. The upper and lower panels show the dawn and dusk side configurations and white arrows in the panels at t = 35.4 [s] indicate the Larmor radii of the sodium ion in each region. Electric field orientation and intensity is described in the leftmost panel. We can see clear differences in the ion behavior due to opposite electric field orientation. Each ion is injected with an initial thermal energy of 1 eV at t = 32.2 [s], which is the beginning of the KH growth.

5.1 From magnetosphere to magnetosheath (heavy ions of planetary origin)

Since all ions were injected as picked up ions, their initial energy depends on the energy calculated from the ***E***x***B*** drift speed in each region. As such, the analysis and discussion should be done separately. Here we focus on the ions picked up in the magnetosphere region which are presented by yellow dots in Figure 5.2. Figure 5.3(a) shows the Na^+ behaviors for Case 1 at given times. Although all colored dots represent Na^+ ions, different colors correspond to the different distances from the magnetopause. Each color has a thickness of the magnetopause, $2a$. For instance, the region within $\pm 0.1R_M$ of the center of the boundary layer is defined as a magnetopause. Magenta dots indicate ions initially picked up $0.1 - 0.3R_M$ from the magnetopause, green dots represent the ions in the region of $0.3 - 0.5R_M$, cyan represents ions in the region of $0.5 - 0.7R_M$, and yellow dots show the ions in the region from $0.7 - 0.9R_M$. The Na^+ ions were injected at t = 32.2 [s] with 1 eV of thermal energy, corresponding to the time when the KH instability begins to develop. For simplicity, we chose a 90° pitch angle for all ions. At t = 128.8 [s], magenta and green dots on the dawnside seem to be distributed randomly and they are transported to the magnetosheath region. On the other hand, no ions are observed in the magnetosheath region on the duskside. This is because of the orientation of convection electric field. At t = 193.2 [s], ions on the dawnside are distributed throughout the simulation box, showing that they are well mixed. In contrast, fewer ions are observed in the magnetosheath region on the duskside, while they are well-mixed only in the magnetosphere side. The three panels in Figure 5.3(b) show, from top to bottom, the growth of the KH instability, number of energized ions, and number of transport ions as a function of time. The 2nd and 3rd panels indicate the occurrence rate, obtained by counting the number of ions and taking the ratio to the total number of ions in each region. For instance, to obtain the data in the second panel, when a magenta ion is accelerated, and its magnetic moment becomes $\mu/\mu_0 \geq 10$, it is counted as an energized ion. Next, the total number of these ions is divided by the total number of ions initially injected in the magenta region. Similarly, counting is conducted for the third panel, where net transport means that an ion crosses the boundary layer and is located up to $+2a$ from the boundary. For example, we count an ion picked up in the $0.3 - 0.5R_M$ region, colored by green for the case of the dawnside, as it crosses the magnetopause and is located above $- 0.3R_M$ in Figure 5.3(a). These rates were calculated at each computational time interval $t_{com} = 10$ (or t = 32.2 [s] in real time). Magenta and dark-orange profiles in the 2nd and 3rd panels in Figure 5.3(b) correspond to the color dots represented in magenta and yellow, which are respectively, the closest region to and the farthest region from the magnetopause. Profiles of ion behavior colored by green and cyan are omitted here for readability.

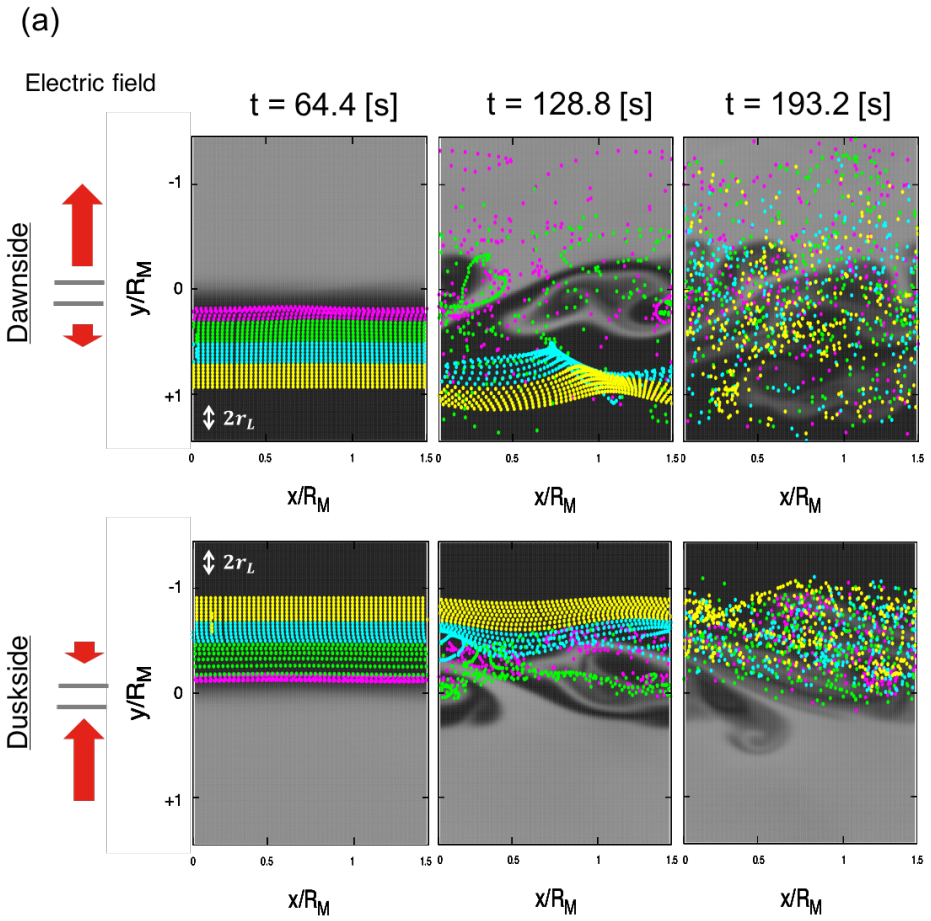
(a)
Electric field
t = 64.4 [s]
t = 128.8 [s]
t = 193.2 [s]
Dawnside
Dusk side
y/R_M
x/R_M
2r_L

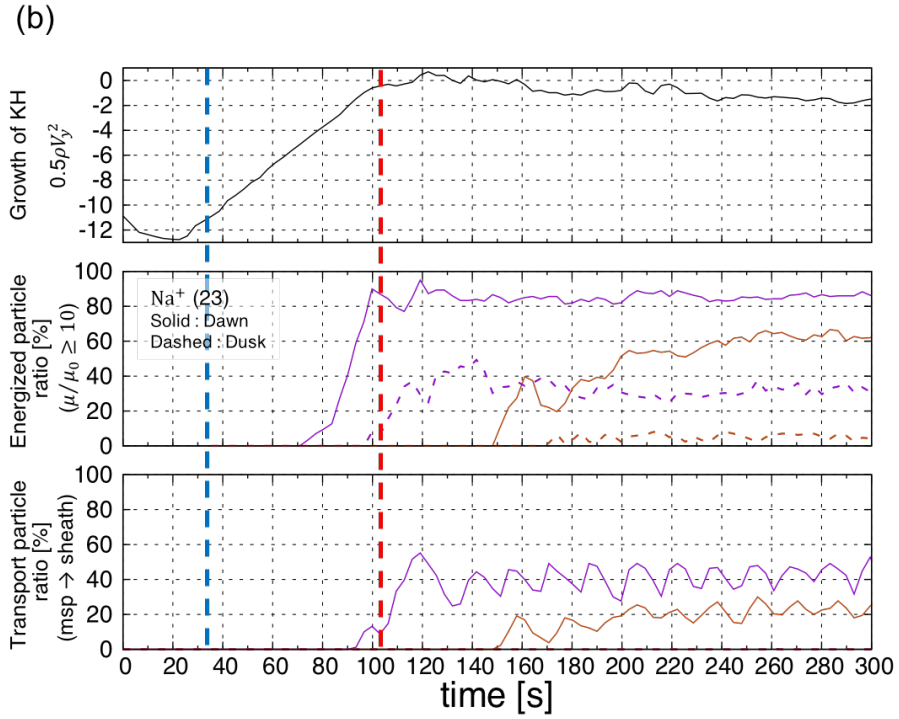
(b)
Growth of KH
0.5ρv_y^2
Energized particle ratio [%]
(μ/μ_0 ≥ 10)
Na+ (23)
Solid : Dawn
Dashed : Dusk
Transport particle ratio [%]
(msp → sheath)
time [s]

Figure 5.3 Energization and transport of sodium ions picked up in the magnetosphere. (a) Color panels in the upper figure represent snapshots of sodium ion behavior at a given time in the dawn (upper) and dusk (bottom) configuration. Magenta is the closest region to and yellow is in the farthest region from the magnetopause. Each region has the same thickness as the magnetopause, $2a$. White arrows in both boxes indicate the Larmor radii of sodium ion at injection time. The leftmost pictures show the initial direction of the electric field for each field configuration. (b) The top to bottom panels show the time series of the peak vertical kinetic energy as a proxy of the KH growth, the ratio of energized ions ($\mu/\mu_0 \geq 10$) to the total number of ions in each region, and ratio of transport ions that entered the magnetosheath region ($y \geq -0.3R_M$ at dawn and $y \geq +0.3R_M$ at dusk) to the total number of ions in each region. Magenta and dark-orange profiles correspond to ions represented in magenta and yellow, respectively, while cyan and green profiles are omitted here. Solid and dashed lines in the 2nd and 3rd panels indicate the dawn and dusk sides. The vertical red dashed line shows the linear growth time of the KH and all ions are injected at t = 32.2 [s] (the vertical blue dashed line) with an initial thermal energy of 1 eV.

Looking at Figure 5.3, we first find that non-adiabatic acceleration occurs on both dawn and dusk sides, but ions are more significantly accelerated on the dawnside. The solid and dashed lines refer to dawn and dusk configurations in Figure 5.3(b). For example, 85% of the ions are picked up in the closest region to the magnetopause at dawn, while only 35% are seen at dusk. The starting time for acceleration corresponds to the KH growth, suggesting that forming KH vortices work towards the acceleration. We also note that the ion transport here means that ions can be observed in the other region by crossing the magnetopause. We observe ions that moved in the other region and solely undergo gyration motion in that region. We also observe ions with a large Larmor radius near the magnetopause crossing the magnetopause during their one cyclotron turn. This latter reason can provide oscillations, which are illustrated in the bottommost panel in Figure 5.3(b).

In Figure 5.3(b), there is no dashed line in the 3rd panel, indicating that no transport occurs from the magnetosphere side in the duskside region because of the orientation of the convection electric field. We note the absence of ion transport even though the ions are energized. In the present analysis, we count all energized ions with $\mu/\mu_0 \geq 10$, thus some of them may be even more energized. Ions with $\mu/\mu_0 \sim 10$ may not cross the boundary but ions with $\mu/\mu_0 \sim 100$ may do so because of the large Larmor radius. The normalized initial Larmor radius of the sodium ion in the

closest region to the half thickness of the magnetopause is approximately about 0.6 ~ 0.9, varying with the magnetic field profile. In Figure 5.4, we show in detail the magnetic moment changes in the energization and transport of ions picked up in the closest region to the magnetopause. Here, the ratio is calculated differently than in Figure 5.3. The ratio is obtained by counting the ions in each region and dividing by that total by the total energized (transported) ions at a given time, meaning the fraction of ions energized (transported). Therefore, each line shows the numbers of fraction of ions energized (transported) in that of total energized (transported) ions. In this way, we can see which magnetic moment changes account for the total (occupation ratio hereinafter).

The major difference between the duskside and the dawnside in Figure 5.4 is the energization profile. The left panel shows that energized ions have a magnetic moment change from 10 to 50, whereas profiles in the right panel show more various magnetic moment changes. On the duskside, an occupation ratio of about 78% of the energization is represented by the magenta profile, having a magnetic moment change of 10 to 25, while the rest of the energization would be occupied by the blue profile. On the other hand, all profiles on the dawnside show a similar occupation ratio of around 20% for the energization. As previously mentioned, Figure 5.4 clearly shows that ions on the dawnside are effectively accelerated. In detail, the occupation ratio of transport by each magnetic moment change does not appear to correspond to the those of energization. Figure 5.5 shows the correlation between the occupation ratio of energization and transport on the dawnside and the case of ions picked up in the closest region to the magnetopause. Each color corresponds to each magnetic moment change profile and multiple dots show the rate at given times. As shown, for example red dots indicate that the occupation ratio of energization is not high (less than 20% of all energized ions) but that of transport shows a high value (30 – 40%). Magenta dots representing ions with $10 \leq \mu/\mu_0 \leq 25$ show 20% of the occupation ratio for energization, but ~ 10% of that in transport. Calculating the correlation between the occupation ratio of energization and transport and fitting by the 1st order liner function, we get each slope and correlation coefficient. From high magnetic moment change to lower, slopes are 1.597, 1.146, 0.5751, 0.1277, and 0.1231. Correlation coefficients are 0.5927, 0.7915, 0.3422, 0.04323, and 0.3009. The value of the slope increases with the magnetic moment changes, but the correlation coefficient does not. Ions with $75 < \mu/\mu_0 \leq 100$ show the highest correlation between the occupation ratio of energization and transport. According to our results, if ions are energized and gain larger energy, they can be transported efficiently because of their large Larmor radius. In addition, though slopes of ions with $10 \leq \mu/\mu_0 \leq 50$ are small, they show some transport. We would like to investigate why we could not see any ions in the magnetosheath region at dusk even though they are energized.

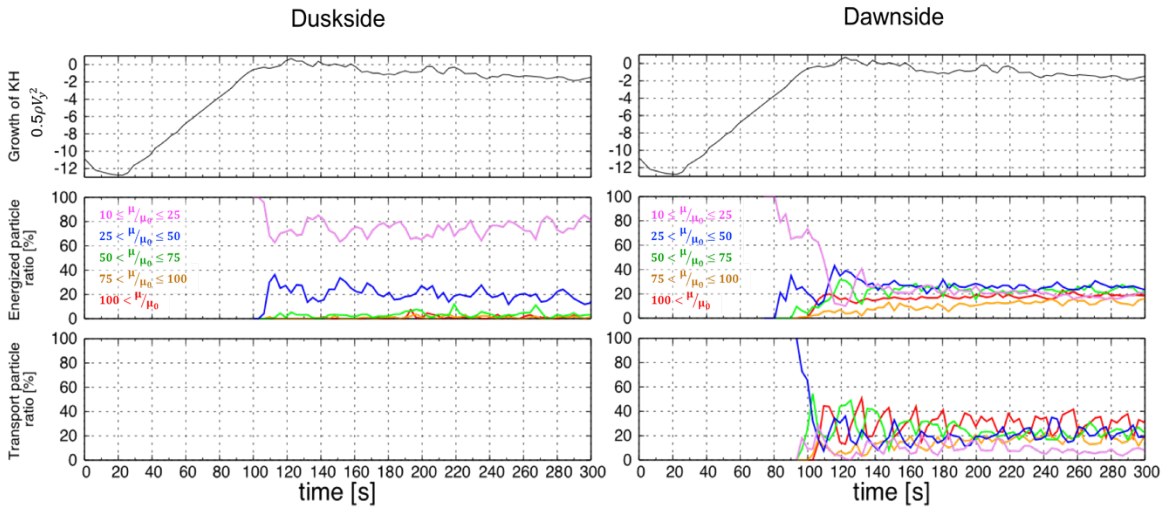

Figure 5.4 Ion energization and transport for Case 1, especially the case where ions are initially picked up in the magnetosphere region. Left (right) side panel shows the results on the duskside (dawnside). Each line color corresponds to a magnetic moment change of the ion. The red line shows ions energized with $\mu/\mu_0 > 100$, orange is within the range of $75 < \mu/\mu_0 \leq 100$, green is in the range of $50 < \mu/\mu_0 \leq 75$, blue is in the range of $25 < \mu/\mu_0 \leq 50$, and magenta is in the range of $10 \leq \mu/\mu_0 \leq 25$.

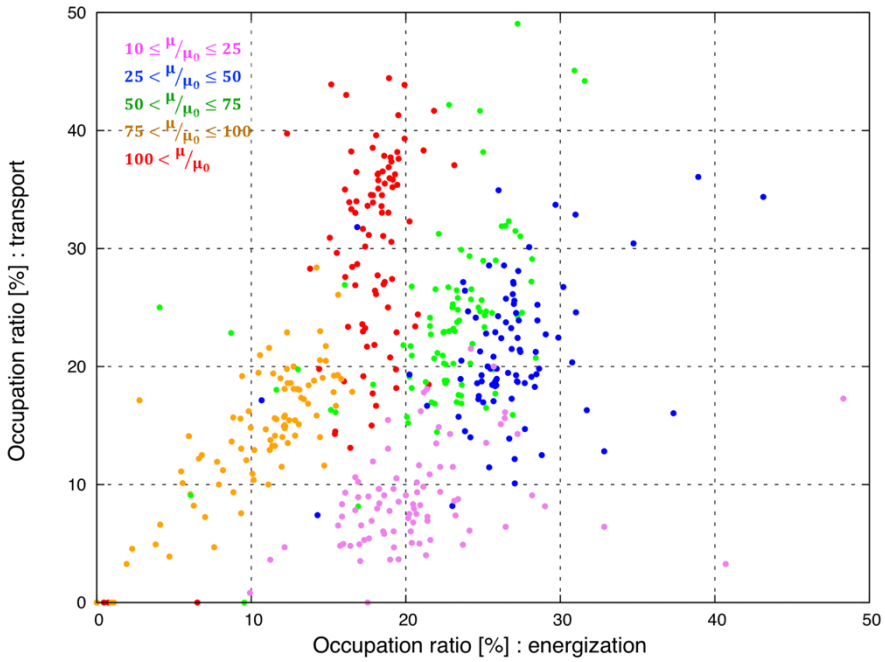

Figure 5.5 Correlation between the occupation ratio of energization and transport on the dawnside. Each color corresponds to each magnetic moment change profile. Multiple dots show the ratio at given times. From high magnetic moment change to lower, slopes are 1.597 (red), 1.146 (orange), 0.5751 (green), 0.1277 (blue), and 0.1231 (magenta). Correlation coefficients are 0.5927, 0.7915, 0.3422, 0.04323, and 0.3009 from the red to the magenta dots, respectively.

The question that emerges here is why do we have effective acceleration and transport on the dawnside and a fewer ions are energized largely, and no transport on the duskside? To address this question, we selected model trajectories to understand the dawn-dusk difference of the energization and transport of ions. Though general non-adiabatic features are presented in the previous chapters, further down this text we will confirm their actual existence.

Figure 5.6 shows two model trajectories of picked up sodium ions in the magnetosphere for both (a) dusk and (b) dawn configurations. In this figure, we selected an ion with $\mu/\mu_0 < 10$ at dusk as an example of less energization and an ion with $\mu/\mu_0 > 100$ at dawn as an example of effective energization. As described in the previous chapter, ions should move in the same direction as the electric field in order accelerate. From top to bottom, we show the ion position in the y-direction with arrows showing the electric field orientation, the electric field intensity that

the ion experiences, magnetic moment (normalized to the initial value), and energy panels. The electric field orientation shown on the 1st panel corresponds to the direction of the Lorentz force that the ion experiences. For example, in Figure 5.6(a) at t = 50 [s], green arrows point towards the magnetosheath side indicating that the ion is accelerated towards that side. In contrast, at t = 250 [s] in the same figure, green arrows point in the opposite direction of the electric field. At this time, the ion is essentially accelerated towards the inside of the magnetosphere. Two selected ions were initially injected at the same distance from the magnetopause. In Figure 5.6(b), the magnetic moment changes can be seen around the linear growth time (red dashed line), and a μ-jump occurred at t ~ 115 [s]. On the other hand, Figure 5.6(a) does not show such clear magnetic moment changes. By checking snapshots of ion behavior and the electric field that the ion experiences, acceleration steps and ion behavior can be explained. At dawn, when the ion is just picked up in the magnetosphere region, it is subject to normal gyration motion. The ion may experience a small electric field variation with the development of the KH instability and thus the ion starts the polarization drift which gradually accelerates the ion (equivalent to Larmor radius increases). This is an adiabatic acceleration. When the ion enters the initial boundary layer region, here at t ~ 115 [s], the ion suddenly experiences a large electric field towards the magnetosheath where the μ-jump occurred. After that, the ion keeps its gyration motion in the magnetosheath region.

A model trajectory in the duskside configuration presented in Figure 5.4(a) shows that although $\boldsymbol{E}$ burst-like signatures can be seen on the 2nd panel, the ion does not gain a large amount of energy. Noting the direction of the electric field (green arrows at the 1st panel), the $\boldsymbol{E}$ burst occurs when the ion moves against the electric field, and thus deceleration occurs. In addition to the relationship between the direction of the ion motion and the electric field, a larger amount of magnetic moment changes on the dawnside can be understood by the net electric field changes across the magnetopause. Investigating other model trajectories allow us to understand the transport of ions, which is controlled by the electric field configuration in the magnetosheath under northward IMF.

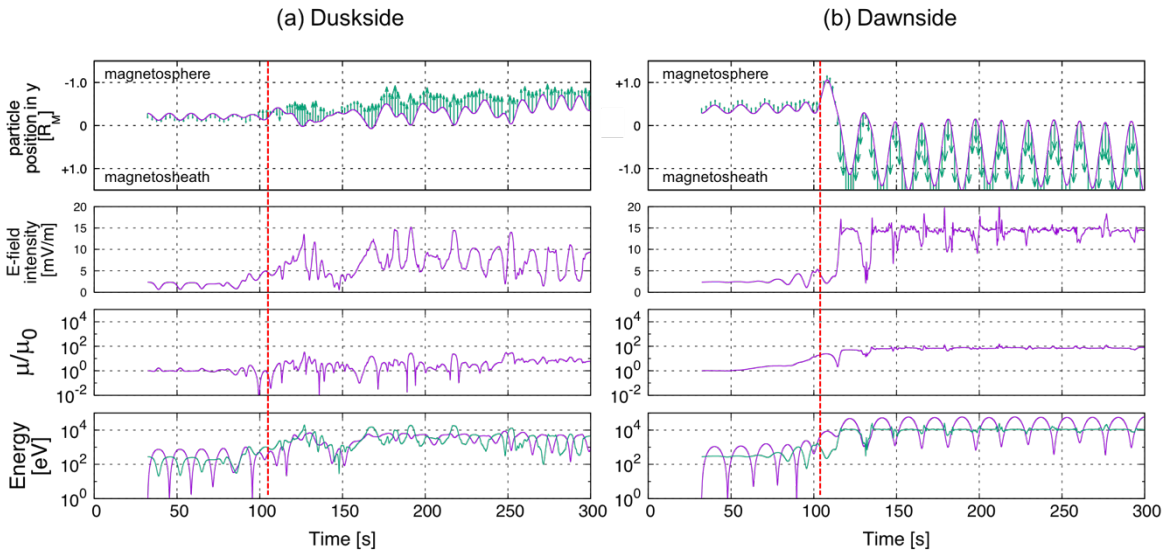

Figure 5.6 Model trajectories at (a) dusk and (b) dawn. The red dashed line represents the linear growth time of the KH instability. From top to bottom, each panel shows the ion position in the y-direction with the electric field orientation (green arrows), the electric field intensity, the magnetic moment (normalized to the initial value), and the energy as a function of time.

In addition, we investigate the influence of the KH structure on the energization and transport of ions so that we can address the following questions: Where can the ion be energized effectively? Is there any spatial relation with the KH vortex structure? Generally, the motion of the charged ion follows the background proton flow, but because of a larger Larmor radius, the ion can behave differently. Thus, they can gain energy. We investigate the relationship between the Larmor radius and the KH structure on ion energization and transport here.

Since KH vortices form in time and their growth goes into the nonlinear phase, it is hard to characterize their spatial structure. One typical characteristic of the KH structure is the pressure distribution. The minimum pressure is basically located at the center of the KH vortex at the linear growth phase because the KH vortex is formed in the balance between centrifugal forces and the pressure gradient. In order to understand the relationship between the energization and transport of ions and the KH structure, we compare these locations. We calculate the location of each pressure-minimum of the KH vortex, and fit it with a linear function. This fitting shows that the center of the KH vortex, which is equivalent to the pressure-minimum point, is propagated with a velocity of ~ 203.8 km/s, a reasonable value for the initial setting of the MHD simulation.

As a proxy of non-adiabatic energization, we set a threshold value for magnetic moment changes ($\mu/\mu_0 > 25$) and add them up one by one. Once an ion is counted as an energized ion, it is not taken into account anymore. Since we know the linear function of the KH structure propagation, we can obtain the deviation of the location. Here, we use only the results of ions picked up in the closest region to the magnetopause at dawn because of the threshold condition of the magnetic moment. For simplicity, we focus on the time near the linear growth time (t = 90 – 120 [s]) because the energization ($\mu/\mu_0 > 25$) significantly occurs. We separate the time by 10.0 sec interval, and show the deviation of the location of energized ions meaning where ions are accelerated. In the time range of 90 – 100 [s], 9.7% of energized ions that are accelerated in that time range are located near the center of the vortex ($\pm 0.2 R_M$ from the minimum-pressure point in the x-direction). The result at t = 100 – 110, which is the just adjacent to the linear growth time, shows 15.1%, and t = 110 – 120 [s] shows the 3.9% of energized ions within the vortex. The region of the center of the KH vortex with $\pm 0.2 R_M$ is about 26% of the KH wavelength, suggesting that the ions are significantly accelerated around the center of the KH vortex. The same analysis, considering the effect of KH structures on the transported ions was done but not shown here. In a similar fashion, 17.6% of transported ions are transported near the center of the KH vortex region in the time period of t = 90 – 100 [s], 12.7% at t = 100 – 110 [s], and 6.97% at t = 110 – 120 [s]. As easily we could imagine, ions are energized around the center of the vortex, which means that ions can be energized in the path on the filament structure of the KH vortex. This result indicates that even ions have larger Larmor radius than the typical scale of the KH vortex, ions seems to follow the filament structure of the KH vortex. This result is valid for the case of sodium ions, and the same investigation was done for other heavy species and they show similar results.

The magnetic reconnection generally occurs during southward IMF, meaning that the configuration of the magnetopause will be more complicated when considering Case 2. However, this case presents a good example for understanding the role of the large convection electric field. In this case, the magnetic field varies reversely (from the magnetosheath to the magnetosphere, varies from - Bz to + Bz) across the magnetopause with the same magnitude in the entire simulation domain. In the dawnside configuration, we have a large electric field towards the magnetopause in the magnetosheath region, while another small electric field points away from the magnetopause in the magnetosphere. Conversely, in the duskside configuration, we have a large electric field pointing away from the magnetopause in the magnetosheath region, and a small electric field directed towards the magnetopause in the magnetosphere. Considering these initial electric field directions, we may predict some features from our examination of Case 1: larger energization of ions picked up in the magnetosphere region, the transport of ions in the duskside, and no transport in the dawnside due to the large inward electric field in the magnetosheath. The

result of Case 2 is shown in Figure 5.7. As a consequence of the southward IMF, ions picked up in the just adjacent region to the boundary layer (magenta dots), the energized ratio is much higher than that of Case 1 for all three heavy ion species (O^+, Na^+, and K^+). The energized ratio increases for both dawn and dusk sides in this case compared to Case 1. The net electric field change across the magnetopause, i.e. the electric fields in Case 1 cancel each other out but add themselves up in Case 2, results in the effective energization in Case 2 and the general features of energization can be explained by the same conclusions from Case 1. We also investigated the breakdown in the same manner as for Case 1. The breakdown contains the lower and higher energized ions, and the amount of transport corresponding to the energization. In contrast, we found that for highly energized ions, $\mu/\mu_0 > 100$, the energization increases in time due to the rotating electric field component. Contrary, although the magnetosheath electric field directs toward the magnetopause at dawn, the ions are transported to the magnetosheath which is inconsistent with our results from Case 1. They are energized ions due to the development of the KH instability and thus they have larger Larmor radius. Such ions can move across the boundary layer during one gyration motion and be observed in the magnetosheath region.

Under the southwards IMF, energization and transport of ions picked up in the magnetosphere region do not show significant differences. Both ions are transported and there is no stagnation inside the magnetopause.

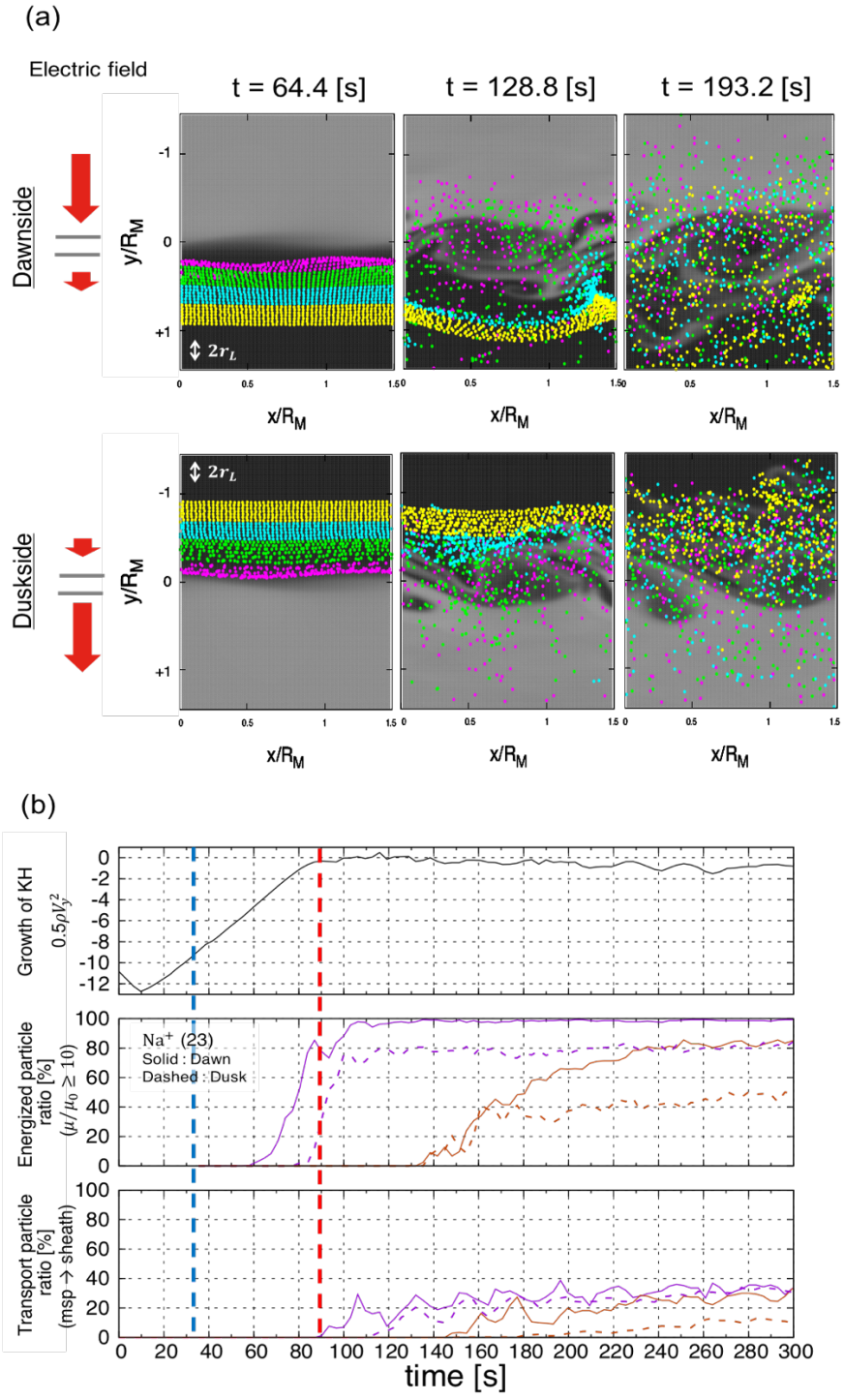

Figure 5.7 Energization and transport of sodium ions picked up in the magnetosphere region under southward IMF (Case 2). This is the same format as Figure 5.3.

Overall, ion transport starts at a later stage in the KH linear growth. In both cases, the results are equivalent. Even though the large convection electric field affects the ion transport, they cannot cross the magnetopause layer without the development of the KH instability. However, actual magnetospheric flanks have other components of the magnetic field, Bx and By, and this may lead to the transport of magnetospheric ions. Other different injection time cases were studied but the results are quantitatively similar.

5.2 From magnetosheath to magnetosphere (heavy ions of planetary origin)

In the previous section, we investigated the ion behavior picked up in the magnetosphere. Here we will study the ion behavior picked up in the magnetosheath region. A marked difference between section 5.1 and this section is the electric field which ions initially experience: ions picked up in the magnetosheath imply that the ion might not experience a large $\boldsymbol{E}$ burst because of the other electric field intensity affecting to the ion is small compared to the electric field in the magnetosheath. Figure 5.8 shows the energization and transport of sodium ions picked up in the magnetosheath in the same format as Figure 5.3, where each colored dot represents the same distance introduced in the previous section.

From Figure 5.8(a), it is clear that ions cannot be transported to the magnetosphere in the dawnside configuration while moving outward from the magnetopause layer. On the other hand, some of them can cross the boundary layer and tend to move into the magnetosphere region in the duskside configuration where they are well mixed. No non-adiabatic acceleration occurs on both configurations (see Figure 5.8(b)). This is due to the ions initially experiencing a large electric field, and thus they do not experience any stronger field during their gyration motions. In contrast to the ion transport discussed in the previous section, here some ions cross the boundary layer in the duskside configuration. This may be explained by the variations of the electric field. Ion transport on the duskside starts at the time corresponding to the linear KH growth time (red dashed line in Figure 5.8(b)). This suggests that the formation of the KH vortex plays a role in the transport of ions even if they have a large Larmor radius. Ions picked up in the magnetosheath region experience a large electric field toward the magnetopause, and they cross the boundary layer during their gyration motions. In this study, the electric field calculated using Ohm's law. Under the mostly stable homogeneous magnetic field configuration, the electric field variation is equivalent to the velocity variation of background protons in the x-y plane. Forming KH vortex curves the velocity distribution, and thus the electric field properties will be changed. Especially

for ions picked up close to the magnetopause, which can experience a larger electric field than the ion initially experiences due to the KH vortex formation. Statistically, ions that experience a much larger maximum electric field than the initial one may cross the boundary layer more easily.

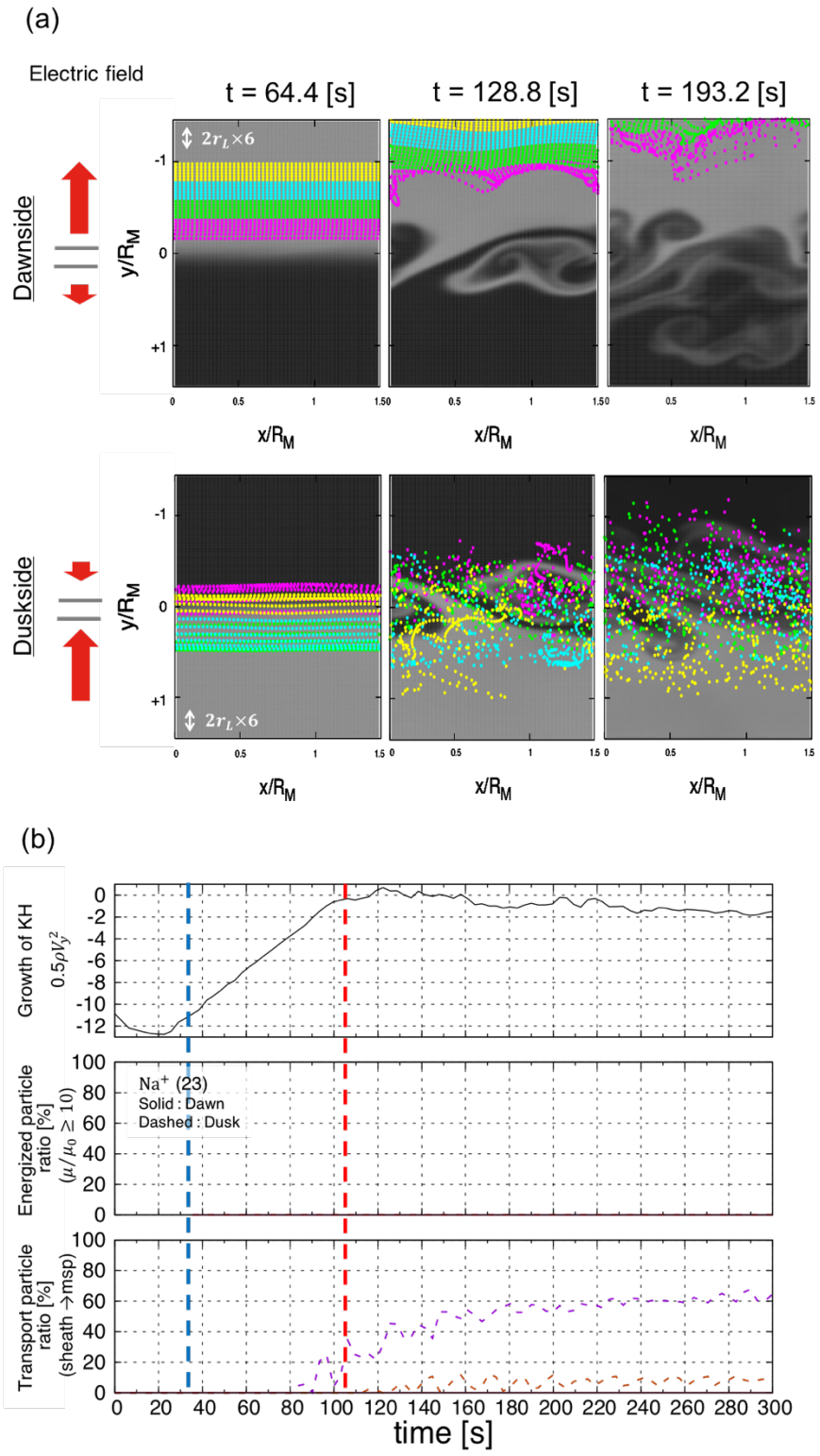

Figure 5.8 Energization and transport of sodium ions picked up in the magnetosheath. The format is the same as that of Figure 5.3 but transport is considered to be moving in the opposite direction.

Mercury's exosphere extends to a few R_M [*McClintok et al.,* 2008] and many ions can be picked up in the magnetosheath. Since they can have a large Larmor radius (approximately the same order of the magnetopause thickness or more), it is believed that ions can penetrate into the magnetosphere region. However, according to our results, without the x and y components of the magnetic field, it is difficult to cross the magnetopause region on the dawnside. In addition, even though the ions were picked up in the duskside configuration, fewer ions were transported to the magnetosphere region compared to the results in the previous section. Combining the results of Case 1 in section 5.1, we can show that ions on the dawnside are less dense than the ions on the duskside under the northward IMF. On the duskside, ions picked up in the magnetosphere cannot cross the magnetopause, and those in the magnetosheath can penetrate the magnetosphere. In order to be accelerated by the electric field variation, the ions should be inside the magnetopause where the initial electric field is smaller than that in the other region. Moreover, the energized and transported ratio in both sides shows threshold values in Figure 5.3 and 5.8. This indicates that heavy ions cannot be affected by small structures (so called fine structures) due to KH vortices breaking in the non-linear growth (saturation) phase. If fine structures have a role in the acceleration of ions, its ratio should increase over time.

Under southward IMF, a small number of ions can be energized and some transport on both the dawn and dusk sides can be seen. However, ion transport suddenly starts when ions are injected at the beginning of the KH growth, not because of the development of the KH instability but because of the effect of the large electric field itself. This leads to the ion transport without KH instability. In this study, because the effect of the field variations due to the development of the KH instability has been discussed, such an ion transport without the KH growth should not be taken into consideration. Additional experiments were performed to see ion transport without the KH growth and similar transport could be seen in the dawnside configuration. In addition, we found that the ion transport without the KH growth shows no large time differences even when we take into account the distance from the magnetopause. If we take into account of the ion transport without the KH growth, we can conclude that small (negligible) energization on both sides and ion transport on the duskside occur due to the development of the KH instability. Ion energization and transport occur significantly on both sides because of the same directed electric field across the magnetopause.

5.3 Behavior of lighter ions of planetary origin

In contrast to the behavior of heavy ions of planetary origin, lighter ion species that were injected with initial energies of 0.047 eV (=540 K) behave differently. Figure 5.9 shows an example of ion behavior for lighter ions of planetary origin, H_2^+, under the northward IMF (Case 1), in the same format as Figures 5.3 and 5.8. Here, lighter species have a small enough Larmor radius to the magnetopause thickness, thus the ions seem to follow the fluid structure. Ions are injected at t = 32.2 [s] (blue dashed line) and the linear KH growth time is noted by a red dashed line in Figure 5.9(b). Some ion energization can be seen after the linear KH growth but no transport occurs. Our results indicate that the fine structure due to the development of the KH instability causes acceleration. Although the scale of fine structures cannot be characterized, it is proven by checking different species. For the hydrogen ion, ion acceleration happens in the closest region to the magnetopause (magenta region) at t ~ 120 [s], and it does at t ~ 140 [s] for protons with a smaller Larmor radius. Ion transport does not occur either at dawn or dusk: it is influenced only within the expanded magnetopause due to the development of the KH instability. On the other hand, ions picked up in the magnetosheath under northward IMF do not show any ion energization. Small transport on the duskside can be observed similar to heavy ions.

As we discussed previously, because the rotation components of the electric field work effectively on the energization and transport of ions. Though the figure for Case 2 is omitted, we found that energization starts earlier than in Case 1 and significant transport can be observed for both dawn and dusk. Ions picked up in the magnetosheath region also show the ion energization and transport on both sides. The main difference in the trend of ion energization and transport compared to that of heavy ions of planetary origin is significant energization and transport of ions picked up in the magnetosheath region under the southward IMF (Case 2). In Case 2, we have only a small amount of energization of picked up heavy ions in the magnetosheath region, which is negligible. In contrast, significant energization can be seen on the motion of lighter ion and its transport seems to be in conjunction with its energization. We discuss why we have such a significant energization with lighter species in the following text.

First, because of the lighter mass of the considered species, it is easy for them to be affected by small electric field variations due to the vortex structure. The electric field variation with the KH vortex evolution is caused by the electric field going the opposite direction in Case 1 and in the same direction in Case 2. The formed rotating components of the electric field in Case 1 are outward from the vortex on the dawnside and inward to the center of the vortex on the duskside. Therefore, an ion always experiences the electric field within the KH vortex with an orientation of the initial electric field. On the other hand, because Case 2 has the electric field in the same direction across the magnetopause, the rotating components include anti-direction for the initial

electric field inside the KH vortex, which then accelerates the ion efficiently. Transport in Case 2 is also explained by this process. In addition to the small MHD-like transport, the ions can be accelerated by the rotation of the electric field component, moving towards the magnetosphere region.

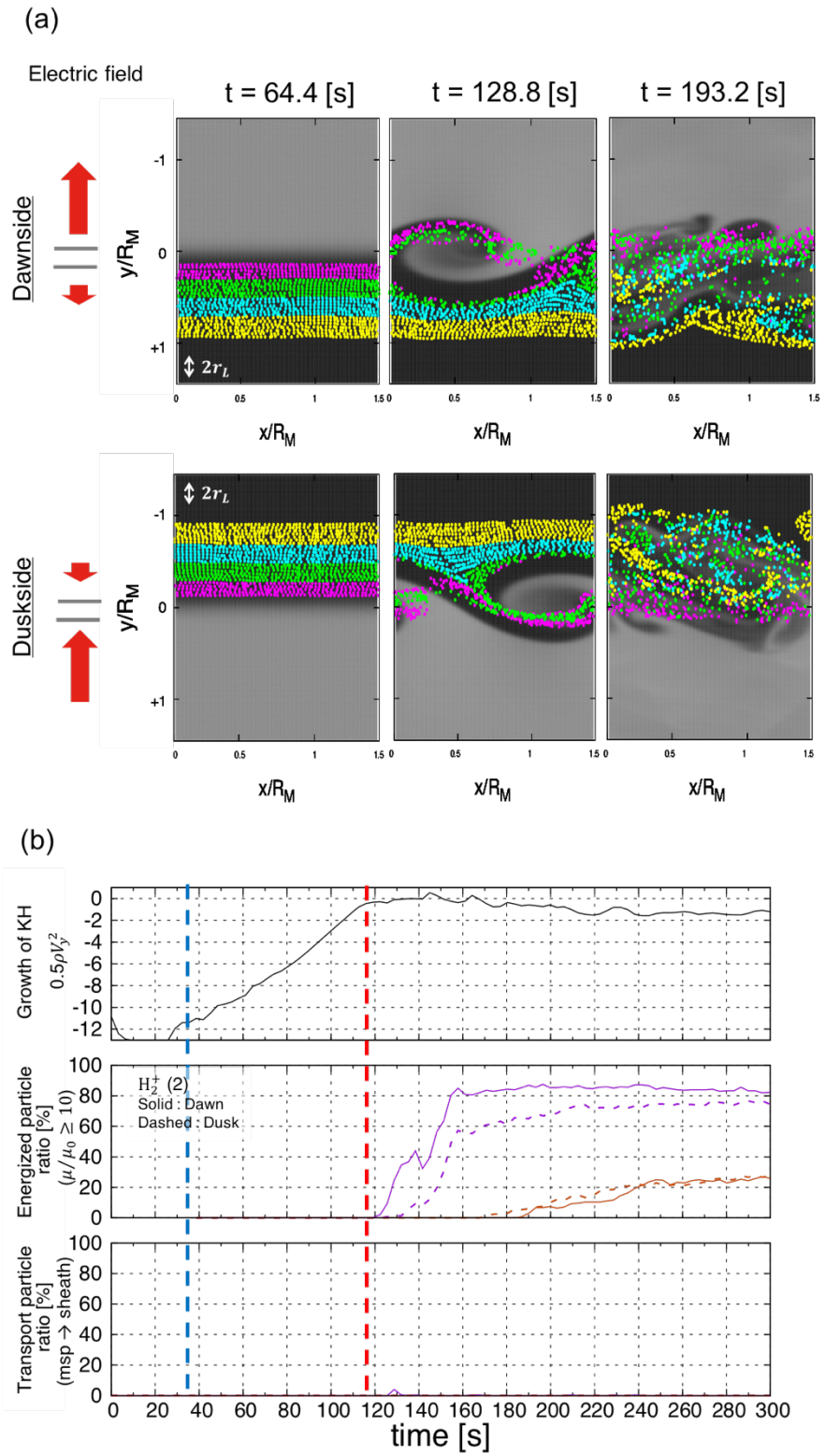

Figure 5.9 Energization and transport of hydrogen ions picked up in the magnetosphere in the same format as Figure 5.3.

5.4 Net energization and transport

The schematic illustration for heavy ions of planetary origin is shown in Figure 5.10.

Heavy ions of planetary origin picked up in the magnetosphere are accelerated at both dawn and dusk. We found no acceleration for ions picked up in the magnetosheath under the northward IMF (Case 1). Ion transport from the magnetosphere to the magnetosheath occurs only at dawn, and a small amount of ion transport in the opposite direction occurs at dusk. Lighter ions have a different behavior under the same northward IMF conditions. Because of a smaller Larmor radius, lighter ions behave magnetohydrodynamically. Ions picked up in the magnetosphere can be accelerated at both dawn and dusk but no transport occurs. If ions are picked up in the magnetosheath region, they cannot be energized. There is some ion transport from the magnetosheath to the magnetosphere at dusk because of the electric field orientation.

If we consider the southward IMF, ion energization and transport from the magnetosphere to the magnetosheath occurs on both the dawnside and duskside for ions picked up in the magnetosphere. On the other hand, negligible energization and a small amount of transport can be observed for ions that were picked up in the magnetosheath region. However, in this case, ion transport from the magnetosheath to the magnetosphere at dawn can occur without the development of the KH instability. Lighter ions picked up in the magnetosphere show the same features as the heavy species previously discussed. In contrast to the heavy ions behavior, lighter ions picked up in the magnetosheath can be accelerated and transported. This is explained by the initial direction of the large electric field across the magnetopause. Since they are light, ions flow by following background protons, and they are affected by small electric variations within the KH vortex. While we have an opposite-directed electric field across the magnetopause for Case 1, we have a same-directed electric field for Case 2. When the KH vortex starts to evolve, the electric field orientation inside the KH vortex is determined by the initial electric field configuration. The initial electric field in Case 1 makes the same-ward electric field, which is the same direction of the initial large electric field. On the other hand, the same-directed electric field can make a multi-directed electric field configuration inside the KH vortex and thus, the ion can experience various electric fields. This leads to efficient acceleration and transport.

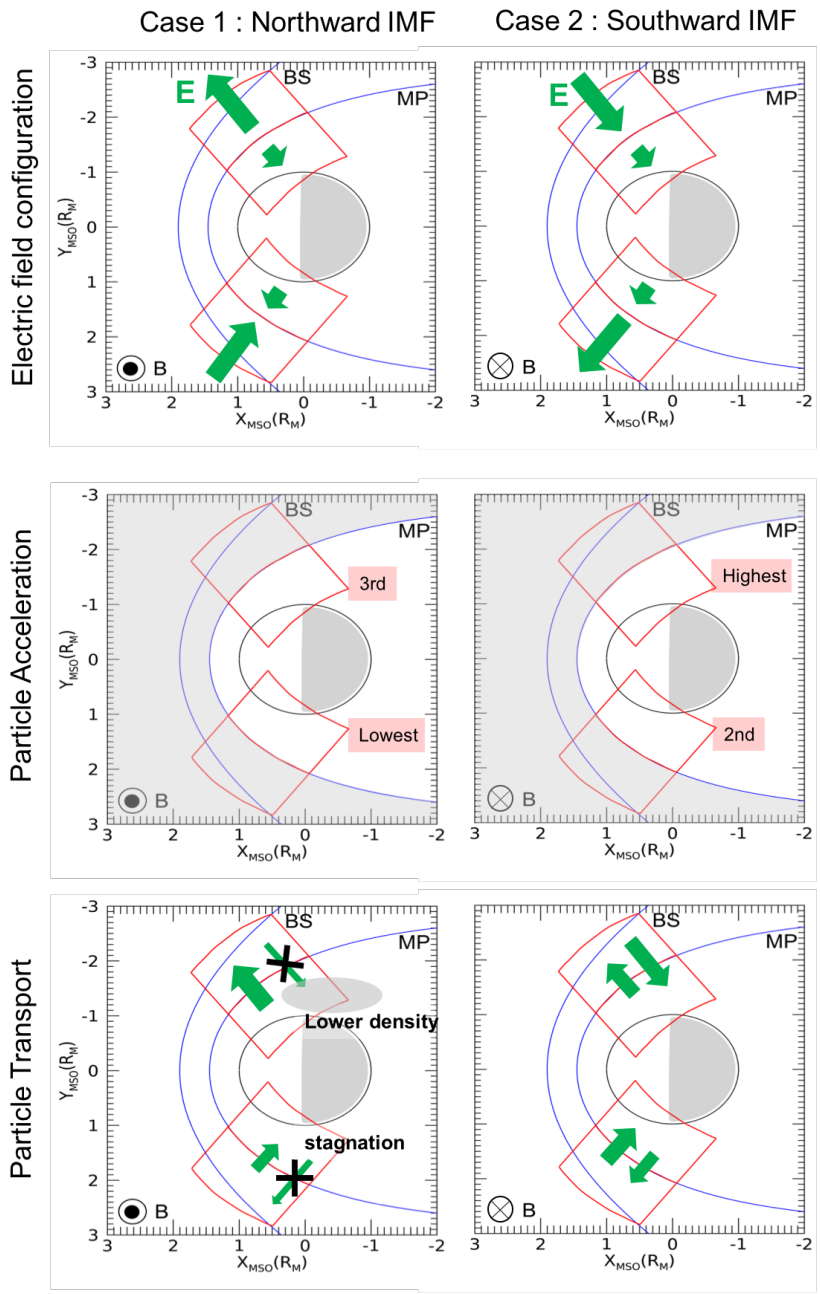

Figure 5.10 Illustration of general features of ion energization and transport of heavy ions of planetary origin (O^+, Na^+, and K^+ in this study) for north and southward IMF cases. From top to bottom, each panel shows the initial large electric field configuration, ion acceleration, and ion transport in the x-y plane. The grey hashed area in the ion acceleration panel shows no energization.

In the previously described cases, we have shown only two species, sodium and hydrogen ions. Here we will summarize the Larmor radius dependence on the ion acceleration and transport. The difference between ion behavior of heavy ions and lighter ions indicates that there is a relationship between the size of the KH vortex (equivalent to the magnetopause thickness) and the Larmor radius of the ion.

Figure 5.11 shows the Larmor radius dependence on the energization of ions picked up in the magnetosphere region, especially the region closest to the magnetopause (magenta area in previous figures) for northward IMF. The x- and y-axes indicate Larmor radius normalized to the initial half magnetopause thickness and 30% energization time normalized to the linear growth time ($t \sim 90$ [s]). The red dashed line represents $x = 1$ and $y = 1$. The circle and triangle symbol show the duskside and dawnside, respectively. We performed additional calculations for helium, carbon, and iron ions. According to this figure, ion energization at dusk shows less energization than that at dawn. Lighter species are accelerated at a later stage of the KH growth, as well. On the other hand, ions with a larger Larmor radius, such as Fe^{2+} and K^{+}, would be accelerated just after formation of the KH vortex. Though the oxygen ions seem to be accelerated effectively, the Larmor radius dependence on the ion energization seems to vary gradually. A similar gradual trend can be seen for Case 2.

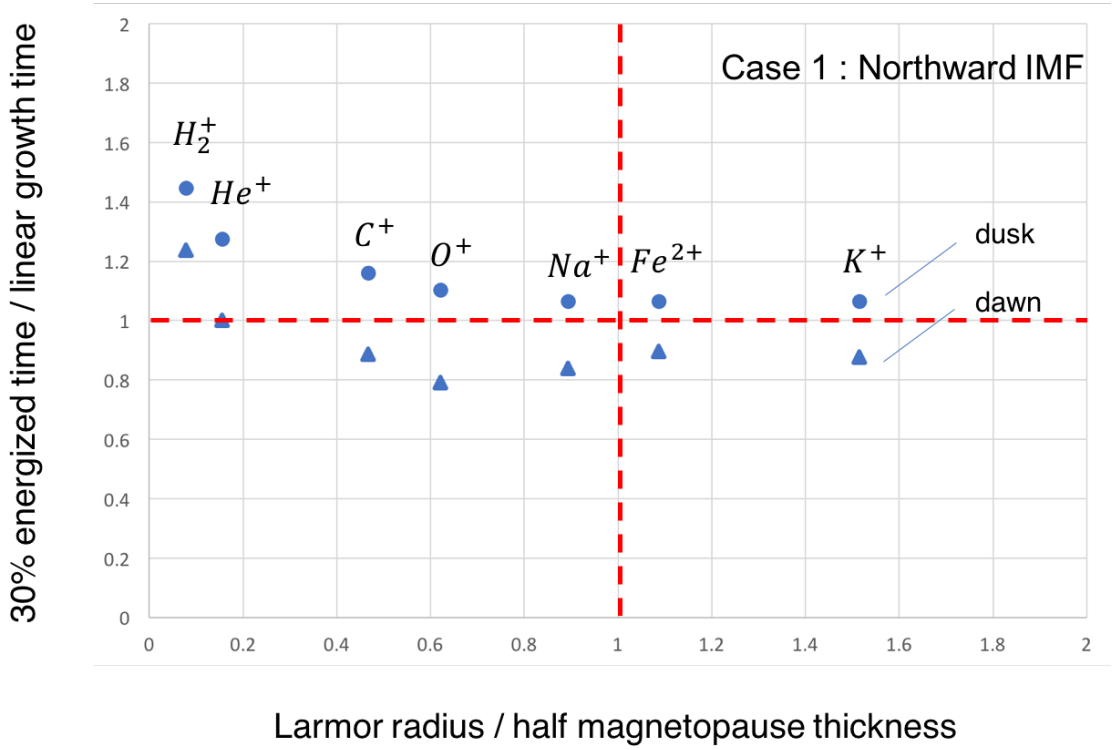

Figure 5.11 Larmor radius dependence on the ion energization of ions picked up in the magnetosphere, which is the region closest to the magnetopause under the northward IMF (Case 1). The area below the horizontal red dashed line corresponds to the linear growth stage and the area above is nonlinear growth phase of the development of the KH instability.

Because we set the "transport line" at $0.3R_M$ km from the magnetopause, lighter species in an MHD-like behavior are not counted. Roughly, the ratio of ion transport increases with increasing mass. However, threshold values of ion transport of heavy ions after a certain development time shows small differences. For example, the amount of ion transport from the magnetosphere to the magnetosheath at dawn for Case 1 for ions are: 42% for carbon, iron with double charges and potassium, 44% for oxygen, and 41% for sodium, which is in contrast to no transport for proton and hydrogen ions, and 10% for helium ions. Dawnside transport from the magnetosphere to the magnetosheath under southward IMF shows: 25% for proton, 31% for hydrogen, 30% for oxygen and sodium, and 32% for potassium ions. We may say that some threshold for MHD-like behavior can be set between helium and hydrogen.

As mentioned in the previous section, most of sodium ions would be accelerated near the vortex center, which is represented by the pressure-minimum location. The same analysis was done for

other species, and shows that 40% of all accelerated oxygen, 41% of sodium, and 18.7% of potassium ions were accelerated within the KH vortex which is represented by the low-pressure region.

5.5 Solar wind plasma entry

Since we have already discussed ion acceleration and transport within KH vortices, we now discuss the possibility of solar wind plasma entry. Two different ion species, H^+ and He^{++} on the $\boldsymbol{E}$x$\boldsymbol{B}$ flow are considered as solar wind plasmas. These ions were injected with initial energies of 10 eV on the $\boldsymbol{E}$x$\boldsymbol{B}$ frame at the simulation start time. Although H^+ can be detected as solar wind plasmas and planetary ions, He^{++} cannot be produced in the Hermean environment, and thus detection of He^{++} can be a proxy of solar wind plasmas and its entrance inside the magnetopause. Previous results suggest that lighter ions cannot be accelerated under northward IMF and that solar wind penetration to the magnetosphere is completely controlled by the large convection electric fields. However, a small amount of solar wind plasma entry into the magnetosphere is expected due to the MHD-like behavior near the magnetopause. In addition, because we assume a proton dominant background for the MHD simulation, the 1st adiabatic invariant of H^+ violation leads to the violation of the MHD approximation. Previous studies on the KH instability did not discuss the limit of the MHD approximation on the nonlinear stage of the KH instability development because of its difficulty. However, when the 1st adiabatic invariant of H^+ is not conserved, it is a clear signature of the MHD approximation violation. In this section, we will discuss Case 1 (northward IMF) and Case 2 (southward IMF). In both cases, we consider protons picked up in the magnetosheath region closest to the magnetopause. Their Larmor radius is 0.018, normalized to the magnetopause thickness. For He^{++}, alpha ion, this radius is ~ 0.026. We show the results from protons to discuss ion energization and transport, and MHD approximation validation at the same time.

In Case 1, large convection electric fields exist in the magnetosheath region towards the magnetopause on the duskside and outwards from the magnetopause in the dawnside. The results shown in Figure 5.12, suggest that H^+ acceleration happens on both the dawn and dusk sides. Acceleration starts at t = 145 [s] while the linear growth time is approximately t = 90 [s]. The energized ion ratio becomes almost the same and corresponds to 20% of injected ions in the closest region to the magnetopause. Conversely, no ion transport was found on either side.

Considering ion injection time (here t = 0 [s]) and that acceleration happens at the same time on both the dawn and dusk sides, fine structures created due to the KH vortex breaking accelerate H^+ ions. Similar behavior is observed for He^{++}, where the acceleration starts at t ~ 122 [s]. The time delay of the energization start for protons is reasonably understood because they have twice smaller different Larmor radius compared to that of He^{++}. Negligible ion transport has been observed at t ~ 130 [s] for protons, and their transport starts before the acceleration starts. This transport is understood as MHD-like transport, as the proton motion seems to follow the motion of fluid background proton. In addition, the Larmor radius of He^{++} is large enough not to follow the fluid background.

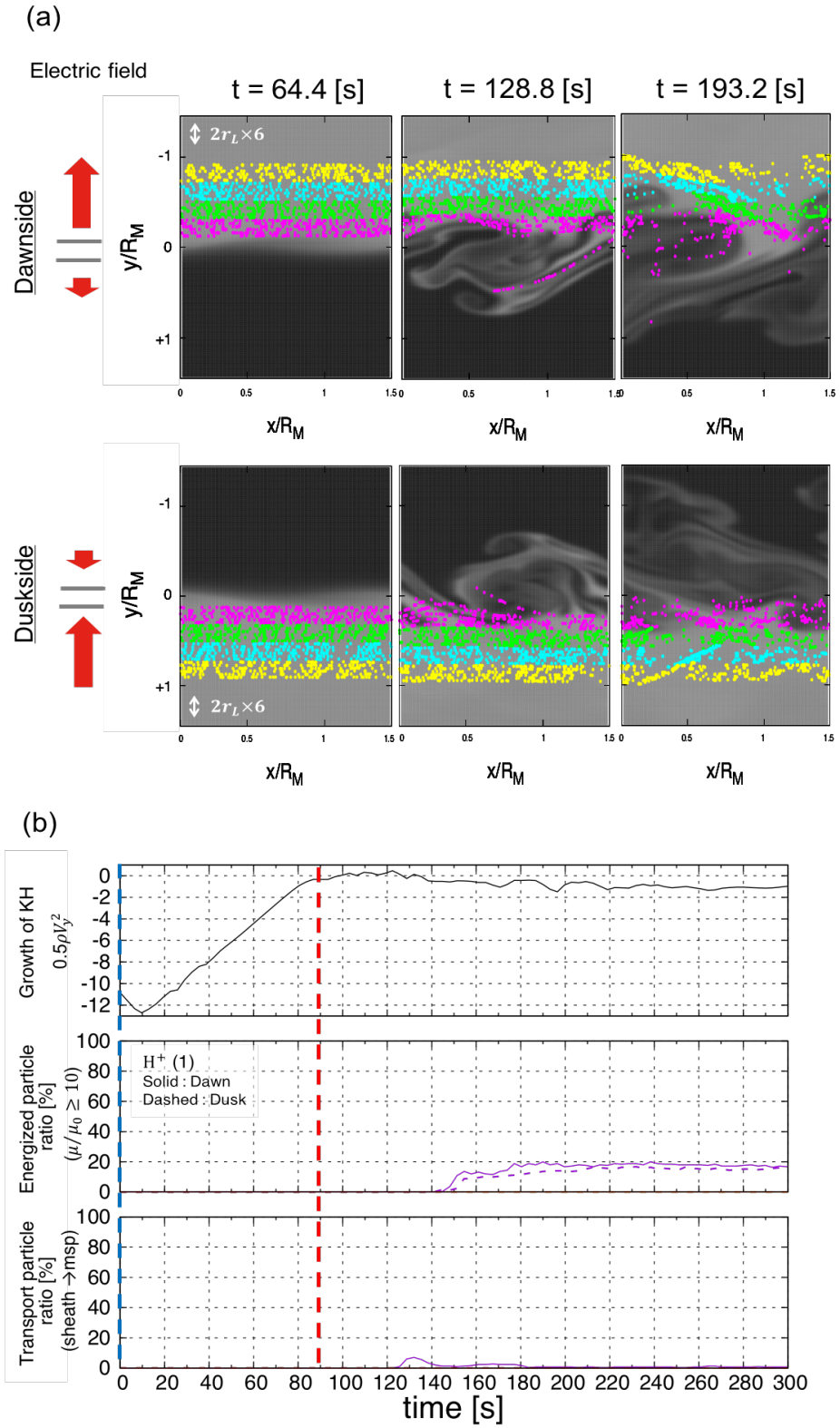

Figure 5.12 Energization and transport of solar wind proton in Case 1. The same format as Figure 5.9.

On the other hand, in Case 2, both He^{++} and H^{+} show qualitatively similar results. Ion energization and transport can be seen on both sides. The ion energization starts at t ~ 110 [s] for H^{+} and t ~ 108 [s] for He^{++}. Moreover, ion transport starts at t ~ 120 [s] for H^{+} and t ~ 120 [s] for He^{++} in contrast to Case 1. Ion acceleration occurs both on the dawn and dusk sides with almost the same ratio, with ion transport being more effective on the duskside. In addition, ion transport in Case 2 starts at the same time as energization starts. This suggests that ions can be transported due to acceleration from the rotational components of the electric field inside the KH vortex in the same manner as for ions of planetary origin.

At same time, the 1st adiabatic moment of a proton at t = 145 [s], for Case 1, indicates that the MHD approximation is not valid anymore. Though our injected proton had different characteristics as the background proton had, it implies that we need to consider the ion kinetics at a later stage of the KH non-linear phase. In this study, we do not focus on this, however this aspect could be studies in the future.

Is it possible to have a solar wind plasma entry through a KH vortex? Our results suggest that the ions can be transported magnetohydrodynamically, meaning that the size of the solar wind plasma entry region is determined by the vortex size. Especially, even if we do not have any magnetic reconnections, solar wind plasmas are subject to enter into the magnetosphere region during southwards IMF due to the convection electric field.

5.6 Chapter summary

In this chapter, we examined the ion energization and transport in Mercury's realistic configurations. Both dawn and dusk side configurations were considered under north- and southward IMF. In addition, though only sodium ions were injected and examined in Chapter 4, here various ion species had been investigated. Here some remarkable characteristics are presented.

General features of the ion acceleration which were presented in the previous chapter were verified in this chapter, and we revealed that the large convection electric field is clearly important to the ion acceleration and transport. Our results from both Case 1 and Case 2 showed that the ion transport is controlled by the electric field orientation in the magnetosheath, having a stronger electric field. The ion energization occurs when ions picked up in the magnetosphere on both dawn and dusk sides under both a north- and southward IMF. Especially, we found that the electric field configuration under southward IMF can significantly make ions accelerate within KH vortices due to the developed electric field orientation inside the vortex.

Regarding lighter ions, including the solar wind plasmas, their Larmor radius is small enough to the magnetopause thickness and thus small enough not to be accelerated during the linear growth phase of the KH instability, resulting in the MHD-like behavior. After the linear growth time, KH vortices start to break and make fine structures, whose scale is comparable to the Larmor radius. Ions can be energized with these fine structures. Non-adiabatic energization of solar wind protons goes beyond the limit of MHD validation. In the later stage of the nonlinear phase, the ion kinetics should be taken into account for physics.

In this study, although we did not consider any x and y component of the magnetic field and the existence of ions already moving non-adiabatically, some general features should be detected by instruments aboard a spacecraft.

First, energized ions in the magnetosphere region on both the dawn and dusk sides with the development of the KH instability are an important feature. If we have a wide range of plasma ion analyzer from a few eV to keV, ion acceleration should be observed and thus, the energy distribution would be changed between the KH and non-KH events. FIPS aboard MESSENGER had an energy range from 100 eV/e to 13 keV/e and an acceleration process of picked up ions could not be observed. Now, we have MSA aboard MIO/BepiColombo with a wider energy range that can cover the picked up ion acceleration theoretically found in this study, and with a wider FOV. Less dense plasma in the dawnside magnetosphere is expected to be observed by MSA. It is not common to discuss the ion behavior during southward IMF because of the magnetic reconnection and flux transfer events. Such a stagnation of ions or low density cannot be detected

during southward IMF because the ion would be transported in both directions between the magnetosphere and the magnetosheath.

Solar wind plasma entry can be expected only near the magnetopause. Because solar wind plasmas behave like MHD, their penetration into the magnetosheath is considered to be fluid-like.

Chapter 6

Simulation based analysis of MESSENGER data

As shown in Chapters 4 and 5, the KH instability plays a role on non-adiabatic acceleration and/or deceleration of heavy ions of planetary origin, in addition to roles on transport of momentum and mixing plasmas. In this chapter, we will discuss observational facts obtained from the MESSENGER spacecraft, especially for the Na^+-group ions.

6.1 Presentation of MESSENGER mission and FIPS instrument

Since Mercury is the closest planet to the Sun, in-situ observation is not an easy task which explains why we only have two sets of spacecraft that have been sent to this remarkable planet. One is the Mariner-10, and the other is MESSENGER. In this thesis, we fortunately had the opportunity to analyze MESSENGER data with the cooperation of Dr. Jim M. Raines and his team from the University of Michigan.

MESSENGER, the first orbital spacecraft to the Mercury that was launched in 2004 and stayed in orbit from March 11, 2011 until April 30, 2015. It had gathered multiple information about Mercury's environment and physics, including the KH instability. In particular, the plasma environment around Mercury had been investigated using the magnetometer (MAG) to measure the ambient magnetic field with a resolution of 20 s^{-1}, and with the Fast Image Plasma Spectrometer (FIPS) to measure the composition of heavy ions (atomic number > 4) with an energy per charge from 50 eV/e up to 13 keV/e. FIPS measured the planetary ions, which are derived from Mercury's exosphere by the photon-ionization. FIPS gives us an idea on Mercury's magnetosphere and surrounding space plasma environment with ~10 s of the time resolution. MESSENGER had to protect itself from the harsh condition closer to the Sun using sunshield. Because of this, the FIPS instrument has only a 1.4π sr of field of view (FOV) with an angular resolution of $\sim 15°$. The location of FIPS instrument on the spacecraft can be seen in Figure. 6.1.

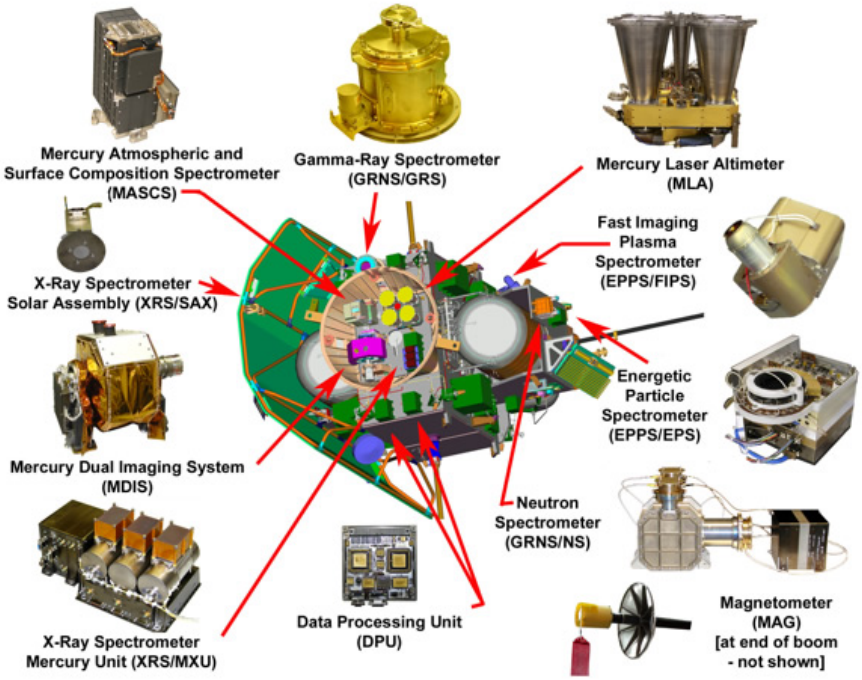

Figure 6.1 Overview of instruments aboard MESSENGER
[credit: http://messenger.jhuapl.edu/About/Spacecraft-and-Instruments.html]

Observational studies of the KH instability have been done by several authors, both on the day and nightside magnetopause, as well as on the dusk and dawn side. *Liljeblad et al*. [2014] analyzed about 2.5 years of MAG data from March 24, 2011 to September 18, 2013, and reported that there is a strong dawn-dusk asymmetry on the KH occurrence: the KH instability tends to occur in the duskside flank region, where the magnetic field lines do not stabilize the KH development efficiently as the magnetic tension. Relying on previous KH studies including *Liljeblad et al*. [2014], we analyze all data passing through the night-duskside magnetospheric flanks collected during the entire MESSENGER orbital phase. In order to discuss a new KH role on acceleration and/or deceleration, the energy distribution of Na^+-group ions (Na^+, Mg^+. and Si^+, among others are considered due to the resolution in mass-per-charge of FIPS) detected by FIPS is investigated, and that of KH events and non-KH events is compared. Thus, we need enough counts of Na^+-group ions in FIPS and this makes us difficult to analyze the energy distribution on the dayside. Since *Sundberg et al*. [2012a] and *Gershman et al*. [2015] put the KH event list on their papers, therefore we first started with KH events already identified (refer it as Sundberg-Gershman (SG) events hereinafter). In this study, the Mercury-Sun-Orbital (MSO) coordinate system is used: The

x-axis is directed from the center of the planet towards the Sun, and the z-axis is normal to Mercury's orbital plane being positive towards the north celestial pole, and the y-axis completes the right-handed system.

Generally, KH waves are identified by only using MAG data. We selected all data with fluctuations near the magnetopause crossing signature, and additional selection was done by verifying whether they fulfill the following criteria:

(1) Quasi-periodicity
(2) No indications of other oscillations, for example, flux transfer events, mirror waves, or magnetopause motions

One may point out that we need to consider the ion cyclotron waves, their direction of rotation is opposite to rolling up KH vortices in the duskside. Typical KH signatures observed on February 1, 2012 during an outbound orbit can be seen in Figure 6.2. To compare the energy distribution, non-KH event should have mostly a similar orbit as the KH event. Although the orbit path is shifting in time, its shift in one orbit is small, and therefore the adjacent orbit of each KH event can be considered as a similar orbit. In this study, we also consider the two adjacent orbits, before and after the KH orbit of the event, so that we can analyze them quantitatively and qualitatively.

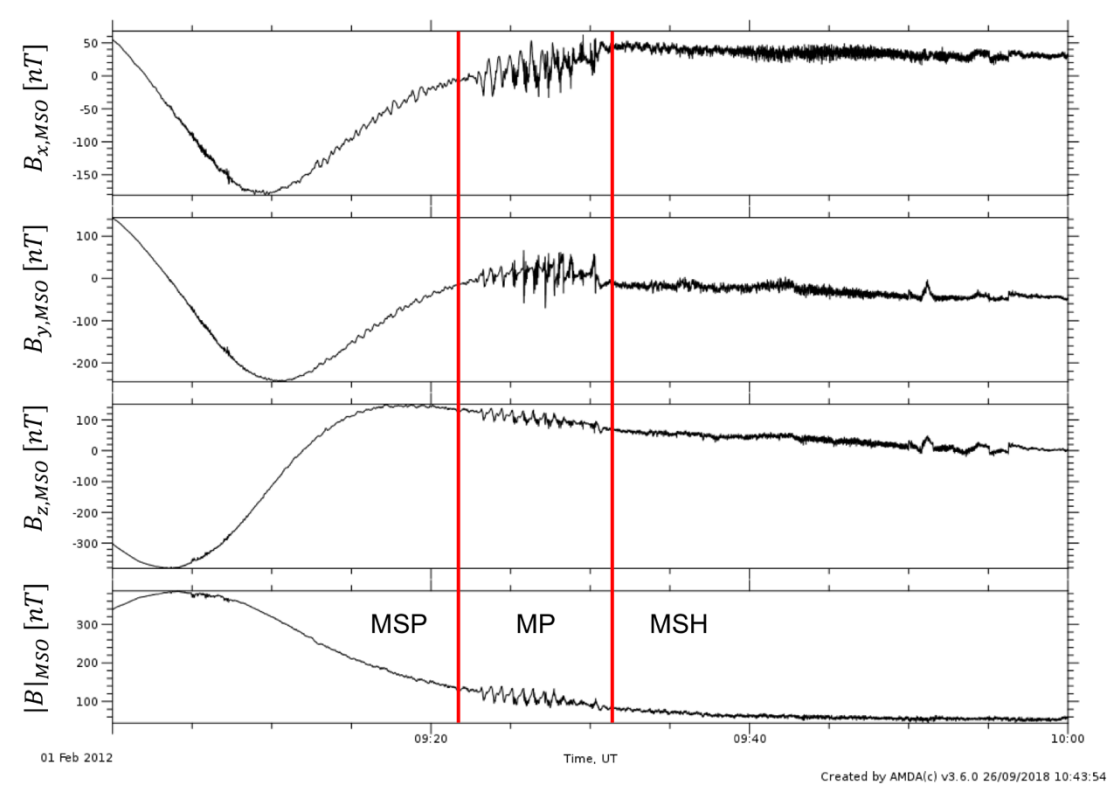

Figure 6.2. Example of typical KH waves at Mercury. Top to bottom, separate components of the magnetic field data in MSO coordinates. The bottommost panel shows the magnetic field intensity. Outbound orbit encountered KH waves at the magnetopause. 'MP', 'MSH', and 'MSP' indicates the magnetopause, the magnetosheath, and the magnetosphere region, respectively.

6.2 Survey of the Sundberg-Gershman study

Sundberg et al. [2012a] and *Gershman et al*. [2015] analyzed the MAG data under northward IMF and identified KH events by using mostly the same criteria shown in the previous section. The number of KH events were 25 in the dayside (between 14:00 and 16:00 LT, not analyzed in this study) and 34 in the nightside (between 18:00 and 21:00 LT). In order to compare the energy distribution of the Na^+-group ions of KH and non-KH events, the magnetopause crossing identification was performed for two each adjacent orbit of a KH event orbit and we collected the total counts of the Na^+-group in the data. A typical KH signature in SG events with a series of analysis is shown in Figure 6.3. The top panel is the proton energy spectrogram in units of flux (s^{-1} cm^{-2} sr^{-1} kV^{-1}), each vertical time step corresponds to one full FIPS scan over a period of 10 s. The second panel is the Na^+-group ions' energy spectrogram in the phase space density (PSD) in units of s^3 km^{-6}. Third panel shows the entire count for Na^+-group ion in each time step. The remaining 4 panels are from MAG data, showing Bx, By, Bz and the magnetic field intensity, respectively. 97% of FIPS detection are protons, thus the energy spectrogram for Na^+-group is presented in the PSD units.

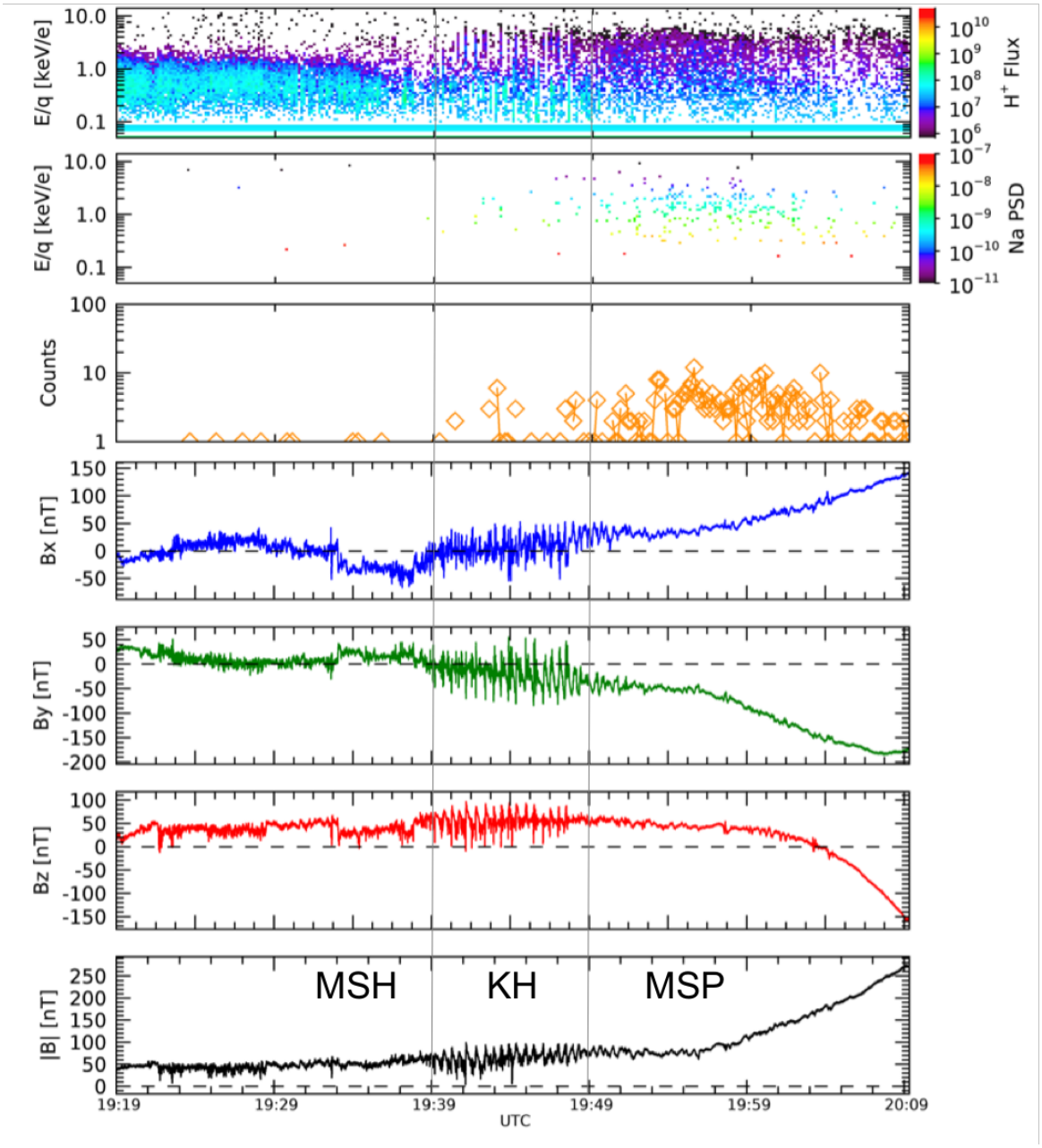

Figure 6.3 A typical KH signature brought from SG events, orbit number 705. From top to bottom, each panel shows the proton energy-time spectrogram in the unit of flux (s^{-1} cm^{-2} sr^{-1} kV^{-1}), Na^{+}-group energy-time spectrogram in PSD units (s^{3} km^{-6}), Total Na^{+}-group counts, time series of magnetic field component (x, y, z) and intensity. KH waves are seen at 19:39-19:49.

The energy distribution in the PSD unit is derived by taking the sum of the energy spectrogram in time. This indicates that the energy distribution is highly dependent on its time range and total counts. Also, it is possible that identified KH orbits show no Na^+-group counts because the existence of their counts is not taken into account for the KH event identification. These things should be considered carefully when we obtain the energy distribution for the Na^+-group ions (Na^+ PSD behavior hereinafter). In this study, we collect the data of +/- 20min from the duration of KH signatures in each identified KH event, and use adjacent orbits with the same duration before and after the KH event. MESSENGER had 12 hour-orbit in the period from March 11, 2011 to April 25, 2012 and 8 hour-orbit in the rest of period. For instance, we consider an adjacent orbit an additional 8 or 12 hour prior time period to the KH orbit of the event.

FIPS clock angle should also be considered as an important factor for the Na^+ PSD behavior. Because of a limited FOV, FIPS may observe a different region of the Hermean magnetosphere. If FIPS has a completely different clock angle between the considered orbit and the adjacent one, detected particles should come from a different region and thus it makes difficult to compare the plasma properties. Considering an examination of a new KH role, acceleration and/or deceleration, the Na^+ PSD behavior may change between the KH and the non-KH events. The Na^+ PSD behavior in other regions (the magnetosheath and the magnetosphere sides of the KH duration) may help us to understand the plasma properties changing across the magnetopause, and its influence from the KH development.

The summarized table for the nightside SG events with some of 34 identified KH events is shown in Table 6.1 (complete table can be found in Appendix). We also show the adjacent orbits in above and below of the KH event orbit. Here, grey hatched columns show the non-available data. Examples of non-available data are: no KH signatures near the magnetospheric flanks, no clear magnetopause crossing signature during the event period, or zero counts of Na^+-group ions in whole data period. In this table, Bz value in the magnetosheath region shows the 5-min average of z-component of the magnetic field in the magnetosheath side which is immediately adjacent to the magnetopause (MP) crossing point. Latitude is the value when the MESSENGER crosses the MP. Local time (LT) and true anomaly angle (TAA) indicates the values when MESSENGER crosses the equatorial plane. The column of Na^+-group counts shows the sum of the counts for each period based on the MP crossing time. Figure 6.4 shows the data division for the analysis. In the nightside SG events, all KH events have been observed in the inbound orbit. In this case, the KH duration is treated as a part of the magnetosheath region and is adjacent region to the clear MP crossing point, being defined uniquely in this study.

Table 6.1 Summary of SG events with adjacent orbits (12/34 events)

	Case		Orbit	Bz in Magnetosheath	MP crossing time (KH duration)	Latitude	LT (equatorial)	TAA (equatorial)	Na+ group counts (10min) MSH	Na+ group counts (10min) KH	Na+ group counts (10min) MSP	Comment
Sundberg-Gerstman events(nightside)	1	Adj_b2	168	15.1	12:27	28.8	-	-	11		0	
		Adj_b	169									Scan type changed
		KH	170	47.2	12:37(12:26 - 12:37)	30.3			0	37	73	
		Adj_a	171	38.4	0:38 (0:21 - 0:38)	25.7	18.9	358.0	0	47	122	
		Adj_a2	172									Scan type changed
	2	Adj_b2	169									Scan type changed
		Adj_b	170	47.2	12:37(12:26 - 12:37)	30.3			0	37	73	
		KH	171	38.4	0:38 (0:21 - 0:38)	25.7	18.9	358.0	0	47	122	
		Adj_a	172									Scan type changed
		Adj_a2	173									Scan type changed
	3	Adj_b2	176	39.6	13:04	34.1	-	-	2		54	
		Adj_b	177									Scan type changed
		KH	178									Scan type changed
		Adj_a	179									Scan type changed
		Adj_a2	180	10.9	12:56	26.0	-	-	3		38	
	4	Adj_b2	339									No MP crossing in data period
		Adj_b	340	5.0	20:33	14.4	20.6	332.2	130		15	
		KH	341	15.3	8:01 (7:48 - 8:01)	-10.2	20.4	335.2	0	24	97	
		Adj_a	342	22.2	20:25 (20:15 - 20:25)	7.4	20.1	338.3	0	20	23	
		Adj_a2	343	27.1	8:41	24.0	19.9	341.4	14	14	7	
	5	Adj_b2	340	5.0	20:33	14.4	20.6	332.2	130		15	
		Adj_b	341	15.3	8:01 (7:48 - 8:01)	-10.2	20.4	335.2	0	24	97	
		KH	342	22.2	20:25 (20:15 - 20:25)	7.4	20.1	338.3	0	20	23	
		Adj_a	343	27.1	8:41	24.0	19.9	341.4	14	14	7	
		Adj_a2	344	27.4	20:32 (20:21 - 20:32)	13.1	19.7	344.6	1	9	45	
	6	Adj_b2	342	23.4	20:25 (20:15 - 20:25)	6.5	20.1	338.3	0	20	24	
		Adj_b	343	27.1	8:41	24.0	19.9	341.4	14		7	
		KH	344	27.4	20:32 (20:21 - 20:32)	12.1	19.7	344.6	0	9	38	
		Adj_a	345	50.1	8:44 (8:20 - 8:41)	25.2	19.5	347.7	0	23	75	
		Adj_a2	346									Scan type changed
	7	Adj_b2	343	27.1	8:41	24.0	19.9	341.4	14		7	
		Adj_b	344	27.4	20:32 (20:21 - 20:32)	12.1	19.7	344.6	0	9	38	
		KH	345	50.1	8:44 (8:20 - 8:41)	25.2	19.5	347.7	0	23	75	
		Adj_a	346	75.4	8:40	22.4	19.1	354.0	1	76	55	
		Adj_a2	347									Scan type changed
	8	Adj_b2	515	3.1	9:25	0.5	21.1	323.6	76		109	
		Adj_b	516									No MP crossing in data period
		KH	517	23.7	09:21 (9:07 - 9:21)	-2.5	20.7	329.6	0	33	140	
		Adj_a	518	12.1	21:30	5.0	20.5	332.6	93		32	
		Adj_a2	519	9.9	9:37	12.3	20.3	335.7	111		59	
	9	Adj_b2	518	12.1	21:30	5.0	20.5	332.6	93		32	
		Adj_b	519	9.9	9:37	12.3	20.3	335.7	111		59	
		KH	520	20.1	21:24 (21:09 - 21:24)	0.2	20.1	338.8	0	47	133	
		Adj_a	521	7.5	9:26	1.7	19.9	341.9	50		21	
		Adj_a2	522	38.9	21:32 (21:11 - 21:32)	7.3	19.6	345.0	0	14	209	
	10	Adj_b2	520	20.1	21:24 (21:09 - 21:24)	0.2	20.1	338.8	0	47	133	
		Adj_b	521	7.5	9:26	1.7	19.9	341.9	50		21	
		KH	522	38.9	21:32 (21:11 - 21:32)	7.3	19.6	345.0	0	14	209	
		Adj_a	523	31.6	9:25 (9:11 - 9:24)	0.9	19.4	348.2	0	19	203	
		Adj_a2	524	46.0	21:38 (21:14 - 21:38)	15.1	19.2	351.3	0	32	222	
	11	Adj_b2	521	7.5	9:26	1.7	19.9	341.9	50		21	
		Adj_b	522	38.9	21:32 (21:11 - 21:32)	7.3	19.6	345.0	0	14	209	
		KH	523	32.7	9:25 (9:11 - 9:24)	0.1	19.4	348.2	0	19	175	
		Adj_a	524	46.0	21:38 (21:14 - 21:38)	15.1	19.2	351.3	0	32	222	
		Adj_a2	525	19.3	9:38	13.7	19.0	354.5	71		27	
	12	Adj_b2	522	38.9	21:32 (21:11 - 21:32)	7.3	19.6	345.0	0	14	209	
		Adj_b	523	32.7	9:25 (9:11 - 9:24)	0.1	19.4	348.2	0	19	175	
		KH	524	46.6	21:38 (21:14 - 21:38)	13.9	19.2	351.3	0	32	204	
		Adj_a	525	19.3	9:38	13.7	19.0	354.5	71		27	
		Adj_a2	526	5.8	21:30	5.5	18.8	357.7	3		27	

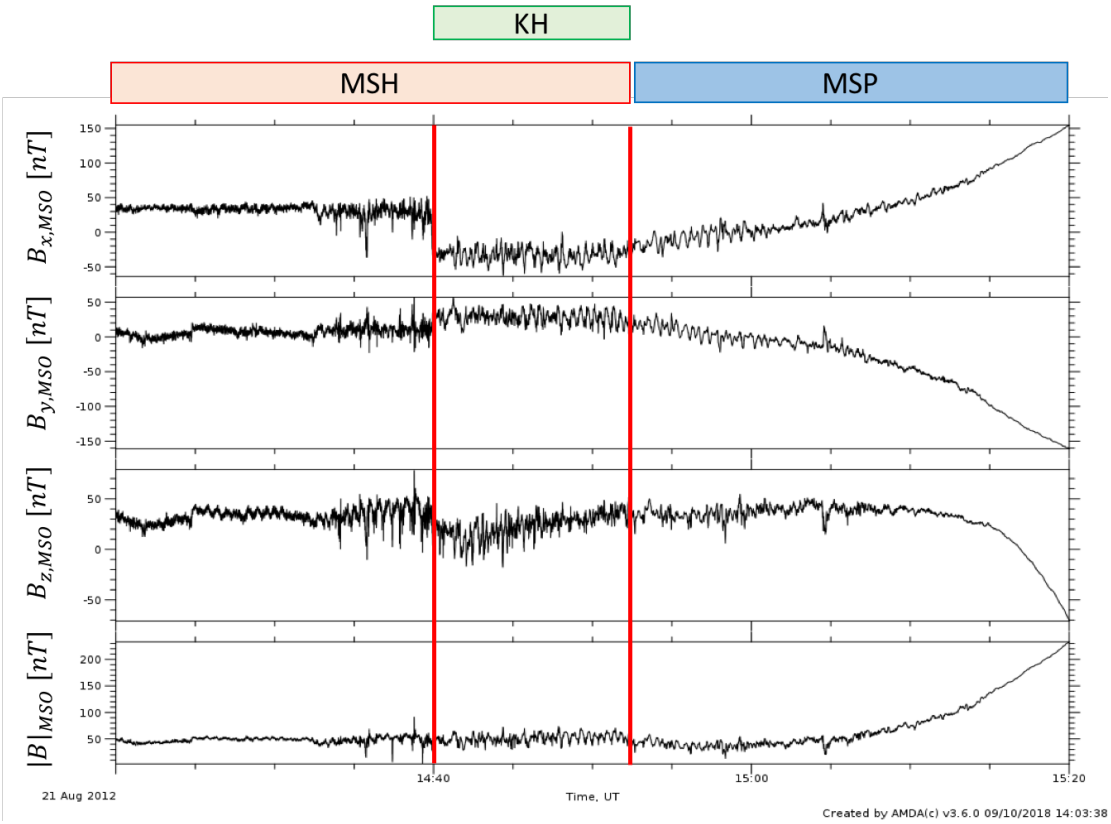

Figure 6.4 Example of the data division of the KH orbit. In this study, magnetopause (MP) crossing point is defined at the boundary between the magnetosheath (MSH) and the magnetosphere (MSP), which is determined by both the proton energy-time spectrogram and the magnetic field variations. The KH region can be a part of MSH (MSP) region in the inbound (outbound) orbit if it is observed on the nightside (dayside).

Southward Bz in the magnetosheath data is not used for the present analysis. Removing those data brings that 34 KH event set, containing 34 KH events and 69 non-KH events, are reduced to 33 KH event set (33 KH events and 43 non-KH events, some events have a lack of available adjacent orbits). Figure 6.5 shows the FIPS clock angle at a certain point compared to the count distribution of Na^+-group in the magnetosheath region. Because some data points show different FIPS clock angles, only FIPS clock angle between 180 – 270 will be analyzed hereafter. Removed number of data here is 6 for both KH events and non-KH events.

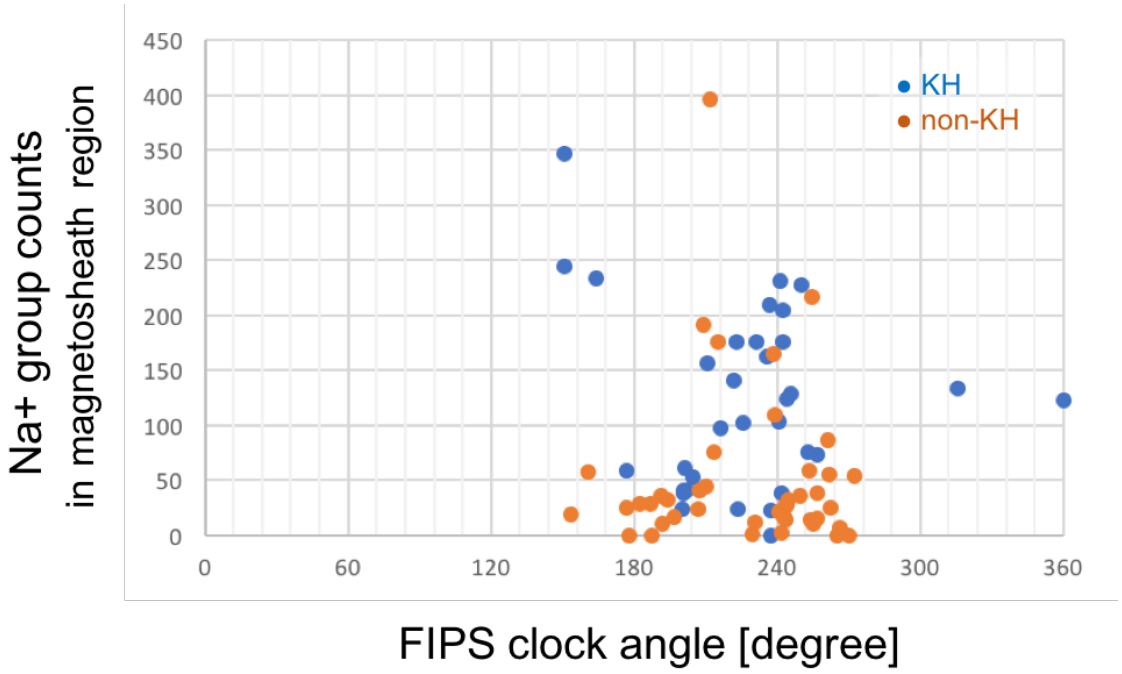

Figure 6.5 Na^+-group counts in the magnetoshath region as a function of the FIPS clock angle. Blue and orange dots represent KH and non-KH events, respectively.

The count distribution of Na^+-group ions in both the magnetosheath and the magnetosphere sides as a function of averaged z-component of the magnetosheath magnetic field is presented in Figure 6.6. We note that KH events have a magnetic field magnitude higher than 15 nT, and that Na^+ counts in KH event increase with increasing Bz component. On the other hand, the Na^+-group count in non-KH events also have large counts in the magnetosheath even though the corresponding magnitude of Bz is small. This may be explained by the linear theory of the KH growth. The parallel component of the magnetic field to the wavenumber of the KH wave (here Bx and By) stabilizes the instability development as a magnetic tension. Looking at Figure 6.6, the KH instability likely occurs when there is a strong Bz and it is consistent to the prediction from the linear theory. As for the Na^+-group counts in the magnetosphere side (bottom panel in Figure 6.6), there is a clear large count difference between KH and non-KH events. This feature can be discussed in two ways. First we can consider that they are energized ions, resulting in acceleration by the KH development. Because of the limited FIPS energy range, ions with low energy, as the case of just being picked up cannot be detected by FIPS. If such ions are energized due to the KH development, they may have enough energy to be detected and thus Na^+ counts increase. The second option is that such a large Na^+ population may enhance the development of the KH instability. Detailed discussion will be done later.

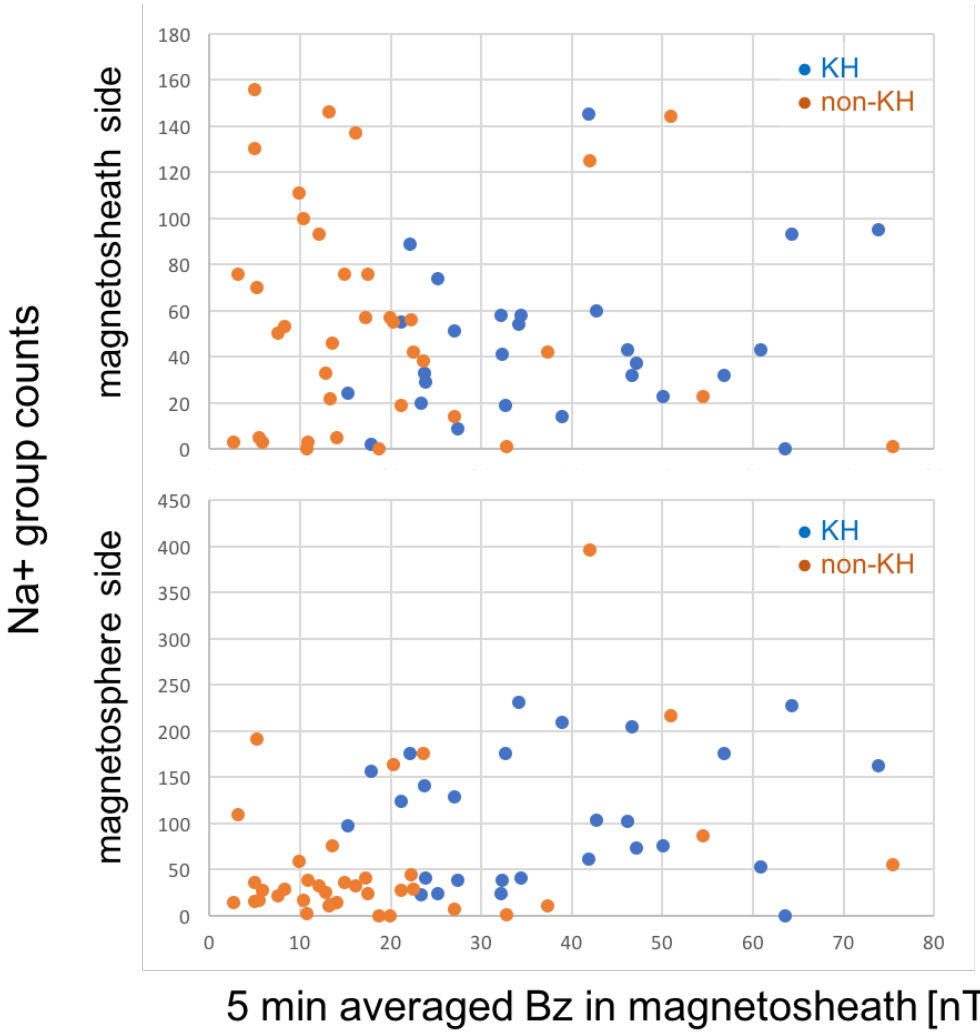

Figure 6.6 Count distribution of Na^+-group ions in the magnetosheath (top) and magnetosphere (bottom) sides as a function of 5-min averaged Bz in the magnetosheath.

To obtain and compare the Na^+ PSD behavior with high accuracy, we removed data having zero Na^+-group counts in one side (MSH or MSP). 1 set of KH events and 4 sets of non-KH events have been removed. Finally, we only consider 26 of the KH and 33 of non-KH events. By pairing the KH orbit and adjacent orbits next to the KH event, 11 event sets are appropriate. The FIPS clock angle of each event set is rechecked at this time to avoid errors. For instance, the KH orbit may have 240° of clock angle at MP crossing but adjacent non-KH orbit may have 190°. Since FIPS has an angular resolution of ～15°, the limited FIPS clock angle between two orbits is set within +/- 15°. As a consequence of this limitation, 2 out of 11 KH event sets are removed. From all the SG events considered, we only finally take into account 9 KH event sets shown in Table 6.2. The number in the KH and non-KH columns represents the respective orbit number.

Table 6.2 Table of 9 paired events with their respective orbit number.

Case	KH	non-KH
1	342	343
2	344	343
3	517	518
4	522	521
5	1179	1180
6	1190	1191
7	1444	1443
8	1445	1446
9	1710	1709

6.2.1 Detailed analysis of selected KH events

Here some detailed analysis of selected KH events will be presented to explore the difference in the Na^+ PSD behavior.

(1) Case 5

From the point of view of total Na^+-group count in each region, Case 5 is shown in Figure 6.7 in the same format as Figure 6.3. In the KH event, the identified KH duration is 14:40-14:51 with MP crossing point at 14:51. In the non-KH event of orbit 1180, the identified MP crossing point is at 22:46. Regions are divided into three as explained in Figure 6.4: the KH region, 10 min magnetosphere region, 10 min magnetosheath region and magnetosheath/magnetosphere regions are given with 30 sec intervals from the KH region. In the KH event of Case 5, 14:29:30-14:39:30 corresponds to the magnetosheath, 14:40-14:51 to the KH, and 14:51:30-15:01:30 to the magnetosphere regions. As for the non-KH event, 22:24:30-22:34:30 corresponds to the magnetosheath, 22:35-22:46 to the KH, and 22:46:30-22:56:30 to the magnetosphere region.

(a)

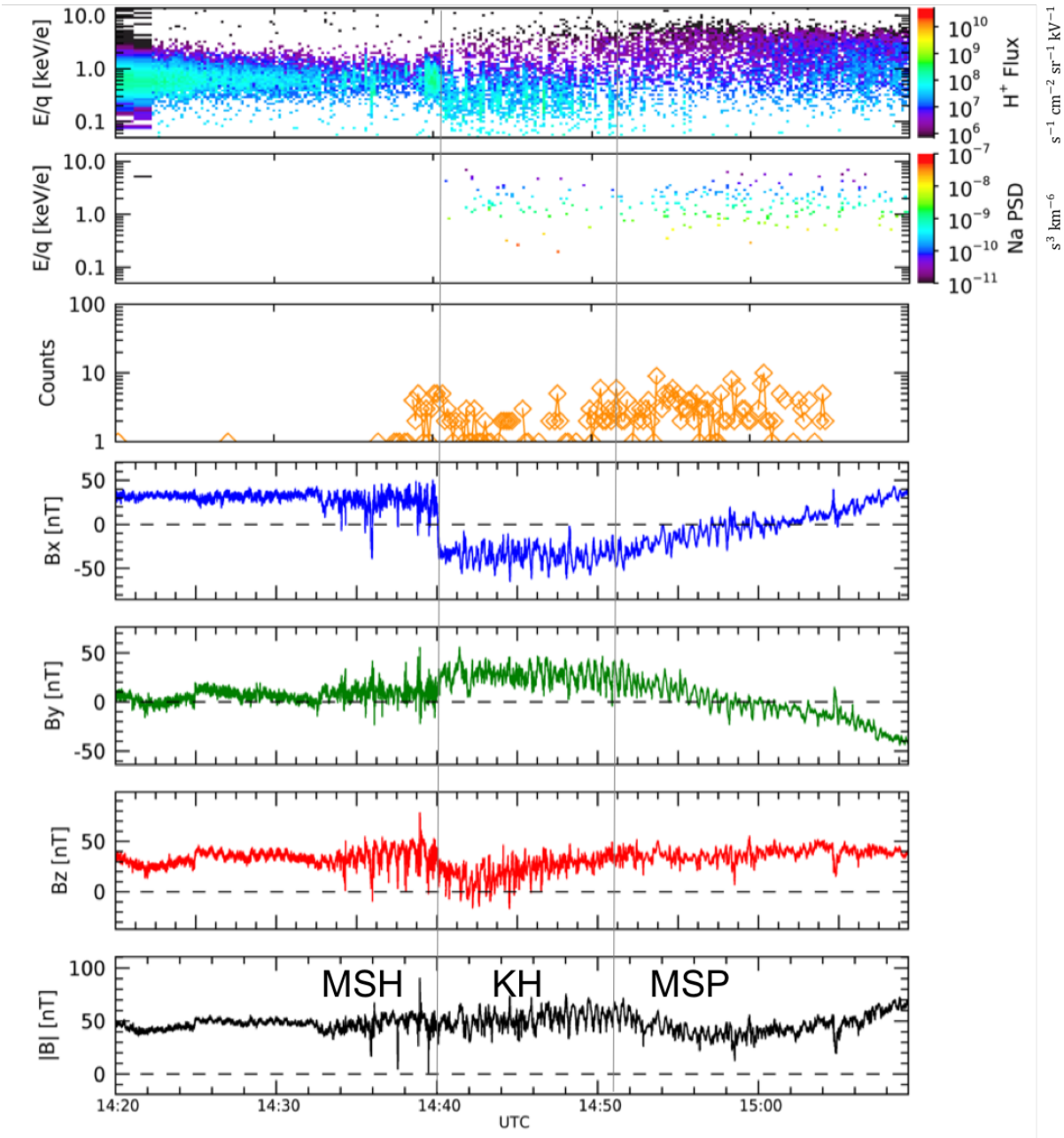
E/q [keV/e]
10.0
1.0
0.1
H+ Flux
s−1 cm−2 sr−1 kV−1
Na PSD
s3 km−6
Counts
100
10
1
Bx [nT]
50
0
-50
By [nT]
Bz [nT]
|B| [nT]
MSH
KH
MSP
14:20
14:30
14:40
14:50
15:00
UTC

(b)

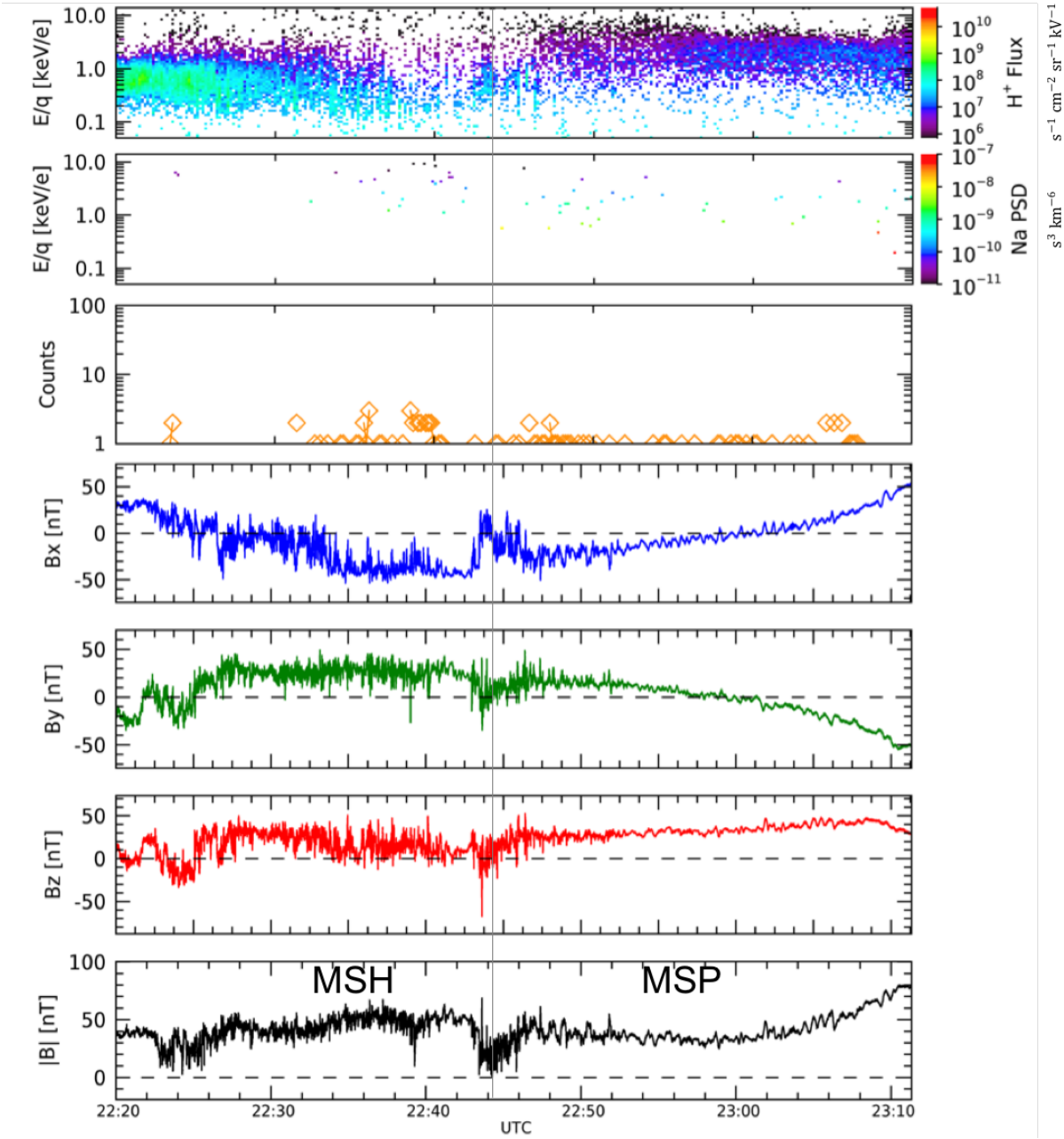

Figure 6.7 (a) Overview of the KH event of orbit number 1179, (b) overview of non-KH event of orbit number 1180. Format is the same as Figure 6.3.

As explained above, the Na^+ PSD behavior is obtained by taking the total sum of the Na^+ energy spectrogram in time. This highly depends on the total counts of Na^+-group ions. To understand

plasma properties in each region, we need to focus not on the PSD values but on the slope of its behavior.

In this study, two different normalizations are applied to seek plasma properties. One is done by using the total PSD value and the other by using the PSD value at 1 keV/e point (or nearest point to 1 keV/e). These two normalizations should be performed so that we can remove the artificial difference on the Na^+ PSD behavior, meaning the differences due just to the ambient density (or flux) or particles not due to the energization. Moreover, the error bar is calculated. If FIPS detects only one counts at a certain energy bin for the whole summation period, the error bar will be zero and it means that data uncertainty becomes automatically 100%. This is why the one Na^+ count at each bin during whole summation time period are removed. The normalized Na^+ PSD behaviors of selected events are finally shown in Figure 6.8. Both normalization methods seem to have globally the same trend. For simplicity, the results of total PSD normalization will be shown hereafter if there is no significant difference in the results obtained from the two ways of normalization.

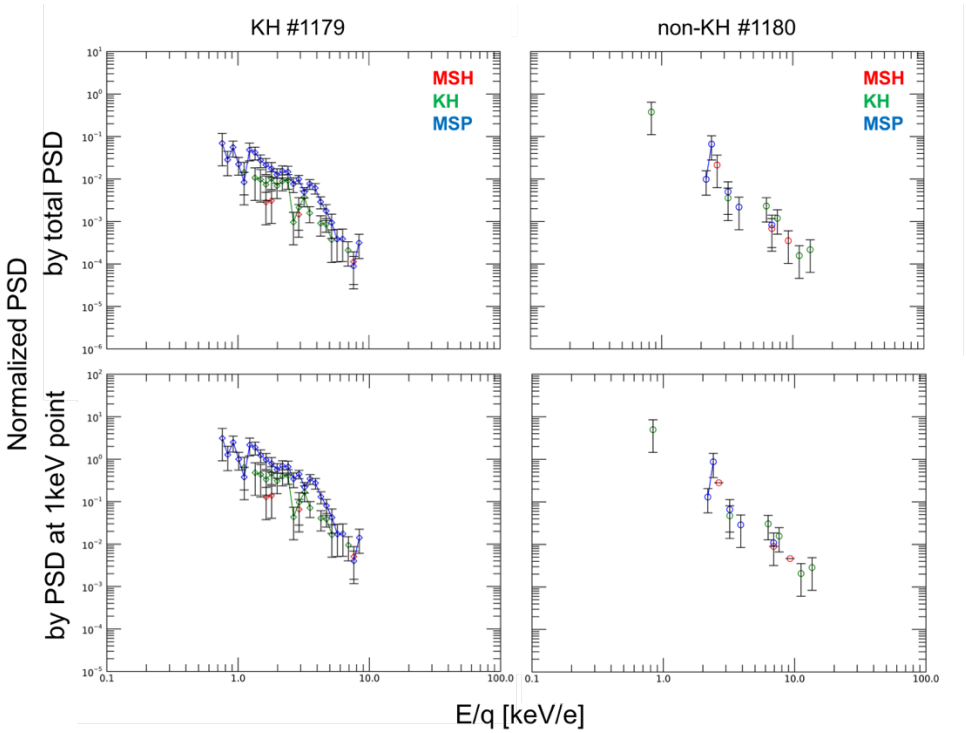

Figure 6.8 Comparison of the normalized Na^+ PSD behavior for the different normalization methods. The black bar shows the error calculated by the Poisson distribution function. MSH, KH, and MSP represent magnetosheath (in red), KH (in green), and magnetosphere (in blue) region, respectively.

The Na^+ PSD behavior comparison in each region are presented in Figure 6.9. Fewer counts in the non-KH event make the comparison difficult. A significant difference between the KH and non-KH events in Case 5 is the total counts of the Na^+-group ions.

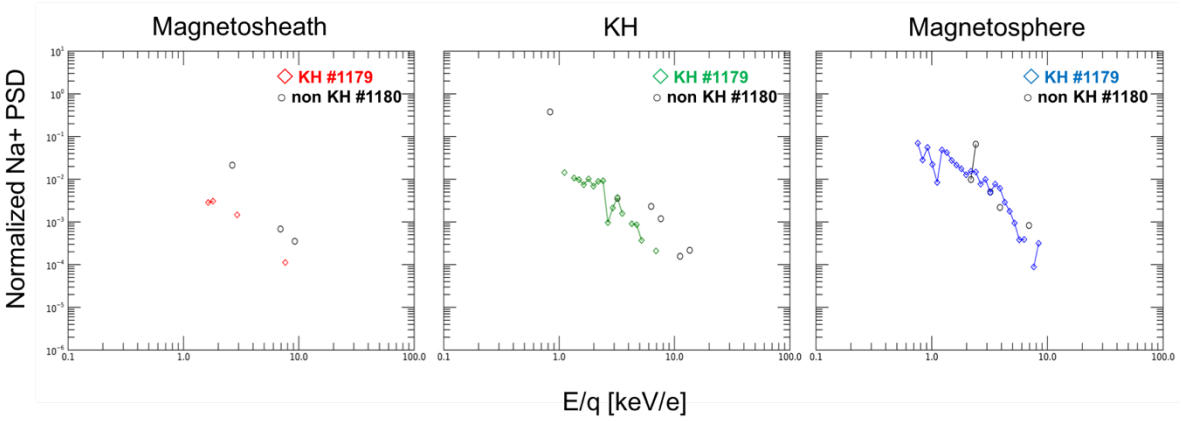

Figure 6.9 Comparison of the normalized Na^+ PSD behavior in each divided region. Black circle with lines shows the Na^+ PSD behavior in the non-KH orbit while colored symbols shows behavior in the KH orbit.

In Case 5, the spacecraft location factors, i.e., LT, TAA, latitude and FIPS clock angle are mostly the same. In addition, averaged Bz is 22.2 nT for the KH and 12.9 nT for the non-KH case, leading to the solar wind conditions are mostly stable. We wonder why do we have such a large difference in the Na^+-group counts even though these two orbits have mostly the same observation conditions?

The Na^+ energy-count distribution for both KH and non-KH events are shown in Figure 6.10 (a). This indicates that the KH event clearly has a larger count in the KH and MSP region. By comparing to the counts in the non-KH event, increasing Na^+-group count ratio (Figure 6.10(b)) is calculated. This ratio is obtained from the difference between counts in the KH and the non-KH, and then divided by the total non-KH counts in each region. Clearly, FIPS detected an important number of counts when we have KH waves, and also some counts appear in the lower energy range, ~ 1 keV/e. This may be because of the acceleration or transport due to the KH instability. For instance, picked up ions with a few eV will be observed around a few keV by non-adiabatic acceleration due to the KH development.

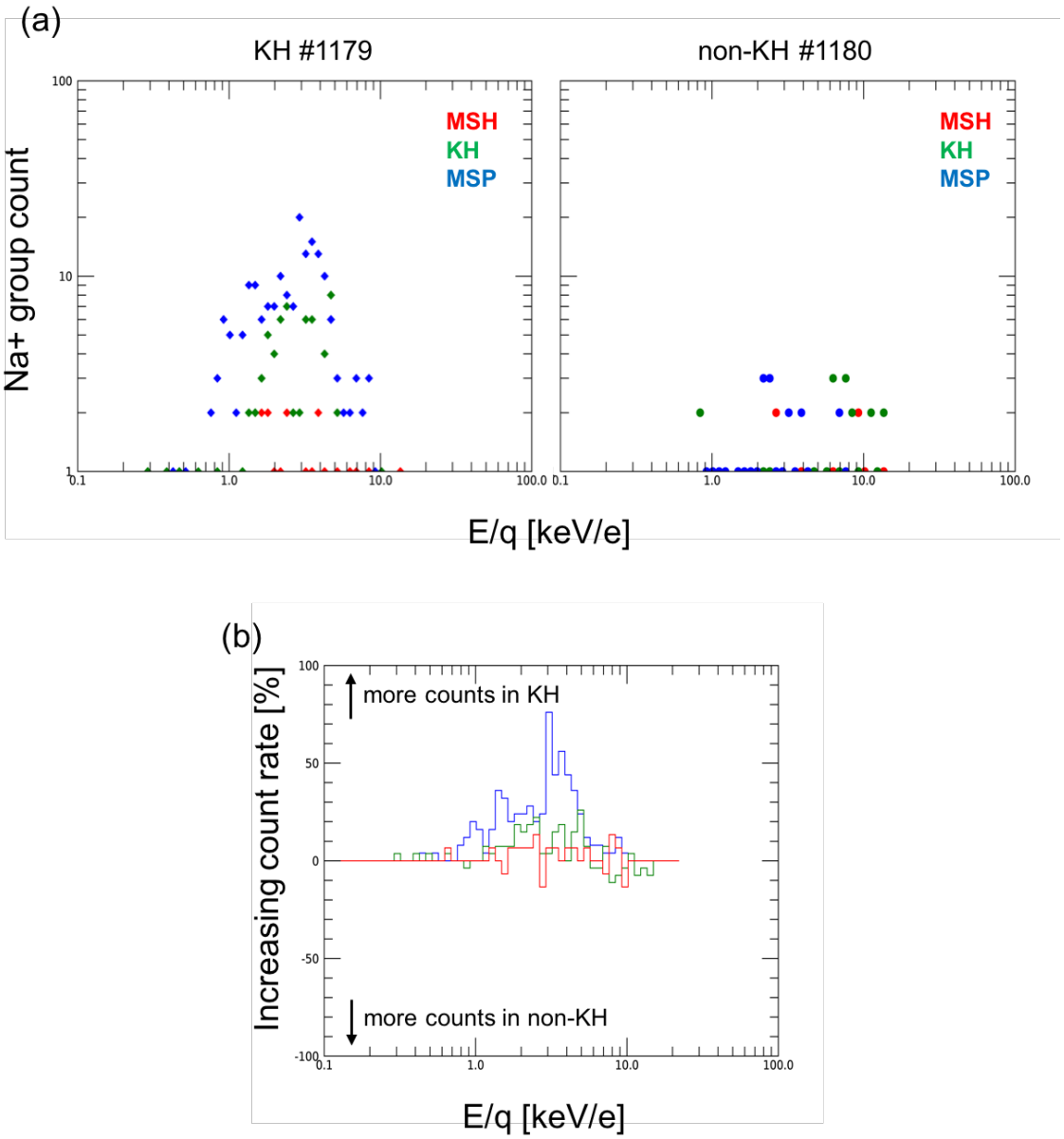

Figure 6.10 Comparison of energy-count distribution. (a) Total count in each energy bins for each orbit with different color symbols. Red is the total count in the magnetosheath, green and blue represents that in the KH and the magnetosphere region, respectively. (b) Na^+ increasing count rate based on the non-KH orbit count. Positive value indicates Na^+ count increases with KH.

We have 9 cases of KH events and Case 5 is one of these. We will investigate an additional case to find different and additional features.

(2) Case 3

Although Case 3 does not have enough counts in the magnetosheath region to obtain the Na^+ PSD behavior, the other two regions have much higher counts compared to those in Case 5. The normalized Na^+ PSD behaviors are shown in Figure 6.11 in the same format as Figure 6.8 and Figure 6.9. Again, we should focus on the shape of the slopes of the PSD behavior. The slopes pf the PSD behavior in both the KH and non-KH events in both KH and magnetosphere regions show similar behaviors and no significant difference between them.

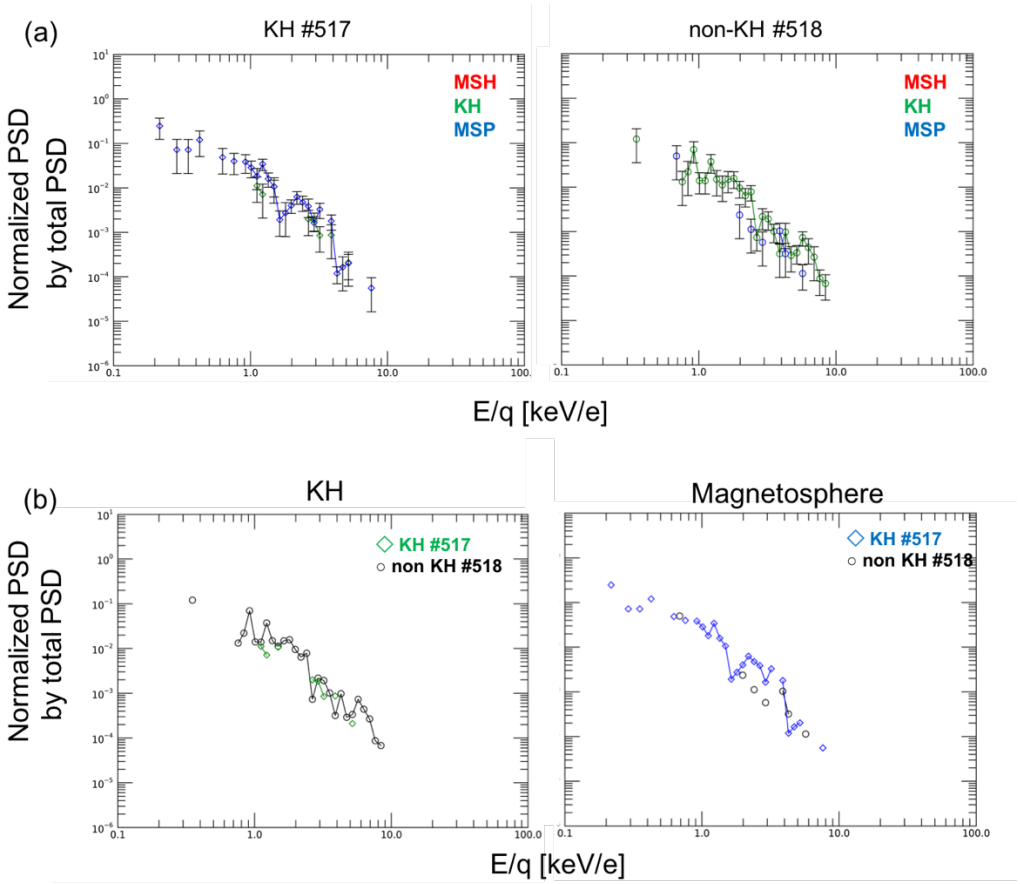

Figure 6.11 The normalized Na^+ PSD behavior of Case 3, for (a) each event and (b) region.

The energy-count distribution of Case 3 is shown in Figure 6.12. We note that counts in the magnetosphere region increase when we have KH waves. This is the same feature as observed in Case 5.

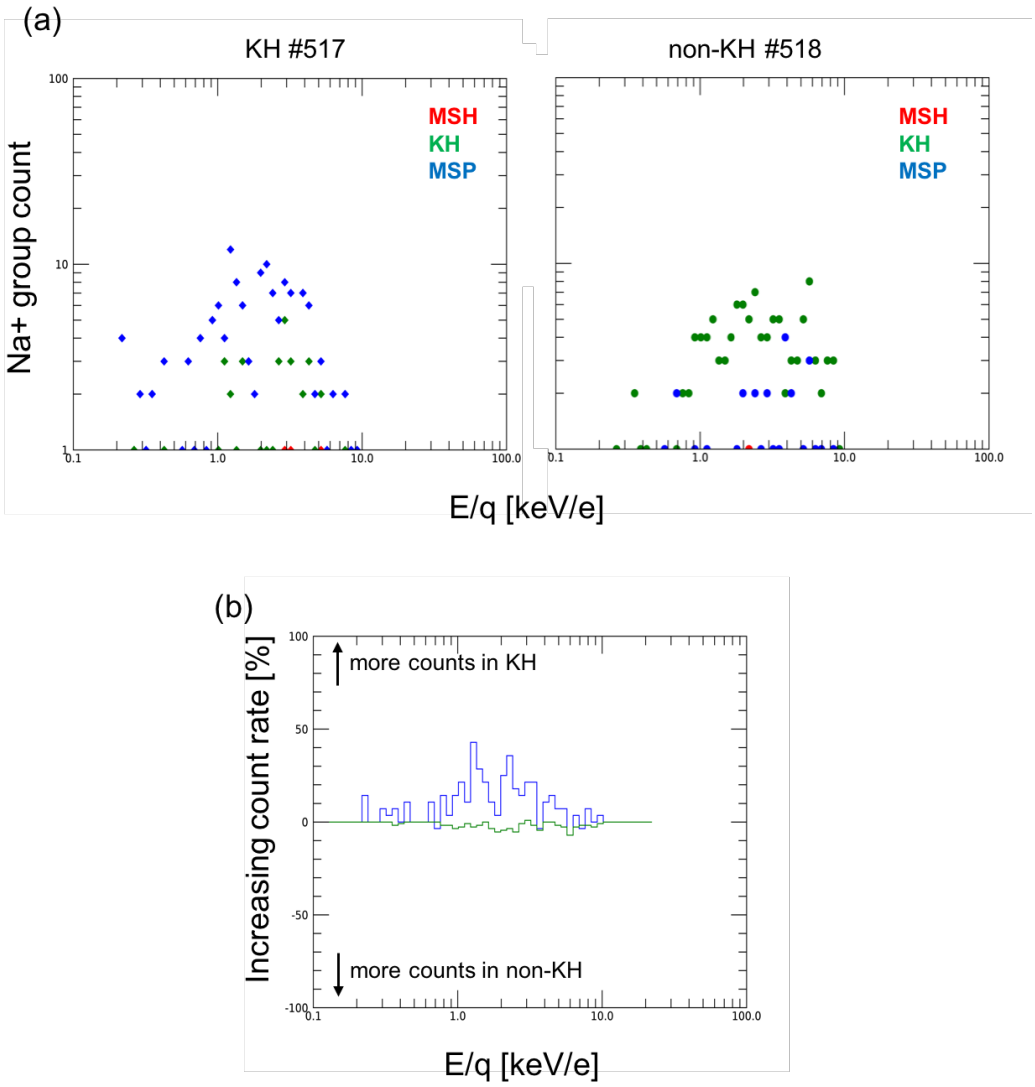

Figure 6.12 The energy-counts distribution in the same format as Figure 6.10. In this case, since there are no available counts in the magnetosheath region, the increasing count rate was not calculated in this region.

Since all 9 cases have a lack of counts in one of the three regions considered, we should do a qualitative analysis. In addition, we have 26 of the KH and 33 of non-KH events as non-paired events, which will be used for qualitative analysis in the next section.

6.2.2 Qualitative analysis of selected KH events

Investigating normalized Na^+ PSD behavior and energy-count distribution of all 9 KH event sets provide us with qualitative characteristics. The restricted criteria for the data selection (i.e., FIPS clock angle limitation, removing data having unclear fluctuations) must bring us reliable results whether there is an interesting feature or not. In Figure 6.13, we show the average of normalized Na^+ PSD behavior, which is calculated by taking the sum of all PSD behavior and dividing by 9 (the number of KH sets) is shown. Even in cases that do not have any PSD points at certain energy bins, averaged Na^+ PSD behavior should show small value at those energy bins. Figure 6.13(a) shows the average of normalized Na^+ PSD behavior for 9 KH event sets. Because of the differences in the Na^+ group count, smoother Na^+ PSD behavior can be seen in the KH event than in the non-KH event. In the KH event, Na^+ PSD behavior in the KH duration (green) and in the magnetosphere (blue) seem to have the same trend. Only the red line, representing the Na^+ PSD behavior in the magnetosheath region shows a different steeper slope. On the other hand, the magnetosheath Na^+ PSD behavior (red) in the non-KH case shows similar slope as the others. The average of normalized Na^+ PSD behavior in each region is compared between the KH and non-KH events in Figure 6.13 (b). The rightmost panel shows the matched slopes for energies above 2 keV/e and below 700 eV/e between the KH and non-KH events. If we take an average by dividing by the number of countable points of all 9 event sets, the difference between the energy area from 700 eV/e to 2 keV/e will be small (the rightmost panel in Figure 6.14). Furthermore, the KH region has large Na^+ counts in both the KH and non-KH events. The slopes of KH and non-KH events in Figure 6.13 (b) shows small differences. Even though we re-calculate the average with the number of countable points, there is no significant difference between the KH and non-KH slopes (center panel in Figure 6.14). This difference may imply that high energy particles (> 2 keV/e) may be decelerated to lower energies due to KH vortices, or picked up sodium ions may be accelerated up to 2 keV/e.

Figure 6.15 shows the average of the increasing Na^+ count ratio for all 9 cases. They are calculated in the same way as previously explained. It is clear that Na^+ counts increase with the existence of KH waves in the region of the KH and in the magnetosphere.

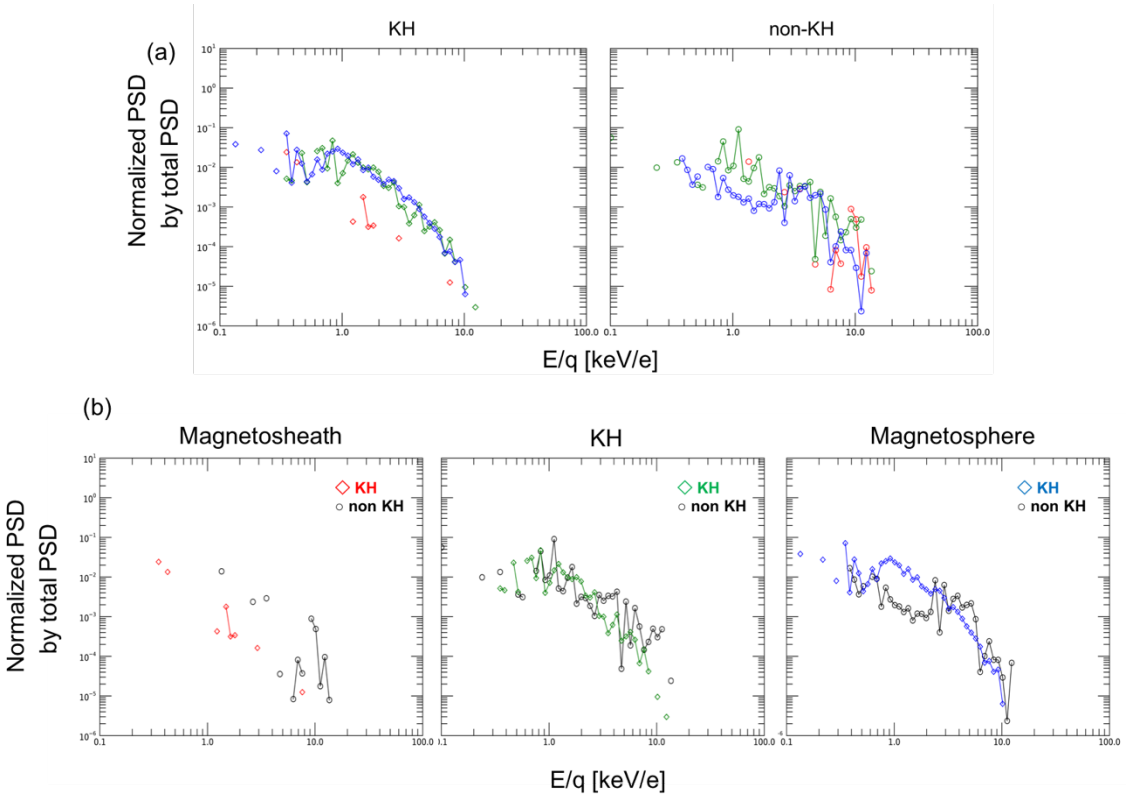

Figure 6.13 The average normalized Na^+ PSD behavior for all 9 KH event sets. (a) Comparison between each PSD behaviors for each region in one orbit. (b) Comparison between the KH and non-KH behaviors in each divided region.

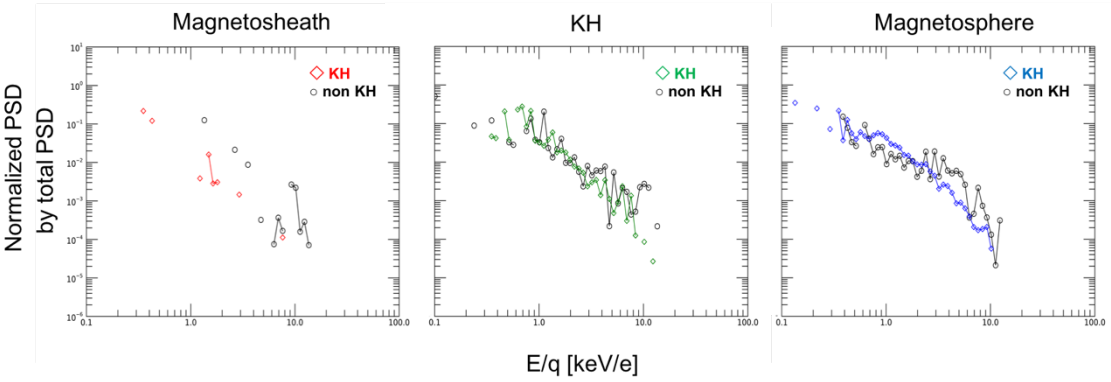

Figure 6.14 The average normalized Na^+ PSD behavior in each region for 9 KH event sets in the same format as Figure 6.9.

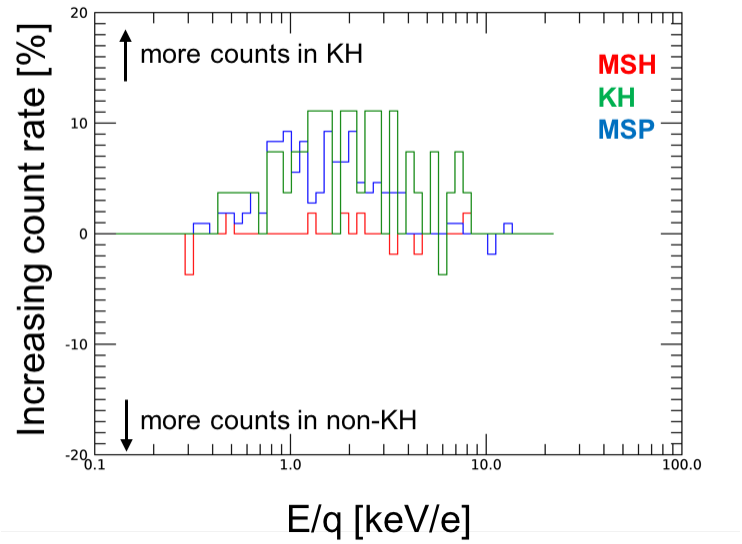

Figure 6.15 Increasing Na^+ count rate for all 9 KH event sets.

6.3 KH events in the nightside magnetopause crossing

Because the KH waves are frequently detected and FIPS detected large counts in the night-duskside of the magnetopause, all magnetopause crossing data collected during the entire orbital phase is analyzed here to obtain more available data.

Since previous studies have reported that there is a certain frequency band for the KH waves, the bandpass filter is used for the KH identification in this study.

Detailed data selection procedure as follows:

(1) Select all orbit with the magnetopause crossing within +/- 30 degree for latitude in the dusk-night side (19LT - 21LT) events

(2) Using bandpass filter (0.01 Hz – 0.1 Hz), we remove data if they do not show any oscillation during its data period

(3) Removing Flux Transfer Events (FTEs), Mirror mode wave, magnetopause fluctuation data by the visual inspection

(4) Identifying the magnetopause crossing time using both Minimum Variance Analysis (MVA) method and the visual inspection

(5) Check periodicity by the visual inspection

In addition to the above procedure, the same criteria mentioned in Section 6.2 is used for the analysis. Data is collected from January 1, 2012 to April 30, 2015. Initially, 598 data follow criteria (1). By applying other criteria ((2) to (4) in above procedure) to identify KH signatures, we end up with 35 KH events including the same events from the SG events. The breakdown of 35 KH events is: 8 of them in 2012, 12 in 2013, 14 in 2014, and 1 of them in 2015, respectively. Removing inappropriate data, such as the data not having any Na^+-group counts, or the southward magnetic field in the magnetosheath region, we analyze all 27 remaining KH event. After this selection, we are confident to have clear magnetopause crossing signatures and enough available Na^+-group count in FIPS data. A catalog for all KH event can be seen in the Appendix. 27 KH events and 49 adjacent non-KH events are selected. Especially, selected events after March 30, 2013 appears newly since no one has analyzed yet.

Because some of the data is missing for the considered period of analysis, for example the MP crossing point is too close to the end of the data period, we have removed these cases. By checking the FIPS clock angle, we remove data which outside of the degree range between 180 – 270°. Finally, we will be analyzing 22 KH and 36 of the non-KH in this thesis. The rest of applicable data, Na^+-group counts in the magnetosheath are increasing with increasing average Bz component in the magnetosheath (Figure 6.16). This feature is consistent with that shown in Figure 6.6. Although some data are the same from the SG events, the same correlation can be seen.

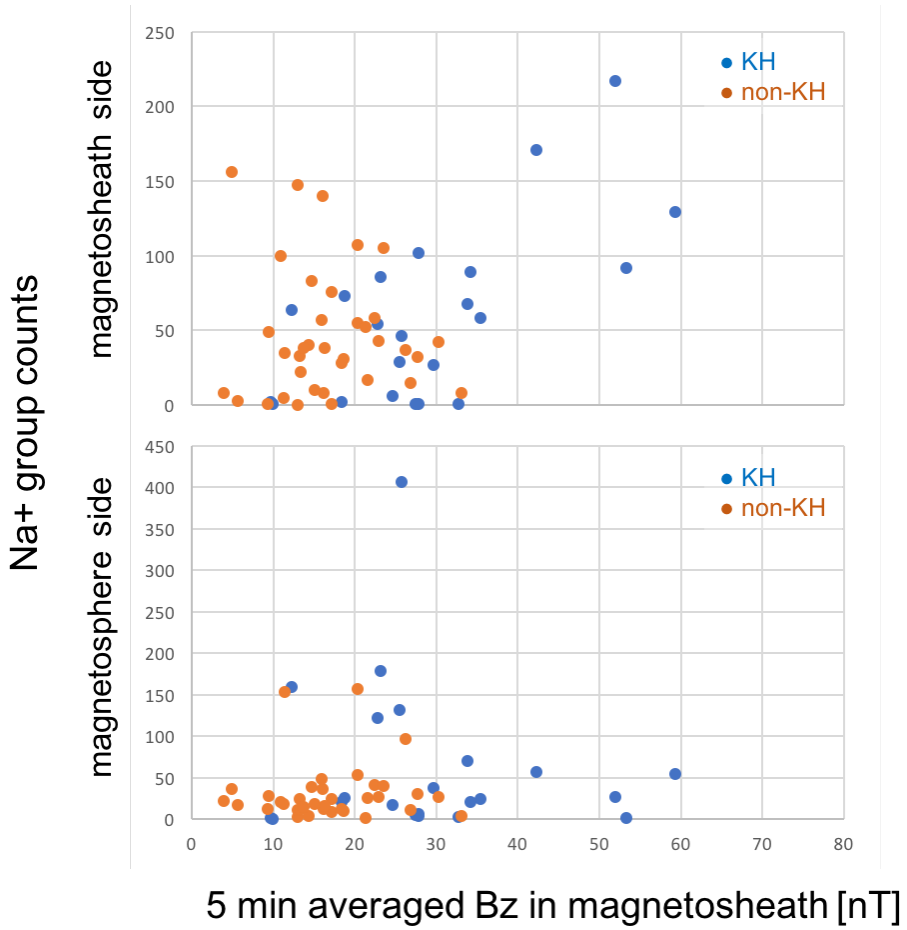

Figure 6.16 Count distribution of Na^+-group ions as a function of 5 min averaged Bz in the magnetosheath. The format is the same as Figure 6.6.

Following the same procedure, being done in the previous section, the data including zero counts of Na^+-group in one side is removed. Then, we paired the considered KH orbit and its adjacent orbits, obtaining 16 KH event sets. Some of the data from SG events are already analyzed and they may lead to the same characteristics found in Figure 6.15, so we removed those cases. The number of final data considered is 5 KH cases. Figure 6.17 shows the qualitative results of the increasing Na^+ count rate for these cases. This also shows the large counts in the magnetosphere region when we have KH waves. Figure 6.18 shows the comparison of average normalized Na^+ PSD behavior in each region for 5 KH event sets. The differences are shown in the rightmost panel in similar way as Figure 6.14.

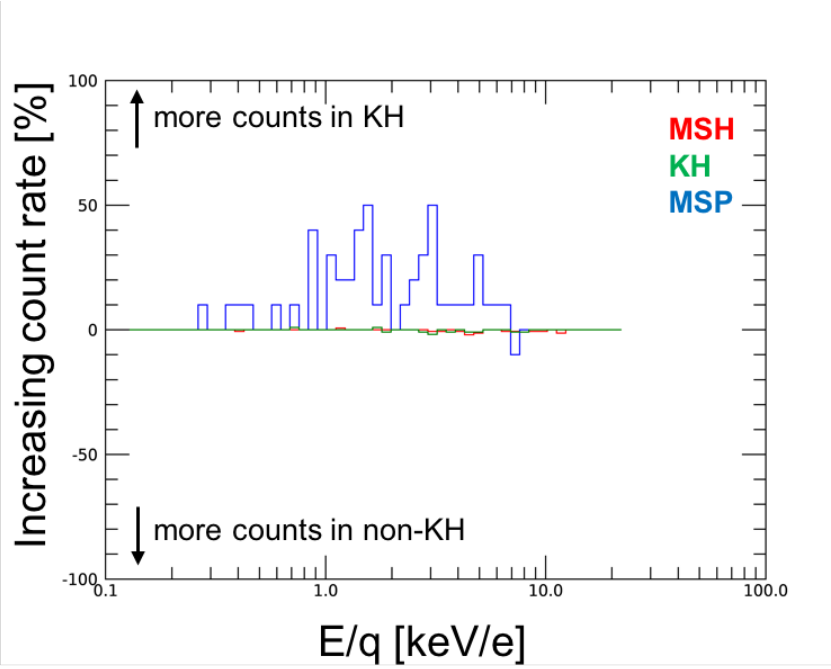

Figure 6.17 The Increasing Na^+ count rate of the KH event pair. Clearly Na^+ group counts in the magnetosphere region increase when the KH waves are detected.

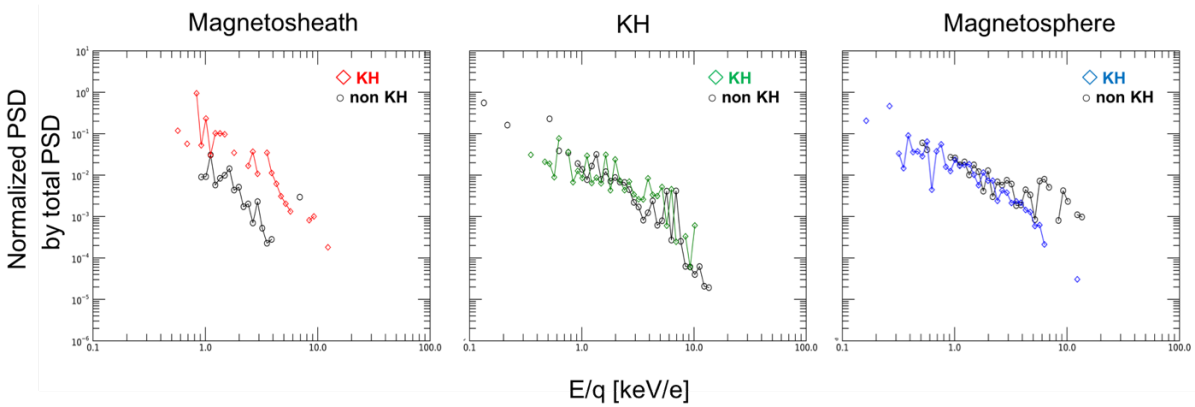

Figure 6.18 The average of the normalized Na^+ PSD behavior for 5 event sets. Similarly, the Na^+ PSD behavior in the magnetosphere shows differences in high energy region.

6.4 Possible mechanisms

By combining the KH event set from SG events and the nightside MP crossing events, the qualitative analysis of whole KH events is presented in Figure 6.19. In Figure 6.19, we found two large differences :

(A) Na^+ PSD behavior difference can only be seen in magnetosphere region. (upper panels)

(B) Large counts in KH and magnetosphere region when we have KH waves. (bottom panel)

A similar trend on the Na^+ PSD behavior in the magnetosheath and KH region can be seen in Figure 6.19(a). However, the rightmost panel, especially above 2.0 keV/e, shows different trends between the KH and non-KH events. Figure 6.19(b) shows the increasing count rate in each region between the KH and non-KH events. The large Na^+ counts are measured in the KH and MSP region with the existence of KH waves. Though the Na^+ counts in the KH region show significant increase when the KH waves are detected, normalized Na^+ PSD behavior has the same trend between the KH and non-KH events. These properties are already shown in Figure 6.14 (analysis for the SG events) and 6.18 (analysis for the all nightside MP crossing events).

From the previous chapters and Figure 6.19, we wonder on the mechanisms behind some of the characteristics found here: why do we have the large counts in the magnetosheath region with increasing Bz? Why are there the large counts in the magnetosphere region when we have KH waves? Why do we see differences in the Na^+ PSD behavior only in the magnetosphere? Are the results consistent with our numerical results?

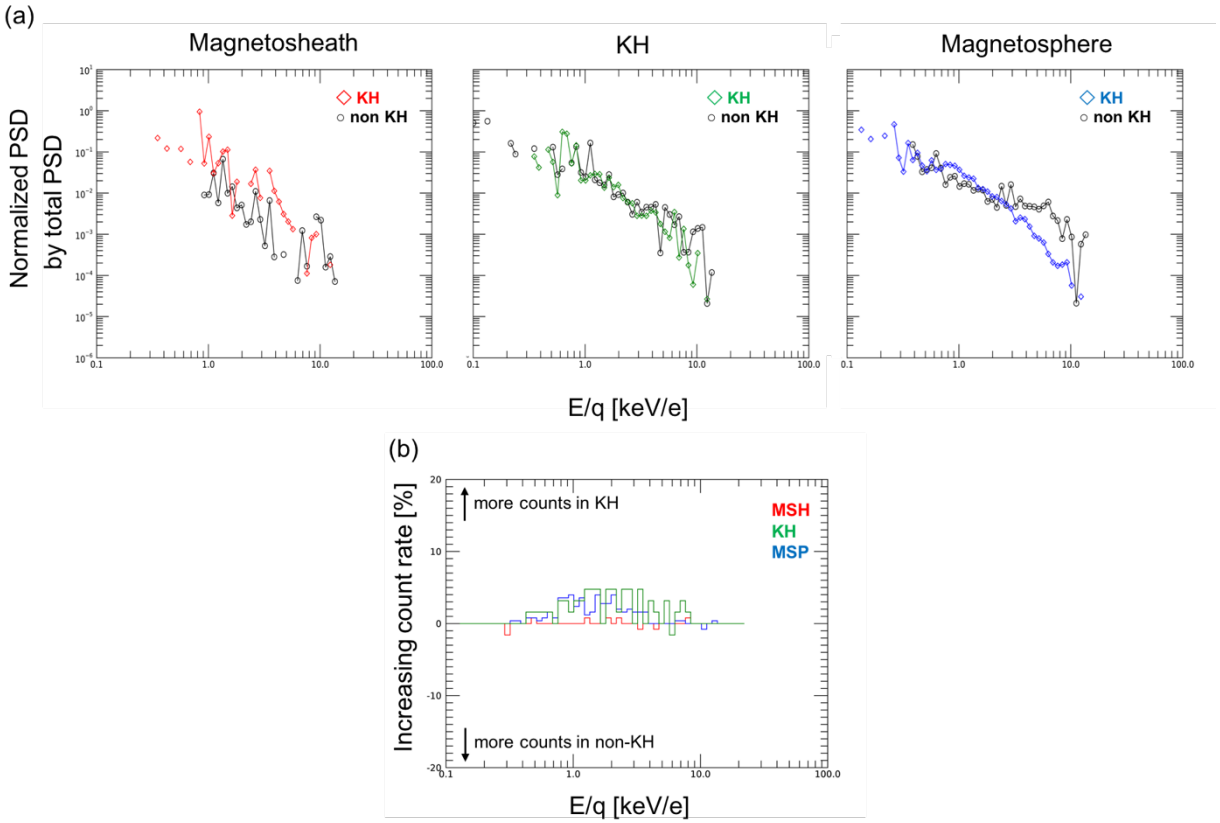

Figure 6.19 (a) Average of normalized Na^+ PSD by the available number of the data at each energy bin. (b) Increasing count rate in each region between the KH and non-KH events.

First of all, we note that all data considered in this study is brought from the night-duskside magnetopause. In that region, ions with energies above 100 eV/e are incoming from both the magnetotail and the exosphere. Particles from the magnetotail region, they are accelerated due to the dawn-to-dusk electric field or due to the dynamics in the magnetotail. They likely have a large energy (several keV), which can be detected by FIPS [*Delcourt et al.*, 2003]. On the other hand, Ions (Na^+-group) from the exosphere have few eV when they are picked up. Because the exosphere extends to few R_M, exospheric neutrals can be picked up around the night-duskside magnetopause. Such picked up ions have only few eV when it is picked up and FIPS cannot detect them. If they are accelerated somehow, particles gain energy and FIPS can detect them. This source can be considered also in the dayside magnetopause. In this study, we selected to analyze only data in the nightside because the FIPS data in the dayside shows low counts of Na^+-group. This low count data cannot provide enough information to examine the KH role at this time. Thus,

the former source is considered as a dominant population in the night-duskside magnetopause. When we try to understand the physical mechanism behind obtained characteristics and compare with our numerical results, this dominant population incoming from the magnetotail makes us difficult to pick up the effect of the KH development. Moreover, if we revisit Figure 5.11, the less ion energization is found in the duskside under northward IMF. These conditions may not allow to change the energy distribution in the considered region.

The difference (B) can be discussed considering two explanations: (1) According to our simulation results, the convection electric field prevent to transport of ions from the magnetosphere to the magnetosheath even though they are energized by the KH development. This effect of the convection electric field on the transport of ions is seen without the KH development. Also, particles near the magnetopause can stagnate within the KH vortices. Considering results of larger counts ~ 1 keV/e with the existence of KH waves, we have two possible ideas: The exospheric neutrals are picked up or low energy ions already exist in the vicinity of KH waves, both are accelerated due to the KH development. Or particles with several keV are decelerated due to the KH development. Although this acceleration/deceleration should modify the Na^+ PSD behavior, we do not see drastic changes in it between KH and non-KH events. If we assume that the dominant population is the ions with several keV incoming from the magnetotail and the number of such accelerated/decelerated particles is rather small, we can understand not having drastic changes in the Na^+ PSD behavior. (2) The other suggestion explaining such a large count in the KH case is that the large Na^+-group population can lead to the growth of the KH instability. This is discussed in *Fujimoto et al*. [2007], however this suggestion cannot explain the Na^+ PSD behavior difference.

Furthermore, we can discuss possible mechanisms to explain the different Na^+ PSD behaviors in the higher energy region (> 2.0 keV/e) in the magnetosphere. When we have KH waves, the value of normalized Na^+ PSD decreases. According to our simulation results, if particles have a similar energy to the background field (ε_{ExB}), particles may be decelerated depending upon the direction of particle motion and the electric field (see blue oblique in Figure 4.4). *Gershman et al*. [2015] estimated solar wind speed for each KH event case and found a velocity range from 360 km/s to 490 km/s. However, sometimes solar wind speed cannot be estimated because of the data conditions. To simplify here we will consider a solar wind speed from 350 km/s to 500 km/s. If we take 350 km/s as the bulk velocity of background proton in the magnetosheath region, its average energy is calculated by $\frac{1}{2}m_{Na}v_{bulk}^2$ and it is about 1.47 keV/e. If we use 500 km/s, it becomes about 3.0 keV/e. Since the difference of Na^+ PSD behavior is seen for energies above 2 keV/e, it can be said that the energy calculated by the estimated solar wind speed is comparable. In this study, though we could not obtain detailed electric field components from FIPS

observations, this may suggest that the difference on the normalized Na^+ PSD behavior is brought by the deceleration due to the KH vortices. Decelerated particles cannot be transported to the magnetosheath, which agrees with the large Na^+ counts in the magnetosphere region.

Two different scenarios explaining the large Na^+ group counts in the magnetosphere cannot be distinguished. If we consider it with the Na^+ PSD behavior, deceleration and stagnation, and transport are all suitable scenarios which are illustrated in Figure 6.20. Please note that this are not the only one mechanisms but other mechanisms could be considered.

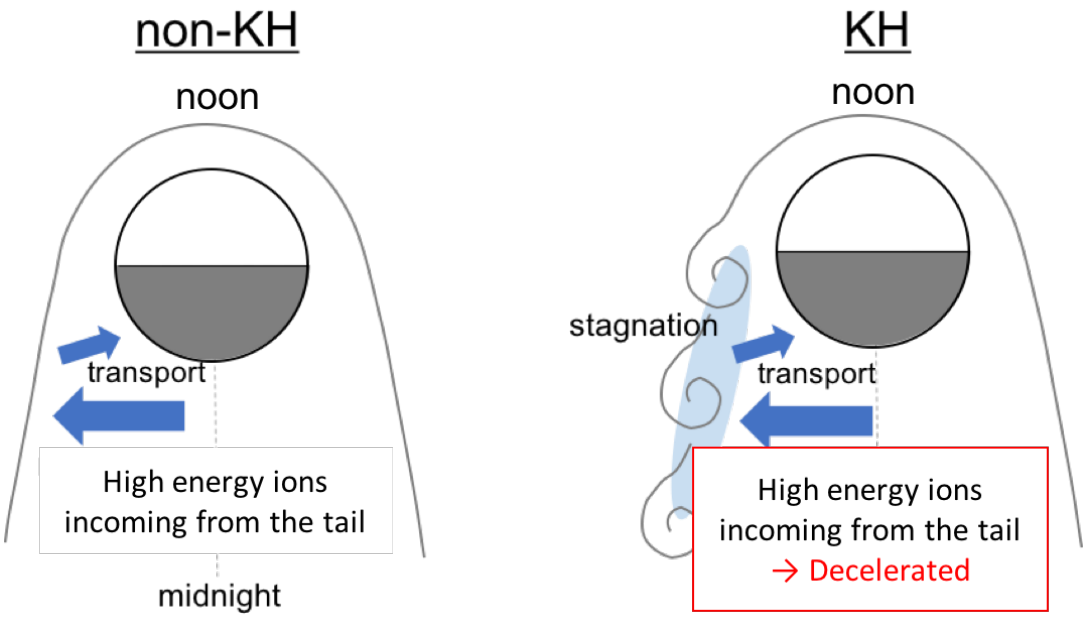

Figure 6.20 Illustration of particle behavior in the vicinity of KH vortices. Under the presence of KH vortices, deceleration and stagnation can be expected. As a result of these roles, different Na^+ PSD signature can be seen and large counts in the KH and magnetosphere region are explained.

6.5 Chapter summary

In order to examine a new KH role introduced in Chapters 4 and 5, FIPS instruments aboard MESSENGER have been used. Since previous studies have provided a KH event list for a former half of MESSENGER mission (SG events), the rest of applicable data with an orbit on the nightside (19LT-21LT) magnetopause crossing has been additionally analyzed.

The differences of both the Na^+ PSD behavior and the energy-count distribution between the KH and non-KH event have been investigated in Chapter 6. By focusing on the behavior of heavy ions of planetary origin, Na^+-group, some interesting features have been revealed.

(1) KH instability likely occurs when Bz is stronger

The growth of the KH instability is controlled not only by the velocity shear, but also by the mass density in two regions: the magnetic field component, and the growing mode. The growth rate γ of the KH instability in the most unstable condition is as follows:

$$\gamma = \sqrt{\frac{(\boldsymbol{k}\cdot\boldsymbol{B_1})^2 + (\boldsymbol{k}\cdot\boldsymbol{B_2})^2}{4\pi(\rho_1+\rho_2)} - \frac{\rho_1\rho_2}{(\rho_1+\rho_2)^2}[\boldsymbol{k}\cdot(\boldsymbol{v_1}-\boldsymbol{v_2})]^2 + k\frac{\rho_2 g_2^* - \rho_1 g_1^*}{\rho_1+\rho_2}}$$

where k is the wavenumber of the KH instability, ρ plasma density and B the magnetic field, and g^* shows the effective gravity, respectively. (see *Elphic and Ekersh*, 1984 for detailed derivation). The small suffix (1 or 2) represents the two different regions across the boundary layer. The plus-sign of the first and third term indicates stability and the minus-sign of the second term indicates instability to the instability growth. In particular, the first term shows the stabilizing effect of the magnetic field. This term shows if there is a magnetic field component in parallel to the wave number of the KH, the magnetic field behaves as a magnetic tension and it stabilizes the instability. Thus, strong Bz leads to a less stabilized effect to the KH growth.

(2) Larger Na^+ counts in the KH region and magnetosphere region with the KH waves and different Na^+ PSD behavior in the magnetosphere region.

Two different scenarios can be considered. Though these scenarios cannot be distinguished, (A) can be the most suitable scenario for our observational results.

(A) Deceleration, transport, and stagnation

A large number of Na^+ counts could be coming from the magnetotail region with energies of several keV due to the dawn-to-dusk electric field in the nightside and/or ion dynamics in that region. On the other hand, the convection electric field in the magnetosheath in the duskside prevents the particle transport from the magnetosphere to the magnetosheath. This

mechanism should work both in the KH and non-KH cases and it creates particles stagnation inside the magnetopause. However, we have large Na^+ counts in the KH case and small difference can be seen in the Na^+ PSD behavior in the magnetosphere. We found that there is a possibility that particles may be decelerated by the electric field variations due to the KH development. This can explain the difference in the Na^+ PSD behavior in the magnetosphere and accounts for the large Na^+ counts. This scenario is the one that fits the best to our results. Because of the limited energy range and FOV of the FIPS instrument, picked up ions were not able to be detected by FIPS. By accelerating particles within the KH vortices, particles with higher energies can exist around the magnetopause. Thus, there is also a possibility to have a large number of energized particles which can be detected by FIPS. If many particles are accelerated, acceleration signatures should be seen in the Na^+ PSD behavior. If this mechanism occurs, the Na^+ PSD behavior would have a peak-like signature around the energy of the background field. According to our analysis, the background field may have an energy of 1.5 keV/e, but our results show no PSD enhancement around that value. If the number of accelerated ions is small, it is reasonable not to have drastic changes in the Na^+ PSD behavior. When we consider the dominant population in the considered region, deceleration would be the dominant process to understand the PSD behavior.

(B) A large population of Na^+- group may enhance the KH development
The propagation speed of the KH instability is given at the center of mass frame, and depends upon not only the magnitude of the velocity shear but also the mass density between two plasmas. Such an interesting feature is discussed in *Fujimoto et al*. [2007]. In our results, large counts in the Na^+-group in the KH events may support it. A large Na^+ group population can enhance the KH instability development and that is why KH waves observed. In this scenario, it is not necessary to change the Na^+ PSD behavior.

Although many restrictions in the analysis lead to the fewer available data, reliable results are obtained. Some observational results can support our numerical results. However, picking up the effect of the KH instability in the night-duskside magnetospheric flanks is difficult because of the dominant population from the magnetotail and less effect of the KH development which mentioned in Chapter 5.

Further investigation is required to understand and examined the suggested scenarios. This future study will be done by using MSA on board MIO in the future BepiColombo mission with wider FOV and energy range.

Chapter 7

Conclusions and future perspectives

7.1 Planetary ion dynamics in Mercury's magnetospheric flanks

In Chapters 4, 5, and 6, we discussed the ion dynamics in the magnetospheric flanks of Mercury using both numerical simulations and observational data collected by MESSENGER. In this study, we have especially focused on non-adiabatic energization and transport of planetary ions due to electric field variations associated with the development of KH vortices.

Developing a numerical code by combining the MHD simulation and the test particle tracing calculation allows us to trace full particle behavior. This results in a detailed discussion of the ion dynamics in the vicinity of KH vortices.

In Chapter 4, we showed that the electric field variations during the development of the KH instability affect the ion gyration motions, leading to the non-adiabatic energization of ions. Previous studies of non-adiabatic energization have focused on the effects of spatial and temporal variations of the magnetic field. Here we introduced a new type of non-adiabatic energization caused by both the temporal and spatial electric field variations, called ***E*** burst. While *Rothwell et al*. [1994] reported that the phase bunching possibly occurs due to the electric field gradients, we especially characterized systematic energy gain due to the ***E*** bursts. By adopting a two-step approach to understand the ion dynamics step by step, the test particle tracing calculations were performed on a fixed KH field configuration obtained from an MHD simulation at first, followed by conducting them in time-varying KH fields.

First, we found that the occurrence of non-adiabatic energization depends on the initial perpendicular energy of ions to the magnetic field line but not on the total ion energy. Secondly, we found the three-branch pattern on the energization map. If the energy of ions before experiencing the ***E*** bursts was smaller than the energy calculated with the maximum ***E***x***B*** drift speed when they encountered the ***E*** burst along the particle path, $\varepsilon_{ExB} = \frac{1}{2} m v_{ExB,max}^2$, ions may be accelerated up to ε_{ExB}, as shown by the 1st branch on the map (the branch encircled in red in Figure 4.4). The 2nd branch could be observed where the initial perpendicular energy of ions was approximately ε_{ExB}. Ions could be decelerated depending on the relationship between the particle

motion and the orientation of the electric field (that encircled in blue). When ions initially had a larger energy than the ε_{ExB}, no acceleration occurred (encircled in green). In addition, we investigated how effective the $\boldsymbol{E}$ burst was. The time scale and amplitude of the $\boldsymbol{E}$ burst were discussed. We found that the amount of net energy gain increased with increasing amplitude of the $\boldsymbol{E}$ burst. As for the effect of the time scale of the $\boldsymbol{E}$ burst, resonance-like features could be observed. When the $\boldsymbol{E}$ burst had approximately the same scale as ion's gyroperiod, the ion was significantly accelerated and/or decelerated. In this study, we characterized the non-adiabatic energization due to both spatial and temporal electric field variations for the first time. Such an acceleration and/or deceleration could be expected due to the arbitrary electric field variations. The electric field variations could happen not only due to the KH growth but also via other mechanisms.

After the investigation of the general characteristics of the acceleration mechanism due to the electric field variations in Chapter 4, realistic field configurations of the Hermean environment and ion parameters were considered in Chapter 5. In Chapter 5, we focused on the effects of the orientation of the convection electric field on the ion energization and transport throughout KH vortices in the magnetospheric flanks of Mercury. For example, the electric field pointing away from the magnetopause could be observed on the dawnside, and toward to the magnetopause on the duskside under northward IMF. We investigated how the orientation of the convection electric field controlled the ion dynamics.

By injecting 10,000 test ions with a specific total initial kinetic particle energy and a random phase angle, a quantitative analysis of the ion energization and transport was performed. We examined the ion dynamics in a time-varying KH field on both dawn and dusk sides so that we could explore the effect of the large convection electric field orientation. A variety of ions of planetary origin (H^+, H_2^+, O^+, Na^+, and K^+) were injected as picked-up ions at three different injection times corresponding to different stages of the KH development (at the beginning, in the linear growth phase, and in the nonlinear growth phase of the KH instability). For the solar wind plasmas, two species (H^+, He^{++}) were considered. They were injected on the $\boldsymbol{E}$x$\boldsymbol{B}$ frame at the beginning of the MHD calculation. Both northward and southward IMF conditions were considered.

Common features in both dawn, dusk, northward, and southward IMF cases were observed on the energization of picked-up ions in the magnetosphere. Because the magnetosphere region had a smaller convection electric field, picked up ions could experience a larger intensification of the electric field ($\boldsymbol{E}$ burst) in KH vortices. If there was no development of the KH instability, no energization occurred. In contrast to ion energization, which commonly occurred in all the cases, ion transport depended on the orientation of the magnetosheath electric field. The ions picked up

in the magnetosphere were transported across the magnetopause on the dawnside under the northward IMF but no transport occurred on the duskside. On the other hand, the ion transport was observed on both the dawn and dusk sides under the southward IMF. When the magnetic moment of an ion changed ten times larger than the initial value, we called it non-adiabatic. According to the detailed analysis in Chapter 5, the ion transport basically depended on the value of the magnetic moment, i.e., the amount of energy the ions gained. On the contrary, ions picked up in the magnetosheath were generally not accelerated because they did not experience a large intensification of the electric field. Lighter ions moving with following background protons could be accelerated and transported as exceptional cases.

Comparison of the results obtained in Case 1 (northward IMF) and Case 2 (southward IMF) highlighted the importance of the convection electric field orientation. The results in Case 2 showed a larger number of ions accelerated and transported than those in Case 1. In Case 1, the electric fields in the magnetosheath and magnetosphere directed oppositely (for instance, at dusk, the electric field in the magnetosheath and the magnetosphere were both toward to the magnetopause). We had the electric fields in the same direction in Case 2, i.e., at dusk, the electric field in the magnetosheath pointed away from the magnetopause and that in the magnetosphere pointed towards the magnetopause. When the KH vortex evolved over time, the electric field also changed its configuration, i.e., rotating components appeared within the vortex. The opposite-directed electric fields (Case 1) could develop the uni-directed electric field from the center of the vortex to the outer or vice-versa, which was the same direction as the field initially had. The same-directed electric fields (Case 2) also made a similar electric field configuration within the vortex, however it could contain the electric field directing oppositely to the initial electric field configuration. In this case, ions could experience variable-oriented electric field during its gyromotion and thus, the acceleration and/or deceleration likely occurred.

Our results in Chapter 5 had some implications for the spacecraft observation. Because of the balance of the transport and energization, energized ions stagnate in the duskside magnetosphere, while less dense energized ions exist in the dawnside magnetosphere under northward IMF. This can be expected to be observed by the spacecraft. Regarding the behavior of picked up ions in the magnetosheath, even though they are picked up being far from the magnetopause, it is thought that they may penetrate into the magnetosphere due to the large Larmor radius of such picked up ions. Our results suggested that this occurred at the duskside under northward IMF and that there was no penetration at the dawnside. In contrast, the ion transport was observable in both dawn and dusksides under southward IMF.

We examined the ion energization and transport under purely northward and southward IMF without any other components. Other components of the magnetic field may enhance the transport

and/or energization of ions. However, we focused on the magnetospheric flanks where the z-component of the magnetic field was dominated, and general features of the ion dynamics revealed here would be the same even if we have other components.

We also investigated solar wind plasma entry (H^+ and He^{++}) and found that the behavior of solar wind plasmas was MHD-like. We also found that solar wind entry occurred only near the magnetopause being determined by the size of KH vortex. The acceleration mechanisms are the same that ions of planetary origin experience, fine structures due to the breaking of KH vortices at the later stage of the development of the KH instability, corresponding to the small scale of the motion of lighter ions, accelerated solar wind plasmas. This non-adiabatic acceleration of solar wind protons would lead to the violation of the MHD approximation. Because the initial settings of injected protons and background MHD protons were not the same, we could not show a certain time of the violation of the MHD approximation. The effect of ion kinetics should be taken into account in the later stage of the KH instability.

The numerical results in Chapters 4 and 5 were compared to in-situ measurements from MESSENGER in Chapter 6. We analyzed data collected by FIPS aboard MESSENGER in entire orbital phase from March 11, 2011 through April 30, 2015. We specifically analyzed the duskside magnetopause crossing event under northward IMF by referring to previous KH studies. FIPS is the time-of-flight type particle analyzer with an energy range from 100 eV/e up to 13 keV/e for data analysis. The spacecraft was designed and protected against strong solar heating, which caused FIPS to have a limited field of view (FOV). Limited energy range and FOV made it difficult to investigate particle acceleration. We started with the phase space density (PSD) distribution of Na^+-group ions. Because our numerical results indicated no energization without the development of the KH instability, and also that the ion energization occurred with KH vortices under northward IMF, we expected some differences on the Na^+ PSDs between the KH and non-KH events. In order to compare the KH event and non-KH event, first, we collected all KH signatures including events reported in previous papers. Because the Na^+ PSDs should be compared in a similar region of the Hermean magnetosphere, we took adjacent orbit before and after the orbit of the KH events. We compared the normalized Na^+ PSD behavior of all orbits that fulfilled our criteria for the comparison. As a result, we could not find any significant difference in the Na^+ PSD behavior between KH and non-KH events. This could be because of the limited FOV and energy range.

The other possible observation facts for the energization and transport within the KH vortices was the density (or counts) of the Na^+-group. As we described in Figure 5.10 and Figure 6.20, highly energized ions could stagnate in the duskside magnetosphere. Because picked up ions have an initial energy of a few eV, they could not be detected by FIPS immediately after their ionization.

Acceleration due to the KH field resulted in higher energy ions, which could be detected by FIPS and were stagnated inside the magnetopause. This results in FIPS observing a high Na^+ population with the KH events. Our analysis showed that Na^+ counts by FIPS increased with the existence of KH waves. This could be explained by the ion energization and transport via KH vortices. Meanwhile, such a large population of sodium ions could be explained differently. Previous research pointed out that the dense Na^+ population leads to the development of the KH instability. Our observations showed that Na^+ occurrence increased in KH vortices. It remains to be determined whether or not those ions play a role in triggering the development of the KH instability.

Our study indicated that ions would be accelerated significantly inside the magnetosphere with KH vortices. Previous studies of non-adiabatic energization have shown that such non-adiabatic ions could sputter the planetary surface. Such a surface sputtering produces a secondary neutral atmosphere making the exosphere. The energized ions predicted by our study could also sputter the planetary surface and they lead to the space weathering and an important role of ions of planetary origin in the Hermean environment. Since we use the simple KH models and limited input parameters, such as an absence of other components of the magnetic field, and of ions already accelerated, we need to have further investigation by global simulations. However, general characteristics of ion transport and energization should be the same.

Further investigation with FIPS data will be done in the future, such as analysis of southward IMF KH case. Also, MIO/BepiColombo has an exhaustive plasma particle analyzer payload (MPPE consortium), having a wider energy range and FOV than FIPS. Low energy ions will be measured by MSA and MIA, which will provide the information on ions of planetary origin with wider energies in the three-dimensional field. Our simulation results will be proven by future MIO observations of direct measurement of picked-up ion acceleration/deceleration.

7.2 Open questions awaiting BepiColombo measurements

BepiColombo was successfully launched on the October 19, 2018 and its seven year journey to Mercury has just begun. The major discovery of Mariner-10 was the existence of Mercury's intrinsic magnetic field. After Mariner-10, some detailed information of the Hermean environment and surface information was collected by the MESSENGER spacecraft, however, a lot of unanswered questions remain. BepiColombo, a joint mission between ESA and JAXA, has two sets of spacecrafts to investigate the mysteries of this innermost planet in our solar system. Revealing the Hermean environment is an important part of discovering the history of our solar system.

MIO, mainly developed by JAXA, is one of the two spacecrafts of BepiColombo. MIO's objective is to observe the planetary magnetic field, exosphere released from the surface, interplanetary space, and its variation and physics. Large topics related to our study are whether or not Mercury's magnetic field, magnetosphere, and exosphere interact with the solar wind and also how much important heavy ions in the Hermean environment are.

Since Mercury is the terrestrial magnetized planet, we expect similar phenomena to occur on Mercury as on Earth. Various instruments aboard MIO will approach such phenomena and raise further questions. The plasma particle analyzer, packed in the MPPE consortium, is one such instrument. For lower energy analyzers for heavy ions of planetary origin and solar wind plasmas, we have MSA and MIA. MSA is a time-of-flight spectrometer that will collect the information on the plasma composition and ion distribution functions [*Delcourt et al.,* 2009b] among the MPPE sensors. MSA has enhanced mass resolution capability with a three-dimensional field of view, which will allow us to identify in detail various materials and species of planetary origin and their propagation and provide unprecedented information about the Hermean environment. MSA has two detectors to obtain the plasma distribution and composition: Linear electric field (LEF), which will provide high mass resolution data using an exerted technique, and the other is straight-through (ST), which will provide high count distributions. A schematic illustration of MSA is shown in Figure 7.1, and detailed information can be found in *Delcourt et al.* [2009b]. These two different types of observation modes are used in response to the objectives of the present study.

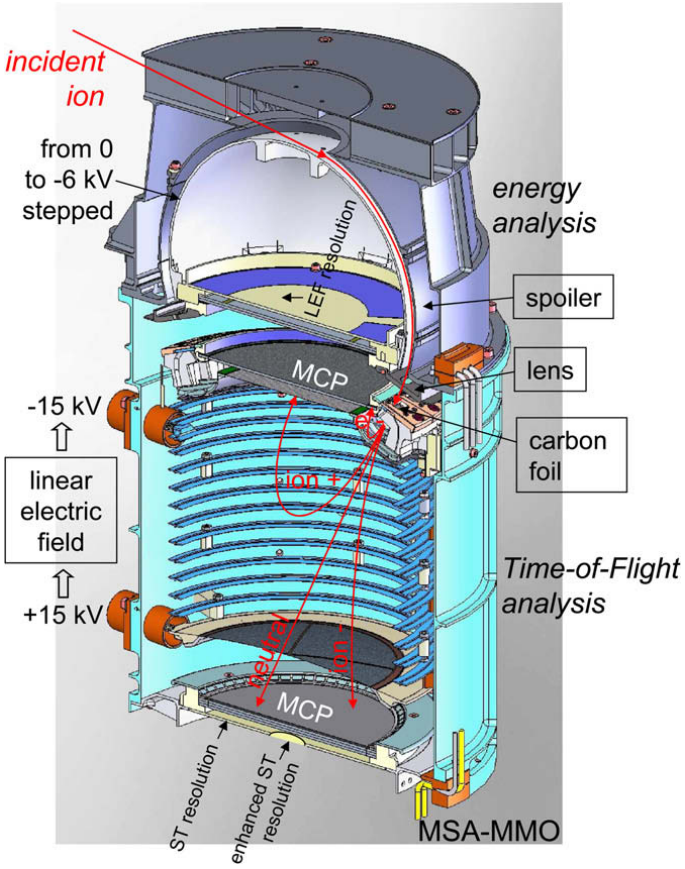

Figure 7.1 Schematic illustration of MSA principle of operation, adapted from *Delcourt et al.* [2009b]

Large differences between the magnetospheres of Earth and Mercury include their size and plasma components. It is theorized that the heavy ions of planetary origin play important roles in the magnetospheric dynamics at Mercury, and thus physical phenomena would be expected to be different than those we observe for Earth. However, its density of the population of heavy ions and its three-dimensional distribution have not yet been revealed. MSA aboard MIO will collect various ion components with a high mass resolution and a wider energy range in the three-dimensional field of view. This will help us to understand general space plasma physics for Mercury. In addition to observation by only MIO, simultaneous measurements by both sets of spacecrafts of BepiColombo are planned during its orbital phase.

In our study, though the ion acceleration and transport were demonstrated numerically, we could not find any significant difference in the Na^+ PSD between the KH and non-KH events because of the limited FIPS conditions. Detection of ions with a lower energy, about a few eV, is allowed by MSA and thus, the ion acceleration is expected to be directly measured. The wave propagation along the magnetopause is also a key interest for the development of the KH instability. It would be provided by the conjunction observation.

Mariner-10's discoveries during the three flybys of Mercury impacted all researchers and exceeded all expectations for the Hermean environment. MESSENGER's exploration of Mercury has led to many new insights and global perspectives on Mercury, such as its surface, exosphere, and magnetosphere as a coupled system around the planet. Though two previous spacecraft have brought as much information as they can, limits to our knowledge and understanding due to the capabilities of these spacecraft have revealed themselves at the same time. Further investigations are expected to be carried out by the BepiColombo mission. BepiColombo will initiate a new era of intensive study on Mercury, including the surface, exosphere, and magnetosphere and their mutual interactions. From the perspective of magnetospheric physics, several new types of instruments were selected in addition to the similar types of them with a higher resolution and a wider range of FOV and energy. New major discoveries are expected to be brought by BepiColombo and understanding the ion dynamics of Mercury will also lead to a better understanding of the magnetospheric dynamics of Earth.

Appendix

All KH event list with information of adjacent orbits in this study.

Please note that the orbit number in red shows the KH event.

1. SG event list
2. KH event from MP crossing in 2012
3. KH event from MP crossing in 2013
4. KH event from MP crossing in 2014
5. KH event from MP crossing in 2015

1. SG event list (1/4)

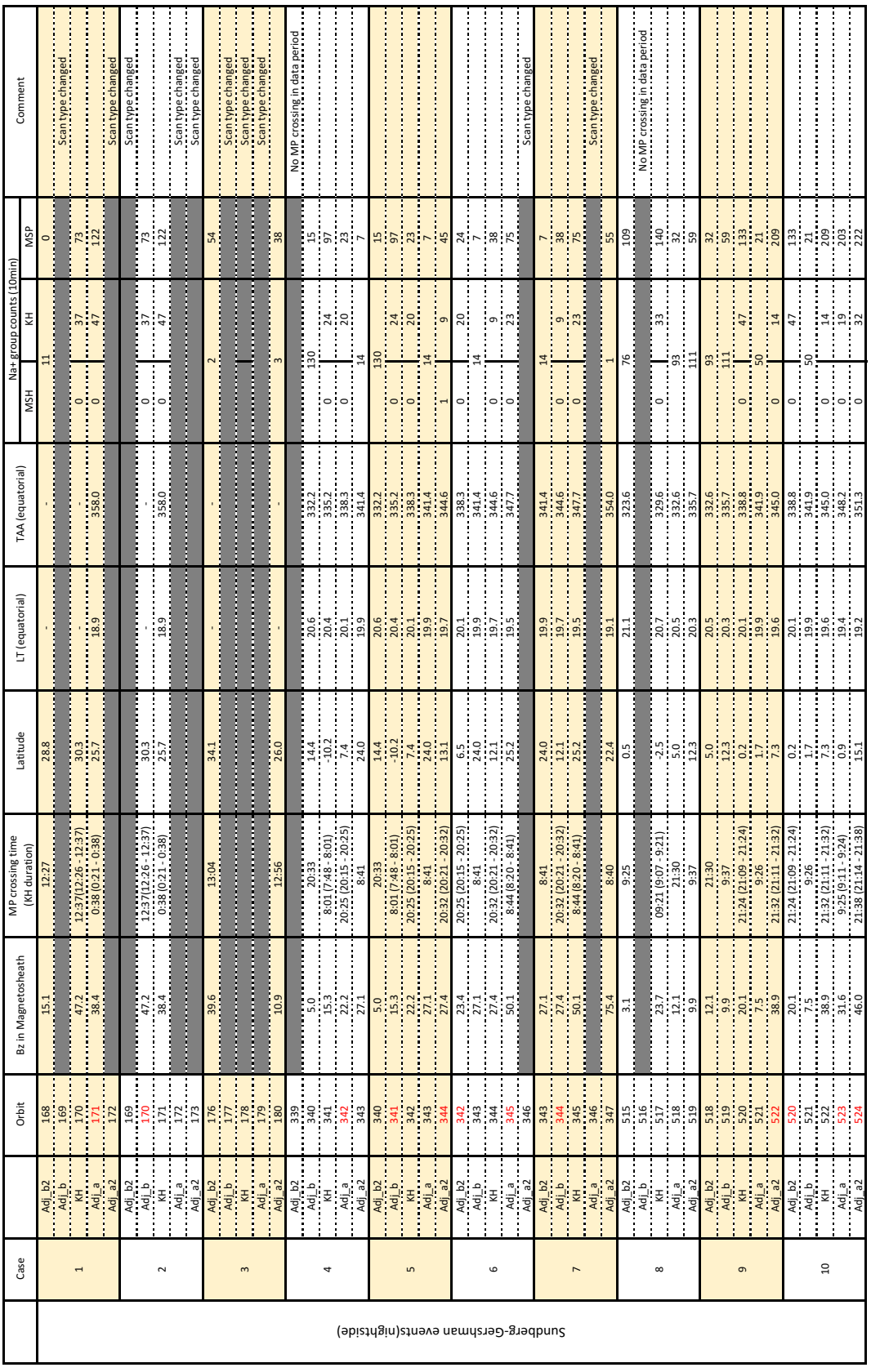

Sundberg-Gershman events(nightside)	Case		Orbit	Bz in Magnetosheath	MP crossing time (KH duration)	Latitude	LT (equatorial)	TAA (equatorial)	Na+ group counts (10min) MSH	Na+ group counts (10min) KH	Na+ group counts (10min) MSP	Comment
	1	Adj_b2	168	15.1	12:27	28.8	-	-	11		0	Scan type changed
		Adj_b	169									
		KH	170	47.2	12:37(12:26 - 12:37)	30.3	-	-	0	37	73	
		Adj_a	171	38.4	0:38 (0:21 - 0:38)	25.7	18.9	358.0	0	47	122	
		Adj_a2	172									Scan type changed
	2	Adj_b2	169									Scan type changed
		Adj_b	170	47.2	12:37(12:26 - 12:37)	30.3	-	-	0	37	73	
		KH	171	38.4	0:38 (0:21 - 0:38)	25.7	18.9	358.0	0	47	122	
		Adj_a	172									Scan type changed
		Adj_a2	173									Scan type changed
	3	Adj_b2	176	39.6	13:04	34.1	-	-	2		54	Scan type changed
		Adj_b	177									
		KH	178									Scan type changed
		Adj_a	179									Scan type changed
		Adj_a2	180	10.9	12:56	26.0	-	-	3		38	
	4	Adj_b2	339									No MP crossing in data period
		Adj_b	340	5.0	20:33	14.4	20.6	332.2	130		15	
		KH	341	15.3	8:01 (7:48 - 8:01)	-10.2	20.4	335.2	0	24	97	
		Adj_a	342	22.2	20:25 (20:15 - 20:25)	7.4	20.1	338.3	0	20	23	
		Adj_a2	343	27.1	8:41	24.0	19.9	341.4	14		7	
	5	Adj_b2	340	5.0	20:33	14.4	20.6	332.2	130		15	
		Adj_b	341	15.3	8:01 (7:48 - 8:01)	-10.2	20.4	335.2	0	24	97	
		KH	342	22.2	20:25 (20:15 - 20:25)	7.4	20.1	338.3	0	20	23	
		Adj_a	343	27.1	8:41	24.0	19.9	341.4	14		7	
		Adj_a2	344	27.4	20:32 (20:21 - 20:32)	13.1	19.7	344.6	1	9	45	
	6	Adj_b2	342	23.4	20:25 (20:15 - 20:25)	6.5	20.1	338.3	0	20	24	
		Adj_b	343	27.1	8:41	24.0	19.9	341.4	14		7	
		KH	344	27.4	20:32 (20:21 - 20:32)	12.1	19.7	344.6	0	9	38	
		Adj_a	345	50.1	8:44 (8:20 - 8:41)	25.2	19.5	347.7	0	23	75	
		Adj_a2	346									Scan type changed
	7	Adj_b2	343	27.1	8:41	24.0	19.9	341.4	14		7	
		Adj_b	344	27.4	20:32 (20:21 - 20:32)	12.1	19.7	344.6	0	9	38	
		KH	345	50.1	8:44 (8:20 - 8:41)	25.2	19.5	347.7	0	23	75	
		Adj_a	346									Scan type changed
		Adj_a2	347	75.4	8:40	22.4	19.1	354.0	1		55	
	8	Adj_b2	515	3.1	9:25	0.5	21.1	323.6	76		109	
		Adj_b	516									No MP crossing in data period
		KH	517	23.7	09:21 (9:07 - 9:21)	-2.5	20.7	329.6	0	33	140	
		Adj_a	518	12.1	21:30	5.0	20.5	332.6	93		32	
		Adj_a2	519	9.9	9:37	12.3	20.3	335.7	111		59	
	9	Adj_b2	518	12.1	21:30	5.0	20.5	332.6	93		32	
		Adj_b	519	9.9	9:37	12.3	20.3	335.7	111		59	
		KH	520	20.1	21:24 (21:09 - 21:24)	0.2	20.1	338.8	0	47	133	
		Adj_a	521	7.5	9:26	1.7	19.9	341.9	50		21	
		Adj_a2	522	38.9	21:32 (21:11 - 21:32)	7.3	19.6	345.0	0	14	209	
	10	Adj_b2	520	20.1	21:24 (21:09 - 21:24)	0.2	20.1	338.8	0	47	133	
		Adj_b	521	7.5	9:26	1.7	19.9	341.9	50		21	
		KH	522	38.9	21:32 (21:11 - 21:32)	7.3	19.6	345.0	0	14	209	
		Adj_a	523	31.6	9:25 (9:11 - 9:24)	0.9	19.4	348.2	0	19	203	
		Adj_a2	524	46.0	21:38 (21:14 - 21:38)	15.1	19.2	351.3	0	32	222	

1. SG event list (continuous; 2/4)

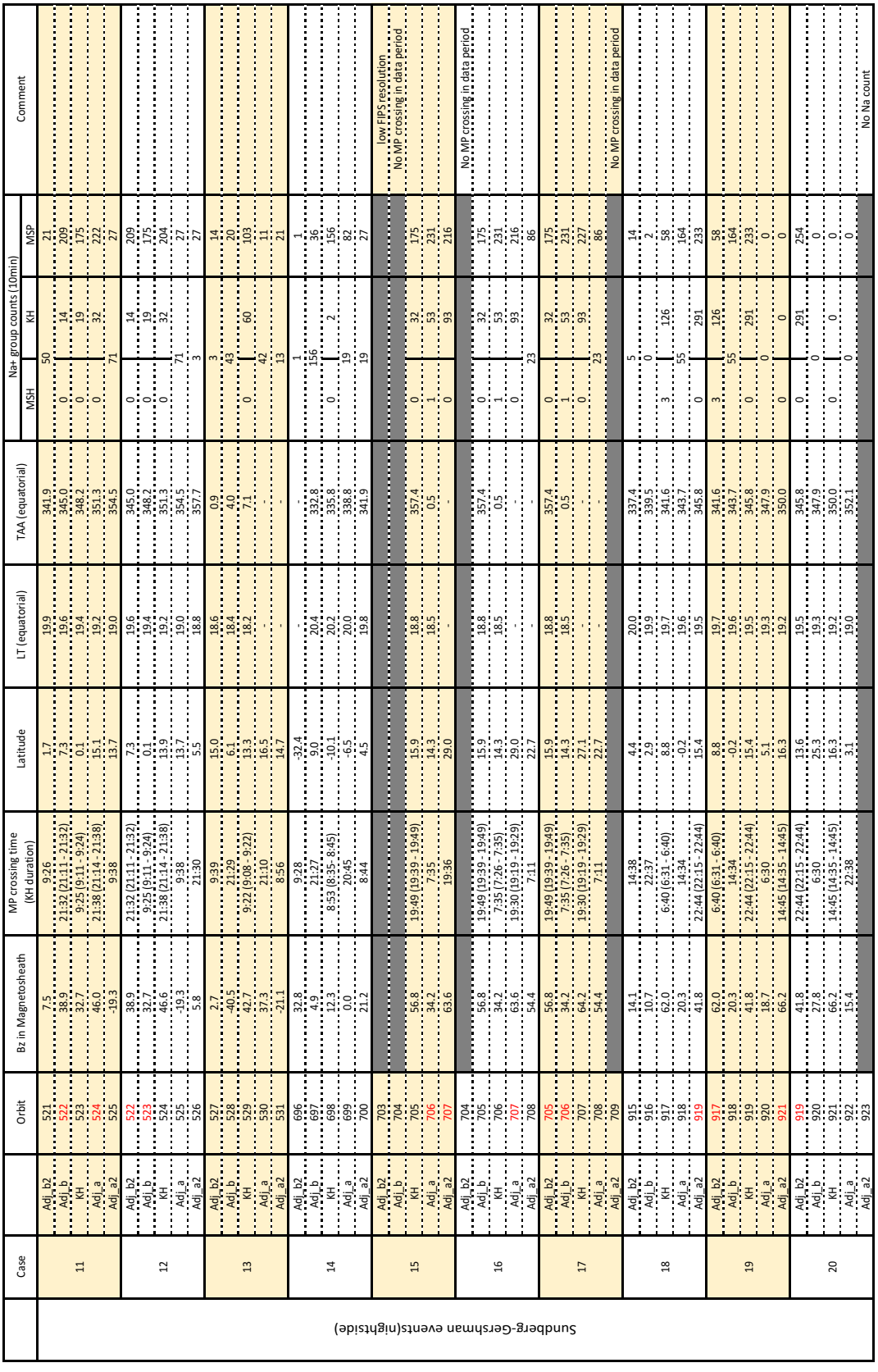

Sundberg-Gershman events(nightside)	Case		Orbit	Bz in Magnetosheath	MP crossing time (KH duration)	Latitude	LT (equatorial)	TAA (equatorial)	Nat group counts (10min) MSH	KH	MSP	Comment
	11	Adj_b2	521	7.5	9:26	1.7	19.9	341.9	50		21	
		Adj_b	522	38.9	21:32 (21:11 - 21:32)	7.3	19.6	345.0	0	14	209	
		KH	523	32.7	9:25 (9:11 - 9:24)	0.1	19.4	348.2	0	19	175	
		Adj_a	524	46.0	21:38 (21:14 - 21:38)	15.1	19.2	351.3	0	32	222	
		Adj_a2	525	-19.3	9:38	13.7	19.0	354.5	71		27	
	12	Adj_b2	522	38.9	21:32 (21:11 - 21:32)	7.3	19.6	345.0	0	14	209	
		Adj_b	523	32.7	9:25 (9:11 - 9:24)	0.1	19.4	348.2	0	19	175	
		KH	524	46.6	21:38 (21:14 - 21:38)	13.9	19.2	351.3	0	32	204	
		Adj_a	525	-19.3	9:38	13.7	19.0	354.5	71		27	
		Adj_a2	526	5.8	21:30	5.5	18.8	357.7	3		27	
	13	Adj_b2	527	2.7	9:39	15.0	18.6	0.9	3		14	
		Adj_b	528	40.5	21:29	6.1	18.4	4.0	43		20	
		KH	529	42.7	9:22 (9:08 - 9:22)	13.3	18.2	7.1	0	60	103	
		Adj_a	530	37.3	21:10	16.5	-	-	42		11	
		Adj_a2	531	-21.1	8:56	14.7	-	-	13		21	
	14	Adj_b2	696	32.8	9:28	-32.4	-	-	1		1	
		Adj_b	697	4.9	21:27	9.0	20.4	332.8	156		36	
		KH	698	12.3	8:53 (8:35 - 8:45)	-10.1	20.2	335.8	0	2	156	
		Adj_a	699	0.0	20:45	6.5	20.0	338.8	19		82	
		Adj_a2	700	21.2	8:44	4.5	19.8	341.9	19		27	
	15	Adj_b2	703									low FIPS resolution
		Adj_b	704									No MP crossing in data period
		KH	705	56.8	19:49 (19:39 - 19:49)	15.9	18.8	357.4	0	32	175	
		Adj_a	706	34.2	7:35	14.3	18.5	0.5	1	53	231	
		Adj_a2	707	63.6	19:36	29.0	-	-	0	93	216	
	16	Adj_b2	704									No MP crossing in data period
		Adj_b	705	56.8	19:49 (19:39 - 19:49)	15.9	18.8	357.4	0	32	175	
		KH	706	34.2	7:35 (7:26 - 7:35)	14.3	18.5	0.5	1	53	231	
		Adj_a	707	63.6	19:30 (19:19 - 19:29)	29.0	-	-	0	93	216	
		Adj_a2	708	54.4	7:11	22.7	-	-	23		86	
	17	Adj_b2	705	56.8	19:49 (19:39 - 19:49)	15.9	18.8	357.4	0	32	175	
		Adj_b	706	34.2	7:35 (7:26 - 7:35)	14.3	18.5	0.5	1	53	231	
		KH	707	64.2	19:30 (19:19 - 19:29)	27.1	-	-	0	93	227	
		Adj_a	708	54.4	7:11	22.7	-	-	23		86	
		Adj_a2	709									No MP crossing in data period
	18	Adj_b2	915	14.1	14:38	4.4	20.0	337.4	5		14	
		Adj_b	916	10.7	22:37	2.9	19.9	339.5	0		2	
		KH	917	62.0	6:40 (6:31 - 6:40)	8.8	19.7	341.6	3	126	58	
		Adj_a	918	20.3	14:34	-0.2	19.6	343.7	55		164	
		Adj_a2	919	41.8	22:44 (22:15 - 22:44)	15.4	19.5	345.8	0	291	233	
	19	Adj_b2	917	62.0	6:40 (6:31 - 6:40)	8.8	19.7	341.6	3	126	58	
		Adj_b	918	20.3	14:34	-0.2	19.6	343.7	55		164	
		KH	919	41.8	22:44 (22:15 - 22:44)	15.4	19.5	345.8	0	291	233	
		Adj_a	920	18.7	6:30	5.1	19.3	347.9	0	0	0	
		Adj_a2	921	66.2	14:45 (14:35 - 14:45)	16.3	19.2	350.0	0	0	0	
	20	Adj_b2	919	41.8	22:44 (22:15 - 22:44)	13.6	19.5	345.8	0	291	254	
		Adj_b	920	27.8	6:30	25.3	19.3	347.9	0		0	
		KH	921	66.2	14:45 (14:35 - 14:45)	16.3	19.2	350.0	0	0	0	
		Adj_a	922	15.4	22:38	3.1	19.0	352.1	0		0	
		Adj_a2	923									No Na count

1. SG event list (continuous; 3/4)

	Case		Orbit	Bz in Magnetosheath	MP crossing time (KH duration)	Latitude	LT (equatorial)	TAA (equatorial)	Na+ group counts (10min) MSH	Na+ group counts (10min) KH	Na+ group counts (10min) MSP	Comment
Sundberg-Gershman events(nightside)	21	Adj_b2	1177	19.9	23:05	21.9	20.2	333.6		57	0	
		Adj_b	1178	16.1	7:00	11.7	20.1	335.6		137	32	
		KH	1179	22.2	14:51 (14:40 - 14:51)	-9.9	19.9	337.7	16	73	176	
		Adj_a	1180	12.9	22:46	-8.6	19.8	339.8		33	25	
		Adj_a2	1181	8.2	6:57	6.0	19.7	341.8		53	28	
	22	Adj_b2	1180	12.9	22:46	-8.6	19.8	339.8		33	25	
		Adj_b	1181	8.2	6:57	6.0	19.7	341.8		53	28	
		KH	1182	19.4	14:55 (14:40 - 14:51)	2.7	19.5	343.9	0	74	24	
		Adj_a	1183	2.6	21:55	2.7	19.4	346.0		20	28	
		Adj_a2	1184	22.6	6:54	0.9	19.3	348.1		42	29	
	23	Adj_b2	1188									low FIPS resolution
		Adj_b	1189									low FIPS resolution
		KH	1190	60.9	7:03 (6:55 - 7:03)	13.4	18.4	0.8	0	43	53	
		Adj_a	1191	21.6	15:06	19.0	18.3	2.9		38	175	
		Adj_a2	1192	13.5	23:05	16.9	18.1	5.0		46	75	
	24	Adj_b2	1442	13.2	7:18	9.9	20.0	335.9	146		11	
		Adj_b	1443	17.5	15:15	4.4	19.9	338.0	76		24	
		KH	1444	29.5	23:11 (22:58 - 23:11)	-1.9	19.7	340.0	0	41	38	
		Adj_a	1445	33.9	7:18 (7:05 - 7:18)	8.7	19.6	342.1	0	58	24	
		Adj_a2	1446	22.2	15:18	8.5	19.5	344.2	56		44	
	25	Adj_b2	1443	17.5	15:15	4.4	19.9	338.0	76		24	
		Adj_b	1444	29.5	23:11 (22:58 - 23:11)	-1.9	19.7	340.0	0	41	38	
		KH	1445	33.9	7:18 (7:05 - 7:18)	8.7	19.6	342.1	0	58	24	
		Adj_a	1446	22.2	15:18	8.5	19.5	344.2	56		44	
		Adj_a2	1447	13.3	23:11	-3.0	19.3	346.3	22		12	
	26	Adj_b2	1451	-17.7	7:09	-6.7	18.8	354.7	58		32	
		Adj_b	1452	-15.6	15:13	-1.3	18.6	356.9	23		12	
		KH	1453	23.9	23:18 (23:10 - 23:18)	6.4	18.5	359.0	1	28	40	
		Adj_a	1454	-50.2	7:14	-0.3	18.3	1.1	11		13	
		Adj_a2	1455	-48.5	15:28	27.1	18.2	3.2	3		19	
	27	Adj_b2	1454	-50.2	7:14	-0.3	18.3	1.1	11		13	
		Adj_b	1455	-48.5	15:28	27.1	18.2	3.2	3		19	
		KH	1456	41.9	23:20 (23:11 - 23:20)	9.3	18.1	5.3	5	140	61	1min MAG
		Adj_a	1457	34.4	7:20 (7:10 - 7:20)	9.2	17.9	7.4	0	58	40	
		Adj_a2	1458	51.0	15:26	21.4	17.8	9.5		144	217	
	28	Adj_b2	1455	-48.5	15:28	27.1	18.2	3.2	3		19	
		Adj_b	1456	41.9	23:20 (23:12 - 23:20)	9.3	18.1	5.3	5	140	61	
		KH	1457	34.4	7:20 (7:10 - 7:20)	9.2	17.9	7.4	0	58	40	
		Adj_a	1458	51.0	15:26	21.4	17.8	9.5	144		217	
		Adj_a2	1459	-24.0	23:21	10.5	17.6	11.6	20		32	
	29	Adj_b2	1699	1.8	23:35	2.8	20.9	322.1	80		19	
		Adj_b	1700	16.5	7:32	-2.4	20.8	324.1	64		25	
		KH	1701	21.2	15:29 (15:18 - 15:29)	6.9	20.6	326.0	0	55	124	
		Adj_a	1702	10.3	7:39	7.4	20.5	328.1	100		17	
		Adj_a2	1703	14.8	15:32	9.2	20.4	330.1	76		36	
	30	Adj_b2	1708	17.2	23:39	7.4	19.7	340.3	57		41	
		Adj_b	1709	5.5	7:27	-11.6	19.5	342.4	5		16	
		KH	1710	25.1	15:29 (15:24 - 15:29)	-9.0	19.4	344.5	1	50	129	
		Adj_a	1711	38.2	23:38 (23:34 - 23:38)	3.6	19.3	346.6	38	179	347	
		Adj_a2	1712	27.6	7:21	-18.9	19.1	348.7		18	57	

1. SG event list (continuous; 4/4)

	Case		Orbit	Bz in Magnetosheath	MP crossing time (KH duration)	Latitude	LT (equatorial)	TAA (equatorial)	Na+ group counts (10min) MSH	Na+ group counts (10min) KH	Na+ group counts (10min) MSP	Comment
Sundberg-Gershman events(nightside)	31	Adj_b2	1709	5.5	7:27	-11.6	19.5	342.4	5		16	
		Adj_b	1710	25.1	15:29 (15:24 - 15:29)	-9.0	19.4	344.5	1	50	129	
		KH	1711	38.2	23:38 (23:34 - 23:38)	3.6	19.3	346.6	38	179	347	
		Adj_a	1712	27.6	7:21	-18.9	19.1	348.7	18		57	
		Adj_a2	1713	-1.8	15:26	-14.1	19.0	350.8	31		34	
	32	Adj_b2	1713	-1.8	15:26	14.1	19.0	350.8	31		34	low FIPS resolution
		Adj_b	1714									
		KH	1715	73.8	7:45 (7:38 - 7:45)	16.3	18.7	355.0	7	88	162	
		Adj_a	1716	46.2	15:38 (15:34 - 15:38)	1.9	18.5	357.1	18	25	102	
		Adj_a2	1717	52.3	23:43 (23:35 - 23:43)	13.9	18.4	359.3	28	364	244	
	33	Adj_b2	1714									low FIPS resolution
		Adj_b	1715	73.8	7:45 (7:38 - 7:45)	16.3	18.7	355.0	7	88	162	
		KH	1716	46.2	15:38 (15:34 - 15:38)	1.9	18.5	357.1	18	25	102	
		Adj_a	1717	52.3	23:43 (23:35 - 23:43)	13.9	18.4	359.3	28	364	244	
		Adj_a2	1718	5.3	7:41	7.1	18.3	1.4	70		191	
	34	Adj_b2	1715	73.8	7:45 (7:38 - 7:45)	16.3	18.7	355.0	7	88	162	
		Adj_b	1716	46.2	15:38 (15:34 - 15:38)	1.9	18.5	357.1	18	25	102	
		KH	1717	52.3	23:43 (23:35 - 23:43)	13.9	18.4	359.3	28	364	244	
		Adj_a	1718	5.3	7:41	7.1	18.3	1.4	70		191	
		Adj_a2	1719	42.0	15:43	10.8	18.1	3.5	125		396	

2. KH event from MP crossing in 2012

KH in 2012 MP crossing event (19LT-21LT)	Case		Orbit	Bz in Magnetosheath (5 min average)	MP crossing time (KH duration)	Latitude	LT (equatorial)	TAA (equatorial)	Na+ group counts(10min) MSH	Na+ group counts(10min) KH	Na+ group counts(10min) PS	Comment
	1	Adj_b2	696	17.1	9:46	-25.8	20.6	329.8		1	9	
		Adj_b	697	4.9	21:27	9.0	20.4	332.8		156	36	
		KH	698	12.3	8:53 (8:39 - 8:53)	-10.0	20.2	335.8	0	64	159	
		Adj_a	699	-15.2	20:36	-12.4	20.0	338.8		35	18	
		Adj_a2	700	21.6	8:44	3.9	19.8	341.9		17	26	
	2	Adj_b2	915	16.2	14:38	5.9	20.0	337.4		8	12	
		Adj_b	916	13.0	22:37	3.9	19.9	339.5		0	3	
		KH	917	59.3	6:40 (6:31 - 6:40)	9.1	19.7	341.6	3	126	55	
		Adj_a	918	20.4	14:34	-0.8	19.6	343.7		55	157	
		Adj_a2	919	41.8	22:44	14.5	19.5	345.8	0	270	228	
	3	Adj_b2	917	59.3	6:40 (6:31 - 6:40)	9.1	19.7	341.6	3	126	55	
		Adj_b	918	20.4	14:34	-0.8	19.6	343.7		55	157	
		KH	919	41.8	22:44 (22:18 - 22:44)	14.5	19.5	345.8	0	270	228	
		Adj_a	920	19.1	6:38	4.6	19.3	347.9		0	0	
		Adj_a2	921									No Na count
	4	Adj_b2	919	41.8	22:44 (22:18 - 22:44)	14.5	19.5	345.8	0	270	228	
		Adj_b	920	27.6	6:38	24.5	19.3	347.9	0	0	0	
		KH	921									No Na count
		Adj_a	922									No Na count
		Adj_a2	923									No data
	5	Adj_b2	1177	21.4	23:05	23.1	20.2	333.6		52	2	
		Adj_b	1178	16.1	7:00	11.1	20.1	335.6		140	37	
		KH	1179	23.1	14:51 (14:40 - 14:51)	2.5	19.9	337.7	0	86	179	
		Adj_a	1180	13.3	22:46	-8.6	19.8	339.8		33	25	
		Adj_a2	1181	9.5	6:57	6.2	19.7	341.8		49	28	
	6	Adj_b2	1180	13.3	22:46	-8.6	19.8	339.8		33	25	
		Adj_b	1181	9.5	6:57	6.2	19.7	341.8		49	28	
		KH	1182	18.8	14:55 (14:40 - 14:55)	3.2	19.5	343.9	0	73	26	
		Adj_a	1183	2.5	22:55	3.2	19.4	346.0		21	27	
		Adj_a2	1184	22.9	6:54	1.6	19.3	348.1		43	27	
	7	Adj_b2	1442	13.0	7:18	9.6	20.0	335.9		147	11	
		Adj_b	1443	17.2	15:15	4.4	19.9	338.0		76	24	
		KH	1444	29.6	23:11 (22:58 - 23:11)	-1.9	19.7	340.0	0	27	38	
		Adj_a	1445	35.5	7:18	9.6	19.6	342.1	0	58	24	
		Adj_a2	1446	22.4	15:18	9.7	19.5	344.2		58	42	
	8	Adj_b2	1443	17.2	15:15	4.4	19.9	338.0		76	24	
		Adj_b	1444	29.6	23:11 (22:58 - 23:11)	-1.9	19.7	340.0	0	27	38	
		KH	1445	35.5	7:18 (7:05 - 7:18)	9.6	19.6	342.1	0	58	24	
		Adj_a	1446	22.4	15:18	9.7	19.5	344.2		58	42	
		Adj_a2	1447	13.4	23:11	-3.2	19.3	346.3		22	12	

3. KH event from MP crossing in 2013 (1/2)

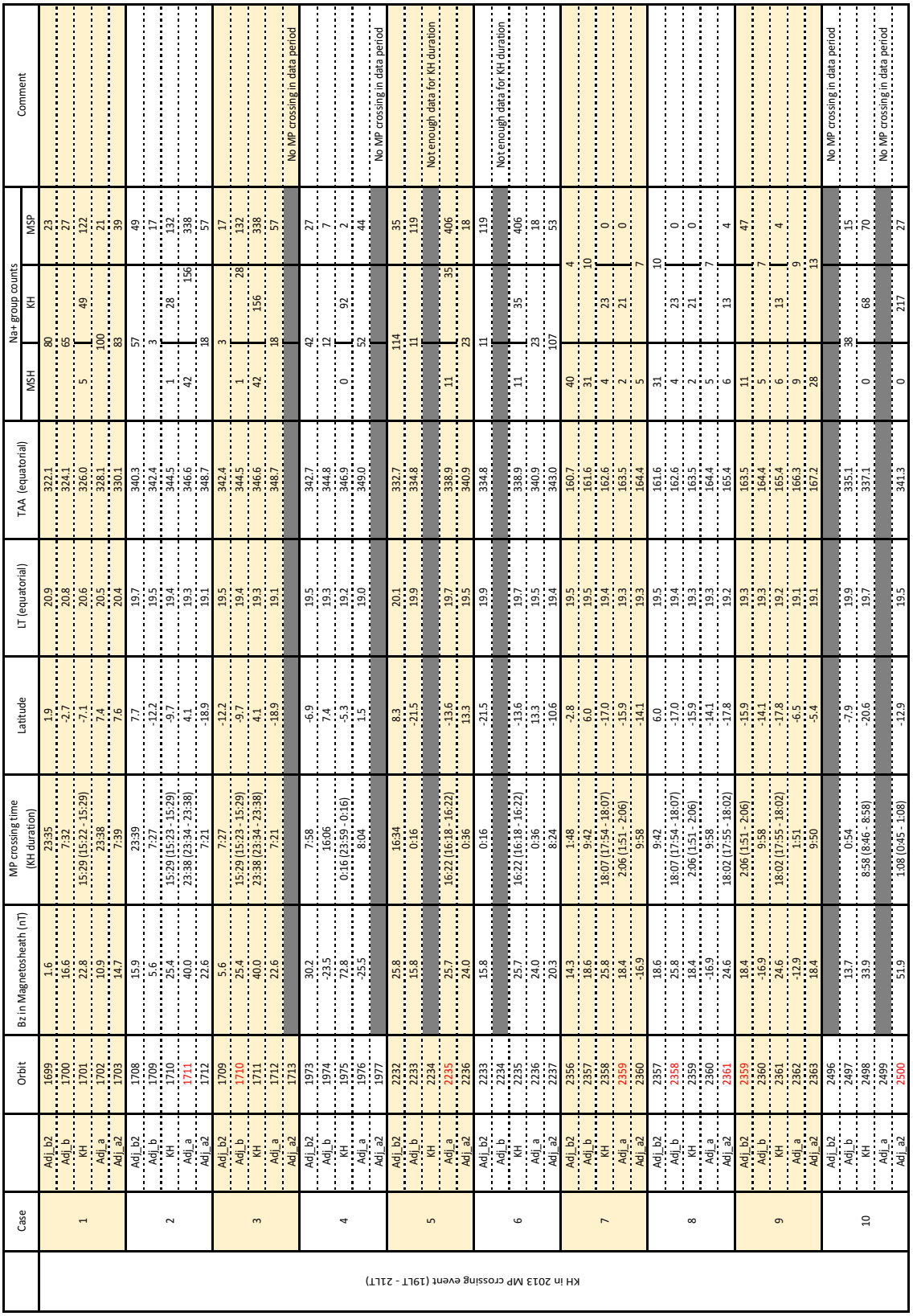

3. KH event from MP crossing in 2013 (continuous; 2/2)

KH in 2013 MP crossing event (19LT - 21LT)	Case		Orbit	Bz in Magnetosheath (nT)	MP crossing time (KH duration)	Latitude	LT (equatorial)	TAA (equatorial)	Na+ group counts		Comment
									MSH	KH	MSP	
	11	Adj_b2	2498	33.9	8:58 (8:46 - 8:58)	-20.6	19.7	337.1	0	68	70	
		Adj_b	2499									No MP crossing in data period
		KH	2500	51.9	1:08 (0:45 - 1:08)	-12.9	19.5	341.3	0	217	27	
		Adj_a	2501	-9.1	8:52 (8:49 - 8:52)	-12.9	19.3	343.3	22	12	81	
		Adj_a2	2502	25.9	17:00	2.4	19.2	345.4	105	1	40	
	12	Adj_b2	2499									No MP crossing in data period
		Adj_b	2500	51.9	1:08 (0:45 - 1:08)	-12.9	19.5	341.3	0	217	27	
		KH	2501	-9.1	8:52 (8:49 - 8:52)	-12.9	19.3	343.3	22	12	81	
		Adj_a	2502	25.9	17:00	2.4	19.2	345.4	1	1	40	
		Adj_a2	2503	-6.5	0:50	-16.0	19.0	347.5	7		34	

4. KH event from MP crossing in 2014 (1/2)

KH in 2014 MP crossing event (19LT - 21LT)	Case		Orbit	Bz in Magnetosheath	MP crossing time (KH duration)	Latitude	LT (equatorial)	TAA (equatorial)	Na+ group counts			Comment
									MSH	KH	MSP	
	1	Adj_b2	2760									No MP crossing in data period
		Adj_b	2761	-13.2	1:46	-16.0	19.8	335.4		7	14	
		KH	2762	42.2	9:29 (9:19 - 9:29)	-6.3	19.7	337.5	0	171	57	
		Adj_a	2763	27.8	17:36 (17:17 -17:36)	11.4	19.5	339.5	0	102	7	
		Adj_a2	2764	-21.3	1:21	-20.9	19.4	341.6	1		60	
	2	Adj_b2	2761	-13.2	1:24	-16.0	19.8	335.4		7	14	
		Adj_b	2762	42.2	9:29 (9:19 - 9:29)	-6.3	19.7	337.5	0	171	57	
		KH	2763	27.8	17:36 (17:17 -17:36)	11.4	19.5	339.5	0	102	7	
		Adj_a	2764	21.3	1:21	-20.9	19.4	341.6	1		60	
		Adj_a2	2765	34.2	9:29 (9:16 - 9:29)	-6.3	19.2	343.7	0	89	21	
	3	Adj_b2	2763	27.8	17:36 (17:17 -17:36)	11.4	19.5	339.5	0	102	7	
		Adj_b	2764	-21.3	1:21	-20.9	19.4	341.6	1		60	
		KH	2765	34.2	9:29 (9:16 - 9:29)	-6.3	19.2	343.7	0	89	21	
		Adj_a	2766	3.9	17:25	-15.9	19.1	345.8		8	22	
		Adj_a2	2767									
	4	Adj_b2	2864									No MP crossing in data period
		Adj_b	2865	9.8	18:57	-11.0	20.6	142.4	37	47		
		KH	2866	12.0	3:21 (2:58 - 3:21)	-11.7	20.6	143.4	26	2	19	
		Adj_a	2867	8.6	11:05	-17.5	20.5	144.4	7		2	
		Adj_a2	2868	18.1	18:49	-2.8	20.4	145.4	51		32	
	5	Adj_b2	2882	-12.1	11:02	-13.5	19.5	159.1	2	7		No MP crossing in data period
		Adj_b	2883									
		KH	2884	14.2	3:13 (2:58 - 3:13)	-9.9	19.4	161.0	2	2	0	
		Adj_a	2885	11.3	10:56	-8.0	19.3	161.9	5		18	
		Adj_a2	2886	17.1	18:53	-4.9	19.3	162.9	17		22	
	6	Adj_b2	2888	1.4	10:55	-6.9	19.1	164.7	0	5		
		Adj_b	2889	-8.0	18:57	-8.0	19.1	165.7	1	5		
		KH	2890	-1.1	2:58 (2:49 - 2:58)	-9.0	19.0	166.6	0	10	1	
		Adj_a	2891									No data
		Adj_a2	2892									No data
	7	Adj_b2	3024									No MP crossing in data period
		Adj_b	3025									No MP crossing in data period
		KH	3026									No MP crossing in data period
		Adj_a	3027									No MP crossing in data period
		Adj_a2	3028									No MP crossing in data period
	8	Adj_b2	3138	33.1	19:18	13.1	20.0	151.6	8	4		
		Adj_b	3139	34.4	3:38	-9.5	19.9	152.5	7	26		
		KH	3140	27.8	11:43 (11:35 - 11:43)	-13.6	19.8	153.5	1	3	1	
		Adj_a	3141	16.3	19:34	-5.9	19.8	154.5	38	16		
		Adj_a2	3142	11.4	3:37	-8.5	19.7	155.4	35	154		
	9	Adj_b2	3150	-25.4	19:45	-14.3	19.2	163.0	2	1		
		Adj_b	3151	9.3	3:41	-11.1	19.1	164.0	1	13		
		KH	3152	30.8	11:47 (11:38 - 11:47)	-8.6	19.1	164.9	1	4	1	
		Adj_a	3153	26.9	19:25	5.6	19.0	165.8	15	11		
		Adj_a2	3154									No data
	10	Adj_b2	3409									No Na count
		Adj_b	3410									No Na count
		KH	3411									No Na count
		Adj_a	3412									No Na count
		Adj_a2	3413									No Na count

4. KH event from MP crossing in 2014 (continuous; 2/2)

	Case		Orbit	Bz in Magnetosheath	MP crossing time (KH duration)	Latitude	LT (equatorial)	TAA (equatorial)	Na+ group counts			Comment
									MSH	KH	MSP	
KH in 2014 MP crossing event (19LT - 21LT)	11	Adj_b2	3411									No Na count
		Adj_b	3412									No Na count
		KH	3413									No Na count
		Adj_a	3414	28.6	3:53	3.0	19.1	164.1	54	13		
		Adj_a2	3415	-41.8	11:53	5.4	19.0	165.0	4	2		
	12	Adj_b2	3652	-1.8	20:01	-13.3	20.4	142.8	1	3		
		Adj_b	3653	-17.5	4:20	17.3	20.4	143.9	2	4		
		KH	3654	33.5	12:21 (12:06 - 12:21)	2.3	20.3	144.9	1	3	0	
		Adj_a	3655	13.5	20:28	-5.6	20.2	145.9	4	19		
		Adj_a2	3656	9.9	5:05 (4:38 - 5:05)	-20.3	20.2	147.0	1	1	0	
	13	Adj_b2	3654	33.5	12:21 (12:06 - 12:21)	2.3	20.3	144.9	1	3	0	
		Adj_b	3655	13.5	20:28	-5.6	20.2	145.9	4	19		
		KH	3656	9.9	5:05 (4:38 - 5:05)	20.3	20.2	147.0	1	1	0	
		Adj_a	3657	26.2	12:39	7.7	20.1	148.0	37	97		
		Adj_a2	3658	-1.3	21:07	-6.5	20.0	149.0	5	51		
	14	Adj_b2	3657	26.2	12:39	7.7	20.1	148.0	37	97		
		Adj_b	3658	-1.3	21:07	-6.5	20.0	149.0	5	51		
		KH	3659	24.3	5:38 (5:17 - 5:38)	-4.0	20.0	150.0	2	1	0	
		Adj_a	3660	15.0	13:23	2.3	19.9	151.0	10	18		
		Adj_a2	3661	27.7	21:23	18.6	19.8	152.0	32	30		

5. KH event from MP crossing in 2015

	Case		Orbit	Bz in Magnetosheath	MP crossing time (KH duration)	Latitude	LT (equatorial)	TAA (equatorial)	Na+ group counts (10min)			Comment
									MSH	KH	MSP	
KH in 2015 MP crossing	1	Adj_b2	3914	25.6	17:35	2.4	20.0	148.7	21	33		
		Adj_b	3915	20.5	1:58	-3.5	19.9	149.7	5	3		
		KH	3916	-5.9	10:08 (09:58 - 10:08)	2.4	19.8	150.7	0	6	0	
		Adj_a	3917									No data
		Adj_a2	3918									No data

Bibliography

Aggson, T. L., P. J. Gambardella, and N. C. Maynard (1983), Electric field measurements at the magnetopause: 1. Observation of large convective velocities at rotational magnetopause discontinuities, *J. Geophys. Res.*, *88*, 10,000–10,010, doi:10.1029/JA088iA12p10000.

Aizawa, S., D. Delcourt, and N. Terada (2018), Sodium ion dynamics in the magnetospheric flanks of Mercury, *Geophys. Res. Lett.*, *45*(2), 595–601, doi:10.1002/2017GL076586.

Alexeev, I. I., E. S. Belenkaya, S. Yu. Bobrovnikov, J. A. Slavin, and M. Sarantos (2008), Paraboloid model of Mercury's magnetosphere, *J. Geophys. Res.*, *113*, A12210, doi:10.1029/2008JA013368.

Alexeev, I. I., E. S. Belenkaya, J. A. Slavin, H. Korth, B. J. Anderson, D. N. Baker, S. A. Boardsen, C. L. Johnson, M. E. Purucker, M. Sarantos, and S. C. Solomon (2010), Mercury's magnetospheric magnetic field after the first two MESSENGER flybys, *Icarus*, *209*(1), 23–39, doi:10.1016/j.icarus.2010.01.024.

Amerstorfer, U. V., N. V. Erkaev, U. Taubenschuss, and H. K. Biernat (2010), Influence of a density increase on the evolution of the Kelvin-Helmholtz instability and vortices, *Phys. Plasmas*, *17*, 072901, doi:10.1063/1.3453705.

Anderson, B. J., C. L. Johnson, H. Korth, M. E. Purucker, R. M. Winslow, J. A. Slavin, S. C. Solomon, R. L. McNutt Jr., J. M. Raines, and T. H. Zurbuchen (2011), The global magnetic field of Mercury from MESSENGER orbital observations, *Science*, *333*, 1859–1862, doi:10.1126/science.1211001.

Anderson, B. J., C. L. Johnson, H. Korth, R. M. Winslow, J. E. Borovsky, M. E. Purucker, J. A. Slavin, S. C. Solomon, M. T. Zuber, and R. L. McNutt Jr. (2012), Low-degree structure in Mercury's planetary magnetic field, *J. Geophys. Res.*, *117*, E00L12, doi:10.1029/2012JE004159.

Andrews, G. B., T. H. Zurbuchen, B. H. Mauk, H. Malcom, L. A. Fisk, G. Gloeckler, G. C. Ho, J. S. Kelley, P. L. Koehn, T. W. LeFevere, S. S. Livi, R. A. Lundgren, and J. M. Raines (2007), The Energetic Particle and Plasma Spectrometer instrument on the MESSENGER spacecraft, *Space Sci. Rev.*, *131*(1–4), 523–556, doi:10.1007/s11214-007-9272-5.

Ashour-Abdalla, M., J. Berchem, J. Büchner, and L. M. Zelenyi (1991), Large and small scale structures in the plasma sheet: A signature of chaotic motion and resonance effects, *Geophys. Res. Lett.*, *18*(8), 1603–1606, doi:10.1029/91GL01853.

Ashour-Abdalla, M., L. M. Zelenyi, J. M. Bosqued, and R. A. Kovrazhkin (1992), Precipitation of fast ion beams from the plasma sheet boundary layer, *Geophys. Res. Lett.*, *19*(6), 617–620, doi:10.1029/92GL00048.

Ashour-Abdalla, M., L. M. Zelenyi, V. Peroomian, and R. L. Richard (1993a), On the structure of the magnetotail current sheet, *Geophys. Res. Lett.*, *20*(19), 2019–2022, doi:10.1029/93GL01695.

Ashour-Abdalla, M., J. P. Berchem, J. Büchner, and L. M. Zelenyi (1993b), Shaping of the magnetotail from the mantle: Global and local structuring, *J. Geophys. Res.*, *98*(A4), 5651–5676, doi:10.1029/92JA01662.

Ashour-Abdalla, M., L. M. Zelenyi, V. Peroomian, and R. L. Richard (1994), Consequences of magnetotail ion dynamics, *J. Geophys. Res.*, *99*(A8), 14,891–14,916, doi:10.1029/94JA00141.

Baker, D. N., J. A. Simpson, and J. H. Eraker (1986), A model of impulsive acceleration and transport of energetic particles in Mercury's magnetosphere, *J. Geophys. Res.*, *91*(A8), 8742–8748, doi:10.1029/JA091iA08p08742.

Baker, D. N., T. I. Pulkkinen, V. Angelopoulos, W. Baumjohann, and R. L. McPherron (1996), Neutral line model of substorms: Past results and present view, *J. Geophys. Res.*, *101*(A6), 12,975–13,010, doi:10.1029/95JA03753.

Baker, D. N., R. M. Dewey, D. J. Lawrence, J. O. Goldsten, P. N. Peplowski, H. Korth, J. A. Slavin, S. M. Krimigis, B. J. Anderson, G. C. Ho, R. L. McNutt Jr., J. M. Raines, D. Schriver, and S. C. Solomon (2016), Intense energetic electron flux enhancements in Mercury's magnetosphere: An integrated view with high-resolution observations from MESSENGER, *J. Geophys. Res.*, *121*(3), 2171–2184, doi:10.1002/2015JA021778.

Baumjohann, W., and R. A. Treumann (1996), Basic Space Plasma Physics, ICP

Baumjohann, W., M. Hesse, S. Kokubun, T. Mukai, T. Nagai, and A. A. Petrukovich (1999), Substorm depolarization and recovery, *J. Geophys. Res.*, *104*(A11), 24,995–25,000, doi:10.1029/1999JA900282.

Boardsen, S. A., T. Sundberg, J. A. Slavin, B. J. Anderson, H. Korth, S. C. Solomon, and L. G. Blomberg (2010), Observations of Kelvin-Helmholtz waves along the dusk-side boundary of Mercury's magnetosphere during MESSENGER's third flyby, *Geophys. Res. Lett.*, *37*, L12101, doi:10.1029/2010GL043606.

Broadfoot, A. L., D. E. Shemansky, and S. Kumar (1976), Mariner 10: Mercury atmosphere, *Geophys. Res. Lett.*, *3*(10), 577–580, doi:10.1029/GL003i010p00577.

Büchner, J., and L. M. Zelenyi (1989), Regular and chaotic charged particle motion in magnetotaillike field reversals: 1. Basic theory of trapped motion, *J. Geophys. Res.*, *94*(A9), 11,821–11,842, doi:10.1029/JA094iA09p11821.

Büchner, J., and L. M. Zelenyi (1990), The separatrix tentacle effect of ion acceleration to the plasma sheet boundary, *Geophys. Res. Lett.*, *17*(2), 127–130, doi:10.1029/GL017i002p00127.

Burkhart, G. R., and J. Chen (1991), Differential memory in the Earth's magnetotail, *J. Geophys. Res.*, *96*(A8), 14,033–14,049, doi:10.1029/91JA01137.

Chen, J., and P. J. Palmadesso (1986), Chaos and nonlinear dynamics of single-particle orbits in a magnetotaillike magnetic field, *J. Geophys. Res.*, *91*(A2), 1499–1508, doi:10.1029/JA091iA02p01499.

Chen, J., G. R. Burkhart, and C. Y. Huang (1990), Observational signatures of nonlinear magnetotail particle dynamics, *Geophys. Res. Lett.*, *17*(12), 2237–2240, doi:10.1029/GL017i012p02237.

Chen, J. (1992), Nonlinear dynamics of charged particles in the magnetotail, *J. Geophys. Res.*, *97*(A10), 15,011–15,050, doi:10.1029/92JA00955.

Chen, S. -H., and M. G. Kivelson (1993), On nonsinusoidal waves at the Earth's magnetopause, *Geophys. Res. Lett.*, *20*(23), 2699–2702, doi:10.1029/93GL02622.

Christon, S. P., S. F. Daly, J. H. Eraker, M. A. Perkins, J. A. Simpson, and A. J. Tuzzolino (1979), Electron calibration of instrumentation for low energy, high intensity particle measurements at Mercury, *J. Geophys. Res.*, *84*(A8), 4277–4288, doi:10.1029/JA084iA08p04277.

Christon, S. P., (1987), A comparison of the Mercury and Earth Magnetospheres: Electron Measurements and Substorm Time Scales, *Icarus*, *71(3)*, 448-471, doi:10.1016/ 0019-1035(87)90040-6.

Daglis, I. A., Y. Kamide, G. Kasotakis, C. Mouikis, B. Wilken, E. T. Sarris, and R. Nakamura (1998), Ion composition in the inner magnetosphere: Its importance and its potential role as a discriminator between storm-time substorms and non-storm substorms, in *Fourth International Conference on Substorms (ICS-4)*, edited by S. Kokubun, and Y. Kamide, Terra/Kluwer Publications, Tokyo, 767–772.

Daglis, I. A. (2001), The storm-time ring current, *Space Sci. Rev.*, *98(3-4)*, 343-363, doi: 10.1023/A:1013873329054.

Delcourt, D. C., A. Pedersen, and J. A. Sauvaud (1990), Dynamics of single-particle orbits during substorm expansion phase, *J. Geophys. Res.*, *95*(A12), 20,853–20,865, doi:10.1029/JA095iA12p20853.

Delcourt, D. C., and J. A. Sauvaud (1994), Plasma sheet ion energization during dipolarization events, *J. Geophys. Res.*, *99*(A1), 97–108, doi:10.1029/93JA01895.

Delcourt, D. C., and R. F. Martin Jr. (1994), Application of the centrifugal impulse model to particle motion in the near-Earth magnetotail, *J. Geophys. Res.*, *99*(A12), 23,583–23,590, doi:10.1029/94JA01845.

Delcourt, D. C., J. A. Sauvaud, R. F. Martin, and T. E. Moore (1995), Gyrophase effects in the centrifugal impulse model of particle motion in the magnetotail, *J. Geophys. Res.*, *100*(A9), 17,211–17,220, doi:10.1029/95JA00657.

Delcourt, D. C., J. -A. Sauvaud, R. F. Martin, and T. E. Moore (1996a), On the nonadiabatic precipitation of ions from the near-Earth plasma sheet, *J. Geophys. Res.*, *101*(A8), 17,409–17,418, doi:10.1029/96JA01006.

Delcourt, D. C., G. Belmont, J. -A. Sauvaud, T. E. Moore, and R. F. Martin (1996b), Centrifugally driven phase bunching and related current sheet structure in the near-Earth magnetotail, *J. Geophys. Res.*, *101*(A9), 19,839–19,847, doi:10.1029/96JA01772.

Delcourt, D. C., and R. F. Martin Jr. (1999), Pitch angle scattering near energy resonances in the geomagnetic tail, *J. Geophys. Res.*, *104*(A1), 383–394, doi:10.1029/1998JA900041.

Delcourt, D. C., T. E. Moore, S. Orsini, A. Millilo, and J. -A. Sauvaud (2002), Centrifugal acceleration of ions near Mercury, *Geophys. Res. Lett.*, *29*(12), 32-1–32-4, doi:10.1029/2001GL013829.

Delcourt, D. C., S. Grimald, F. Leblanc, J. -J. Berthelier, A. Millilo, A. Mura, S. Orsini, and T. E. Moore (2003), A quantitative model of the planetary Na^+ contribution to Mercury's magnetosphere, *Ann. Geophys.*, *21*, 1723–1736, doi:10.5194/angeo-21-1723-2003.

Delcourt, D. C., K. Seki, N. Terada, and Y. Miyoshi (2005), Electron dynamics during substorm dipolarization in Mercury's magnetosphere, *Ann. Geophys.*, *23*, 3389–3398, doi:10.5194/angeo-23-3389-2005.

Delcourt, D. C., F. Leblanc, K. Seki, N. Terada, T. E. Moore, and M. -C. Fok (2007), Ion energization during substorms at Mercury, *Planet. Space Sci.*, *55*, 1502–1508, doi:10.1016/j.pss.2006.11.026.

Delcourt, D. C., Y. Saito, K. Seki, and N. Terada (2009a), Dynamics of magnetospheric ions at Mercury: some open questions awaiting BepiColombo measurements, *AIP Conference Proceedings*, *1144*(1), 102–108, doi:10.1063/1.3169272.

Delcourt, D. C., Y. Saito, J. -M. Illiano, N. Krupp, J. -J. Berthelier, D. Fontaine, M. Fraenz, F. Leblanc, H. Fischer, S. Yokota, H. Michalik, M. Godefroy, E. Saint-Jacques, J. -D. Techer, B. Fiethe, J. Covinhes, J. Gastou, and D. Attia (2009b), The Mass Spectrum Analyzer onboard BepiColombo MMO: Scientific objectives and prototype results, *Adv. Space Res.*, *43*, 869–874, doi:10.1016/j.asr.2008.12.002.

Delcourt, D. C., T. E. Moore, and M. -C. H. Fok (2010), Ion dynamics during compression of Mercury's magnetosphere, *Ann. Geophys.*, *28*, 1467–1474, doi:10.5194/angeo-28-1467-2010.

Delcourt, D. C., K. Seki, N. Terada, and T. E. Moore (2012), Centrifugally stimulated exospheric ion escape at Mercury, *Geophys. Res. Lett.*, *39*, L22105, doi:10.1029/2012GL054085.

Delcourt, D. C., Y. Saito, F. Leblanc, C. Verdeil, S. Yokota, M. Fraenz, H. Fischer, B. Fiethe, B. Katra, D. Fontaine, J. -M. Illiano, J. -J. Berthelier, N. Krupp, U. Buhrke, F. Bubenhagen, and H. Michalik

(2016), The Mass Spectrum Analyzer (MSA) on board the BepiColombo MMO, *J. Geophys. Res.*, *121*(7), 6749–6762, doi:10.1002/2016JA022380.

Delcourt, D. C., H. V. Malova, and L. M. Zelenyi (2017), On the response of quasi-adiabatic particles to magnetotail reconfigurations, *Ann. Geophys.*, *35*, 11-23, doi:10.5194/angeo-35-11-2017.

DiBraccio, G. A., J. A. Slavin, S. A. Boardsen, B. J. Anderson, H. Korth, T. H. Zurbuchen, J. M. Raines, D. N. Baker, R. L. McNutt Jr., and S. C. Solomon (2013), MESSENGER observations of magnetopause structure and dynamics at Mercury, *J. Geophys. Res.*, *118*(3), 997–1008, doi:10.1002/jgra.50123.

Dungey, J. W. (1961), Interplanetary magnetic field and the auroral zones, *Phys. Rev. Lett.*, *6*(2), 47–48, doi:10.1103/PhysRevLett.6.47.

Elphic, R. C., and A. I. Ershkovich (1984), On the stability of the ionopause of Venus, *J. Geophys. Res.*, *89*(A2), 997–1002, doi:10.1029/JA089iA02p00997.

Eraker, J. H., and J. A. Simpson (1986), Acceleration of charged particles in Mercury's magnetosphere, *J. Geophys. Res.*, *91*(A9), 9973–9993, doi:10.1029/JA091iA09p09973.

Fritts, D. C., T. L. Palmer, Ø. Andreassen, and L. Lie (1996), Evolution and breakdown of Kelvin-Helmholtz billows in stratified compressible flows. part 1: Comparison of two-and three-dimensional flows, *J. Atmos. Sci.*, *53*(22), 3173–3191, doi:10.1175/1520-0469(1996)053<3173:EABOKB>2.0.CO;2.

Fujimoto, M., and T. Terasawa (1994), Anomalous ion mixing within an MHD scale Kelvin-Helmholtz vortex, *J. Geophys. Res.*, *99*(A5), 8601–8613, doi:10.1029/93JA02722.

Fujimoto, M., T. Tonooka, and T. Mukai (2003), Vortex-like fluctuations in the magnetotail Flanks and their possible roles in plasma transport, the Earth's Low-Latitude Boundary Layer, *Geophys. Monogr. Ser.,* 133, edited by P. T. Newell and T. Onsager (23), 241, doi:10.1029/133GM24.

Fujimoto, M., W. Baumjohann, K. Kabin, R. Nakamura, J. A. Slavin, N. Terada, and L. Zelenyi (2007), Hermean magnetosphere-solar wind interaction, *Space Sci. Rev.*, *132*(2–4), 529–550, doi:10.1007/s11214-007-9245-8.

Fuselier, S. A., and W. S. Lewis (2011), Properties of near-Earth magnetic reconnection from in-situ observations, *Space Sci. Rev.*, *160*, 95–121, doi:10.1007/s11214-011-9820-x.

Gershman, D. J., J. M. Raines, J. A. Slavin, T. H. Zurbuchen, T. Sundberg, S. A. Boardsen, B. J. Anderson, H. Korth, and S. C. Solomon (2015), MESSENGER observations of multiscale Kelvin-Helmholtz vortices at Mercury, *J. Geophys. Res.*, *120*(6), 4354–4368, doi:10.1002/2014JA020903.

Gingell, P. W., T. Sundberg, and D. Burgess (2015), The impact of a hot sodium ion population on the growth of the Kelvin-Helmholtz instability in Mercury's magnetotail, *J. Geophys. Res.*, *120*(7), 5432–5442, doi:10.1002/2015JA021433.

Goldsten, J. O., E. A. Rhodes, W. V. Boynton, W. C. Feldman, D. J. Lawrence, J. I. Trombka, D. M. Smith, L. G. Evans, J. White, N. W. Madden, P. C. Berg, G. A. Murphy, R. S. Gurnee, K. Strohbehn, B. D. Williams, E. D. Schaefer, C. A. Monaco, C. P. Cork, J. Del Eckels, W. O. Miller, M. T. Burks, L. B. Hagler, S. J. DeTeresa, and M. C. Witte (2007), The MESSENGER Gamma-Ray and Neutron Spectrometer, *Space Sci. Rev.*, *131*(1–4), 339–391, doi:10.1007/s11214-007-9262-7.

Hasegawa, H., M. Fujimoto, T. -D. Phan, H. Reme, A. Balogh, M. W. Dunlop, C. Hashimoto, and R. TanDokoro (2004), Transport of solar wind into Earth's magnetosphere through rolled-up Kelvin-Helmholtz vortices, *Nature*, *430*(7001), 755–758, doi:10.1038/nature02799.

von Helmholtz, H. (1868), XLIII. On discontinuous movements of fluids , *The London, Edinburgh, and Dublin Philosophical Magazine and Journal of Science 4*, *36*(244), 337-346, doi:10.1080/14786446808640073.

Ho, G. C., R. D. Starr, S. M. Krimigis, J. D. Vandegriff, D. N. Baker, R. E. Gold, B. J. Anderson, H. Korth, D. Schriver, R. L. McNutt Jr., and S. C. Solomon (2016), MESSENGER observations of suprathermal electrons in Mercury's magnetosphere, *Geophys. Res. Lett.*, *43*(2), 550–555, doi:10.1002/2015GL066850.

Hwang, K. -J., M. M. Kuznetsova, F. Sahraoui, M. L. Goldstein, E. Lee, and G. K. Parks (2011), Kelvin-Helmholtz waves under southward interplanetary magnetic field, *J. Geophys. Res.*, *116*(A8), A08210, doi:10.1029/2011JA016596.

Jia, X., J. A. Slavin, T. I. Gombosi, L. K. S. Daldorff, G. Toth, and B. van der Holst (2015), Global MHD simulations of Mercury's magnetosphere with coupled planetary interior: Induction effect of the planetary conducting core on the global interaction, *J. Geophys. Res.*, *120*(6), 4763–4775, doi:10.1002/2015JA021143.

Johnson, C. L., M. E. Purucker, H. Korth, B. J. Anderson, R. M. Winslow, M. M. H. Al Asad, J. A. Slavin, I. I. Alexeev, R. J. Phillips, M. T. Zuber, and S. C. Solomon (2012), MESSENGER Observations of Mercury's Magnetic Field Structure, *J. Geophys. Res.*, *117*(E12), E00L14, doi:10.1029/2012je004217.

Keiling, A., H. Rème, I. Dandouras, J. M. Bosqued, V. Sergeev, J. -A. Sauvaud, C. Jacquey, B. Lavraud, P. Louarn, T. Moreau, C. Vallat, C. P. Escoubet, G. K. Parks, M. McCarthy, E. Möbius, E. Amata, B. Klecker, A. Korth, R. Lundin, P. Daly, and Q. -G. Zong (2004), New properties of energy-dispersed ions in the plasma sheet boundary layer observed by Cluster, *J. Geophys. Res.*, *109*(A5), A05215, doi:10.1029/2003JA010277.

Kelvin, W., The influence of wind on waves in water supposed frictionless. (1871) *Philos.Mag.*, 42:368-374.

Koskinen, H. E. J., and T. I. Pulkkinen (1995), Midnight velocity shear zone and the concept of Harang discontinuity, *J. Geophys. Res.*, *100*(A6), 9539–9547, doi:10.1029/95JA00228.

Kurganov, A., and E. Tadmor (2000), New high-resolution central schemes for nonlinear conservation laws and convection-diffusion equations, *J. Comput. Phys.*, *160*(1), 214–282, doi:10.1006/jcph.2000.6459.

Lawrence, D. J., Brian J. Anderson, D. N. Baker, W. C. Feldman, G. C. Ho, H. Korth, R. L. McNutt Jr., P. N. Peplowski, S. C. Solomon, R. D. Starr, J. D. Vandegriff, and R. M. Winslow (2015), Comprehensive survey of energetic electron events in Mercury's magnetosphere with data from the MESSENGER Gamma-Ray and Neutron Spectrometer, *J. Geophys. Res.*, *120*(4), 2851–2876, doi:10.1002/2014JA020792.

Leblanc, F., D. C. Delcourt, and R. E. Johnson (2003), Mercury's sodium exosphere: Magnetospheric ion recycling, *J. Geophys. Res.*, *108*(E12), 5136, doi:10.1029/2003JE002151.

Lee, D. -Y., H. -S. Kim, S. Ohtani, and M. Y. Park (2012), Statistical characteristics of plasma flows associated with magnetic dipolarizations in the near-tail region of $r < 12\ R_E$, *J. Geophys. Res.*, *117*(A1), A01207, doi:10.1029/2011JA017246.

Liljeblad, E., T. Sundberg, T. Karlsson, and A. Kullen (2014), Statistical investigation of Kelvin-Helmholtz waves at the magnetopause of Mercury, *J. Geophys. Res.*, *119*(12), 9670–9683, doi:10.1002/2014JA020614.

Liljeblad, E., T. Karlsson, T. Sundberg, and A. Kullen (2016), Observations of magnetospheric ULF waves in connection with the Kelvin-Helmholtz instability at Mercury, *J. Geophys. Res.*, *121*(9), 8576–8588, doi:10.1002/2016JA023015.

Lin, Y., J. R. Johnson, and X. Y. Wang (2010), Hybrid simulation of mode conversion at the magnetopause, *J. Geophys. Res.*, *115*(A4), A04208, doi:10.1029/2009JA014524.

Lyons, L. R., and T. W. Speiser (1982), Evidence for current sheet acceleration in the geomagnetic tail, *J. Geophys. Res.*, *87*(A4), 2276–2286.

McClintock, W. E., E. T. Bradley, R. J. Vervack Jr., R. M. Killen, A. L. Sprague, N. R. Izenberg, and S. C. Solomon (2008), Mercury's exosphere: Observations during MESSENGER's first Mercury flyby, *Science*, *321*(5885), 92–94, doi:10.1126/science.1159467.

Miura, A. (1984), Anomalous transport by magnetohydrodynamic Kelvin-Helmholtz instabilities in the solar wind-magnetospheric interaction, *J. Geophys. Res.*, *89*(A2), 801–818, doi:10.1029/JA089iA02p00801.

Mozer, F. S., H. Hayakawa, S. Kokubun, M. Nakamura, T. Okada, T. Yamamoto, and K. Tsuruda (1994), The morningside low-latitude boundary layer as determined from electric and magnetic field measurements on Geotail, *Geophys. Res. Lett.*, *21*(25), 2983–2986, doi:10.1029/94GL01296.

Ness, N. F., K. W. Behannon, R. P. Lepping, Y. C. Whang, and K. H. Schatten (1974), Magnetic field observations near Mercury: Preliminary results from Mariner 10, *Science*, *185*(4146), 151–160, doi:10.1126/science.185.4146.151.

Ness, N. F., K. W. Behannon, R. P. Lepping, and Y. C. Whang (1975), The magnetic field of Mercury, 1, *J. Geophys. Res.*, *80*(19), 2708–2716, doi:10.1029/JA080i019p02708.

Ness, N. F. (1979), The Magnetic field of Mercury, *Phys. Earth Planet. Inter.*, *20*(1979), 209–217, doi:10.1016/0031-9201(79)90044-X.

Northrop, T. G. (1963). The adiabatic motion of charged particles. New York: Wiley Intersci.

Nosé, M., A. T. Y. Lui, S. Ohtani, B. H. Mauk, R. W. McEntire, D. J. Williams, T. Mukai, and K. Yumoto (2000a), Acceleration of oxygen ions of ionospheric origin in the near-Earth magnetotail during substorms, *J. Geophys. Res.*, *105*(A4), 7669–7677, doi:10.1029/1999JA000318.

Nosé, M., S. Ohtani, A. T. Y. Liu, S. P. Christon, R. W. McEntire, D. J. Williams, T. Mukai, Y. Saito, and K. Yumoto (2000b), Change of energetic ion composition in the plasma sheet during substorms, *J. Geophys. Res.*, *105*(A10), 23,277–23,286, doi:10.1029/2000JA000129.

Nykyri, K., and A. Otto (2001), Plasma transport at the magnetospheric boundary due to reconnection in Kelvin-Helmholtz vortices, *Geophys. Res. Lett.*, *28*(18), 3565–3568, doi:10.1029/2001GL013239.

Paral, J., and R. Rankin (2013), Dawn-dusk asymmetry in the Kelvin-Helmholtz instability at Mercury, *Nat. Commun.*, *4*, 1645, doi:10.1038/Ncomms2676.

Peer, A. A. I., A. Gopaul, M. Z. Dauhoo, and M. Bhuruth (2008), A new fourth-order non-oscillatory central scheme for hyperbolic conservation laws, *Applied Numerical Mathematics*, *58*(5), 674–688, doi:10.1016/j.apnum.2007.02.004.

Potter, A. E., and T. H. Morgan (1985), Discovery of sodium in the atmosphere of Mercury, *Science*, *229*(4714), 651–653, doi:10.1126/science.229.4714.651.

Potter, A. E., and T. H. Morgan (1997), Sodium and potassium atmospheres of Mercury, *Planet. Space. Sci.*, *45*(1), 95–100, doi: 10.1016/S0032-0633(96)00100-6.

Potter, A. E., and R. M. Killen (2008), Observations of the sodium tail of Mercury, *Icarus*, *194*(1), 1–12, doi:10.1016/j.icarus.2007.09.023.

Press, W. H., S. A. Teukolsky, W. T. Vetterling, and B. P. Flannery (1992) Neumerical Recipies in C: The art of scientific computing second edition, Cambridge university press, p.710-713.

Raines, J. M., J. A. Slavin, T. H. Zurbuchen, G. Gloeckler, B. J. Anderson, D. N. Baker, H. Korth, S. M. Krimigis, and R. L. McNutt Jr. (2011), MESSENGER observations of the plasma environment near Mercury, *Planet. Space Sci.*, *59*(15), 2004–2015, doi:10.1016/j.pss.2011.02.004.

Raines, J. M., D. J. Gershman, T. H. Zurbuchen, M. Sarantos, J. A. Slavin, J. A. Gilbert, H. Korth, B. J. Anderson, G. Gloeckler, S. M. Krimigis, D. N. Baker, R. L. McNutt Jr., and S. C. Solomon (2013), Distribution and compositional variations of plasma ions in Mercury's space environment: The first three Mercury years of MESSENGER observations, *J. Geophys. Res.*, *118*(4), 1604–1619, doi:10.1029/2012JA018073.

Raines, J. M., D. J. Gershman, J. A. Slavin, T. H. Zurbuchen, H. Korth, B. J. Anderson, and S. C. Solomon (2014), Structure and dynamics of Mercury's magnetospheric cusp: MESSENGER measurements of protons and planetary ions, *J. Geophys. Res.*, *119*(8), 6587–6602, doi:10.1002/2014JA020120.

Rothwell, P. L., M. B. Silevitch, L. P. Block, and C. -G. Falthammar (1994), O^+ phase bunching and auroral arc structure, *J. Geophys. Res.*, *99*(A2), 2461–2470, doi:10.1029/93JA02541.

Russell, C. T., and R. C. Elphic (1978), Initial ISEE magnetometer results: Magnetopause observations, *Space Science Rev.*, *22*(1978), 681–715, doi:10.1007/BF00212619.

Russell, C. T., and R. J. Walker (1985), Flux transfer events at Mercury, *J. Geophys. Res.*, *90*(A11), 11067–11074, doi:10.1029/JA090iA11p11067.

Saito, Y., J. -A. Sauvaud, M. Hirahara, S. Barabash, D. C. Delcourt, T. Takashima, K. Asamura, and BepiColombo MMO/MPPE team (2010), Scientific objectives and instrumentation of Mercury Plasma Particle Experiment (MPPE) onboard MMO, *Planet. Space Sci.*, *58*(1–2), 182–200, doi:10.1016/j.pss.2008.06.003.

Schriver, D., P. M. Trávníček, B. J. Anderson, M. Ashour-Abdalla, D. N. Baker, M. Benna, S. A. Boardsen, R. E. Gold, P. Hellinger, G. C. Ho, H. Korth, S. M. Krimigis, R. L. McNutt Jr., J. M. Raines, R. L. Richard, J. A. Slavin, S. C. Solomon, R. D. Starr, and T. H. Zurbuchen (2011a), Quasi-trapped ion and electron populations at Mercury, *Geophys. Res. Lett.*, *38*(23), L23103, doi:10.1029/2011GL049629.

Schriver, D., P. M. Trávníček, M. Ashour-Abdalla, R. L. Richard, P. Hellinger, J. A. Slavin, B. J. Anderson, D. N. Baker, M. Benna, S. A. Boardsen, R. E. Gold, G. C. Ho, H. Korth, S. M. Krimigis, W. E. McClintock, J. L. McLain, T. M. Orlando, M. Sarantos, A. L. Spragur, R. D. Starr, (2011b), Electron transport and precipitation at Mercury during the MESSENGER flybys: Implications for electron-stimulated desorption, *Planet. Space Sci.*, 59(15), 2026-2036, doi:10.1016/j.pss.2011.03.008.

Seki, K., N. Terada, M. Yagi, D. C. Delcourt, F. Leblanc, and T. Ogino (2013), Effects of the surface conductivity and the IMF strength on the dynamics of planetary ions in Mercury's magnetosphere, *J. Geophys. Res.*, *118*(6), 3233–3242, doi:10.1002/jgra.50181.

Sergeev, V. A., E. M. Sazhina, N. A. Tsyganenko, J. Å. Lundblad, and F. Søraas (1983), Pitch-angle scattering of energetic protons in the magnetotail current sheet as the dominant source of their isotropic precipitation into the nightside ionosphere, *Planet. Space Sci.*, *31*(10), 1147–1155, doi:10.1016/0032-0633(83)90103-4.

Sergeev, V. A., T. I. Pulkkinen, R. J. Pellinen, and N. A. Tsyganenko (1994), Hybrid state of the tail magnetic configuration during steady convection events, *J. Geophys. Res.*, *99*(A12), 23571–23582, doi:10.1029/94JA01980.

Shu, C. -W. and S. Osher (1989), Efficient implementation of essentially non-oscillatory shock capturing schemes, II, *J. Comput. Phys.*, *83*(1), 32–78, doi:10.1016/0021-9991(89)90222-2.

Shue, J. -H., P. Song, C. T. Russell, J. T. Steinberg, J. K. Chao, G. Zastenker, O. L. Vaisberg, S. Kokubun, H. J. Singer, T. R. Detman, and H. Kawano (1998), Magnetopause location under extreme solar wind conditions, *J. Geophys. Res.*, *103*(A8), 17,691–17,700, doi:10.1029/98JA01103.

Simpson, J. A., J. H. Eraker, J. E. Lamport, and P. H. Walpole (1974), Electrons and protons accelerated in Mercury's magnetic field, *Science*, *185*(4146), 160–166, doi:10.1126/science.185.4146.160.

Siscoe, G. L., N. F. Ness, and C. M. Yeates (1975), Substorms on Mercury?, *J. Geophys. Res.*, *80*(31), 4359–4363, doi:10.1029/JA080i031p04359.

Slavin, J. A., and R. E. Holzer (1979), The effect of erosion on the solar wind stand-off distance at Mercury, *J. Geophys. Res.*, *84*(A5), 2076–2082, doi:10.1029/JA084iA05p02076.

Slavin, J. A., M. H. Acuña, B. J. Anderson, D. N. Baker, M. Benna, G. Gloeckler, R. E. Gold, G. C. Ho, R. M. Killen, H. Korth, S. M. Krimigis, R. L. McNutt Jr., L. R. Nittler, J. M. Raines, D. Schriver, S. C. Solomon, R. D. Starr, P. Trávníček, and T. H. Zurbuchen (2008), Mercury's magnetosphere after MESSENGER's first flyby, *Science*, *321*(5885), 85–89, doi:10.1126/science.1159040.

Slavin, J. A., M. H. Acuña, B. J. Anderson, D. N. Baker, M. Benna, S. A. Boardsen, G. Gloeckler, R. E. Gold, G. C. Ho, H. Korth, S. M. Krimigis, R. L. McNutt Jr., J. M. Raines, M. Sarantos, D. Schriver, S. C. Solomon, P. Trávníček, and T. H. Zurbuchen (2009a), MESSENGER observations of magnetic reconnection in Mercury's magnetosphere, *Science*, *324*(5927), 606–610, doi:10.1126/science.1172011.

Slavin, J. A., B. J. Anderson, T. H. Zurbuchen, D. N. Baker, S. M. Krimigis, M. H. Acuña, M. Benna, S. A. Boardsen, G. Gloeckler, R. E. Gold, G. C. Ho, H. Korth, R. L. McNutt Jr., J. M. Raines, M. Sarantos, D. Schriver, S. C. Solomon, and P. Trávníček (2009b), MESSENGER observations of Mercury's magnetosphere during northward IMF, *Geophys. Res. Lett.*, *36*(2), L02101, doi:10.1029/2008GL036158.

Slavin, J. A., B. J. Anderson, D. N. Baker, M. Benna, S. A. Boardsen, G. Gloeckler, R. E. Gold, G. C. Ho, H. Korth, S. M. Krimigis, R. L. McNutt Jr., L. R. Nittler, J. M. Raines, M. Sarantos, D. Schriver, S. C. Solomon, R. D. Starr, P. M. Trávníček, and T. H. Zurbuchen (2010a), MESSENGER observations of extreme loading and unloading of Mercury's magnetic tail, *Science*, *329*(5992), 665–668, doi:10.1126/science.1188067.

Slavin, J. A., R. P. Lepping, C. -C. Wu, B. J. Anderson, D. N. Baker, M. Benna, S. A. Boardsen, R. M. Killen, H. Korth, S. M. Krimigis, W. E. McClintock, R. L. McNutt Jr., M. Sarantos, D. Schriver, S. C. Solomon, P. Trávníček and T. H. Zurbuchen (2010b), MESSENGER observations of large flux transfer events at Mercury, *Geophys. Res. Lett.*, *37*(2), L02105, doi:10.1029/2009GL041485.

Slavin, J. A., B. J. Anderson, D. N. Baker, M. Benna, S. A. Boardsen, R. E. Gold, G. C. Ho, S. M. Imber, H. Korth, S. M. Krimigis, R. L. McNutt Jr., J. M. Raines, M. Sarantos, D. Schriver, S. C. Solomon, P. Trávníček, and T. H. Zurbuchen (2012), MESSENGER and Mariner 10 flyby observations of magnetotail structure and dynamics at Mercury, *J. Geophys. Res.*, *117*(A1), A01215, doi:10.1029/2011JA016900.

Slavin, J. A., G. A. DiBraccio, D. J. Gershman, S. M. Imber, G. K. Poh, J. M. Raines, T. H. Zurbuchen, X. Jia, D. N. Baker, K. -H. Glassmeier, S. A. Livi, S. A. Boardsen, T. A. Cassidy, M. Sarantos, T. Sundberg, A. Masters, C. L. Johnson, R. M. Winslow, B. J. Anderson, H. Korth, R. L. McNutt Jr., and S. C. Solomon (2014), MESSENGER observations of Mercury's dayside magnetosphere under extreme solar wind conditions, *J. Geophys. Res.*, *119*(10), 8087–8116, doi:10.1002/2014JA020319.

Speiser, T. W. (1965), Particle trajectories in model current sheets: 1. Analytical solutions, *J. Geophys. Res.*, *70*(17), 4219–4226, doi:10.1029/JZ070i017p04219.

Sundberg, T., S. A. Boardsen, J. A. Slavin, L. G. Blomberg, and H. Korth (2010), The Kelvin-Helmholtz instability at Mercury: An assessment, *Planet. Space Sci.*, *58*(11), 1434–1441, doi:10.1016/j.pss.2010.06.008.

Sundberg, T., S. A. Boardsen, J. A. Slavin, L. G. Blomberg, J. A. Cumnock, S. C. Solomon, B. J. Anderson, and H. Korth (2011), Reconstruction of propagating Kelvin-Helmholtz vortices at Mercury's magnetopause, *Planet. Space Sci.*, *59*(15), 2051–2057, doi:10.1016/j.pss.2011.05.008.

Sundberg, T., S. A. Boardsen, J. A. Slavin, B. J. Anderson, H. Korth, T. H. Zurbuchen, J. M. Raines, and S. C. Solomon (2012a), MESSENGER orbital observations of large-amplitude Kelvin-Helmholtz waves at Mercury's magnetopause, *J. Geophys. Res.*, *117*(A4), A04216, doi:10.1029/2011JA017268.

Sundberg, T., S. A. Boardsen, B. J. Anderson, H. Korth, G. C. Ho, D. Schriver, V. M. Uritsky, T. H. Zurbuchen, J. M. Raines, D. N. Baker, S. M. Krimigis, R. L. McNutt Jr., and S. C. Solomon (2012b), MESSENGER observations of dipolarization events in Mercury's magnetotail, *J. Geophys. Res.*, *117*(A12), A00M03, doi:10.1029/2012JA017756.

Tsyganenko, N. A. (1982), Pitch angle scattering of energetic particles in the current sheet of the magnetospheric tail and stationary distribution functions, *Planet. Space Sci.*, *30*(1982), 433–437, doi:10.1016/0032-0633(82)90052-6.

Tsyganenko, N. A. (1989), A magnetospheric magnetic field model with a warped tail current sheet, *Planet. Space Sci.*, *37*(1989), 5–20, doi:10.1016/0032-0633(89)90066-4.

Wagner, J. S., J. R. Kan, and S. -I. Akasofu (1979), Particle dynamics in the plasma sheet, *J. Geophys. Res.*, *84*(A3), 891–897, doi:10.1029/JA084iA03p00891.

Wang, Y. -C., J. Mueller, U. Motschmann, and W. -H. Ip (2010), A hybrid simulation of Mercury's magnetosphere for the MESSENGER encounters in year 2008, *Icarus*, *209*(1), 46–52, doi:10.1016/j.icarus.2010.05.020.

West Jr., H. I., R. M. Buck, and M. G. Kivelson (1978a), On the configuration of the magnetotail near midnight during quiet and weakly disturbed periods: State of the magnetosphere, *J. Geophys. Res.*, *83*(A8), 3805–3817, doi:10.1029/JA083iA08p03805.

West Jr., H. I., R. M. Buck, and M. G. Kivelson (1978b), On the configuration of the magnetotail near midnight during quiet and weakly disturbed periods: Magnetic field modeling, *J. Geophys. Res.*, *83*(A8), 3819–3829, doi:10.1029/JA083iA08p03819.

Whang, Y. C. (1977), Magnetospheric magnetic field of Mercury, *J. Geophys. Res.*, *82*(7), 1024–1030, doi:10.1029/JA082i007p01024.

Winslow, R. M., B. J. Anderson, C. L. Johnson, J. A. Slavin, H. Korth, M. E. Purucker, D. N. Baker, and S. C. Solomon (2013), Mercury's magnetopause and bow shock from MESSENGER Magnetometer observations, *J. Geophys. Res.*, *118*(5), 2213–2227, doi:10.1002/jgra.50237.

Yan, G. Q., F. S. Mozer, C. Shen, T. Chen, G. K. Parks, C. L. Cai, and J. P. McFadden (2014), Kelvin-Helmholtz vortices observed by THEMIS at the duskside of the magnetopause under southward interplanetary magnetic field, *Geophys. Res. Lett.*, *41*(13), 4427–4434, doi:10.1002/2014GL060589.

Zurbuchen, T. H., J. M. Raines, G. Gloeckler, S. M. Krimigis, J. A. Slavin, P. L. Koehn, R. M. Killen, A. L. Sprague, R. L. McNutt Jr., and S. C. Solomon (2008), MESSENGER observations of the composition of Mercury's ionized exosphere and plasma environment, *Science*, *321*(5885), 90–92, doi:10.1126/science.1159314.

Zurbuchen, T. H., J. M. Raines, J. A. Slavin, D. J. Gershman, J. A. Gilbert, G. Gloeckler, B. J. Anderson, D. N. Baker, H. Korth, S. M. Krimigis, M. Sarantos, D. Schriver, R. L. McNutt Jr., and S. C. Solomon (2011), MESSENGER observations of the spatial distribution of planetary ions near Mercury, *Science*, *333*(6051), 1862–1865, doi:10.1126/science.1211302.

AGU PUBLICATIONS

Geophysical Research Letters

RESEARCH LETTER
10.1002/2017GL076586

Key Points:
- Nonadiabatic transport of heavy ions of planetary origin has been investigated in Mercury's magnetospheric flanks
- Impulsive ion energization and pitch angle scattering can occur in Kelvin-Helmholtz vortices
- Mixing of planetary and solar wind materials at the magnetopause is expected with impulsive ion energization

Correspondence to:
S. Aizawa,
aizawas@pat.gp.tohoku.ac.jp

Citation:
Aizawa, S., Delcourt, D., & Terada, N. (2018). Sodium ion dynamics in the magnetospheric flanks of Mercury. *Geophysical Research Letters*, *45*. https://doi.org/10.1002/2017GL076586

Received 28 NOV 2017
Accepted 12 JAN 2018
Accepted article online 19 JAN 2018

Sodium Ion Dynamics in the Magnetospheric Flanks of Mercury

Sae Aizawa[1,2], Dominique Delcourt[1], and Naoki Terada[2]

[1]Laboratoire de Physique des Plasmas, Ecole Polytechnique-CNRS-UPMC, Paris, France, [2]Department of Geophysics, Graduate School of Science, Tohoku University, Sendai, Japan

Abstract We investigate the transport of planetary ions in the magnetospheric flanks of Mercury. In situ measurements from the MErcury Surface, Space ENvironment, GEochemistry, and Ranging spacecraft show evidences of Kelvin-Helmholtz instability development in this region of space, due to the velocity shear between the downtail streaming flow of solar wind originating protons in the magnetosheath and the magnetospheric populations. Ions that originate from the planet exosphere and that gain access to this region of space may be transported across the magnetopause along meandering orbits. We examine this transport using single-particle trajectory calculations in model Magnetohydrodynamics simulations of the Kelvin-Helmholtz instability. We show that heavy ions of planetary origin such as Na^+ may experience prominent nonadiabatic energization as they $\boldsymbol{E} \times \boldsymbol{B}$ drift across large-scale rolled up vortices. This energization is controlled by the characteristics of the electric field burst encountered along the particle path, the net energy change realized corresponding to the maximum $E \times B$ drift energy. This nonadiabatic energization also is responsible for prominent scattering of the particles toward the direction perpendicular to the magnetic field.

1. Introduction

The MErcury Surface, Space ENvironment, GEochemistry, and Ranging (MESSENGER) spacecraft that was in orbit about Mercury from 11 March 2011 to 30 April 2015 has brought a wealth of information on the structure and dynamics of the ionized environment of this planet. The data collected by MESSENGER have revealed a number of magnetospheric processes similar to those occurring at Earth such as Flux Transfer Events at the magnetopause (e.g., Slavin et al., 2008, 2014), Kelvin-Helmholtz (KH) vortices in the magnetospheric flanks (e.g., Gershman et al., 2015; Slavin et al., 2008; Sundberg, Boardsen, et al., 2012), or substorm-like dipolarization events in the magnetotail (e.g., Slavin et al., 2008; Sundberg, Slavin, et al., 2012). The MESSENGER data also provide evidences of heavy ions in different regions of Mercury's magnetosphere that result from ionization of exospheric neutrals by solar UV (e.g., Raines et al., 2013; Zurbuchen et al., 2008, 2011). The large-scale circulation of these ions of planetary origin in the magnetosphere is of importance as they may locally contribute to mass loading and structural stability.

The present study focuses on the dynamics of these ions of planetary origin in the magnetospheric flanks of Mercury in the event of a prominent velocity shear between magnetosheath and magnetospheric plasma flows. Such a shear that is responsible for the development of large-scale KH vortices can lead to transport of material across the magnetopause. Evidences of such a KH instability development can be found for instance in Figure 3 of Sundberg, Boardsen, et al. (2012) that shows magnetic field and ion data in the dusk flank of Mercury's magnetosphere on 15 May 2011. In this figure, repeated decreases and increases of the magnetic field can be seen in association with repeated appearance and disappearance of protons, indicative of transition from magnetosphere to magnetosheath (and vice versa) as is the case with large amplitude KH waves. The repeated detection of Na^+ ions of planetary origin during these transitions raises questions concerning the transport of this heavy material that has gyroradii comparable to the characteristic scales of KH vortices. To explore the behavior of heavy ions under such conditions, we performed single-particle trajectory computations in model KH vortices obtained from Magnetohydrodynamics (MHD) simulations.

In essence, such KH vortices rapidly evolve in time. However, to gain detailed understanding of the particle behavior, we adopted here a two-step approach, that is, we first analyzed the ion dynamics in a steady vortex configuration, and second in a time-varying configuration. The first step allowed us to remove phasing effects between the particle trajectories and the rapidly changing KH vortices and to concentrate on the effect of

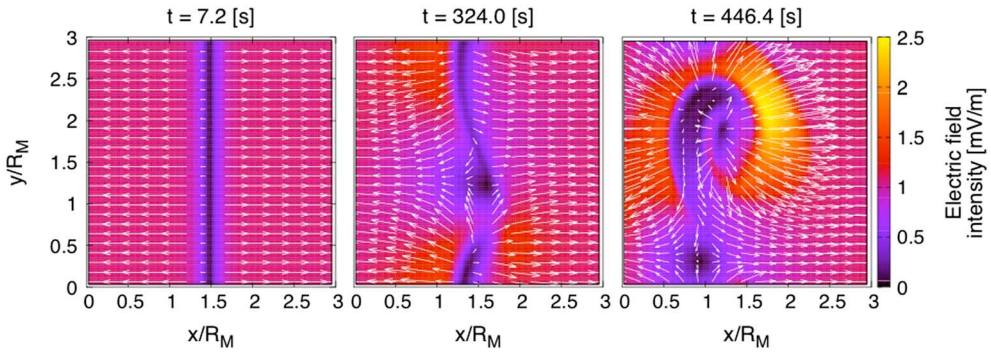

Figure 1. Color-coded electric field intensity obtained from MHD modeling in the equatorial (*X*-*Y*) plane. Panels from left to right correspond to distinct times (indicated on top) of KH instability development. White arrows show the orientation of the electric field.

abrupt electric field variations. The second step allowed us to catch the particle response in a realistic case and to generalize the nonadiabatic behaviors that were first obtained. In the following, we describe the modeling approach adopted in section 2. The results of the systematic trajectory computations will then be presented and discussed in sections 3 and 4, respectively.

2. Field Configuration and Model Ion Trajectories

Because of the large velocity shear between magnetospheric and magnetosheath plasma flows in the flanks of Mercury's magnetosphere, KH instabilities may develop along the magnetopause and possibly lead to the formation of large-scale rolled up vortices (see, e.g., Slavin et al., 2008, for first observations of these surface waves by MESSENGER). To investigate the dynamics of planetary ions under such conditions, we adopted an approach similar to that used in Large-Scale Kinetics studies at Earth (e.g., Ashour-Abdalla et al., 1994). That is, we traced test particles within field configurations derived from MHD modeling and we quantitatively examined their energy and pitch angle variations for different initial conditions.

Modeling of the KH instability development in the magnetospheric flanks was performed assuming that the velocity shear at the magnetopause is due to the tailward flow of magnetosheath protons of solar wind origin. The MHD code that we used solves the ideal MHD equations with third-order Total Variation Diminishing Runge-Kutta for time differencing and semidiscrete central scheme (Kurganov & Tadmor, 2000) combined with a fourth-order limiter (Peer et al., 2008) for space differencing. We assume that the boundary layer is a transition region between two plasma flows and that, in this region, the plasma characteristics rapidly change from one regime to the other. Here the boundary is viewed as the magnetopause, and initial profiles of velocity, magnetic field, and mass density across this boundary are set using hyperbolic tangent profiles in the usual way. All quantities are normalized by four key parameters (viz., proton mass, electron charge, initial velocity $V_0 = 10^5$ m/s, and initial number density $N_0 = 10^7$ ions/m^3 in the magnetosphere), and the instantaneous electric field calculation is performed according to Ohm's law using background flow velocity and magnetic field. Figure 1 presents an example of different $\boldsymbol{E} \times \boldsymbol{B}$ flows (equivalently, different electric field configurations) obtained at distinct times of the KH instability development. The different panels in this figure show the $\boldsymbol{E} \times \boldsymbol{B}$ flow field in the equatorial plane (*X*-*Y*), the magnetic field $\boldsymbol{B}$ pointing out of this plane (in the *Z* direction). Starting from two well-delineated regions in Figure 1 (left), it can be seen in the other panels (from left to right) that gradual mixing occurs as time goes on, with development of large rolled up vortices.

It should be stressed here that, in the present MHD simulations, the velocity shear across the boundary was set to 200 km/s and that the characteristic time scale for KH vortex growth directly depends upon this model value. For instance, would a twice larger velocity shear (viz., 400 km/s) be considered, the characteristic time scale for KH vortex growth would be twice smaller. As for propagation of this perturbation in the magnetospheric flanks, it is controlled not by the magnetosheath velocity alone but also by the magnetospheric velocity and the mass density ratio across the boundary (e.g., Nagano, 1978). This yields in the present case a propagation speed of ~80 km/s. Thus, from a quantitative viewpoint, the results presented here do

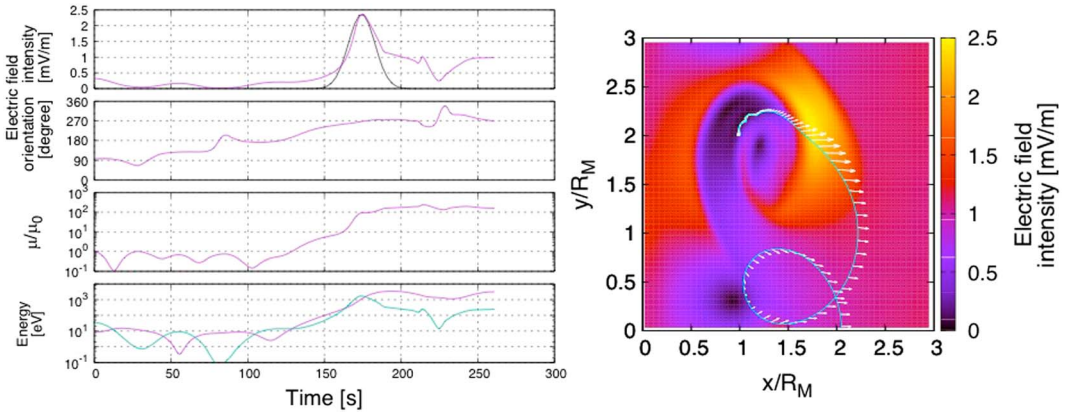

Figure 2. Model Na^+ trajectory in ***E*** configuration obtained from our MHD model (Figure 1, right). The trajectory in the *X-Y* plane is shown at right on top of color-coded ***E*** contours (white arrows show selected *E* orientations). The left panels show (from top to bottom) ***E*** intensity, ***E*** orientation, Na^+ magnetic moment (normalized to the initial value), and Na^+ energy as a function of time. The test Na^+ is initialized with 10 eV energy and 95° pitch angle. The profile in black in the top left panel shows a Gaussian fit to the prominent *E* burst, while the profile in green in the bottom left panel shows the kinetic energy corresponding to the $\boldsymbol{E} \times \boldsymbol{B}$ drift speed.

substantially depend upon the model parameters adopted but they are of general significance as far as the net outcome on ion dynamics and adiabaticity violation are concerned.

Once MHD simulations were performed, all quantities were unnormalized and test ions were traced in the field configurations obtained. This single-particle tracing was performed using the full equation of motion to account for possible variations of the particle magnetic moment (first adiabatic invariant). Indeed, for the adiabatic (guiding center) approximation to be valid, negligible field variations must occur within a cyclotron turn (see, e.g., Northrop, 1963). It will be shown hereinafter that, although the magnetic field is nearly constant (in the *Z* direction), the rapid change of ***E*** within KH vortices can lead to significant change of the particle magnetic moment (denoted μ hereinafter).

Although nonadiabatic behaviors generally are associated with prominent changes of the magnetic field, be they spatial (e.g., Ashour-Abdalla et al., 1993; Büchner & Zelenyi, 1989; Delcourt et al., 2003) or temporal (e.g., Delcourt, 2002), we focus here on a specific type of nonadiabaticity that relates to the rapid change of the electric field, or equivalently of the $\boldsymbol{E} \times \boldsymbol{B}$ flow field. A similar type of nonadiabatic behaviors was reported for instance in the region connected to the Harang discontinuity in the near-Earth magnetosphere (Rothwell et al., 1994). In the present computations, the local electric field at each step of the test ion trajectories was linearly interpolated from the $\boldsymbol{E} \times \boldsymbol{B}$ maps obtained from MHD modeling. For simplicity and to thoroughly understand the particle behavior, we first consider the field configuration that is shown in Figure 1 (right) and we assume this configuration to be steady throughout the trajectory computations. As mentioned above, such a use of a given MHD simulation frame allows us to remove as a first step phasing effects between particle trajectories and the time-evolving KH vortices and to focus on the impact of the electric field variations. As a second step, particles were traced in the time-evolving configuration and the computation results were made more general as will be seen in section 4. The trajectory computations were performed using a fourth-order Runge-Kutta technique with a variable time step corresponding to a few degrees of particle gyration.

It should be stressed also here that the periodical boundary condition in the *Y* direction that was assumed in our MHD simulations was not used for particle tracing in a fixed simulation frame, this tracing being interrupted when the test particle exits the simulation box. In contrast, the periodical boundary condition was used for tracking the particles in the time-evolving configuration to allow for phasing effects between the particles and the development of the KH vortices. Also, in situ measurements from MESSENGER suggest that the typical wavelength of KH vortices is ~1.5 R_M (e.g., Sundberg et al., 2011), a typical spatial scale that is well reproduced in our simulation box (see Figure 1). As for the velocity shear, it was assumed to spread over 1 R_M which was considered as an upper limit for this characteristic scale. Simulations like the present ones usually

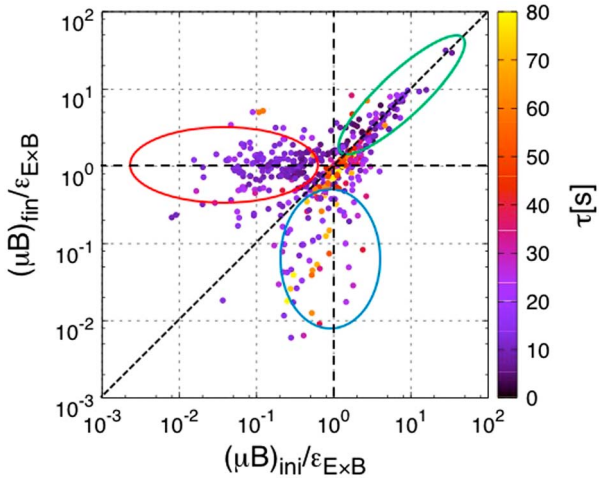

Figure 3. Final perpendicular energy (normalized to the maximum $\boldsymbol{E}\times\boldsymbol{B}$ drift energy) of Na^+ ions as a function of initial perpendicular energy (normalized to the maximum $\boldsymbol{E}\times\boldsymbol{B}$ drift energy). The time scale of the corresponding *E* burst is coded according to the color scale at right.

contain sets of parameters that can be adjusted in different ways, but these do not affect in essence the main outcomes such as the adiabaticity violation that we describe hereinafter.

Figure 2 shows an example of ion trajectories obtained. We consider here a test Na^+ with a few eV initial energy in the nearly perpendicular direction (95° pitch angle) as would be the case for instance for a sodium neutral in the extended exosphere of Mercury that would be located in the vicinity of the magnetopause and that would be suddenly ionized by a solar UV photon. In Figure 2 (right), this test Na^+ was launched from an arbitrary position inside the KH vortex and traced until it leaves the simulation box. In Figure 2 (left), it can be seen that, after ~150 s time of flight, the Na^+ magnetic moment rapidly increases by about 2 orders of magnitude. This μ change coincides with an impulsive enhancement of the electric field intensity (top left panel) up to ~2.5 mV/m, while the electric field orientation (second panel from top) does not change appreciably. On the other hand, looking at Figure 2 (left, bottom), it can be seen that the final energy realized by the test Na^+ approximately corresponds to the maximum energy associated with the $\boldsymbol{E}\times\boldsymbol{B}$ drift (green profile). Figure 2 thus suggests that particle motion inside KH vortices essentially is adiabatic except for short time intervals during which particles are subjected to bursts of electric field that rapidly raise the ion perpendicular energy up to the peak $\boldsymbol{E}\times\boldsymbol{B}$ drift energy (denoted by $\varepsilon_{E\times Bmax}$ hereinafter).

Here it should be stressed that similar nonadiabatic behaviors with large μ increase were obtained for nearly field-aligned particles with large initial energies (equivalently, small perpendicular energy). In contrast, no μ change was obtained for test ions with initial energies and pitch angles such that their initial perpendicular energy exceeds $\varepsilon_{E\times Bmax}$. The nonadiabatic character of the motion thus appears to depend upon the initial perpendicular energy that particles have with respect to the maximum kinetic energy $\varepsilon_{E\times Bmax}$ (equivalently, maximum $\boldsymbol{E}\times\boldsymbol{B}$ drift speed) encountered along their path.

3. Statistical Analysis of Ion Energization

To investigate the transport of heavy ions through KH vortices in a more quantitative manner, we performed systematic Na^+ trajectory computations and compiled a statistics of $\boldsymbol{E}$ bursts and associated μ changes. This statistics was obtained by considering test Na^+ in different simulation frames after the linear growth phase (396 s, 424.8 s, and 446.4 s) with different initial energies (10 eV, 50 eV, 100 eV, 500 eV, 1 keV, 2.5 keV, 5 keV, and 10 keV), pitch angles (from 0° to 180° by steps of 10°), gyration phases (from 0° to 360° by steps of 10°) and launched in the vicinity of the KH vortices. In this statistical analysis, $\boldsymbol{E}$ bursts were characterized using Gaussian fits of the form: $E = E_{max}\exp\{-[(t-t_o)/\tau]^2\}$ (E_{max} being the maximum $\boldsymbol{E}$ intensity, t_o, the time of the burst center, and τ, the characteristic time scale of the burst). We checked all particle trajectories by eye and selected only those experienced clear $\boldsymbol{E}$ bursts also including the case of multiple $\boldsymbol{E}$ bursts. A data set of ~500 model cases of $\boldsymbol{E}$ bursts and associated μ changes was obtained that is summarized in Figure 3. Here the postburst perpendicular energy of Na^+ (normalized to $\varepsilon_{E\times Bmax}$) is presented as a function of preburst perpendicular energy (normalized to $\varepsilon_{E\times Bmax}$) together with color-coded time scale of the $\boldsymbol{E}$ bursts encountered along the ion trajectories.

Figure 3 displays several features of interest. First, it can be seen that ions that have an initial perpendicular energy $(\mu B)_{ini}$ smaller than $\varepsilon_{E\times Bmax}$ tend to be systematically energized up to $\varepsilon_{E\times Bmax}$ (horizontal branch encircled in red). This behavior corresponds to that illustrated in Figure 2. Figure 3 also reveals that ions with initial perpendicular energies comparable to $\varepsilon_{E\times Bmax}$ may actually lose energy during transport (vertical branch encircled in blue). This latter behavior is that of particles traveling against the electric field during the burst. Finally, a third behavior is noticeable in Figure 3 for ions with initial energies larger than $\varepsilon_{E\times Bmax}$. Here no significant energization is obtained and postburst perpendicular energies spread along the first bisector (oblique branch encircled in green).

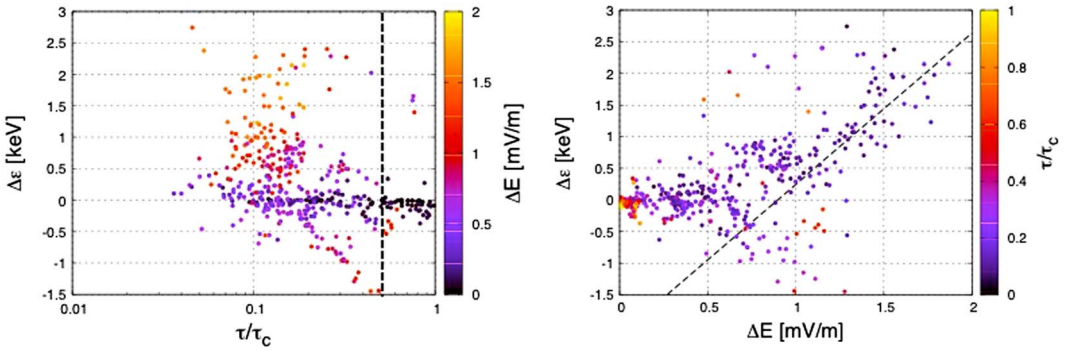

Figure 4. Net energy change of Na^+ ions as a function of (left) ***E*** burst time scale (normalized to the ion gyroperiod) and (right) ***E*** burst amplitude. Color codes correspond to (left) *E* burst amplitude and (right) ***E*** burst time scale (normalized to the ion gyroperiod). The dashed lines in the right and left panels show the linear profile obtained from a least squares fit and the $\tau/\tau_C = 0.5$ ratio, respectively.

Another view of the ion behaviors during transport through KH vortices can be obtained from Figure 4 that shows the above statistical results using a different format, viz., net energy change versus *E* burst time scale (normalized to the ion gyroperiod, τ_C) in the left panel and versus ***E*** burst amplitude in the right panel. Not surprisingly, it can be seen in Figure 4 (right) that the larger the burst amplitude ΔE, the larger the energy gain. Note here the nearly linear correlation between these two quantities (oblique dashed line). On the other hand, in Figure 4 (left), it can be seen that when the *E* burst duration nears the gyroperiod (i.e., $2\tau = \tau_C$, or equivalently $\tau/\tau_C = 0.5$ as indicated by the vertical dashed line), ions may be subjected to energy loss. In contrast, when the ***E*** burst duration is significantly smaller than the gyroperiod (i.e., $\tau/\tau_C \ll 0.5$), most ions are subjected to energy gain, this gain being more pronounced for larger burst amplitude as evidenced from the color-coded ΔE variations.

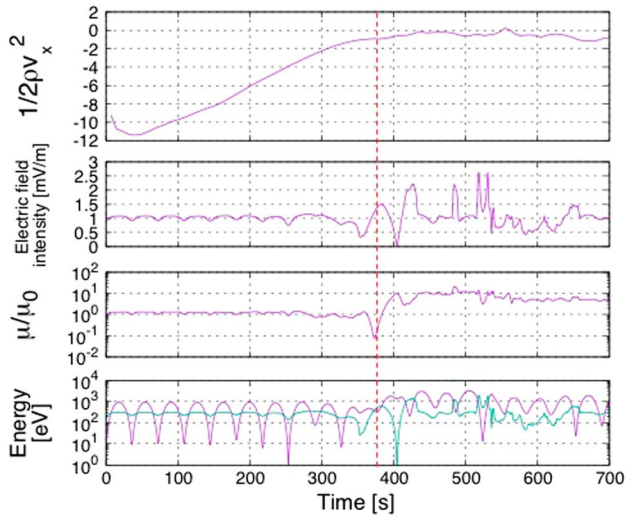

Figure 5. (top) Time evolution of the maximum kinetic energy in the direction perpendicular to the shear layer, $0.5\ \rho V_X^2$. The vertical dotted line near 370 s indicates the duration of KH linear growth. (bottom) Trajectory parameters of a test Na^+ in the time-varying case: ***E*** intensity, magnetic moment (normalized to the initial value), and energy versus time. The test Na^+ is initialized with 10 eV energy and 90° pitch angle. The green profile in the bottom panel shows the kinetic energy corresponding to the $\boldsymbol{E} \times \boldsymbol{B}$ drift speed.

4. Discussion

The above simulations of Na^+ transport in MHD field configurations demonstrate that planetary ions may be subjected to prominent nonadiabatic energization while drifting through KH vortices in Mercury's magnetospheric flanks. This nonadiabatic response results from abrupt (on the time scale of the ion gyroperiod or less) ***E*** bursts at some point of the particle trajectories and it can lead to net energization up to the maximum $\boldsymbol{E} \times \boldsymbol{B}$ drift energy. To better understand the particle behavior, the above computations were performed assuming steady KH vortices (see, e.g., Figure 2). To make these results more general, further computations were carried out considering the full temporal development of KH vortices. Test Na^+ ions were launched with given initial energy and pitch angle at the onset of the KH instability growth, and their trajectories were reconstructed in the time varying MHD field recalculated at every update time step derived from the maximum $\boldsymbol{E} \times \boldsymbol{B}$ value in the simulation box.

Figure 5 shows an example of Na^+ behaviors obtained. To characterize the growth of the KH instability, it is useful to monitor the kinetic energy in the direction perpendicular to the shear layer, viz., $0.5\ \rho V_X^2$ (e.g., Keppens et al., 1999). The temporal variation of this quantity is shown in the top panel of Figure 5. Here the vertical dashed line indicates the duration of KH linear growth and it can be seen that this linear phase terminates at $t \approx 370$ s. The bottom panels of Figure 5 show selected Na^+ trajectory parameters. By comparison of center and bottom panels, it can be seen that, after ~370 s time of flight (i.e., during the KH linear

growth according to the top panel of Figure 5), the test Na^+ is subjected to a prominent ***E*** burst and its magnetic moment (normalized to the initial value) rapidly increases by nearly 2 orders of magnitude (the Na^+ energy reaching approximately the $\varepsilon_{E \times Bmax}$ level shown in green). In other words, the particle behavior in time-varying conditions closely resembles that described above in a steady state configuration (see, e.g., Figure 2). The nonadiabatic behavior of Na^+ ions within rolled up KH vortices thus appears as a robust feature of planetary plasma transport in Mercury's magnetospheric flanks. Also, in view of the results of Figure 5, we may speculate that, during the KH nonlinear phase with ***E*** variations on smaller scales, particles with smaller gyroradii may be transported in a nonadiabatic manner as well. The present study was dedicated to theoretical investigation of the planetary Na^+ dynamical behavior. A detailed comparison with MESSENGER data and examination of the efficiency of this nonadiabatic transport for plasma mixing and energization at the magnetopause will be the subject of a future study.

5. Conclusions

MESSENGER observations in the dusk flank of Mercury's magnetosphere provide evidences of Kelvin-Helmholtz instability development in the vicinity of the magnetopause. Test particle simulations performed in an MHD model of such KH vortices demonstrate that exosphere originating Na^+ ions can be subjected to prominent nonadiabatic transport in this region of space due to a rapid (although localized) intensification of the large-scale electric field. The net energy gain realized by the particles nears the maximum $\boldsymbol{E} \times \boldsymbol{B}$ drift energy encountered along their paths when the time scale of the electric field burst is comparable to or smaller than the particle gyroperiod. Such an energy gain leads to scattering of the particles toward the perpendicular direction. This localized nonadiabatic transport of planetary material may play a prominent role in mixing of magnetosphere and magnetosheath populations in the magnetopause vicinity.

Acknowledgments
The work of S. Aizawa was supported by the International Joint Graduate Program in Earth and Environmental Sciences (GP-EES). The methods used in this paper are properly cited and referred to in the reference list. The computed data are available from a repository (http://c.gp.tohoku.ac.jp/~teradan/simulation/mercury/aizawa_18grl).

References

Ashour-Abdalla, M., Zelenyi, L. M., Peroomian, V., & Richard, R. L. (1994). Consequences of magnetotail ion dynamics. *Journal of Geophysical Research*, *99*(A8), 14891. https://doi.org/10.1029/94JA00141

Ashour-Abdalla, M., Zelenyi, L. M., Peroomian, V., & Rocjard, R. L. (1993). On the structure of the magnetotail current sheet. *Geophysical research Letters*, *20*(19), 2019–2022. https://doi.org/10.1029/93GL01695

Büchner, J., & Zelenyi, L. M. (1989). Regular and chaotic charged particle motion in magnetotaillike field reversals: 1. Basic theory of trapped motion. *Journal of Geophysical Research*, *94*(A9), 11821. https://doi.org/10.1029/JA094iA09p11821

Delcourt, D. C. (2002). Particle acceleration by inductive electric fields in the inner magnetosphere. *Journal of Atmospheric and Solar - Terrestrial Physics*, *64*(5-6), 551–559. https://doi.org/10.1016/S1364-6826(02)00012-3

Delcourt, D. C., Grimald, S., Leblanc, F., Berthelier, J.-J., Millilo, A., Mura, A., … Moore, T. E. (2003). A quantitative model of planetary Na^+ contribution to Mercury's magnetosphere. *Annales de Geophysique*, *21*(8), 1723–1736. https://doi.org/10.5194/angeo-21-1723-2003

Gershman, D. J., Raines, J. M., Slavin, J. A., Zurbuchen, T. H., Sundberg, T., Boardsen, S. A., … Solomon, S. C. (2015). MESSENGER observations of multiscale Kelvin-Helmholtz vortices at Mercury. *Journal of Geophysical Research: Space Physics*, *120*, 4354–4368. https://doi.org/10.1002/2014JA020903

Keppens, R., Tóth, G., Westermann, R. H. J., & Goedbloed, J. P. (1999). Growth and saturation of the Kelvin-Helmholtz instability with parallel and antiparallel magnetic fields. *Journal of Plasma Physics*, *61*(1), 1–19. https://doi.org/10.1017/S0022377898007223

Kurganov, A., & Tadmor, E. (2000). New high-resolution central schemes for nonlinear conservation laws and convection-diffusion equations. *Journal of Computational Physics*, *160*(1), 241–282. https://doi.org/10.1006/jcph.2000.6459

Nagano, H. (1978). Effect of finite ion Larmor radius on the Kelvin-Helmholtz instability. *Journal of Plasma Physics*, *20*(02), 149. https://doi.org/10.1017/S0022377800021450

Northrop, T. G. (1963). *The adiabatic motion of charged particles*. New York: Wiley Intersci.

Peer, A. A. I., Gopaul, A., Dauhoo, M. Z., & Bhuruth, M. (2008). A new fourth-order non-oscillatory central scheme for hyperbolic conservation laws. *Applied Numerical Mathematics*, *58*(5), 674–688. https://doi.org/10.1016/j.apnum.2007.02.004

Raines, J. M., Gershman, D. J., Zurbuchen, T. H., Sarantos, M., Slavin, J. A., Gilbert, J. A., … Solomon, S. C. (2013). Distribution and compositional variations of plasma ions in Mercury's space environment: The first three Mercury years of MESSENGER observations. *Journal of Geophysical Research: Space Physics*, *118*, 1604–1619. https://doi.org/10.1029/2012JA018073

Rothwell, P. L., Silevitch, M. B., Block, L. P., & Fälthammar, C.-G. (1994). O^+ phase bunching and auroral arc structure. *Journal of Geophysical Research*, *99*(A2), 2461. https://doi.org/10.1029/93JA02541

Slavin, J. A., Acuña, M. H., Anderson, B. J., Baker, D. N., Benna, M., Gloeckler, G., … Zurbuchen, T. H. (2008). Mercury's magnetosphere after MESSENGER's first flyby. *Science*, *321*(5885), 85–89. https://doi.org/10.1126/science.1159040

Slavin, J. A., DiBraccio, G. A., Gershman, D. J., Imber, S. M., Kai Poh, G., Raines, J. M., … Solomon, S. C. (2014). MESSENGER observations of Mercury's dayside magnetosphere under extreme solar wind conditions. *Journal of Geophysical Research: Space Physics*, *119*, 8087–8116. https://doi.org/10.1002/2014JA020319

Sundberg, T., Boardsen, S. A., Scott, A., Slavin, J. A., Blomberg, L. G., Cumnock, J. A., … Korth, H. (2011). Reconstruction of propagating Kelvin-Helmholtz vortices at Mercury's magnetopause. *Planetary and Space Science*, *59*(15), 2051–2057. https://doi.org/10.1016/j.pss.2011.05.008

Sundberg, T., Boardsen, S. A., Slavin, J. A., Anderson, B. J., Korth, H., Zurbuchen, T. H., … Solomon, S. C. (2012). MESSENGER orbital observations of large-amplitude Kelvin-Helmholtz waves at Mercury's magnetopause. *Journal of Geophysical Research*, *117*, A04216. https://doi.org/10.1029/2011JA017268

Sundberg, T., Slavin, J. A., Boardsen, S. A., Anderson, B. J., Korth, H., Ho, G. C., … Solomon, S. C. (2012). MESSENGER observations of dipolarization events in Mercury's magnetotail. *Journal of Geophysical Research*, *117*, A00M03. https://doi.org/10.1029/2012JA017756

Zurbuchen, T. H., Raines, J. M., Gloeckler, G., Krimigis, S. M., Slavin, J. A., Koehn, P. L., … Solomon, S. C. (2008). MESSENGER observations of the composition of Mercury's ionized exosphere and plasma environment. *Science*, *321*(5885), 90–92. https://doi.org/10.1126/science.1159314

Zurbuchen, T. H., Raines, J. M., Slavin, J. A., Gershman, D. J., Gilbert, J. A., Gloeckler, G., … Solomon, S. C. (2011). MESSENGER observation s of the spatial distribution of planetary ions near Mercury. *Science*, *333*(6051), 1862–1865. https://doi.org/10.1126/science.1211302